

NOVEL METHODS FOR NOISE LEVEL REDUCTION AT TURBINE EXIT GUIDE VANES AND CASING END WALLS OF FUTURE AERO ENGINES

Doctoral Thesis

in fulfilment of the requirements for the academic degree
Doktor der technischen Wissenschaften (Dr. techn.)

Dipl.-Ing. Manuel Zenz, BSc

submitted at the
Institute for Thermal Turbomachinery and Machine Dynamics
Faculty of Mechanical Engineering
Graz University of Technology

First Expert: Priv.-Doz. Dipl.-Ing. Dr. techn. Andreas Marn

Second Expert: Ao. Univ. Prof. Dipl.-Ing. Dr. techn. Reinhard Willinger



Graz, August 2020

*Two possibilities exist...
Either we are alone in the universe or we are not.
Both are equally terrifying*

Arthur C. Clarke

Statutory Declaration

I declare that I have authored this thesis independently, that I have not used other than the declared sources / resources, and that I have explicitly marked all material which has been quoted either literally or by content from the used sources.

Eidesstattliche Erklärung

Ich erkläre an Eides statt, dass ich die vorliegende Arbeit selbstständig verfasst, andere als die angegebenen Quellen / Hilfsmittel nicht benutzt und die den benutzten Quellen wörtlich und inhaltlich entnommenen Stellen als solche kenntliche gemacht habe.

Graz, am/at _____

Dipl.-Ing. Manuel Zenz BSc

Abstract

Modern state-of-the-art aero engines have to fulfil a various number of requirements. The main goals are to increase the endurance and efficiency while lowering the weight and fuel consumption. But also the reduction of emitted noise is of high importance. In the last decades, many investigations concerning this topic were conducted for all components (fan, turbine, compressor, combustor) of an engine. To further reduce the emitted noise, every possibility has to be taken into account. Because the low pressure turbine (LPT) is one of the main contributor of the noise emissions, a reduction there would be of great benefit. One possibility to do so, is the inclusion of acoustic liners. Such devices are already successfully used in the inlet and the bypass duct, to reduce fan noise, of aero engines but not yet in a LPT. In fact, the rough environment in the core duct exit including high temperatures, high flow velocities, as well as the presence of higher order acoustic duct modes and the limited space in this engine component is the reason for not using them there.

This thesis is about the implementation of such acoustic liners in an engine representative one and a half stage low pressure turbine test rig, which corresponds to the last stage of an aero engine, located at Graz University of Technology. Absorbers were integrated in the turbine exit guide vanes (TEGV) as well as in the outer and inner duct end walls of the vane passages. Investigations concerning the change of the absorber neck diameter onto the noise attenuation performance were done.

Additional investigations were done by applying so-called riblets on the suction side of the exit guide vanes. This microstructure, inspired by the shark skin, is primarily used to reduce skin friction and therefore to increase the aerodynamic performance of a device. In the present work, their ability of lowering noise is examined by connecting the sound generation mechanisms with the aerodynamics according to Lighthills acoustic analogy.

Measurements were successfully carried out concerning the acoustical and aerodynamical behaviour of all mentioned optimised devices and compared with baseline configurations. The chosen operating point was the noise certification point Approach, which represents operating conditions of a civil aircraft during the landing phase. It could be shown, that all the investigated components have the ability to reduce the overall emitted noise level. The physical reasons behind this reduction are different from case to case and reported here.

To summarize, although there is a rough environment at the location of the low pressure turbine, a significant noise reduction could be achieved by including acoustically optimized components. The results of engine representative investigations showed a significant benefit of implementing acoustic liners at the LPT.

Nomenclature

Abbreviations

APP	Approach
BPF	Blade Passing Frequency
CC	Combustion Chamber
FHP	Five – Hole – Probe
FoI	Frequency of Interest
HPC	High Pressure Compressor
HPT	High Pressure Turbine
IGV	Inlet Guide Vane
LE	Leading Edge
LPC	Low Pressure Compressor
LPT	Low Pressure Turbine
LPV	Lower Passage Vortex
PWL	Sound Power Level
STTF-AAAI	Subsonic Test Turbine Facility for Aerodynamic, Acoustic, and Aeroelastic Investigations
SPL	Sound Pressure Level
TE	Trailing Edge
TEC	Turbine Exit Casing
TEGV	Turbine Exit Guide Vane
UPV	Upper Passage Vortex
VF	Vibration Frequency

Latin Symbols

A	Complex amplitude	
A	Acoustic admittance	[m ² /kg]
A	Cross section area	[m ²]
B	Blade count	[-]
b	Wake width, distance	[m]
c	Speed of sound	[m/s]
f	Modal shape factor	[-]
f	Frequency	[Hz]
h	Harmonic index	[-]
h	Specific enthalpy	[m ² /s ²]
H	Shape factor, frequency response function	[-]
k	Wave number	[1/m]
k	Integer number, boundary layer parameter	[-]
k	Spring stiffness	[kg/s ²]
l	Length	[m]
m	Azimuthal mode order	[-]
m	Mass	[kg]
Ma	Mach number	[-]
n	Radial mode order	[-]
n	Rotational speed	[rpm]
p	Pressure	[Pa]
P	Sound power level	[dB]

R	Outer radius of the annulus	[m]
R	Reflection coefficient	[-]
R	Specific gas constant of air	[J/kgK]
s	Rib tip spacing, distance	[m]
S	Cross sectional area	[m ²]
r	Radius	[m]
t	Time	[s]
T	Lighthill tensor	
T	Temperature	[K]
U	Velocity component	[m/s]
v	Velocity	[m/s]
V	Vane count	[-]
V	Volume	[m ³]
x	Spatial coordinate	[m]
Z	Acoustic impedance	[kg s/m ²]

Greek Symbols

α	Yaw angle	[deg]
α	complex factor, absorption coefficient	[-]
α	axial wave number	[1/m]
γ	Adiabatic gas index	[-]
δ	Wake parameter, neck end correction	[m]
δ	Particle displacement	[m]
Δ	Laplace operator	
λ	Wavelength	[m]
μ	Dynamic viscosity	[kg/m s]
ν	Velocity	[m/s]
ν	Kinematic viscosity	[m ² /s]
ρ	Density	[kg/m ³]
σ	Eigenvalue of the Bessel function, area ratio	[-]
τ	Viscous stress tensor	
φ	Circumferential coordinate	[deg]
ψ	Stage loading parameter	[-]
Ω	Rotational speed	[rpm]
ω	Angular frequency	[1/s]

Subscript

ax	Axial
cut	Cut-off
i	Inner
in	Incident
m, n	Azimuthal, radial mode order
o	Outer
od	Off-design point
r	Resonance
ref	Reflected
t	Total
tr	Transmitted

Superscript

\pm	Propagation in (+) and against (-) the flow direction
\sim	Area averaged
$\bar{\sim}$	Mass averaged
'	Fluctuation
$-$	Time averaged
*	Scattered mode

Table of Content

1	Introduction	1
2	Theoretical Background.....	7
2.1	Acoustics	7
2.1.1	Sound Generation in Turbines.....	7
2.1.2	Sound Propagation.....	9
2.1.3	Boundary Condition Change Due to Different End Wall Characteristics	15
2.1.4	The Cut-Off Condition.....	16
2.1.5	About Discontinuities in a Duct	17
2.2	Theory of Acoustic Resonators	20
2.2.1	Reflection Coefficient.....	21
2.2.2	Basic Liner Concepts	22
2.3	Aerodynamics.....	28
2.3.1	Blade and Vane Passage	28
2.3.2	Rotor Tip Leakage Flow	31
2.3.3	Analysis of a Trailing Edge Wake.....	32
2.4	Riblets	34
2.4.1	The Riblets Effect.....	35
2.4.2	Acoustic Analysis of Riblets – Lighthills Acoustic Analogy	37
2.5	Operating Point Definition – Aircraft Noise Certification.....	40
3	Literature Study	41
3.1	Literature of Acoustic Liners and their use in Turbomachines	41
3.2	Literature on Riblets	43
3.3	Overview on Compressor / Turbine Aerodynamics	45
4	Experimental Facility.....	47
4.1	Subsonic Test Turbine Facility.....	47
4.2	Operating Conditions and Stage Geometry.....	48
4.3	Turbine Exit Guide Vanes.....	49
4.3.1	Standard and Helmholtz Vanes	50
4.3.2	Resonator Vanes	52
4.3.3	Standard Vanes with Riblets	53
4.3.4	Leaned Vanes	54
4.4	Soft End Walls.....	55
4.5	Impedance Tube.....	59

5	Measurement Setup.....	63
5.1	Acoustics	63
5.2	Aerodynamics.....	65
5.2.1	Five – Hole – Probe	65
5.2.2	Trailing Edge Probe.....	70
5.2.3	Oil Flow Visualization.....	70
5.3	Measurement Uncertainties.....	71
5.4	Acoustic Post Processing	71
5.4.1	Adaptive Resampling.....	72
5.4.2	Phase Averaging	72
5.4.3	Azimuthal Mode Analysis (AMA).....	73
5.4.4	Radial Mode Analysis (RMA)	75
5.4.5	Calculation of the Modal Sound Power.....	75
6	Results and Discussion.....	76
6.1	Pre-tests – Impedance - Tube	76
6.2	Test Rig Investigations.....	86
6.2.1	Helmholtz Vanes	90
6.2.2	Soft End Walls.....	99
6.2.3	Combination of Helmholtz Vanes and Soft End Walls	109
6.2.4	Resonator Vanes	112
6.2.5	Acoustical Comparison of Lined Configurations.....	117
6.2.6	Riblets	124
7	Conclusions	134
8	Publications	138
8.1	Journal Publications.....	138
8.2	Conference Publications.....	138
9	List of Figures.....	140
10	List of Tables	144
11	References.....	145
12	Annex.....	152
12.1	Change of Modal Content due to Impedance Discontinuity	152
12.2	Riblets Investigations in an Off-design Point.....	157
12.3	Inverse Cut-off Vane Design Including Microperforated Absorbers.....	160
12.4	Peak Reduction Procedure.....	164

1 Introduction

Due to the steady growth of worldwide commercial air traffic, regulations concerning the pollution of the environment have been defined by the Advisory Council for Aeronautical Research in Europe (ACARE) in a paper called 'Vision 2020'. The goals defined in there are a reduction of CO₂ emissions by 50%, NO_x emissions by 80% and in addition a reduction of the perceived noise level by 50% (10 dB) with respect to a modern aircraft of the year 2000. All these goals have been set to be reached in the year 2020. Meanwhile, the boundary conditions changed what lead to a reformulation of the goals and to an extension for a successful achievement until the year 2050. The new plan was then called 'Flightpath 2050', was released in 2011 and set new targets: a reduction of the CO₂ emissions per passenger kilometre by 75%, a decrease of the NO_x emissions by 90%, and a perceived noise reduction of a flying aircraft by 65% (15 dB) relative to the technology in 2000 (see also [1]).

Noise emissions of an aircraft are not only due to the engines. Figure 1.1 shows the main sources of aircraft noise directly on a modern airplane. The contributing components of the airframe itself are depicted in green, which become more relevant during the landing phase, sources of the aero engine are written in red, and interaction noise of the engine and the frame components are shown in blue. Airframe noise is mainly due to unsteady flow over the flap, slats, and landing gear, particularly in the case of landing. The noise generated by the engine can be split up into the sources fan, compressor, combustion chamber, turbine, and the jet.

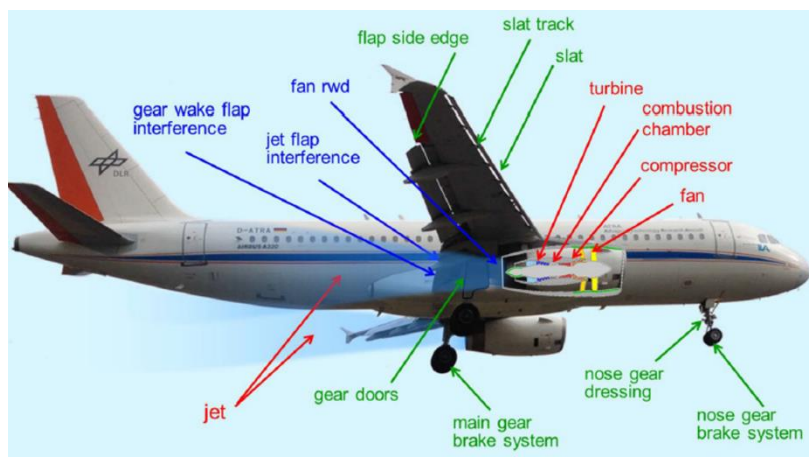


Figure 1.1: Noise sources of a modern airplane (taken from [2])

The emitted aircraft noise is geographically seen a local problem, in terms of the flight phase. Especially the phases takeoff (departure) and approach (landing) are of high importance to the surrounding environment of an airport. In fact, cities are growing and the urban borders get closer and closer to existing flightpaths of these two flight phases. People living there are then feeling this as “acoustical pollution”. Since the launch of the first turbojet engines in the early 1960s, already a lot has been achieved concerning the noise emission reduction. The big steps in decreasing the noise level depicted in Figure 1.2 are mostly due to changes in design and increase in bypass ratio, which is the ratio between the air mass flow rate outside of the core (bypass duct) and inside the core duct.

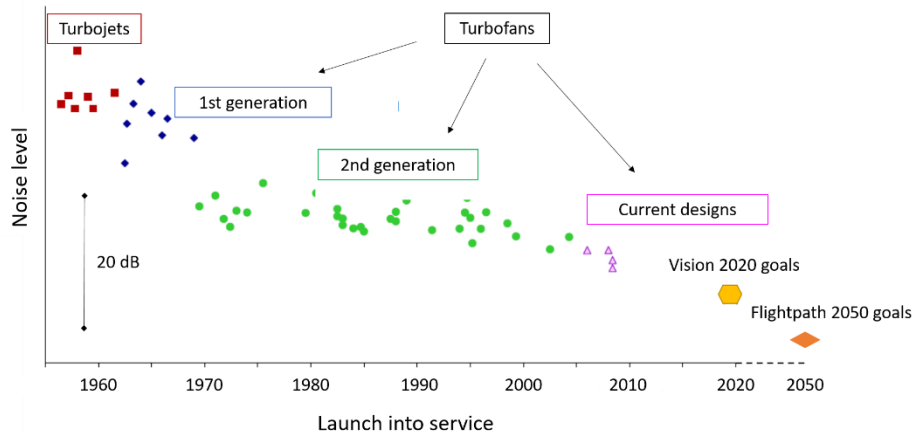


Figure 1.2: History of aircraft noise reduction (adapted from [2])

An example for a modern 2 spool high bypass ratio aero engine is given in Figure 1.3. Having a certain amount of air mass flowing outside of the core through the bypass duct, in addition to the mass flow through the core duct, reduces the specific thrust f of an engine while keeping the thrust F constant. This can be seen by the definition of the specific thrust

$$f = \frac{F}{\dot{m}} \quad (1.1)$$

Due to this additional thrust of the bypass duct, the exhaust velocity of the jet can be decreased to result in the same overall thrust as with only a core duct (turbojet engine). This exhaust jet velocity is directly connected with the broadband noise generation by the engine.

With a large fan diameter also disadvantages occur. The diameter and hence the rotational speed are limited by the occurring maximum blade tip velocity, the load capacity at the connection of the blade root and the disc, as well as the increasing weight. Hence, also the rotational speed of the low pressure turbine and the low pressure compressor, which are all connected via a shaft, are limited. A low rotational speed of the turbine is not wanted because the power output is directly connected with it. This problem can be solved by a more aggressive duct between the HPT and the LPT, increasing the diameter of the flow path, and therefore also the circumferential velocity at the LPT, rapidly. These ducts are known as mid turbine frame, turbine centre frame or intermediate turbine duct.

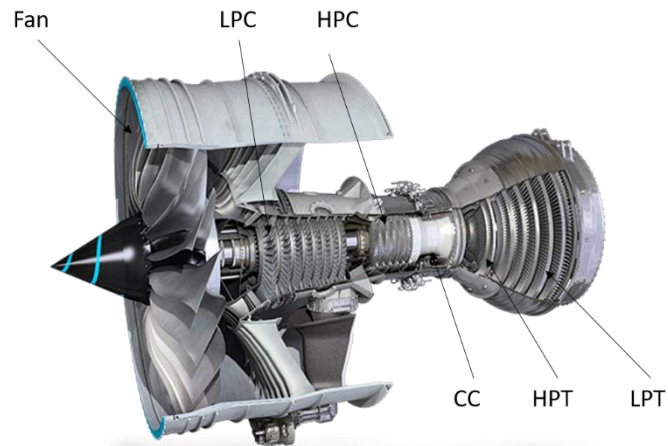


Figure 1.3: Modern high-bypass turbofan engine Trent 7000 (adapted from [3])

Without using such an aggressive duct another possibility to raise the power output of the turbine is needed. Due to this, the next step towards a more efficient engine design was to include a gear box between the fan and the LPT, which decouples these two parts from each other. This allows both components to be operated closer to their respective optimum operating speed. Figure 1.4 shows an example of a geared turbofan. Another advantage of such an engine is the fact that less stages, compressor as well as turbine stages, are needed which results in less weight and consequently also in less fuel consumption.

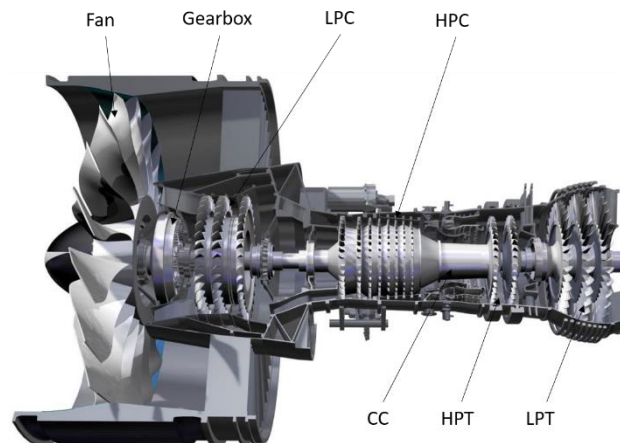


Figure 1.4: Modern geared turbofan PW1100G (adapted from [4])

In Figure 1.5, a comparison between a geared turbofan and a conventional two spool aero engine is shown, concerning the number of stages. Especially the HPC and the LPT work with way less stages with respect to a two-spool engine, resulting in a shorter overall length of the engine.

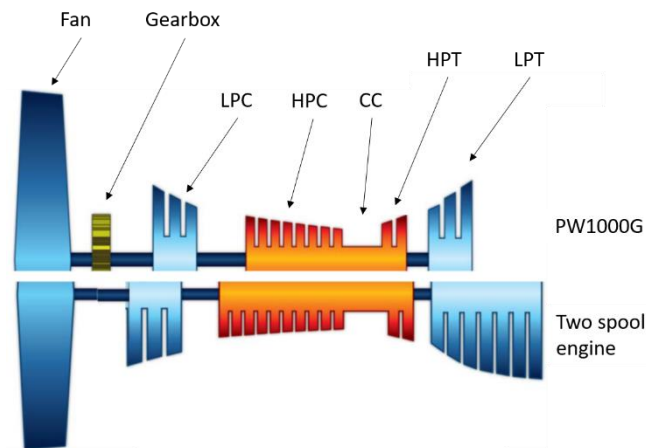


Figure 1.5: Comparison of a geared turbofan (top) and a conventional turbofan (bottom) (adapted from [5])

With the decrease of the engine broadband noise due to the reduction of the jet exhaust velocity, the tonal noise of the fan has become a more dominant contributor to the overall noise emissions. A solution was found by implementing acoustically absorbing devices in the intake duct. The most common device in use are acoustic absorbers, especially from the type $\lambda/4$ absorber, which consists of a perforated face sheet backed by a cavity with a depth corresponding to the quarter wavelength of the frequency which should be dampened. But, it is only an efficient noise reducing device at this certain frequency, where the damping effect is the highest, and a narrow bandwidth around this frequency of interest. If designed properly, this bandwidth can be extended to a reasonable size.

Anyway such acoustic liners have to fulfil many requirements, as for example a high efficiency over a wide range of operating conditions, low weight, cost efficiency in manufacturing and maintenance. A special problem is the limited space which can be provided by the existing engine design, due to the goal of compact designs. Additionally, the aerodynamics of lined areas have still to fulfil their desired performance. Figure 1.6 shows the intake of a lined aero engine. These liners are in general designed according to the first and second blade passing frequency of the fan.

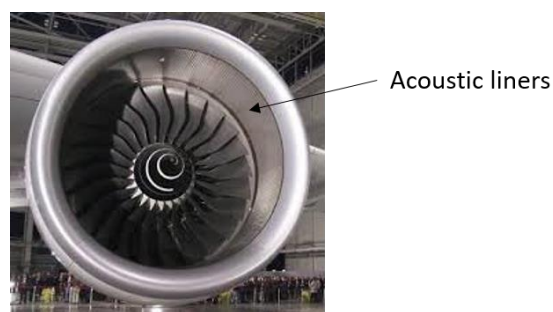


Figure 1.6: Acoustic liners at the inlet of an Airbus A380 (adapted from [6])

The duct inlet has not been the only possible location to include acoustic liners, which can be seen in the following figure. Obviously, the bypass duct is most suitable, besides the engine inlet, for such components while the core duct is not much of use for applying absorbers in commercial aircraft engines so far. Reasons for this could be the rough environment in terms of high temperature, high flow velocities, multiple acoustic interaction modes etc. But also the strong 3D curvature makes an implementation difficult also due to the already mentioned limited existing space. In the core duct it is even more important to avoid negative effects on the aerodynamical performance of the components.

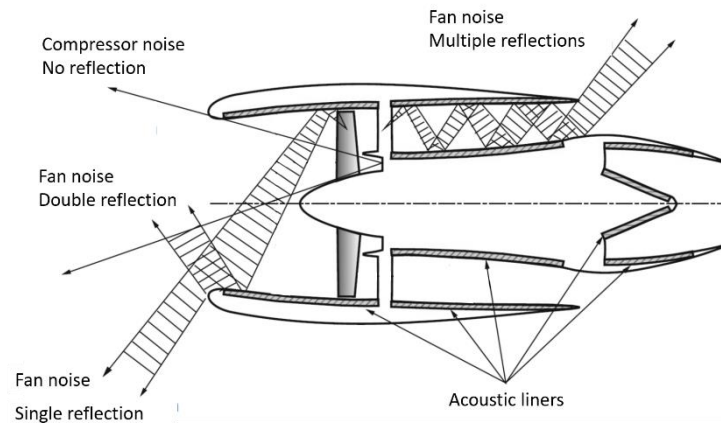


Figure 1.7: Possible locations for acoustic liners (adapted from [7])

A breakdown of the engine noise into its main components concerning their contribution at the flight phases takeoff and approach can be seen in Figure 1.8. This data is valid for a modern high bypass ratio turbofan aircraft. Both cases show, that the fan is, besides the jet, a major contributor to the overall noise emitted by an aircraft. In total, the engine has the higher sound power level compared with the airframe. Research projects have been conducted to reduce the noise at each of the shown sources, for example by improved inlet liners and lip liners, chevrons at the rear part of the engine or quieter landing gear [8].

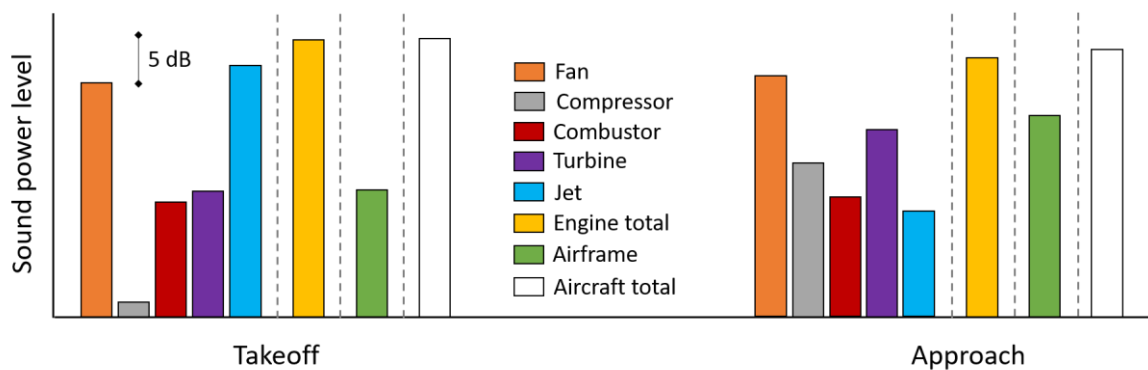


Figure 1.8: Contributors to aircraft noise (adapted from [9])

After decreasing the jet noise (higher bypass ratio) and reducing also the noise emitted by the fan (implementing acoustic liners in the engine inlet, reducing the rotational speed), the turbine becomes a big contributor to the overall noise, especially at the flight phase approach. Investigations showed, that the sound field downstream of the turbine exit casing is dominated by the blade passing frequencies, which are unavoidable. Especially the first blade passing frequency of a rotating stage is dominant, which can be seen in Figure 1.9. In this figure, an exemplary spectrum of a low bypass ratio engine is depicted. As indicated, multiple blade passing frequencies and harmonics of the respective stage of an engine are present, as well as the noise generated by the interaction of the stages (differential noise).

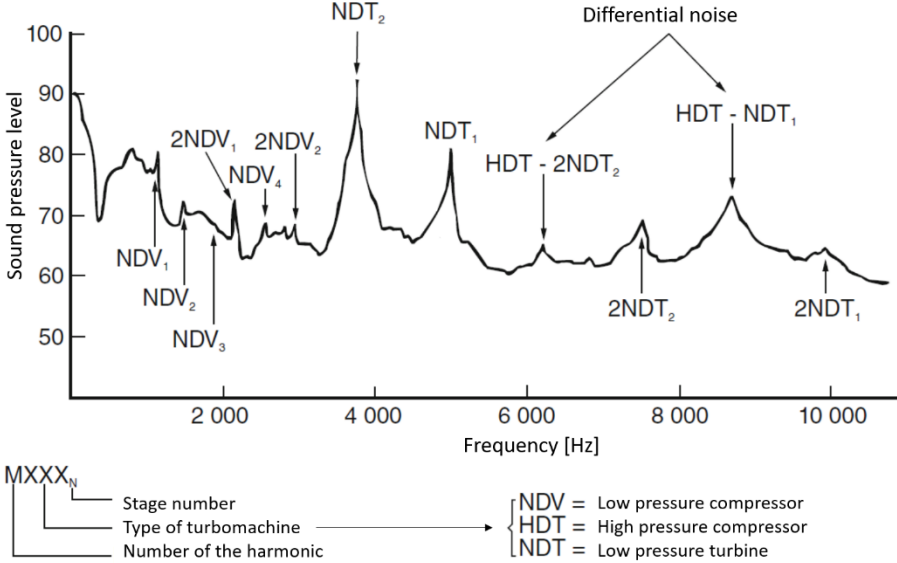


Figure 1.9: Example of a noise spectrum from a low bypass ratio engine (adapted from [7])

Reducing the mentioned first blade passing frequency of the low pressure turbine would lead to a great benefit concerning the overall noise emissions of the engine. Similar to the absorbers used for the fan blade passing frequency, also liners inside the engine could be used to reach this goal. As mentioned before, the core duct is not much of use concerning the application of acoustic liners. Consequently, there is still room for improvements using such devices to be able to achieve the goals set in the project Flightpath 2050. Investigations on the possible use of these liners in this actual location, more specific in the last stage of the low pressure turbine, is one of the main topics worked on in the present thesis.

2 Theoretical Background

This section contains a theoretical background of the different fields which have been in the focus of the investigations done during this work. First, an introduction of the main topic acoustics is given followed by a deeper look in the theory of different resonator types and their working principle. The second part is containing the field of aerodynamics, especially concerning thermal turbomachines. At the end, the physics of so called riblets, which have been used as another noise reduction method, is described.

2.1 Acoustics

The main topic within this thesis is how to influence the acoustical behaviour of a turbomachine using devices to reduce the emitted noise. Based on this, the acoustic field downstream of the turbine exit guide vanes is investigated. This includes the knowledge of sound generation and propagation in aero engines, what is described in the following subsections.

2.1.1 Sound Generation in Turbines

The main noise sources of a turbofan engine are the fan, the compressor, the turbine, and the combustor. By increasing the bypass ratio of modern aircraft engines, the noise emission of the jet could be decreased due to a lower exit velocity. This led to more pronounced contributions in the overall noise emission of an engine from the compressor and turbine stages. Depending on the operating point of an engine, the contingent of the noise contributor concerning the overall emitted noise changes.

The total noise of an aircraft engine is a combination of broadband noise and of tonal noise which is produced by the components of the engine.

Tonal Noise

Tonal noise is a discrete tone which results in a single peak in a frequency spectrum. It is the most important part of noise generated in an aircraft engine and results from a periodic non-

uniformity of the flow field such as pressure fluctuations caused by a rotating blade row. The frequency of these periodic fluctuations can be calculated with the following equation and is called Blade Passing Frequency (BPF). This equation is valid for a rotor alone generated noise.

$$BPF = \frac{n \cdot B}{60} \quad (2.1)$$

Herein, B is the number of rotor blades and n is the rotor rotational speed in rpm. Other peaks of this tonal noise are generated at integer multiples called higher harmonics. Usually, but not necessarily, the higher the number of the harmonic is, the lower its amplitude becomes.

An aircraft engine has a number of combinations of rotating blade rows and stationary vanes. The interaction of these components results again in tonal noise. Tyler and Sofrin [10] named three main sources of noise generated by these interactions:

- The cutting of wakes from an upstream located stator by a rotor
- The collision of rotor wakes and downstream located stator vanes
- The impact of the potential effect of stator vanes onto a rotor

According to Tyler and Sofrin it is possible to make a linear combination of a stator and a rotor which results in a characteristic pressure pattern. These patterns are also known as modes m and can be calculated as follows under the assumptions that each wake produces only one pressure perturbation and that reflections on neighbouring vanes are neglected.

$$m = h \cdot B + k \cdot V \quad (2.2)$$

Herein, h is the harmonic index of the BPF ($h = 1, 2, 3, \dots$), B is the number of rotor blades, k is a positive or negative integer value ranging between plus and minus infinite, and V is the number of stator vanes.

For a certain circumferential mode m the rotational speed can be calculated as follows

$$\Omega_m = \Omega \frac{h \cdot B}{m} = \Omega \frac{h \cdot B}{h \cdot B + k \cdot V} \quad (2.3)$$

It can be seen, that according to the sign of k the rotational direction of the mode is not always identical to the rotor rotational direction. Depending on this, a mode is either co-rotating (same direction) or counter-rotating (opposing direction).

Equation (2.2) can be extended to be able to investigate more stages in an engine. The mode m is scattered at another vane row with the vane count V_2 and an integer value k_2 according to the following equation showing the scattered mode m^*

$$m^* = m + k_2 \cdot V_2 \quad (2.4)$$

Theoretically, there is an infinite number of interaction modes. But in reality the number is limited by the duct geometry. This limit is called cut-off condition (explained in upcoming section 2.1.4) and has a certain frequency, the cut-off frequency, to specify a minimum for a certain mode order which is needed to be able to propagate.

Broadband Noise

Broadband noise is emitted noise in a wide frequency range. This second type of noise is caused, amongst others, by fluctuating pressure distributions or forces on vanes respectively. Reason for this is a discontinuity flow, due to a changing incident angle, which is hitting the leading edge of the vanes. This can lead for example to a separation or other turbulent structures like vortices.

If there are more than one stages, such structures can lead again to a wrong incidence angle for downstream located vane or blade rows. Running an engine in an off-design point leads to this situation. Therefore, also the broadband noise is an important part of the overall noise although the tonal noise is a significantly higher contributor.

2.1.2 Sound Propagation

This section should serve as an explanation for the propagation of sound in general, which can be described by the wave equation which is shown in equation (2.5) for the sound pressure p'

$$\frac{1}{c^2} \frac{\partial^2 p'}{\partial t^2} - \Delta p' = 0 \quad (2.5)$$

With $\Delta = \frac{\partial^2}{\partial x^2} + \frac{\partial^2}{\partial y^2} + \frac{\partial^2}{\partial z^2}$ being the Laplace operator for this coordinate system. From this equation can be seen that the pressure perturbation p' is propagating with the speed of sound c . When looking at a plane wave, only one spatial dimension is of interest. In the following equation, this direction of the wave propagation is described with x .

$$\frac{1}{c^2} \frac{\partial^2 p'}{\partial t^2} = \frac{\partial^2 p'}{\partial x^2} \quad (2.6)$$

The solution for this one-dimensional wave equation is according to d'Alembert

$$p' = F(ct - x) + G(ct + x) \quad (2.7)$$

wherein F and G describe random, real functions which have at least two derivatives. $F(ct - x)$ is a wave, which propagates on the curve $ct - x = \text{constant}$ in the positive x -direction and $G(ct + x)$ propagates on the curve $ct + x = \text{constant}$ in the negative one.

Cylindrical flow duct without hub

Because this section is about the sound propagation in a cylindrical flow duct, it is necessary to transform equation (2.5) into cylindrical coordinates.

$$\frac{1}{c^2} \frac{\partial^2 p'}{\partial t^2} - \frac{1}{r} \frac{\partial}{\partial r} \left(r \frac{\partial p'}{\partial r} \right) - \frac{1}{r^2} \frac{\partial^2 p'}{\partial \theta^2} - \frac{\partial^2 p'}{\partial x^2} = 0 \quad (2.8)$$

To solve this partial differential equation, a separation of the variables has to be performed.

$$p'(x, r, \theta, t) = f(x) \cdot g(r) \cdot h(\theta) \cdot e^{i\omega t} \quad (2.9)$$

After deriving and inserting this equation into the wave equation (2.8) yields to following

$$\left(\frac{\omega}{c}\right)^2 + \frac{1}{f} \frac{d^2 f}{dx^2} + \frac{1}{g} \left[\frac{1}{r} \frac{d}{dr} \left(r \frac{dg}{dr} \right) \right] + \frac{1}{h} \frac{1}{r^2} \frac{d^2 h}{d\theta^2} = 0 \quad (2.10)$$

To be able to determine the functions $f(x)$, $g(r)$ and $h(\theta)$ it is necessary that the left and right side of this equation are identical. The only possible way to ensure this for all combinations of x , r and θ is, that both sides are constant. This leads to the following equations

$$\frac{1}{h} \frac{d^2 h}{d\theta^2} = -\sigma^2 \quad (2.11)$$

$$\frac{1}{f} \frac{d^2 f}{dx^2} = -\alpha^2 \quad (2.12)$$

The solution concerning the r coordinate is not that simple because the terms including a dependency on this coordinate can't be isolated from the other terms. In this case, one of the constants α or σ needs to be known already. It is assumed, that σ is known, which leads to the following equation

$$\frac{1}{h} \frac{1}{r^2} \frac{d^2 h}{d\theta^2} = -\frac{\sigma^2}{r^2} \quad (2.13)$$

Inserted into (2.10) gives

$$\frac{1}{g} \left[\frac{1}{r} \frac{d}{dr} \left(r \frac{dg}{dr} \right) \right] - \frac{\sigma^2}{r^2} = -\left(\frac{\omega}{c}\right)^2 - \frac{1}{f} \frac{d^2 f}{dx^2} \quad (2.14)$$

In equation (2.14) only the left side is dependent on r which gives a third constant named β

$$\frac{1}{g} \left[\frac{1}{r} \frac{d}{dr} \left(r \frac{dg}{dr} \right) \right] - \frac{\sigma^2}{r^2} = -\beta^2 \quad (2.15)$$

Substituting (2.12) and (2.15) into the wave equation (2.10) leads to the following relation

$$\left(\frac{\omega}{c}\right)^2 = \alpha^2 + \beta^2 = k^2 \quad (2.16)$$

As a first step, the function $h(\theta)$ can be determined according to the following ansatz

$$h(\theta) = A_3 e^{-i\sigma\theta} + B_3 e^{i\sigma\theta} \quad (2.17)$$

Herein, the constants A_3, B_3 and σ have to be determined in a way that they satisfy the boundary conditions of $h(\theta)$ which are at $\theta = 0$ and $\theta = 2\pi$. The location of $\theta = 0$ should have no influence on the solution of the wave equation. Additionally, the periodic boundary condition $h(\theta) = h(\theta + 2\pi)$ needs to be fulfilled. Therefore, it is required that the constant σ has to have an integer value. This results in a not unique solution of the constant. The same is valid for A_3 and B_3 which can also be chosen independently from each other.

The first step to get to a solution for the function $g(r)$ is to rearrange equation (2.15)

$$r^2 \frac{d^2 g}{dr^2} + r \frac{dg}{dr} + r^2 \beta^2 - \sigma^2 g = 0 \quad (2.18)$$

This form of equation is the so-called Bessel differential equation. Its solution is a combination of the Bessel function 1st kind J_m and the Bessel function 2nd kind or Neumann function Y_m and can be written as follows

$$g(r) = A_2 \cdot J_m(\beta r) + B_2 \cdot Y_m(\beta r) \quad (2.19)$$

With m being the order of the function.

One boundary condition for this function is a hard wall at the outer duct wall $r = R$. This means, that at this position, the velocity normal to the wall is zero (no movement at this position). Therefore, the pressure gradient has to fulfill the requirement $\frac{dp'}{dr} \Big|_{r=R} = 0$.

The second boundary condition for the center of the duct ($r = 0$) is that there can't be a source term. Otherwise it would lead to a singularity. Therefore, the function B_2 in equation (2.19) has to be zero to eliminate the Bessel function 2nd kind. Figure 2.1 shows the distribution of both functions for the first six modes $m = [0, 5]$ over the diameter.

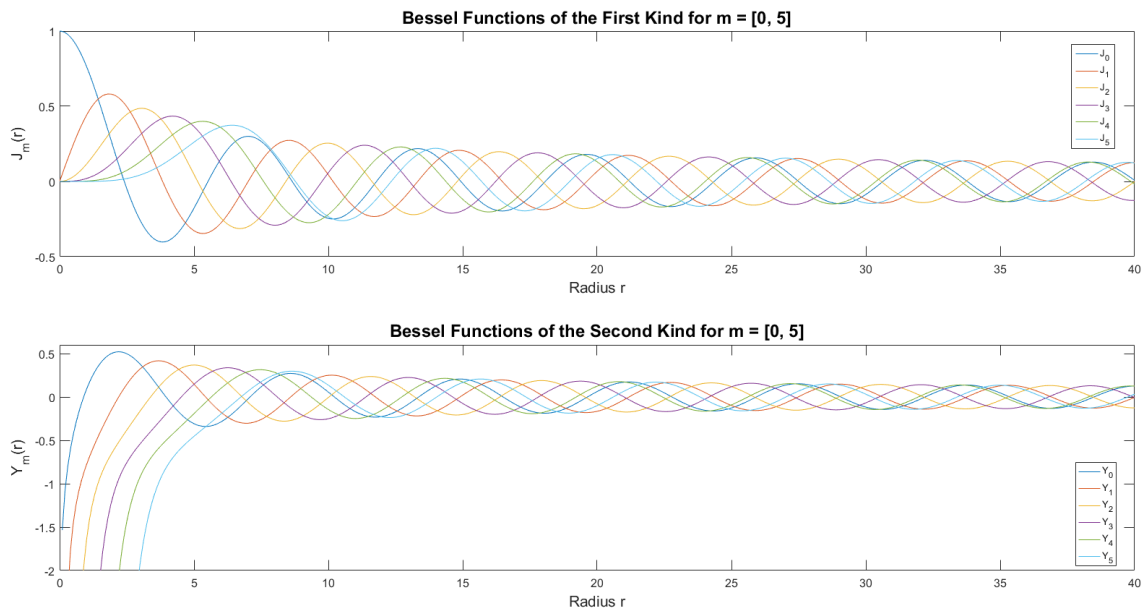


Figure 2.1: Bessel functions of the first (top) and second (bottom) kind for modes [0,5]

This results in a solution for the function $g(r)$ as follows

$$g(r) = A_2 \cdot J_m(\beta r) \quad (2.20)$$

The requirement for the pressure gradient on the outer wall ($\frac{dp'}{dr}|_{r=R} = 0$) leads to the solution that also $\frac{dg}{dr}|_{r=R} = 0$ and $\frac{dJ_m}{dr}|_{r=R} = 0$. This means, that the Bessel function 1st kind has to have either a minimum or a maximum at this radial position. Therefore, the variable β_{mn} is introduced, which scales the function of r . Because the Bessel function has an infinite number of local extrema, another variable is needed to describe the n^{th} extremum of the m^{th} order of the function, which is named s_{mn} . This results in the definition of the variable β as

$$\beta = \frac{s_{mn}}{R} \equiv \beta_{mn} \quad (2.21)$$

Using this scaling variable results in the final solution for the function $g(r)$

$$g(r) = A_{mn2} \cdot J_m(\beta_{mn}r) \quad (2.22)$$

Herein, A_{mn2} stands for the amplitude of the radial function. Introducing β_{mn} into equation (2.16) this leads to

$$\alpha = \sqrt{\left(\frac{\omega}{c}\right)^2 - \beta_{mn}^2} \equiv \alpha_{mn} \quad (2.23)$$

Using the same procedure for the function $f(x)$ as shown for the function $h(\theta)$, results in the solution

$$f(x) = A_1 e^{-i\alpha x} + B_1 e^{i\alpha x} \quad (2.24)$$

A combination of the equations (2.17), (2.22) and (2.24) with equation (2.9) leads to a general solution for the sound pressure

$$p'(x, r, \theta, t) = \sum_{m=0}^{\infty} \sum_{n=0}^{\infty} (A_{mn3} e^{-im\theta} + B_{mn3} e^{im\theta}) \cdot A_{mn2} J_m(\beta_{mn}r) \cdot (A_{mn1} e^{-i\alpha_{mn}x} + B_{mn1} e^{i\alpha_{mn}x}) \cdot e^{i\omega t} \quad (2.25)$$

The propagation of the sound wave in axial direction is influenced by the constants A_{mn1} and B_{mn1} , while the influence in the circumferential direction is given by A_{mn3} and B_{mn3} . If for example $A_{mn1} = 1$ and $B_{mn1} = 0$, the corresponding mode is only propagating into the positive axial direction. The same is valid for $A_{mn1} = 0$ and $B_{mn1} = 1$, but with a propagation in the negative direction. In case both constants have the same values, a standing wave occurs.

In circumferential direction, a similar behaviour can be observed. Such a mode is then called spinning mode with the rotation direction according to the values of the coefficients A_{mn3} and B_{mn3} . Again, if both constants are similar, a standing wave occurs.

Coefficient A_2 has no influence onto the mode shape in radial direction but is a scaling factor for the amplitude. The shape on the other hand is given by the Bessel function.

The orders m and n determine the shape of the solution and are called modes. There is always a combination of both variables which represents one special pressure distribution. m indicates the number of nodes in the circumferential direction and n in the radial direction. Therefore, the modes m are called azimuthal modes and n are called radial modes. Examples for different mode shapes are presented in Figure 2.2.

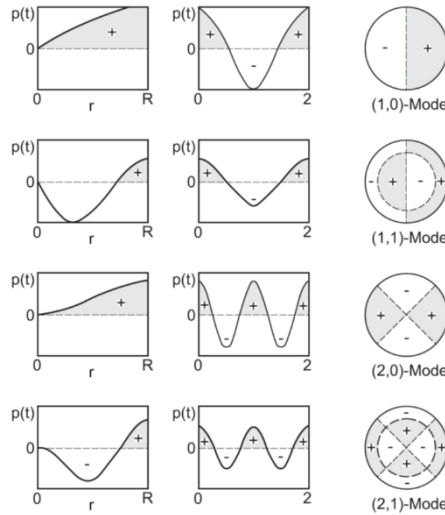


Figure 2.2: Examples of sound pressure distributions in a cylindrical duct (taken from [11])

Propagation through a cylindrical duct with hub

In case of a propagation in a duct with a hub wall, the constant B_{mn2} in equation (2.19) can't be set zero. Therefore, the general solution for the sound pressure looks like follows

$$p'(x, r, \theta, t) = \sum_{m=0}^{\infty} \sum_{n=0}^{\infty} (A_{mn3} e^{-im\theta} + B_{mn3} e^{im\theta}) \cdot (A_{mn2} J_m(\beta_{mn} r) + B_{mn2} Y_m(\beta_{mn} r)) \cdot (A_{mn1} e^{-i\alpha_{mn} x} + B_{mn1} e^{i\alpha_{mn} x}) \cdot e^{i\omega t} \quad (2.26)$$

Propagation with superimposed flow

Since in a turbomachine the fluid is not stationary but has a mean flow velocity above zero, the wave equation (2.5) is not valid anymore. The wave equation in cylindrical coordinates should be mentioned here once again

$$\frac{1}{c^2} \frac{\partial^2 p'}{\partial t^2} - \frac{1}{r} \frac{\partial}{\partial r} \left(r \frac{\partial p'}{\partial r} \right) - \frac{1}{r^2} \frac{\partial^2 p'}{\partial \theta^2} - \frac{\partial^2 p'}{\partial x^2} = 0$$

To introduce a flow velocity, the partial derivative in equation (2.5) is exchanged with the substantial derivative $\frac{D}{Dt} = \frac{\partial}{\partial t} + \nabla \vec{U}$ (see also [12]), including the mean convection speed U . After doing so it results in the following

$$\frac{1}{c^2} \frac{D^2 p'}{Dt^2} - \Delta p' = 0 \quad (2.27)$$

Transforming this into cylindrical coordinates leads to a different version of the equation mentioned above

$$\frac{1}{c^2} \frac{D^2 p'}{Dt^2} - \frac{1}{r} \frac{\partial}{\partial r} \left(r \frac{\partial p'}{\partial r} \right) - \frac{1}{r^2} \frac{\partial^2 p'}{\partial \theta^2} - \frac{\partial^2 p'}{\partial x^2} = 0 \quad (2.28)$$

A simplification concerning a flow velocity is that the fluid has a component in only one direction as the vector $\vec{U} = (U, 0, 0)$ and it is permitted to set $\nabla \vec{U} = U \frac{\partial}{\partial x}$ which results for the substantial derivation of the pressure fluctuation as

$$\frac{D^2 p'}{Dt^2} = \left(\frac{\partial}{\partial t} + U \frac{\partial}{\partial x} \right)^2 p' \quad (2.29)$$

Herein, the term $\frac{\partial}{\partial t}$ represents the local derivative and the term $U \frac{\partial}{\partial x}$ the convective one. With this, the wave equation can be rewritten as follows, and is called the convective wave equation

$$\frac{1}{c^2} \left[\frac{\partial^2 p'}{\partial t^2} + 2U \frac{\partial^2 p'}{\partial t \partial x} + U^2 \frac{\partial^2 p'}{\partial x^2} \right] - \frac{1}{r} \frac{\partial}{\partial r} \left(r \frac{\partial p'}{\partial r} \right) - \frac{1}{r^2} \frac{\partial^2 p'}{\partial \theta^2} - \frac{\partial^2 p'}{\partial x^2} = 0 \quad (2.30)$$

Inserting the axial Mach number $Ma_x = \frac{U}{c}$ leads to

$$\frac{1}{c^2} \left[\frac{\partial^2 p'}{\partial t^2} + 2U \frac{\partial^2 p'}{\partial t \partial x} \right] - \frac{1}{r} \frac{\partial}{\partial r} \left(r \frac{\partial p'}{\partial r} \right) - \frac{1}{r^2} \frac{\partial^2 p'}{\partial \theta^2} - (1 - Ma_x^2) \frac{\partial^2 p'}{\partial x^2} = 0 \quad (2.31)$$

This equation can be solved again according to the method shown before in the case without mean flow. The only change is in equation (2.16) which has to be replaced by

$$\beta^2 = k^2 \left(1 - U \frac{\alpha}{\omega} \right)^2 - \alpha^2 \quad (2.32)$$

If the geometry of the flow duct is given, the values for β can be calculated using the eigenvalues $s_{mn} = R\beta_{mn}$. Combining this eigenvalue with equation (2.32) and with the wave number $k = \frac{\omega}{c}$, gives the following

$$\left(\frac{s_{mn}}{R} \right)^2 = k^2 \left(1 - U \frac{\alpha}{\omega} \right)^2 - \alpha^2 = k^2 - 2kMa_x\alpha + (Ma_x^2 - 1)\alpha^2 \quad (2.33)$$

Transforming this equation gives the quadratic equation

$$\alpha^2 + \frac{2kMa_x}{1 - Ma_x^2} \alpha - \frac{1}{1 - Ma_x^2} \left(k^2 - \left(\frac{s_{mn}}{R} \right)^2 \right) = 0 \quad (2.34)$$

And finally leads to a solution for α as follows

$$\alpha_{mn}^{\pm} = k_{mn}^{\pm} = \frac{k}{1 - Ma_x^2} \left[-Ma_x \pm \sqrt{1 - (1 - Ma_x^2) \left(\frac{S_{mn}}{kR} \right)^2} \right] \quad (2.35)$$

This equation is now the solution for the axial wave number including an axial Mach number $Ma_x \neq 0$. It is valid for all modes m and n in and against the direction of propagation.

2.1.3 Boundary Condition Change Due to Different End Wall Characteristics

The boundary conditions mentioned in section 2.1.2 concerning the solution of the wave equation with hard end walls is not valid anymore, if a sound absorbing segment is included into the flow duct. The pressure gradient at the outer duct radius ($r = R$) or also the inner one in case of an annular duct ($r = r_0$) is not zero when using an acoustic liner with a specific impedance Z there.

An acoustically soft end wall ($Z = 0$) is the other extreme with respect to the hard end wall. If such a configuration is used, the sound pressure at the wall is zero and the sound particle velocity has a maximum. This means, that a wave which is travelling towards the soft end wall gets reflected with a 180 deg phase shift but the same amplitude. The result is a cancellation of both sound waves.

With a treated duct, the solution is somewhere in-between the two extreme cases. Herein, the radial pressure gradient is dependent onto the complex wall impedance $Z = \frac{p}{v_n}$ or acoustic admittance $A_a = \frac{1}{Z}$. Following equation gives the radial component of the acoustic momentum equation including a mean flow according to Hubbard [13]

$$\frac{\partial p}{\partial r} = -\rho \left(\frac{\partial}{\partial t} + U \frac{\partial}{\partial x} \right) v_r \quad (2.36)$$

If an acoustically treated duct is investigated, the normal velocity of the fluid at the duct wall is the same as the one of the duct wall (v_n) itself. Both are the derivative of the local particle displacement δ which has the definition

$$\delta = \delta e^{i\omega t} \quad (2.37)$$

The normal component of the duct wall particle velocity is

$$v_n = \frac{\partial \delta}{\partial t} = i\omega \delta \quad (2.38)$$

In case of the normal component of the fluid particle velocity normal to the duct wall, the substantial derivative has to be taken into account because of the convection effect of the fluid

$$v_f = \frac{D\delta}{Dt} = \left(\frac{\partial}{\partial t} + U \frac{\partial}{\partial x} \right) \delta = \left(i\omega + U \frac{\partial}{\partial x} \right) \delta \quad (2.39)$$

And with $\delta = -i \frac{v_n}{\omega}$ and $v_n = A_a p$ it yields

$$v_f = A_a \left(1 - i \frac{U}{\omega} \frac{\partial}{\partial x} \right) p \quad (2.40)$$

In case of an circular duct the radial velocity component v_r equals to the fluid velocity normal to the duct wall v_f . Inserting v_f into equation (2.36) gives

$$\frac{\partial p}{\partial r} = -i\omega\rho A_a \left(1 - i \frac{U}{\omega} \frac{\partial}{\partial x} \right)^2 p \quad (2.41)$$

A substitution can be done using the relation $\frac{\partial p}{\partial x} = -ik_{mn}p$ which leads to

$$\frac{\partial p}{\partial r} = -i\omega\rho A_a \left(1 - \frac{U}{\omega} k_{mn} \right)^2 p \quad (2.42)$$

Using this equation gives the solution for the changed boundary condition, compared to the hard wall case, for the position $r = R$ (at the duct wall). The second boundary condition at the duct centre line $r = 0$ stays unchanged (finite solution).

$$\frac{\partial p}{\partial r} \Big|_{U \neq 0, r=R} = -i\omega\rho A_a \left(1 - \frac{U}{\omega} k_{mn} \right)^2 p \quad (2.43)$$

This leads than to the eigenvalue equation according to [13], for a cylindrical duct with a mean flow as follows

$$\beta_{mn} \frac{J_{m-1}(\beta_{mn})}{J_m(\beta_{mn})} - m = -i\omega\rho A_a \left(1 - \frac{U}{\omega} k_{mn} \right)^2 \quad (2.44)$$

Using equation (2.35) leads to

$$\beta_{mn} \frac{J_{m-1}(\beta_{mn})}{J_m(\beta_{mn})} - m = -i\omega\rho A_a \left(1 - \frac{U}{\omega} \cdot \frac{k}{1 - Ma_x^2} \left[-Ma_x \pm \sqrt{1 - (1 - Ma_x^2) \left(\frac{\beta_{mn}}{k} \right)^2} \right] \right)^2 \quad (2.45)$$

It can be seen, that there is a high complexity concerning the dependency of the eigenvalues β_{mn} on several parameters. This problem can be possibly solved by using numerical tools or iteratively. A detailed explanation of this topic can be found in [13].

2.1.4 The Cut-Off Condition

A very important parameter concerning duct acoustics is the axial wave number. It determines if an acoustic duct mode can propagate in the usual sense or if it has an exponential decay in axial direction. If the mode attenuates over the axial distance, it doesn't carry acoustic power into the far field and it is referred to as cut-off mode. Such modes form the near field of

the sound source. A propagation is only possible if the axial wave number is a real number. Looking at equation (2.35) one can see that this is true if the term underneath the square root is positive.

$$\frac{\omega}{c} = k > \sqrt{1 - Ma_x^2} \cdot \frac{S_{mn}}{R} \quad (2.46)$$

If this inequation is not satisfied, α gets imaginary and the perturbation can either grow (which is a nonphysical solution and therefore it is excluded) or decay. Rearranging this inequation leads to a formulation of the so-called cut-off frequency. Below this frequency, a mode with certain order (m, n) is not able to propagate.

$$f_{cut} = \sqrt{1 - Ma_x^2} \cdot \frac{c \cdot S_{mn}}{2\pi R} \quad (2.47)$$

From this equation it can be seen, that the flow velocity lowers the cut-off frequency for a given mode (m, n) . Vice versa this means that with higher flow velocity, higher mode orders (for a given frequency) are able to propagate which would otherwise be cut-off in a case without mean flow.

This cut-off condition is only valid for hard walled ducts but not for soft walled ones.

2.1.5 About Discontinuities in a Duct

Having a discontinuity in the flow duct, e.g. a change in diameter or in the wall impedance, leads to a reflection and transmission of the incident field at the point of the discontinuity. That means, that each mode is scattered into a modal spectrum of reflected as well as transmitted modes. Each segment neighbouring a discontinuity can be investigated concerning their modal representation separately.

In this section, a description of the formulations concerning these investigations is shown according to [14]. Therefore, a cylindrical duct without flow but with a change in diameter at the axial position $x = 0$ is considered as it is shown in Figure 2.3. The first segment has a radius of $r = a$ and is bigger than the one from the second segment with $r = b$. A symmetry in circumferential direction is given for both segments and therefore there is no mode scattering into other m modes but only in n modes. Due to this, only one certain single m mode is considered in the following explanations.

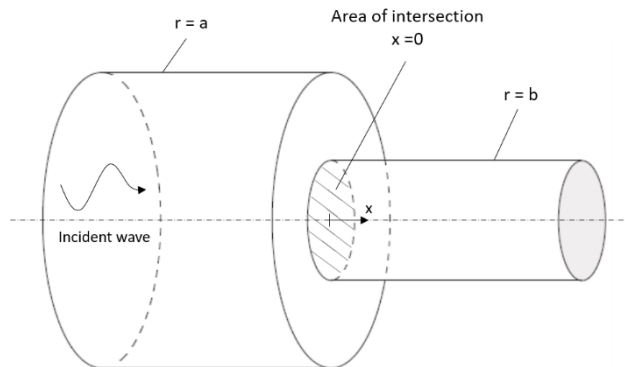


Figure 2.3: Diameter discontinuity (adapted from [14])

The incident wave travelling from $x = -\infty$ in direction of the discontinuity can be described similar to equation (2.25)

$$p'_{in}(x, r, \theta) = \sum_{n=0}^{\infty} A_{mn} \cdot J_m(\beta_{mn}r) \cdot e^{-i\alpha_{mn}x - im\theta} \quad (2.48)$$

Herein, A_{mn} stands for the amplitude of the incident wave. At the area of intersection ($x = 0$), this wave scatters into a reflected (p'_{ref}) and a transmitted wave (p'_{tr}).

$$p'_{ref}(x, r, \theta) = \sum_{n=0}^{\infty} B_{mn} \cdot J_m(\beta_{mn}r) \cdot e^{i\alpha_{mn}x - im\theta} \quad (2.49)$$

$$p'_{tr}(x, r, \theta) = \sum_{n=0}^{\infty} C_{mn} \cdot \widehat{J}_m(\delta_{mn}r) \cdot e^{-i\gamma_{mn}x - im\theta} \quad (2.50)$$

γ_{mn} and δ_{mn} are the equivalent to α_{mn} (wave number) and β_{mn} respectively but considering the different duct diameter of the second segment. Same is valid for \widehat{J}_m being the Bessel function of the first kind of the second segment.

In those equations, B_{mn} and C_{mn} describe the amplitude of the reflected and the transmitted wave respectively.

$$B_{mn} = \sum_{a=0}^{\infty} R_{mna} \cdot A_{ma} \quad or \quad \mathbf{B} = \underline{\underline{R}}\mathbf{A} \quad (2.51)$$

$$C_{mn} = \sum_{a=0}^{\infty} T_{mna} \cdot A_{ma} \quad or \quad \mathbf{C} = \underline{\underline{T}}\mathbf{A} \quad (2.52)$$

As mentioned earlier, there is no scattering in other azimuthal modes (due to the axisymmetric shape of both segments) but there is a modal energy redistribution between the radial modes within the azimuthal mode order (also mentioned in Montétagaud and Batard [15]). Therefore, the amplitude A_{ma} is needed, including another radial mode order a . In combination with the incident amplitude vector \mathbf{A} , the reflection matrix $\underline{\underline{R}}$ and the transmission matrix $\underline{\underline{T}}$ are generating the corresponding amplitude vectors \mathbf{B} and \mathbf{C} .

As an example, the situation having only a plane wave in a circular duct should be shown now. At the area of intersection ($x = 0$), continuity concerning mass m and acoustic energy E is assumed.

$$\rho_0 S_a u'_a(0, t) - \rho_0 S_b u'_b(0, t) = \frac{\Delta m}{\Delta t} \Big|_{x=0} = 0 \quad (2.53)$$

$$S_a p'_a(0, t) u'_a(0, t) - S_b p'_b(0, t) u'_b(0, t) = \frac{\Delta E}{\Delta t} \Big|_{x=0} = 0 \quad (2.54)$$

Herein, S_a and S_b are the cross sectional areas of the first (a) and the second (b) segment respectively and u'_a and u'_b are the velocity fluctuations of each segment. Combining these two equations give the relation between the pressure fluctuations at the location $x = 0$

$$p'_a = p'_b \quad (2.55)$$

What can also be written as follows, when splitting up the pressure fluctuation from the first segment a concerning the forward (incident) and backward (reflected) moving wave

$$p'_{in} + p'_{ref} = p'_{tr} \quad (2.56)$$

Using equations (2.48), (2.49), and (2.50) for a plane wave at the location $x = 0$ together with this relation, leads to a correlation between the amplitudes as follows

$$A_{mn} + B_{mn} = C_{mn} \quad (2.57)$$

Including equation (2.53) into the following harmonic ansatz concerning the velocity fluctuations

$$u'_a(x, t) = \frac{A_{mn}}{\rho_0 c} e^{i(\omega t - kx)} - \frac{B_{mn}}{\rho_0 c} e^{i(\omega t + kx)} \quad (2.58)$$

$$u'_b(x, t) = \frac{C_{mn}}{\rho_0 c} e^{i(\omega t - kx)}$$

leads to a relation between the amplitudes as follows

$$S_a(A_{mn} - B_{mn}) = S_b C_{mn} \quad (2.59)$$

If one knows the amplitude of incident wave A_{mn} , the ones for the reflected and transmitted waves can be calculated.

$$B_{mn} = \frac{S_a - S_b}{S_a + S_b} A_{mn} = R_{mn} \cdot A_{mn} \quad (2.60)$$

$$C_{mn} = \frac{2S_b}{S_a + S_b} A_{mn} = T_{mn} \cdot A_{mn} \quad (2.61)$$

With R_{mn} and T_{mn} being the reflection and the transmission factor respectively for a specific mode order. It can be seen, that these two equations look the same as (2.51) and (2.52).

Also when using acoustic liners, or in general treated parts in an untreated duct, leads to impedance discontinuities. Figure 2.4 indicates the transmitted and reflected components of the incident wave, resulting from an impedance change between a hard wall duct and acoustic liners. The first discontinuity produces a reflected (red arrow) and a transmitted wave

component (blue arrow) which is then also the incident wave of the following discontinuity. There, again a reflection (orange arrow) and a transmission (green arrow) happens.

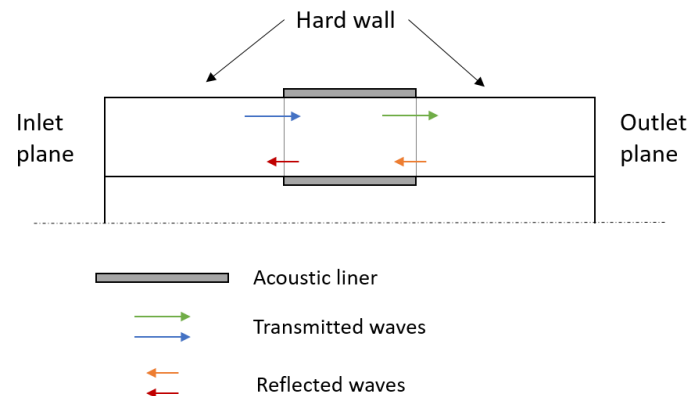


Figure 2.4: Transmitted and reflected waves due to impedance discontinuities in a duct

These steps in impedance can result in a significant redistribution of modal energy. Montétagaud and Batard [15] investigated this redistribution and stated three causes for it, which are also valid for the investigated setups in this thesis:

- The first discontinuity at the interface of an untreated and a treated part
- The absorption due to the acoustic liner
- The second discontinuity at the interface between the liner and the hard duct wall

They also mention, that in an axisymmetric duct, the redistribution of the modal energy of radial modes is within the azimuthal modes but in case the duct geometry gets more difficult, a change also between the azimuthal modes takes place.

A second phenomenon is called “mode conversion”. If this happens, it is possible that the mode content of the sound field after passing the treated part is different with respect to the incident sound field coming from the rigid part of the duct (see also Montétagaud et al. [16]).

In case of a simple flow duct, the reflected and transmitted modal content can be evaluated numerically having an easy or moderate complex problem. Tam et al. [17] made intensive analytically investigations on a more complex situation compared to [15], namely the influence of axial splices between liners as it is common at the inlet of aero engines. But when having vanes in the flow duct, an accurate examination of the change in modal content can only be done by measuring the incident sound field as well as the field downstream of such a discontinuity and then compare them, or by a numerical investigation which would require a lot of computational resources.

2.2 Theory of Acoustic Resonators

Resonators, or also named absorbers, are devices which are used to dampen acoustic pressure fluctuations. As the name states already, such devices make use of the absorption of a sound wave. When sound waves hit a surface, the incoming energy is split up into three portions: a reflected part, a dissipated part, and a transmitted part. In acoustics it is common to sum up the dissipated and transmitted energy and name it absorbed energy because it is not important if the acoustic energy is transformed into thermal energy or if it is transmitted into the neighbouring

room or ambient. To characterize an acoustic resonator the reflection and absorption can be determined by the following two equations, stating the reflection coefficient R and the absorption coefficient α .

$$R = \frac{\text{sound pressure of the reflected wave}}{\text{sound pressure of the incoming wave}} \quad (2.62)$$

$$\alpha = \frac{\text{absorbed energy}}{\text{incoming energy}} = 1 - |R|^2 \quad (2.63)$$

This absorption coefficient is a real number and varies from 0 to 1, where 0 means no absorption at all and 1 is a complete absorption. The reflection coefficient is a complex number and includes also the phase shift of an incoming and a reflected wave.

Despite the above mentioned assumption, another important parameter is defined when using acoustic absorbers namely the transmission loss which is defined as the relation between the incident acoustic power at a defined area (e.g. acoustically treated part) and the transmitted acoustic power downstream of the area of interest.

$$TL = 10 \log_{10} \frac{\text{Power of the incident wave}}{\text{Power of the transmitted wave}} [dB] \quad (2.64)$$

2.2.1 Reflection Coefficient

As an indication of how good a material or device is absorbing the incident sound field, the reflection coefficient is a widely used parameter. Basically, it is a relation between the sound pressure of the incident and the reflected waves of an investigated specimen.

$$R = \frac{A^-}{A^+} \quad (2.65)$$

Herein, A^- is the amplitude of the reflected wave and A^+ the one of the incident wave. This coefficient can have a value between the limits of $+1$ and -1 . Those limits are set by the two idealized boundary conditions. The first one is set by the so-called hard wall condition, which is given by a perfectly rigid wall. In this case, a total reflection can be achieved yielding in a reflection coefficient of $R = 1$. The opposing limit is given by a so-called soft wall condition with $R = -1$.

Both conditions result in a standing wave with a periodicity of $\frac{\lambda}{2}$ as can be seen in Figure 2.5, indicating the sound pressure as well as the sound particle velocity for each case. Concerning the hard wall condition, the pressure p has a maximum directly at the wall with an amplitude twice as high as the pressure of the incident wave p_1 . The reason is, that the reflected pressure has the same value and phase as the incident one. The sound particle velocity v on the other hand has a node directly at the wall and a maximum at a distance of $\frac{\lambda}{4}$ away from it. There the sound pressure has then a node. For the soft wall condition, it is the other way around, having a pressure node and a normal sound particle velocity maximum directly at the wall ($v_1 = 2v$).

The pressure has the same value as the incident one but a negative sign. Concerning the phase, a shift of π happens at the wall.

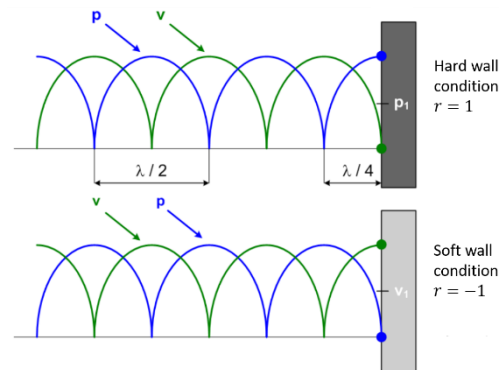


Figure 2.5: Hard and soft wall conditions - Standing wave (taken from [18])

2.2.2 Basic Liner Concepts

Acoustic liners can be split up regarding how they affect an incoming sound field. The different types are explained in e.g. [19].

Porous absorbers:

Porous absorbers, or also non-locally reacting absorbers, are mainly made from acoustic foams, organic or mineral fibres. This type can be split up into two subtypes, namely a bulk absorber, which only consist of a porous material, and an absorber using a porous layer placed in a certain distance away from a hard wall. Both types are shown in Figure 2.6. With this kind of absorber, a broadband noise reduction can be achieved.

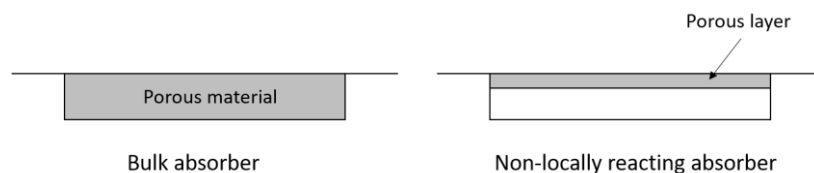


Figure 2.6: Schematic sketch of porous absorbers

Using such absorbers, the sound attenuation is mostly due to the movement of air between the pores. Such a movement results in friction which causes a dissipation of the acoustic energy. Hence, the most important acoustic parameter is the sound particle velocity. The propagation direction of the acoustic wave is not restricted as for the second big type of absorber explained later. Because the velocity is zero at a hard wall boundary, it is necessary to realize the right thickness of either the porous material or the distance between the porous layer and the hard end wall. This distance is crucial concerning the frequency which should be absorbed. The thicker the porous layer, the lower the frequency which can be absorbed. A porous layer backed by a cavity is not useful if the frequency of interest is low because due to the long wavelength, the distance between the layer and the hard end wall would become very large.

Resonant absorbers:

These absorbers are also known as locally reacting absorbers and can be separated into three different main types. The first one is named after its inventor Hermann von Helmholtz, who made the first important work concerning this type of resonator [20]. This main type consists of a cavity which is connected to the environment via an opening called neck. It can again be split up into the subtypes perforated absorbers and microperforated absorber. In general, they are the same with the only difference, that the perforation of the microperforated absorber is in the submillimetre range compared to the normal perforated absorber. The second main type of resonant absorbers is the $\lambda/4$ absorber, which is a combination of a porous layer and a honeycomb cell backed by a rigid wall. This porous layer permits an incident acoustic wave of entering the back cavity. The third main type is called membrane absorber or panel absorber and is simply a foil or thin plate combined with an air buffer and a rigid back wall. All these types are shown schematically in Figure 2.7.

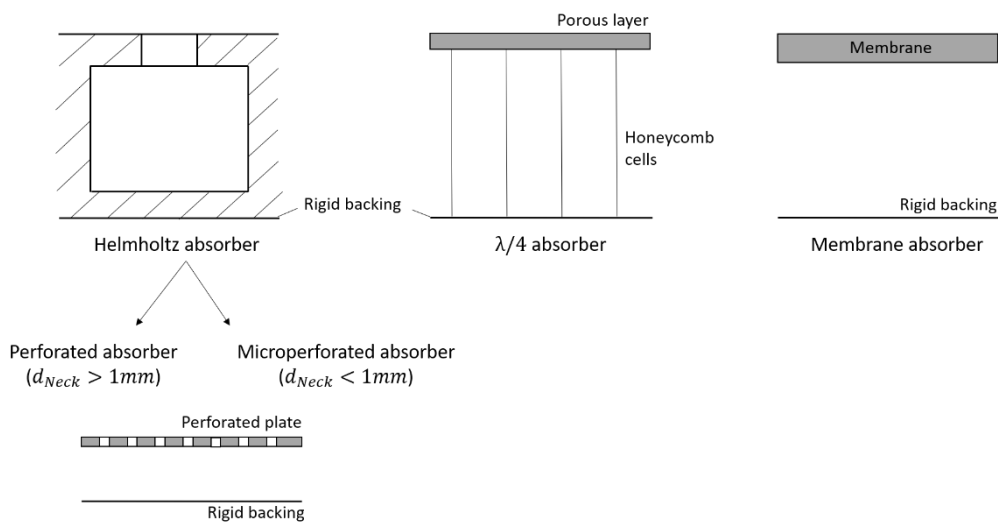


Figure 2.7: Schematic sketch of resonant absorbers

Compared to the non-locally reacting absorbers, which have a broadband absorption characteristic, these absorbers have a peak absorption at their resonance frequency. This means, that the noise attenuation is working best at one certain frequency plus a small bandwidth around this frequency.

For all resonant absorbers the basic theory is a combination of a moving mass m applying a load onto a spring with a stiffness k . The spring is in all absorber types the compressible air in the cavity. Concerning the mass, in case of the Helmholtz absorber, it is the air oscillating in the neck and in case of the membrane absorber and the $\lambda/4$ absorber it is a sheet of material which vibrates. A theoretical model concerning the Helmholtz and membrane resonators can be seen in Figure 2.8.

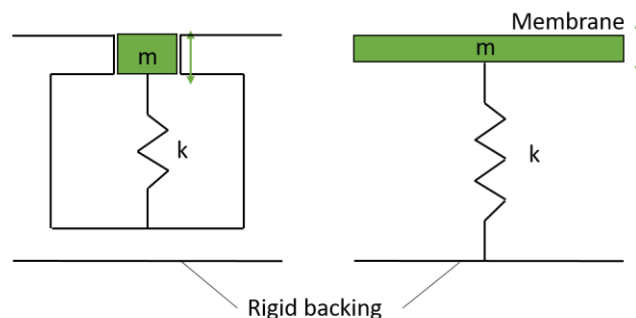


Figure 2.8: Substituted systems of resonant absorbers

The resonance frequency of such a system can now be tuned by changing the two parameters m and k .

In Figure 2.9, the absorption characteristics of a bulk absorber, a Helmholtz absorber and a $\lambda/4$ absorber can be seen. As already mentioned, the bulk absorber, or porous absorber in general, has a broadband noise reduction, whereas the resonant absorbers have a peak reduction at their resonance frequency with an attenuation within a narrow bandwidth around this frequency. This bandwidth is even a bit wider in the case of a $\lambda/4$ absorber with respect to a Helmholtz absorber. The best absorption can be achieved, when combining a porous absorber and a resonant absorber as for example by placing a porous material in the cavity of a Helmholtz absorber right behind the neck opening.

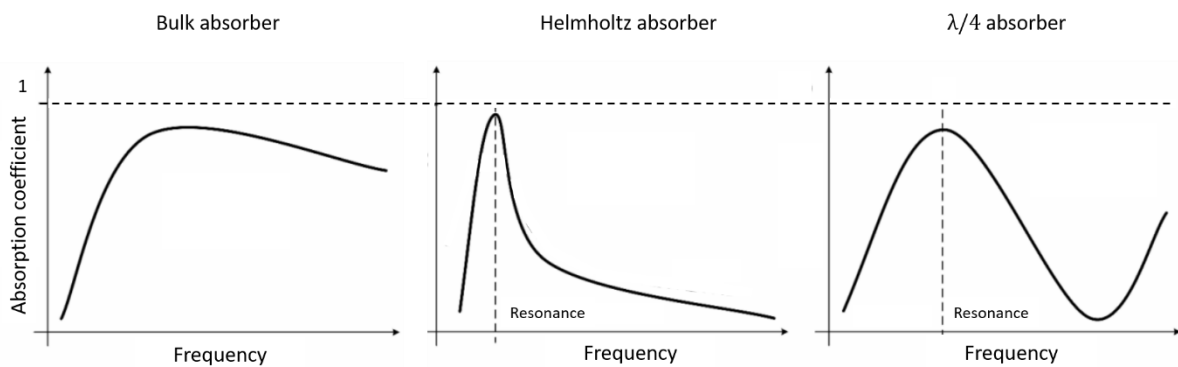


Figure 2.9: Absorption characteristics (adapted from [18])

Helmholtz absorber

During the work for this thesis, Helmholtz absorbers have been used. Therefore, the theory of this resonator type should be explained now in more detail.

In general, this type of absorber is a combination of a backed volume connected with the environment via an opening called neck. The volume acts then as a spring with a stiffness k and causes an oscillation of the air in the neck which can be seen as a mass m . Therefore, a Helmholtz absorber can be represented as a simple spring-mass system what can be seen in Figure 2.10. Due to pressure perturbations, this system gets excited.

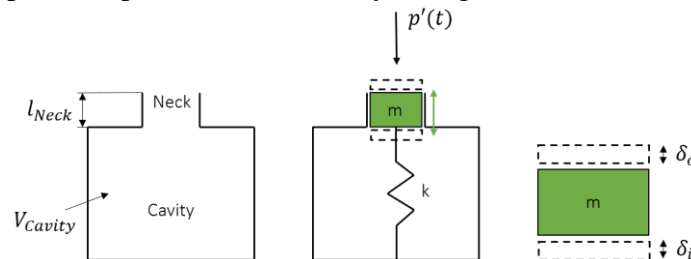


Figure 2.10: Helmholtz absorber as a spring mass system

The eigenangularfrequency of such a simple oscillating single degree of freedom system can be calculated according to

$$\omega = \sqrt{\frac{k}{m}} \tag{2.66}$$

With k being the spring stiffness and m the mass of the air in the neck. Latter one can be also written as

$$m = \rho \cdot A_{Neck} \cdot l_{Neck} \quad (2.67)$$

Herein, l_{Neck} is the length of the neck and A_{Neck} is its cross-section area of the neck. The spring stiffness is defined as follows

$$k = \frac{dF}{dl_{Neck}} \quad (2.68)$$

With dF representing the change of the force on the spring and dl_{Neck} the change in length due to this force. The change of the force can be written with the change of pressure dp working on the neck cross section

$$dF = dp \cdot A_{Neck} \quad (2.69)$$

Assuming an adiabatic process and ideal gas leads to

$$pV^\gamma = const. \quad (2.70)$$

With γ being the adiabatic gas index and V the cavity volume. When differentiating this equation, it leads to

$$V^\gamma dp + p\gamma V^{\gamma-1} dV = 0 \quad (2.71)$$

The change of the volume due to the movement of air in the neck behaves inverse to the change of the neck length

$$dV = -A_{Neck} \cdot dl_{Neck} \quad (2.72)$$

Substituting (2.69) and (2.72) in (2.71) gives the following

$$V^\gamma \frac{dF}{A_{Neck}} - p\gamma V^{\gamma-1} A_{Neck} dl_{Neck} = 0 \quad (2.73)$$

which shows after some transformation the equation for the spring stiffness k

$$\frac{dF}{dl_{Neck}} = \frac{p\gamma A_{Neck}^2}{V} = k \quad (2.74)$$

If one considers again ideal gas with $p = \rho RT$ and $c = \sqrt{\gamma RT}$ equation (2.74) can be written as

$$k = \frac{\rho c^2 A_{Neck}^2}{V_{Cavity}} \quad (2.75)$$

With $V_{Cavity} = V$. This equation includes now the speed of sound c . Substituting (2.67) and (2.75) in (2.66) leads to the eigenangularfrequency of a Helmholtz resonator, which depends only onto the air density, the speed of sound and the resonator geometry

$$\omega = \sqrt{\frac{\rho c^2 A_{Neck}}{V_{Cavity} l_{Neck}}} \quad (2.76)$$

This type of absorber has a high transmission loss in a very narrow frequency range with the maximum at its resonance frequency. At this certain frequency, the highest sound attenuation takes place due to wall friction, acoustic radiation, and vortex shedding on both sides of the neck (see also Roche et al. [21]). The most used type of equation to calculate the resonance frequency is

$$f_r = \frac{c}{2\pi} \sqrt{\frac{A_{Neck}}{V_{Cavity} \cdot (l_{Neck} + \delta)}} \quad (2.77)$$

δ is the so-called end correction, which is necessary to take an additional portion of mass in the vicinity of the neck opening into account which is oscillating with the mass in the neck. That means, that the actual oscillating mass is larger than the mass only enclosed in the neck. This end correction consists of an inner δ_i and an outer correction δ_o . Rayleigh suggested an end correction for an infinite flat plate with a cylindrical hole, where a piston is radiating into half-space as follows

$$\delta_o = 0.85 \cdot r_{Neck} \quad (2.78)$$

He also stated, that this is only valid for one side and needs to be considered twice for an inner and an outer correction. Ingard [22] showed an equation for an inner end correction based on a model of a piston radiating into a tube of radius R (here declared with R_{Cavity})

$$\delta_i = 0.48 \cdot \sqrt{A_{Neck}} \cdot \left(1 - 1.25 \frac{r_{Neck}}{R_{Cavity}}\right) = \frac{8}{3\pi} \cdot r_{Neck} \cdot \left(1 - 1.25 \frac{r_{Neck}}{R_{Cavity}}\right) \quad (2.79)$$

He stated that the limit for this correction is $\frac{r_{Neck}}{R_{Cavity}} = 0.4$. Furthermore, this equation is valid for cylindrical cavities with centred, circular orifices. Chanaud [23] investigated a validity in a range of $0.22 \leq \frac{r_{Neck}}{R_{Cavity}} \leq 0.52$.

During this work a test turbine is investigated with a not negligible mean flow velocity. Therefore, also the Mach number has to be taken into account in the end correction. Rice [24]

suggested in his work a total end correction including the grazing flow Mach number effect as follows

$$\delta = 0.85 \cdot d_{Neck} \cdot (1 - 0.7 \cdot \sqrt{\sigma}) \cdot \frac{1}{1 + 305 \cdot Ma^3} \quad (2.80)$$

With the area ratio between the neck and the cavity $\sigma = \frac{A_{Neck}}{A_{cavity}}$.

During the design phase of resonators, all dimensions should be kept small compared to the wavelength of the frequency of interest, to guarantee only a plane wave motion inside the absorber cavity.

Microperforated panel absorber (MPP absorber)

This type of absorber is mostly used if a broadband noise reduction is needed. In this case, the acoustic energy gets converted into viscous losses. The reason behind this is that the openings are in the submillimetre range, hence in the same dimension as the viscous boundary layer thickness, and this results in a high energy dissipation due to friction losses in the absorber necks.

During this thesis, one vane design including a microperforated absorber is also investigated (see in upcoming section 4.3). Although this is a subtype of the classical Helmholtz absorber described above, there is not such an easy equation to calculate the resonance frequency. Therefore, a short explanation of how this frequency can be calculated is shown here.

In general, one has to calculate the impedance of the system. Starting with the one of a single neck opening and a normal incidence of the soundwave as stated by Maa [25] and Qian et al. [26]. The real part of this impedance stands for the viscous effect (friction between the air moving in the neck and the inner neck surface), which decreases with an increase of the neck diameter.

$$Z_{Neck} = \frac{32\eta l_{Neck}}{d_{Neck}^2} \left(\sqrt{1 + \frac{k^2}{32}} + \frac{\sqrt{2}}{8} k \frac{d_{Neck}}{l_{Neck}} \right) + i2\pi f \rho l_{Neck} \left(1 + \frac{1}{\sqrt{9 + \frac{k^2}{2}}} + 0.85 \frac{d_{Neck}}{l_{Neck}} \right) \quad (2.81)$$

In this equation, k stands for the dimensionless boundary layer parameter including the dynamic viscosity η and can be written as

$$k = \frac{d_{Neck}}{2} \sqrt{\frac{2\pi f \rho}{\eta}} \quad (2.82)$$

This parameter is proportional to the ratio between the neck diameter and the viscous boundary layer thickness inside the neck. The last term in the resistance as well as in the reactance part of equation (2.81) are due to the neck end correction.

To get the total impedance of all openings, a scaling with the perforation area ratio is done, using the distance between the openings b (if they are arranged in a square lattice)

$$Z_{all\ necks} = Z_{Neck} \cdot 78.5 \frac{d_{Neck}^2}{b^2} \quad (2.83)$$

The acoustic reactance of the cavity is calculated as follows

$$Z_{cavity} = -i\rho c \cdot \cot\left(\frac{2\pi f l_{cavity}}{c}\right) \quad (2.84)$$

Herein, l_{cavity} is the depth of the cavity. Combining those two impedances lead to a total impedance of the microperforated absorber as

$$Z_t = Z_{all\ necks} + Z_{cavity} \quad (2.85)$$

With this total impedance, the reflection coefficient R can be calculated by simply making the ratio with the local impedance $Z_0 = \rho c$.

$$R = \frac{Z_t - Z_0}{Z_t + Z_0} \quad (2.86)$$

2.3 Aerodynamics

The second part of the present work is the aerodynamical behaviour of the investigated setups. Therefore, this chapter is about the fundamentals of turbine aerodynamics, with a limitation to the most important effects concerning the investigations performed during this thesis.

2.3.1 Blade and Vane Passage

Usually, modern aircraft engines consist of multiple compressors and turbines, which in turn consist of multiple stages. A turbine stage is a combination of a stator followed by a rotor and a compressor stage a rotor followed by a stator. During this thesis a 1 ½ stages test turbine was investigated what means that downstream of the rotor another stator vane row is located.

The presence of static and/or rotating vane/blade rows result in characteristic aerodynamic structures which are called secondary flows, and include vortices forming on various positions upstream, in, and downstream a vane/blade passage. Without any disturbances, these formations are generated due to the viscous effects on the end walls at the inlet of a row. The resulting boundary layer induces than vorticity to the flow. Figure 2.11 shows the end wall boundary layer impinging onto a stationary vane row leading edge and forming the so-called horseshoe vortex. This vortex splits up in a suction side and a pressure side leg, depending on which side of the vane the roll up happens. It can be seen, that the pressure side leg is feeding

the so-called passage vortex, whilst the counter rotating suction side leg is interacting with the same.

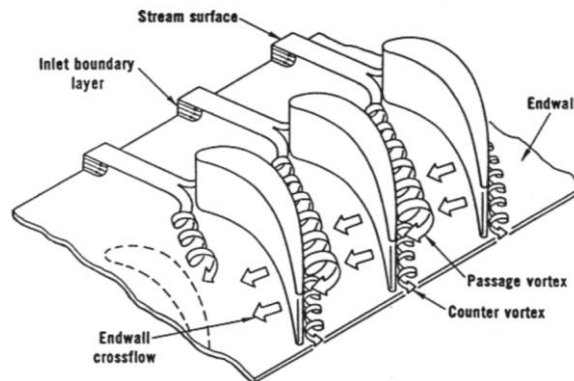


Figure 2.11: Secondary flows (taken from [27])

The passage vortex is growing along the passage ending up as the dominant secondary flow structure downstream of a vane/blade passage. Because of this, the origin of the passage vortex should be explained more in detail.

Figure 2.12 shows streamlines and velocity profiles in a turbomachine, which includes curved vanes. Due to these curved vanes, also the streamlines are bent. The streamline \overline{AAA} (blue arrow) is outside of the boundary layer and has a velocity v_A , whereas the streamline \overline{BBB} (orange arrow) is inside the boundary layer with a velocity v_B . The trajectory of particles on \overline{AAA} has a radius R_A and the ones on \overline{BBB} the radius R_B . Both radii are identical.

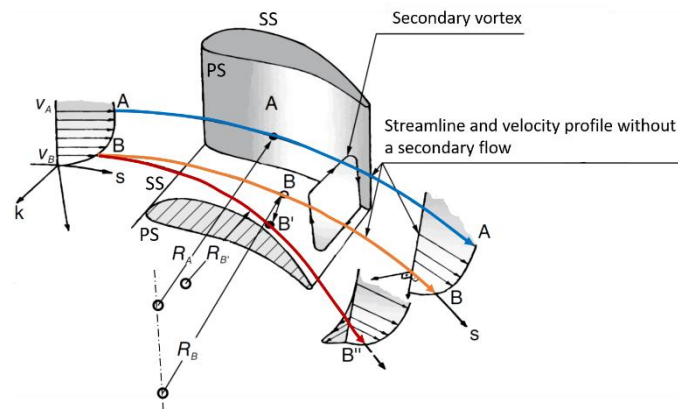


Figure 2.12: Secondary flow origin (adapted from [7])

Due to the curved streamline, each fluid particle receives a centripetal acceleration perpendicular to the streamline as follows

$$\left(\frac{\partial p}{\partial k}\right)_A = \rho \frac{v_A^2}{R_A} \quad \text{and} \quad \left(\frac{\partial p}{\partial k}\right)_B = \rho \frac{v_B^2}{R_B} \quad (2.87)$$

With the assumptions that the pressure difference between the vane sides in the passage is neglected and that there is no variation of the boundary layer in circumferential direction, the pressure gradient $\frac{\partial p}{\partial k}$ has to be constant. Because of the difference of the velocities $v_A > v_B$, this can only be achieved if the radius R_B changes to a smaller one $R_{B'}$. The flow in the boundary layer is then following the streamline $\overline{BB'B''}$ (red arrow). This movement of the flow is known as secondary flow. If the pressure gradient in the vane passage between the vane suction and

pressure side is not neglected, this effect of a bent streamline gets even bigger. Due to the movement, a shift in mass happens which has to be corrected. Therefore, mass moves from the vane pressure side outer casing area downwards to the inner end wall region and moves then back upwards on the suction side of the neighbouring vane. The result is a secondary vortex, which is also known as passage vortex.

The same effect of movement inside the boundary layer is also valid for the outer end wall. This results in a second passage vortex, which is counter rotating to the one on the inner casing. To differentiate between those two vortices, the one at the outer casing is called upper passage vortex (UPV) and the one on the inner end wall is called lower passage vortex (LPV).

Figure 2.13 shows both counter rotating passage vortices downstream of a vane passage, as well as a smaller trailing edge vortex, which results of the different velocity components between the vane suction and pressure side due to the passage vortices. It can also be seen, that these small vortices are counter rotating with respect to the dominant passage vortices.

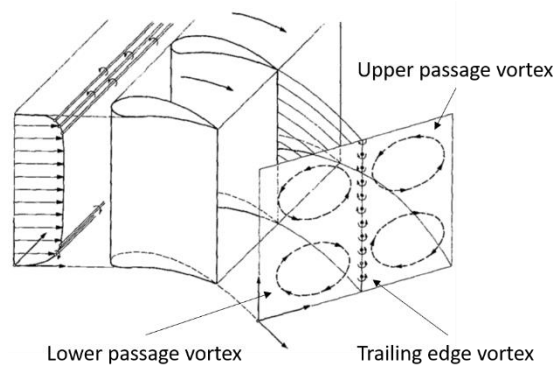


Figure 2.13: Vortices downstream a vane passage (adapted from [28])

To complete, Figure 2.14 indicates the various characteristic vortices which are formed in a vane or blade passage. The two legs of the horseshoe vortex due to the impinging boundary layer at the vane/blade leading edge are named V_{sh} (suction side leg) and V_{ph} (pressure side leg) respectively. V_p shows the passage vortex, which has the same sense of rotation as the pressure side leg of the horseshow vortex. Additionally, smaller vortices induced by the passage vortex can be identified forming in the corners between the endwall and the vane. In the sectional view B-B, the counter rotating wall vortex V_{wip} , located at the intersection of the duct endwall and the vane suction side, can be identified. Moreover, two corner vortices are induced, one at each intersection of the endwall and the vane pressure (V_{pc}) and suction side (V_{sc}) respectively. Also these two vortices are counter rotating with respect to the passage vortex.

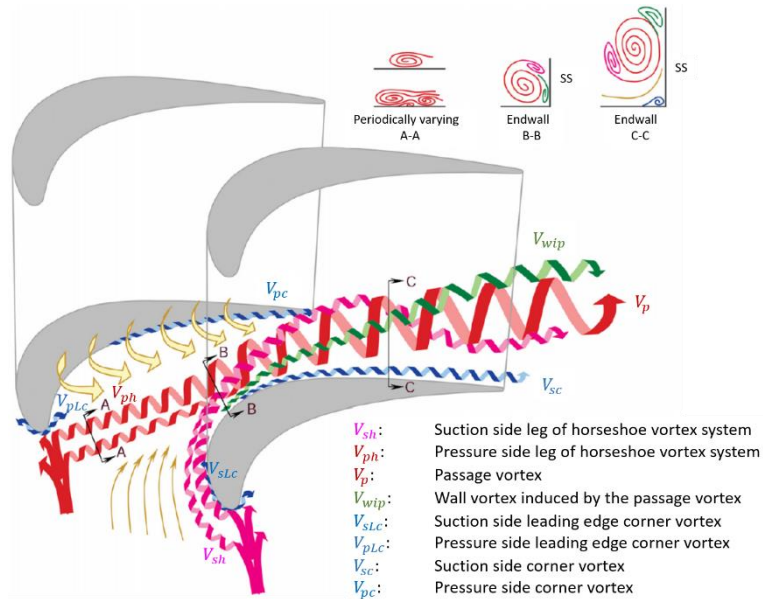


Figure 2.14: Secondary flow structures in a turbine vane passage (adapted from [29])

All figures shown so far indicate the origin of the secondary flow effects on the hub. The same is also valid for the outer casing of a flow channel, with the only difference, that the vortices there are counter rotating with respect to the ones at the inner casing.

The same explanations concerning the origin of vortices done for a stationary vane row are also valid for a moving rotor blade row.

2.3.2 Rotor Tip Leakage Flow

A tip leakage flow is present in a turbomachine if there is a clearance between a rotating and a standing part (rotating blade row and stationary casing or stationary vane row and rotating casing). This type of flow results firstly, which is also the dominant cause, from the flow due to the pressure difference between the suction side and the pressure side of a blade or vane, and secondly from a no-slip condition between the boundary layers of the blade/vane tip and the casing (see also [30], [31], [32]). Figure 2.15 shows a rotor blade tip with an indication of the tip leakage flow leading to a high velocity tip jet. It can be clearly seen, how this tip jet is forming a vortex on the blade suction side when interacting with the passage main flow. This characteristic vortex is the so-called tip leakage vortex. In case of a turbine, its rotational direction is identical with the direction of the rotor and counter rotating with respect to the passage vortex.

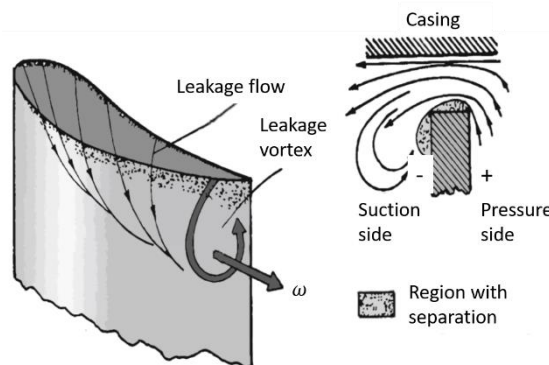


Figure 2.15: Origin of the tip leakage vortex (adapted from [7])

The optimum concerning the work extraction of the fluid would be of course no vortex at all because it is inducing losses. These losses result mainly from the mixing of the tip jet and the main flow (see also Denton [33]). A positive effect on the other side can be a more energetic boundary layer on the casing downstream of a rotor. This results from the momentum transfer from the higher energetic flow of the vortex to the lower energetic one on the casing end wall.

2.3.3 Analysis of a Trailing Edge Wake

During this thesis, a guiding structure called riblets is part of the performed investigations. Because riblets or surface roughness in general are influencing the boundary layer, also the trailing edge wake changes if they are present. Reason for this is that the boundary layers from both sides of a vane are forming a wake when they meet at the vane trailing edge. Figure 2.16 shows this procedure schematically. Therefore, boundary layer parameters can be used to evaluate the differences of the wakes with respect to the investigated surfaces.

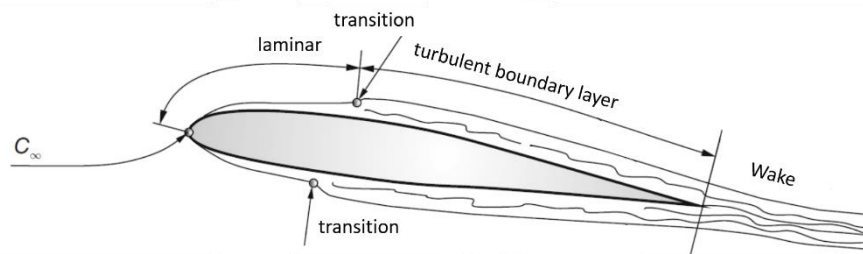


Figure 2.16: Origin of the trailing edge wake (adapted from [7])

Schobeiri and John [34] showed a way to analyse wakes downstream of a body using those parameters. Figure 2.17 gives an overview of the values which are needed to calculate specific characteristics of a wake. On the ordinate of this figure, the streamwise velocity component \bar{U} is depicted and the abscissa shows the coordinate ζ , which is perpendicular to the flow direction. The black line indicates the distribution of these two values downstream of a body, in which the body is located directly upstream of the velocity minimum. The red line indicates a hypothetical potential velocity \bar{U}_p , which is a fitting of the \bar{U} distribution outside of the wake.

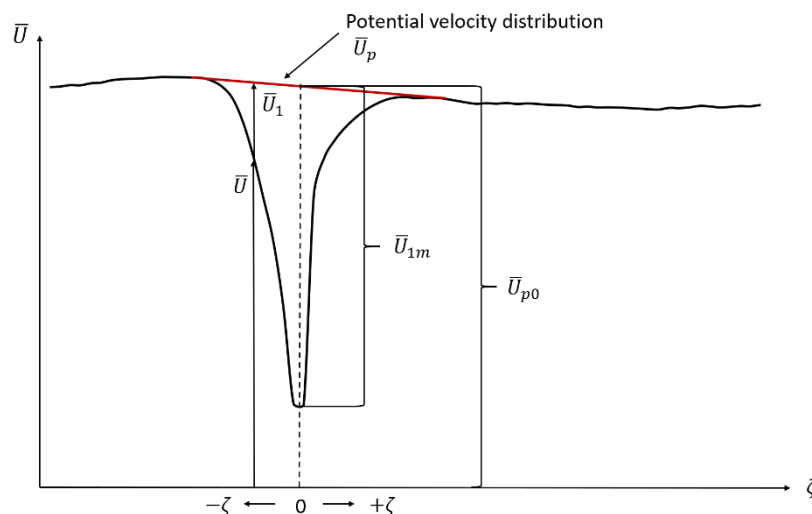


Figure 2.17: Streamwise components needed to analyse the trailing edge wake (adapted from [34])

It is now possible to calculate the width of the wake, which is a length scale to nondimensionalize ζ , as explained in the following equation:

$$b = \frac{1}{\bar{U}_{1m}} \int_{-\infty}^{+\infty} \bar{U}_1 d\zeta \quad (2.88)$$

Herein \bar{U}_{1m} is the maximum velocity defect of the whole distribution and $\bar{U}_1 = \bar{U}_p - \bar{U}$ is the locally velocity defect of the component in streamwise direction. The wake width is an important parameter because the wider it is, the higher the aerodynamic losses are.

Another parameter to characterize a wake is the momentum thickness δ_2 which gives the deficit of the momentum due to the wake. This thickness gives the shift of the free stream fluid in which the momentum would be the same as without a boundary layer. It can be calculated as follows

$$\delta_2 = \frac{1}{\bar{U}_{p0}^2} \int_{-\infty}^{+\infty} \bar{U}(\bar{U}_p - \bar{U}) d\zeta \quad (2.89)$$

Also the parameters displacement thickness and energy thickness are used in the present thesis. Therefore, equations based on the definitions from [34] are developed.

The displacement thickness δ_1 is given by the following equation.

$$\delta_1 = \frac{1}{\bar{U}_{p0}} \int_{-\infty}^{+\infty} (\bar{U}_p - \bar{U}) d\zeta \quad (2.90)$$

It is the thickness, by which the frictionless outer flow gets shifted away from the wall due to the velocity decrease in the boundary layer. It gives the deficit of mass flow due to the presence of a boundary layer. \bar{U}_{p0} is the velocity defect of the potential velocity distribution at the wake centre. This centre is indicated by the dashed wake centre line in Figure 2.17.

Using the streamwise components defined above, the energy thickness δ_3 can be calculated as shown in equation (2.91). This distance describes the shift of the free stream to reach the same kinetic energy as would be available without the presence of a boundary layer.

$$\delta_3 = \frac{1}{\bar{U}_{p0}^3} \int_{-\infty}^{+\infty} \bar{U}(\bar{U}_p^2 - \bar{U}^2) d\zeta \quad (2.91)$$

With the displacement thickness and momentum thickness, another aerodynamic parameter can be obtained by simply making the ratio of both. It is the so-called shape factor H . This parameter can be determined for the vane pressure and suction side separately by using the correspondent values δ_1 and δ_2 , both calculated for each vane side by adapting the integration limits.

$$H = \frac{\delta_1}{\delta_2} \quad (2.92)$$

According to Schlichting and Gersten [35], this shape factor can be used to determine the predominant type of the boundary layer (laminar, turbulent, or even a separation) on a surface. A turbulent boundary layer is existing, if the shape factor has a value in the range of about 1.3 – 1.4 and a laminar boundary layer is starting if H has a value of 2.59. With a value of 4 or higher, a separation is occurring. The following figure is taken from [35] and shows the distribution of the shape factor concerning flat plate boundary layer measurements.

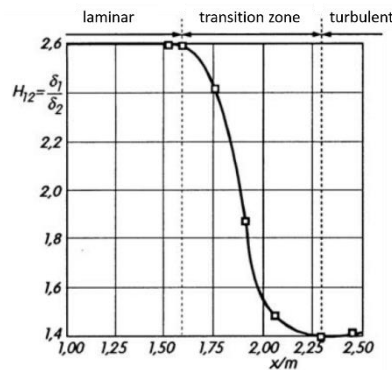


Figure 2.18: Shape factor distribution on a flat plate (taken from [35])

During this thesis these flat plate shape factor values are taken as a reference because the static pressure gradient along both sides of the used vanes is very low and can therefore be seen as constant (see also the work of Selic [36]).

2.4 Riblets

Since modern aero engines have to become better and better from an efficiency point of view, researches are conducted in many different directions in order to achieve this goal. One possibility to raise the efficiency of an engine is to decrease the aerodynamical losses, which include skin friction at vanes and blades of both, the compressor as well as the turbine stages.

Small ribs placed on a surface and oriented in the same direction as the mean flow can reduce skin friction. These grooved surface structures are also called riblets and are passive devices to reduce drag, if the geometry is set properly and the surface boundary layer is turbulent. It is a bionic mimic with the purpose to be used in technical applications, e.g. on aerodynamic parts of race cars, planes or boats. This can be realised by applying a foil with this microstructure or directly manufacturing it into the existing surface.

As already mentioned, the structure is mimic from the nature. More precisely, it is a replicate of the shark skin because of their low resistant while moving through the water (see e.g. Bechert et al. [37]). Some improvements are done for riblets mainly concerning their manufacturing. A real shark skin has an overlapping structure, which can of course not be manufactured in this way. Therefore, riblets are made as straight lines with grooves in-between. The difference can be seen in the following figure showing close ups of both, the real skin and the inspired one.

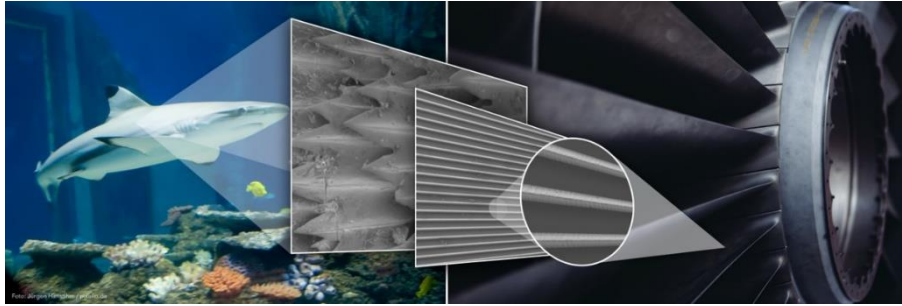


Figure 2.19: Evolution from shark skin to riblet foil (taken from [38])

2.4.1 The Riblets Effect

In general, riblets only reduce skin friction if their dimensions are correctly adjusted to the local boundary layer size. The reason is that they only work properly if they don't exceed the viscous sublayer, which is the nearest layer to the wall. Otherwise this microstructure even increases the skin friction. A viscous sublayer is only present if the boundary layer is turbulent what limits the usability of such riblets to these flow conditions. Figure 2.20 gives an overview of the different layers in a turbulent boundary layer and its evolution from a laminar boundary layer shown on the left side, separated from the turbulent one by the transition zone (area within the dashed lines).

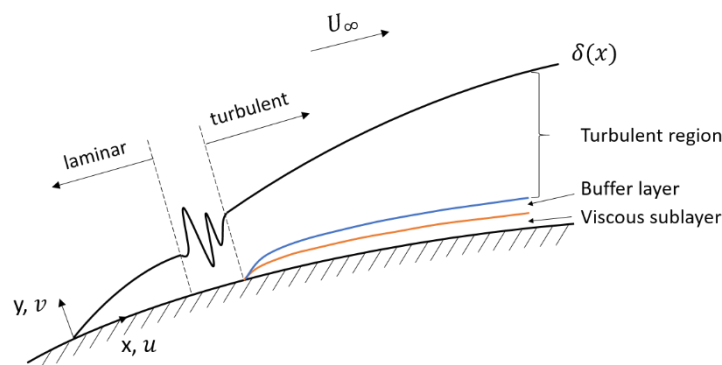


Figure 2.20: Boundary layer types

Two possible mechanisms are reported in literature which affect the skin friction reduction when using riblets compared to a smooth surface.

The first one is the hindering of the cross flow velocity and vorticity fluctuations of the turbulent flow by aligning the riblet structure with the flow direction. Such a cross flow is created by velocity differences between the layers inside the viscous sublayer. Low speed streaks inside this sublayer carry away slow fluid from the wall in direction of the main flow ('ejections'). To fulfil continuity, fast high energy fluid has to be transported to the wall ('sweeps'). This fluid momentum transport, created by the vertical motion of fluid, is always accompanied with cross flow and increases the turbulent shear stress (or Reynolds stress). With the riblets hindering now the cross flow, also the vertical motion is suppressed and hence this results in a reduction of the turbulent shear stresses and as a consequence also the skin friction. Figure 2.21 shows schematically the longitudinal (orange arrows) and cross flow (blue arrows) over riblets.

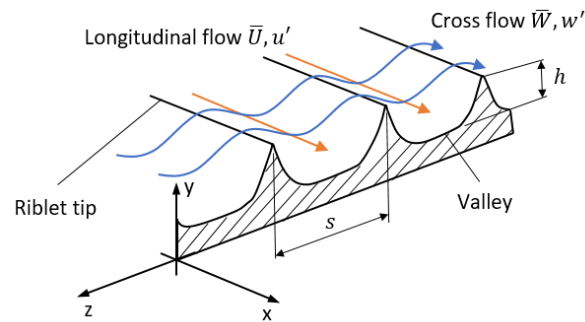


Figure 2.21: Riblets theory – Mechanism one (adapted from Hafizovic [39])

Additional to the velocity and vorticity fluctuations, there can be a second movement inside the boundary layer which is again in the cross flow direction. This movement is the already explained secondary flow structure called passage vortex (see section 2.3.1).

Both effects result in a cross flow movement which is to a certain amount suppressed by the riblet structure. If now the cross flow can be suppressed, shear stresses are reduced, and hence skin friction is decreased.

The second mechanism of reducing skin friction when using riblets is a limitation of the surface area, which is interacting with streamwise vortices and hence minimizing shear stresses. This is realized by lifting those vortices away from the flat surface and restricting the area which is exposed to the downwash motion of high-speed fluid caused by them. An interaction of a high-speed fluid and a low-speed one, which is present close to a wall, would increase the velocity gradient and hence the viscous shear stress.

Although using riblets is increasing the wetted surface, the distance between the rib tips can be chosen in a way, that the vortices are only interacting with these tips and not with the whole riblet surface. This happens when the spacing between the tips is smaller than the diameter of the mentioned streamwise vortices. In this case, the region with high skin friction is lower compared to the case without a ribbed structure. This decrease of the skin friction overcomes the increase near the riblet tips due to the increased wetted surface. If the spacing on the other hand is chosen too big, the vortices can enter the valleys between the riblets due to a downwash motion. The result is an increase of the interacting area and hence also of the skin friction (see also Choi et al. [40]).

Figure 2.22 shows a schematic description of the second mechanism. At the top, a visualisation of a flat plate is shown with a streamwise vortex interacting with the viscous sublayer. In the middle, a riblet case with a rib tip spacing s smaller than the vortex diameter d is shown followed by a case with the spacing larger than the diameter on the figure bottom. The interactions of vortex and sublayer, which result in a high skin friction, are indicated with the red frames. It is clearly visible, how the size of this zone is changing with different riblet geometries.

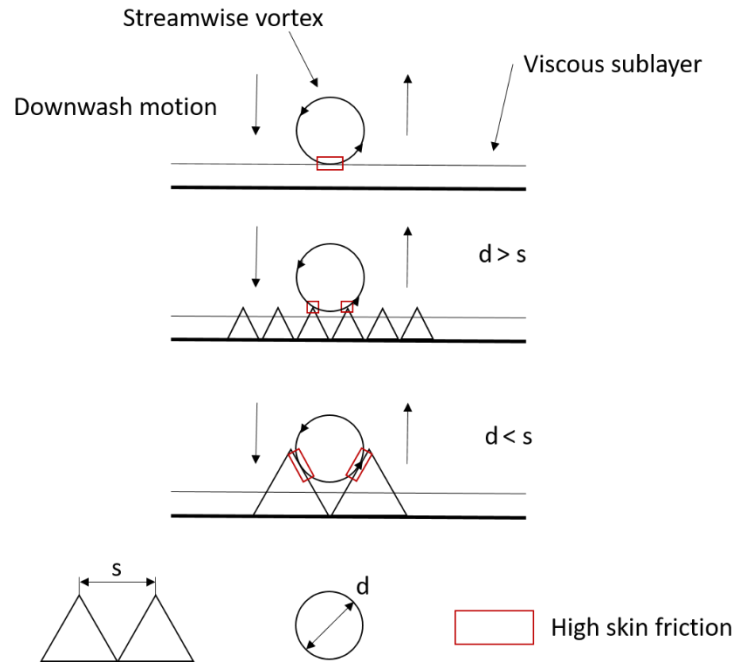


Figure 2.22: Riblets theory – Mechanism two (adapted from [40])

The first mechanism concerning the skin friction reduction is directly connected with the second one. Keeping the vortices above the riblets results in a reduction of the velocity fluctuations in cross flow direction inside the valleys. The consequence is a reduction of the shear stress and momentum transfer compared to a smooth surface.

2.4.2 Acoustic Analysis of Riblets – Lighthills Acoustic Analogy

Riblets, or surface roughness in general, cannot reduce tonal noise but can influence the broadband noise (see Skudrzyk and Haddle [41]) and this is exactly what is investigated in this thesis. Therefore, a connection between fluid mechanics and acoustics is needed. In 1951, Lighthill made the most important work concerning the noise production due to turbulent flow, which is known as Lighthills acoustic analogy (see Lighthill [42] and [43]). The basic idea is to derive a wave equation that is not neglecting friction, which leads to a nonlinear solution for the wave equation. An exact derivation of this problem can be found in literature, e.g. in Rienstra and Hirschberg [14].

To get to a solution, the first step is to use the equation for continuity

$$\frac{\partial \rho}{\partial t} + \frac{\partial}{\partial x_i} (\rho u_i) = 0 \quad (2.93)$$

and the equation for momentum but without linearization or simplification

$$\frac{\partial}{\partial t} (\rho u_i) + \frac{\partial}{\partial x_j} (\rho u_i u_j + P_{ij}) = 0 \quad (2.94)$$

In the upper equations, ρ stands for the density, x_i for the spatial coordinate with $i = x, y, z$, and u_i is the velocity. P_{ij} stands for the compressive stress tensor, which is including frictional effects, and can be written as

$$P_{ij} = (p - p_0)\delta_{ij} - \tau_{ij} \quad (2.95)$$

The formulation of this equation is unusual from an aerodynamical point of view (usually only p without p_0) but used in acoustics. In this equation, p is the pressure, p_0 is a constant pressure which can be chosen freely first, τ_{ij} is the viscous stress tensor and δ_{ij} is the Kronecker delta which is defined as

$$\delta_{ij} = \begin{cases} 1, & i = j \\ 0, & i \neq j \end{cases} \quad (2.96)$$

Because by setting p_0 as a constant, it can be added to the derivation of P_{ij} without changing the outcome of equation (2.94). When using the definition $p' = p - p_0$, equation (2.95) can be rewritten as follows

$$P_{ij} = p'\delta_{ij} - \tau_{ij} \quad (2.97)$$

Herein, τ_{ij} is the viscous stress tensor.

It should be mentioned, that p' is no linearization. The physical meaning is depending on the definition of the constant p_0 .

Differentiating the equation of continuity (2.93) in time gives

$$\frac{\partial^2 \rho}{\partial t^2} + \frac{\partial}{\partial x_i} \frac{\partial}{\partial t} (\rho u_i) = 0 \quad (2.98)$$

Taking the divergence of the nonlinear momentum equation (2.94) leads to

$$\frac{\partial}{\partial x_i} \frac{\partial}{\partial t} (\rho u_i) + \frac{\partial^2}{\partial x_i \partial x_j} (\rho u_i u_j + P_{ij}) = 0 \quad (2.99)$$

Subtracting this equation from (2.98) eliminates the term $\frac{\partial}{\partial x_i} \frac{\partial}{\partial t} (\rho u_i)$ and results in

$$\frac{\partial^2 \rho}{\partial t^2} - \frac{\partial^2}{\partial x_i \partial x_j} (\rho u_i u_j + P_{ij}) = 0 \quad (2.100)$$

The second term in this equation includes the nonlinearities and the frictional effects. As already done for the pressure, also a definition for the density is introduced: $\rho' = \rho - \rho_0$. Herein, ρ_0 is being again a constant which can at first be chosen freely. Concerning the

differentiation of the density in the first term of equation (2.100), this constant vanishes and it can be rewritten as

$$\frac{\partial^2 \rho'}{\partial t^2} - \frac{\partial^2}{\partial x_i \partial x_j} (\rho u_i u_j + P_{ij}) = 0 \quad (2.101)$$

To get from this equation to a wave equation, both sides are subtracted with

$$c_0^2 \Delta \rho' = c_0^2 \frac{\partial^2 \rho'}{\partial x_i^2} = c_0^2 \frac{\partial^2}{\partial x_i \partial x_j} (\delta_{ij} \rho') \quad (2.102)$$

Herein, c_0 is a constant velocity which can again be chosen freely at first. Subtracting now (2.102) from (2.101) gives

$$\frac{\partial^2 \rho'}{\partial t^2} - c_0^2 \Delta \rho' = \frac{\partial^2}{\partial x_i \partial x_j} (\rho u_i u_j + P_{ij} - c_0^2 \delta_{ij} \rho') \quad (2.103)$$

The terms on the right side inside the brackets can be written as the so-called Lighthill (turbulence stress) tensor. Using also equation (2.97) gives

$$T_{ij} = \rho u_i u_j + (p' - c_0^2 \rho') \delta_{ij} - \tau_{ij} \quad (2.104)$$

This Lighthill tensor includes also the fluctuating Reynolds stresses, which can be written as the so-called Reynolds stress tensor as follows, wherein $\overline{u'_i}$ and $\overline{u'_i u'_j}$ stand for time averaged values of the velocity fluctuations.

$$\overline{\rho u'_i u'_j} = \rho \begin{pmatrix} \overline{u'^2} & \overline{u'v'} & \overline{u'w'} \\ \overline{v'u'} & \overline{v'^2} & \overline{v'w'} \\ \overline{w'u'} & \overline{w'v'} & \overline{w'^2} \end{pmatrix} \quad (2.105)$$

Inserting equation (2.104) into equation (2.103) results in the well-known nonlinear wave equation concerning the density named after Lighthill

$$\frac{\partial^2 \rho'}{\partial t^2} - c^2 \frac{\partial^2 \rho'}{\partial x_i \partial x_i} = \frac{\partial^2 T_{ij}}{\partial x_i \partial x_j} \quad (2.106)$$

The left side of this equation gives the linear propagation of the sound with the speed of sound c and the right side is a nonlinear source term. As mentioned above, this source term contains the so-called fluctuating Reynold stresses $\overline{\rho u'_i u'_j}$, which describe the unsteady convection of the flow as well as can be connected with the (turbulent) velocity fluctuations. From this tensor one can see that noise is generated by those stresses and serves now as a connection between turbulence and noise.

As the riblets are able to suppress the crossflow, it is assumed that entries in T_{ij} which are connected with this movement are also decreasing. But also the viscous part is decreased by

riblets as described in section 2.4.1. Therefore, it is assumed that this microstructure is able to reduce the overall noise level.

2.5 Operating Point Definition – Aircraft Noise Certification

Every new aircraft engine has to undergo a certification procedure, in which specific measurement points, defined by the International Civil Aviation Organization (ICAO), are investigated concerning their noise impact onto the area neighbouring an airport. With the measurement points ‘Cutback’ and ‘Sideline’ two out of three points are related to the starting of an aircraft and with ‘Approach’ one is linked with the landing. Figure 2.23 indicates the defined locations of the three measurement points with respect to the beginning of an airport runway.

‘Approach’ is settled in a distance of 2000 m in front of the runway begin and in a height of approximately 120 m over ground. The airplane has a glide angle of about 3 deg. ‘Sideline’ measurements take place 450 m beside the runway. At the certification point ‘Cutback’, which is located 6500 m after the runway begin, the thrust is reduced to 80 % with respect to the ‘Full power’ point. This thrust reduction is performed to lower the noise emitted to the surrounding area. On the contrary, the reduction also flattens the possible climb angle which results in a longer duration closer to the surface and hence to a longer impact of noise.

All information can be found in the technical report [44], submitted as guideline for the whole noise certification procedure of aircrafts.

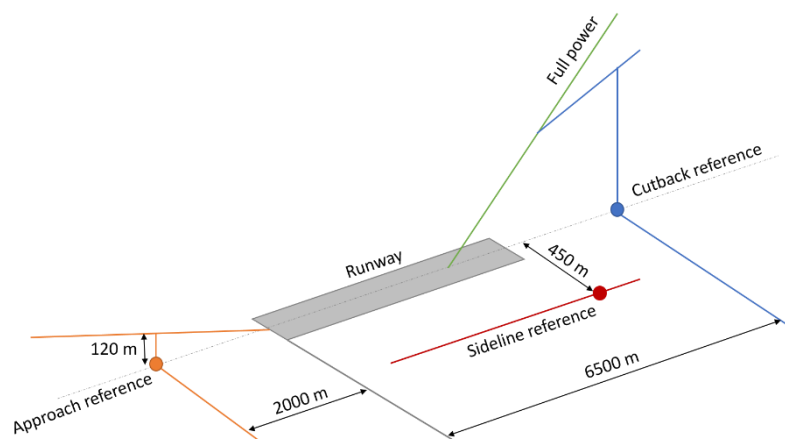


Figure 2.23: Definition of aircraft noise certification points

Concerning the examinations performed during this thesis, the certification point ‘Approach’ was taken as the test rig operating point. The reason is, that although ‘Cutback’ has more thrust and is hence louder close to the ground compared to ‘Approach’, the landing procedure of an airplane takes longer in lower heights and is therefore a bigger area is affected by the emitted noise.

3 Literature Study

3.1 Literature of Acoustic Liners and their use in Turbomachines

Acoustic liners have been used to suppress noise in everyday situations since decades. Numerous investigations on this topic have been performed and published in literature. Most of them were targeted on the impact of the absorber geometry onto the absorption performance, the influence of grazing as well as bias flow, and the effect of high sound pressure amplitudes. In this section, only a short overview of important publications should be given.

Hermann von Helmholtz made the first investigations on a cavity connected to the environment via an opening concerning the ability of sound attenuation. In his work [20] he mentioned the first equation to calculate the resonance frequency of such a device, and hence the frequency of maximum absorption. Many others should follow him by evolving his equation. For example Lord Rayleigh [45], as well as Ingard [22], which both investigated an end correction for both sides of the neck, to include the movement of the mass. Ingard examined very early the influence of different aperture geometries as well as cavity geometries and their relative location to each other onto the absorption performance of a resonator and the change of the mass end correction.

Panton and Miller [46] gave a slightly different form to the equation concerning the resonance frequency suggested by von Helmholtz (again under no flow conditions). They mentioned that the classical formulation is not valid if the resonator length is larger than $\lambda/16$ of the frequency which should be dampened, hence they included a term into the classical equation which is considering the resonator depth.

Although only the cavity volume size, without taking into account the shape or geometrical dimensions, is used in the resonance frequency equation (2.77), Selamet et al. [47] made investigations on this topic. They performed numerical and experimental studies for resonators with a fixed volume but altering the diameter as well as the depth. The results showed, that if the ratio of depth to diameter is increasing, the resonance frequency gets lower.

Chanaud [48] investigated the influence of different cavity and orifice shapes and their relative position to each other onto the validity of the equation calculating the resonance

frequency. He found out, that the shape of the absorber neck has not much of an influence but so has the shape of the cavity as well as the positioning of the neck with respect to the cavity centre. In the following investigation, Chanaud [23] found that a variable positioning of the orifices can extend the absorption bandwidth by 5 %.

Another important topic is the effect of a grazing air flow over the resonator openings. Many studies have been carried out concerning the attenuation performance of an absorber in the vicinity of such an axial grazing flow.

Seo and Kim [49] made investigations onto the use of low frequency Helmholtz absorber in serial and parallel arrangement inside a duct in the absence of flow. They showed, that the transmission loss is increasing with the number of absorbers in the duct for both cases, and that in a parallel arrangement, also the bandwidth or absorption is expanding.

Anderson [50] showed in his work the effect of an air flow onto a side branch Helmholtz resonator. During the experiments both, a sound wave as well as an air flow propagating in the same direction could be tested in a circular duct. It was found, that the resonance frequency increased with increasing flow velocity. Experiments were taken for a velocity range up to 80 m/s. As a reason for the frequency increase they referred to Phillips [51], who suggested that flow was affecting the mass end correction. In the case of Anderson, he assumed that this end correction was fully vanished due to the high flow velocity.

Selamet et al. [52] also examined the effect of a grazing mean flow on Helmholtz absorbers, numerically as well as experimentally. The main outcomes of these low frequency investigations were: the transmission loss decreases with increasing flow velocity, the peak absorption also decreases and there is a shift of the resonance frequencies to higher values. Following figure is taken from their work and is presenting their results concerning the dependency of the transmission loss onto the mean flow velocity.

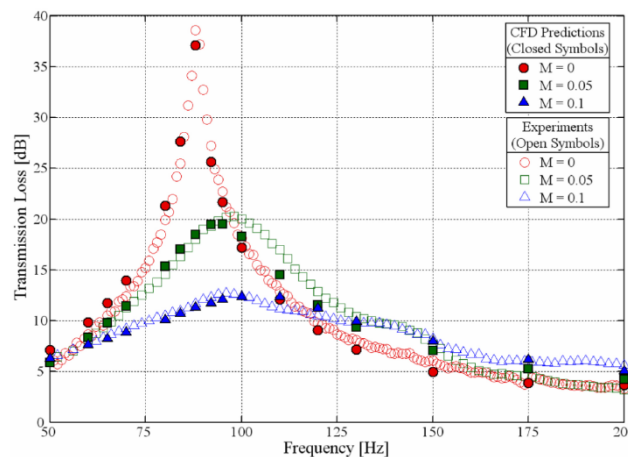


Figure 3.1: Shift of resonance frequency due to grazing Ma number (taken from [52])

Such a shift of the resonance frequency is a very important information during the design process. Unfortunately, this topic is not very clear in literature. The opinions of different authors differ a lot.

For example, Bell et al. [53] showed in their experimental work about the liner performance in the presence of a 3D wave motion as well as a mean flow past the absorber, that there is no need to correct the mass end correction (see equation (2.80)) up to a flow Mach number $Ma \leq 0.24$.

When it comes to the use of absorbers in a turbomachine, focused on the turbine, the available literature is very limited, especially experimental work.

Serrano and Torres [54] performed numerical investigations onto the implementation of acoustic liners in outlet guide vanes of a three stage low pressure turbine. They made calculations for a liner used at both sides of the vane, resulting in the outcome that the pressure side can attenuate better modes which are co-rotating whereas modes which are counter rotating, with respect to the rotor rotational direction, are attenuated better using a lined suction side. A comparison of a hard walled outlet guide vane and a treated one showed a reduction between almost 1.2 dB (pressure side) and 0.5 dB (suction side) concerning the 1st BPF, and 1.5 dB (pressure side) and more than 3 dB (suction side) in case of the 2nd BPF.

Elliot et al. [55] made experimental investigations on two topics related to the noise reduction of the fan. One was the acoustic treatment of stator vanes and the second one was a so-called “over the rotor technology” which is an implementation of metallic foam in the outer casing exactly over the rotor. Experiments were performed in a windtunnel for ultra high-bypass ratio fans, investigating the combination of a fan and a stator vane row. The acoustically treated stator vanes had internal cavities to achieve a noise reduction at a distinct frequency. They showed a resulting decrease of about 1 dB.

Broszat et al. [56] presented in their work experimental and numerical results, investigating the performance of acoustic liners of the type $\lambda/4$ included into the inner and outer end walls of the vane passage in a turbine exit casing. They investigated the three operating points approach, cutback and sideline at the test rig located at the Institute of Thermal Turbomachinery and Machine Dynamics at Graz, University of Technology. The results showed a reasonable noise reduction at all three operating points concerning the 1st BPF, between 3.5 dB at approach up to 5.7 dB at sideline.

3.2 Literature on Riblets

In the past years, many investigations using this guiding microstructure adapted from nature to lower the skin friction and raise the efficiency were performed and are still ongoing. Besides this reduction, also the noise can be decreased. The results of these experiments are described in a section below. During the work of this thesis, one of the first if not the first publication concerning this topic was done. There is numerous literature on the aerodynamical performance of riblets but none regarding the acoustics. Therefore, only some publications investigating the aerodynamical behaviour are mentioned in this section.

There is a various number of possible riblet geometries, which were also investigated experimentally in the past and can be found in literature. Especially Bechert et al. [57] showed an overview of the differences. According to this work, the favourable geometry concerning the skin friction reduction would be a so-called ‘Blade’ design followed by a trapezoidal geometry and the ‘Sawtooth’. Figure 3.2 shows the results of [57] concerning the wall shear stress reduction over the dimensionless rib tip spacing which can be determined according to the following equation.

$$s^+ = s \frac{u_\tau}{\nu} \quad (3.1)$$

Herein s is the rib tip spacing, u_τ is the wall shear stress velocity, and ν stands for the kinematic viscosity of the fluid.

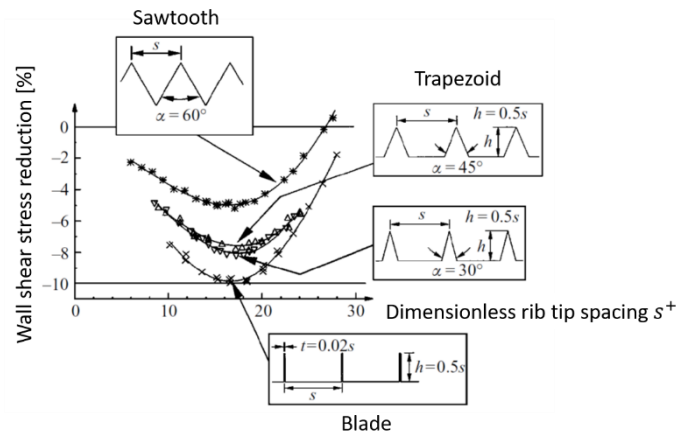


Figure 3.2: Effectiveness of different riblet geometries (taken from [57])

The mentioned spacing as well as the aspect ratio of the riblets depend on the wall Reynolds number and has therefore to be adjusted with respect to the case of use.

Choi et al. [40] performed direct numerical simulations of a turbulent flow over a riblet surface. The main goal of this research was to find an explanation of how this microstructure can reduce drag. Together with the work of Luchini et al. [58], who also did investigations to clarify the mechanisms of turbulent drag reduction using riblets, these works give a very good insight into the reduction phenomena and were also taken for the description of the riblets effect in section 2.4.1.

The suggested optimal positions of riblets on blades are not uniform according to different sources in literature as can be seen from the listed publications below.

Fang et al. [59] performed experiments using a compressor cascade with a riblet structure applied on the pressure side of the blades. They studied a loss reduction using this microstructure and achieved 10 % less when using them only on the blade pressure side at moderate and high loading. Placing them also on the blade suction side, led to a smaller benefit of 2 %. As a reason they mentioned, that the riblets on the suction side lower the ability of the flow to withstand the adverse pressure gradient on the curved wall.

On the contrary, Boese and Fottner [60] stated in their work, investigating a highly loaded compressor cascade, that the main positive effect of riblets results from the application only on the compressor blade suction side. Furthermore was found, that the boundary layer thickness of a smooth blade and one with added riblets is equal.

Lietmeyer et al. [61] made also investigations on this topic. They placed triangular riblets with constant geometry on both sides of a compressor blade, according to the dominating wall shear stress, in a linear cascade. With riblets along the suction side, they could achieve a profile loss reduction of 4 %. The results concerning the application on the pressure side was 1 % and on both sides 4.9 %. In their work, they performed additionally experiments with a strong incidence on the blade pressure side plus a laminar separation bubble on the suction side. The gained profile loss reduction was with 7.2 % significantly higher. They argued, that the reason for this is an elimination of the separation bubble due to an earlier triggering of transition using riblets. Another important outcome was the prove that riblets applied already on the blade

leading edge, and hence in the laminar region, increase the profile losses. Again, because they trigger an earlier transition.

Debischop and Nieuwstadt [62] made investigations on V-shaped riblets in the presence of an adverse pressure gradient, which results in a skin friction reduction of 13 % and therefore in a significant increase compared to the 6 % gained by the zero pressure gradient boundary layer test. Also Nieuwstadt et al. [63] reported such a result.

Miao et al. [64] performed numerical as well as experimental investigations on the efficiency of riblets added on the turbine end walls in low-speed linear cascade. They found that the riblets reduce the horseshoe vortex pressure side leg, decrease the pressure gradient in the cross passage direction, and the move the passage vortex loss core in the direction of the end wall. They also stated that in a real engine, the performance of riblets would be different due to the unsteady flow and high turbulence level.

3.3 Overview on Compressor / Turbine Aerodynamics

Turbine exit guide vanes have the same aerodynamical purpose than a compressor blading, namely reducing the swirl in the flow and transforming it into thrust. Guiding the mean flow into an axial direction with respect to the flow duct axis results in a homogeneous exit flow and hence in a higher propulsive efficiency in case of a real aero engine (see also Koch and Kozulovic [65]). The first part of this section gives an insight into investigations conducted during the last decades concerning the aerodynamics of compressors.

Kang and Hirsch [66] conducted experiments to achieve data upstream, inside and downstream of a linear compressor cascade to investigate the three-dimensional flow at design conditions. They observed, besides the well-known passage, horseshoe, corner, and trailing edge vortex, that the flow is also characterised by concentrated vortices, which shed from spiral node points at the blade suction side close to the trailing edge. They turn in the opposing direction with respect to the dominant passage vortex. The spiral node points are formed by separation lines on the blade suction side.

In the review of Lakshminarayana [30], information about the secondary flow in cascades as well as turbomachines for both, compressor and turbine are stated. It also includes the basics of leakage flow and gives a suggestion of the nature and location of vortices in a compressor rotor.

A series of publications on the understanding of boundary layer development on airfoils was given by Halstead et al. [67], [68], [69], and [70]. They investigated multistage, axial flow compressors and low pressure turbines experimentally, using hot film gauges and hot wire probes, as well as computationally, performing steady and unsteady simulations. In this series of papers, they examined the impact of Reynolds number and loading on low speed research facilities by varying both parameters.

Investigations on the secondary flow effects in axial turbines were performed extensively and very well described in the publications of e.g. Sieverding [28], Wang et al. [29], and Langston [27]. They all suggested and developed models of secondary flow effects in a turbine vane passage, with [29] giving the most detailed one.

These publications are of great interest concerning the flow within a vane/blade passage but the influence of an unshrouded rotor, as it was used during this thesis, is not examined there.

The clearance between an unshrouded rotor tip and the outer duct wall leads to a tip leakage flow as described theoretically in section 2.3.2. As mentioned, this flow results in increased losses and therefore many investigations concerning this topic have been conducted in the last decades. This leakage flow is strongly influencing the downstream located stages and makes it therefore to an important topic within this thesis, focusing on the EGVs downstream of the LPT rotor.

McCarter et al. [71] made experimental investigations to understand the physics of tip leakage flow. They mentioned that the tip leakage flow clings on the blade suction surface up to about mid chord, to lift off at around 80% of the axial chord. After the lift off, it forms the tip leakage vortex by interacting with the main flow. The roll up happens close to the suction side of the blade tip. Downstream of the blade trailing edge, the effects from the tip leakage vortex vanish faster than the ones from the passage vortex. They also stated, that with 25% higher losses compared with the passage vortex, the leakage flow is the more dominant disturbance in the tip region.

Xiao et al. [72] investigated the same setup as [71]. They stated that the interaction between the leakage and the passage vortex is weak until 90% axial chord. Beyond this point, both tend to merge and to interact strongly resulting in noticeable losses. Furthermore, they stated that the loss coefficient in the tip leakage vortex region is almost twice as high as the one in the passage vortex region. But it is also mentioned, that the leakage vortex losses are only confined to a small region with respect to the one of the passage vortices and therefore, the latter one produces higher losses in total.

Yoon et al. [73] investigated the efficiency of a turbine rotor once with a shroud and once unshrouded. They found a “break-even-clearance” which is a point, in which both types of the rotor, shrouded and unshrouded, showed the same efficiency. They further stated, that if it is possible to go below this point, also an unshrouded rotor could be used resulting in an increased aerodynamical efficiency, lower weight as well as stresses in the blade disc connection.

Selic et al. [74] showed in their work a comparison of different tip gap sizes concerning the rotor which was also used during the present thesis but at a different operating point. They performed numerical as well as experimental investigations concerning the effect of a tip leakage vortex onto a downstream located exit guide vane. The result was a significant influence of the leakage vortex onto the secondary flows. With an increase in the tip gap, a separation on the TEGV pressure side formed close to the leading edge. Furthermore, a decrease of the tip clearance showed a reduction of the guide vane wake width, resulting from removing the trailing edge vortex. The CFD results showed a decrease of the TEGV losses by 54% comparing zero and 1% (of the span) tip gap.

Bauinger et al. [75] presented different shroud configurations of a LPT rotor. The baseline rotor including a shroud with two sealing fins was compared with the same rotor but having a radial bore through the shroud close to the blade pressure side between the two fins. Allowing a flow through the bore into the rotor shroud cavity resulted in an aerodynamical blocking effect. With the bore, a lower Mach number and total pressure as well as a more uniform swirl angle close to the tip region downstream of the rotor could be achieved compared to the baseline setup.

4 Experimental Facility

4.1 Subsonic Test Turbine Facility

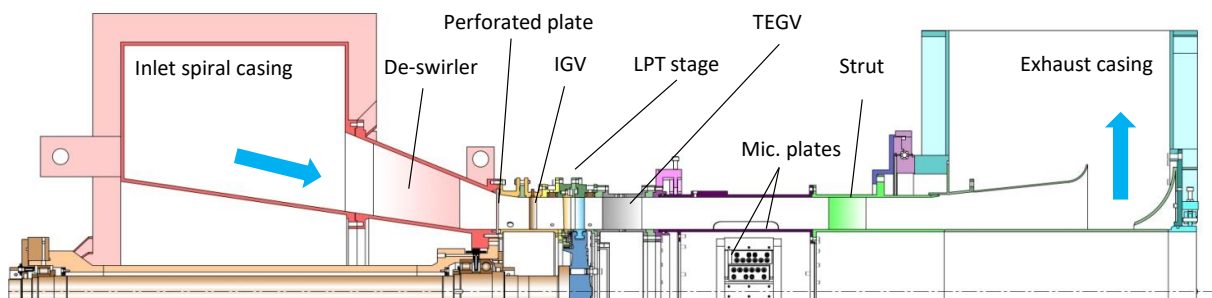


Figure 4.1: Experimental facility STTF-AAAI

The Institute of Thermal Turbomachinery and Machine Dynamics at Graz University of Technology operates a 3MW compressor station in order to supply a couple of test facilities continuously with pressurized air. During the present work, a 1 ½ stages subsonic test turbine facility was used to investigate the different novel turbine exit casing (TEC) setups. This subsonic test turbine facility has a maximum pressure ratio of 2 due to the inlet spiral casing. A mass flow rate between 2.5 and 15 kg/s at a stage inlet temperature of 100°C can be realized. This inlet temperature can be adjusted by coolers within the range of 40-140°C. In general, the test rig is designed for a rotational speed up to 6300 rpm and a maximum power of 500 kW.

Figure 4.1 shows a meridional cut of the LPT test facility. Pressurized air enters through a spiral inlet casing where the flow turns from radial into axial direction. This casing is needed due to the arrangement of the test rig and the water brake, which makes only a radial inflow possible. It can be seen, that the turbine has an overhang-type turbine shaft, which has its front bearing located within this spiral casing. The basic idea for such a turbine type is the possibility of an easy rotor setup change. The shaft is connected with a water brake, which is used to set the correct operating speed during a test run. A cooling plant at the institute delivers the needed water for the brake.

Because of the already mentioned inlet casing, an unavoidable swirl is added to the flow. In order to provide well defined and uniform inflow conditions a de-swirler together with a perforated plate is located upstream of the LPT stage inlet.

Downstream of this perforated plate, inlet guide vanes (IGVs) can be found which simulate additional wakes of other low pressure turbine stages located upstream in a real aero engine. Following these IGVs, the LPT stage is located. It contains an unshrouded rotor with a flat rotor tip, followed by a stator and a turbine exit casing including the turbine exit guide vanes (TEGVs). This last vane row turns the flow into an axial direction. The air leaves the test rig through an acoustic measurement section, supporting struts, exhaust casing, and the exhaust stack to ambient. As an additional safety device, a flywheel has been installed in case of a brake failure.

The acoustic measurement section, which is containing plates with included microphones, is not connected with the LPT casing but with the exhaust casing. Because of this, an axial movement of this section is possible and hence an easy change of the TEC and the LPT stage is possible. A full 360 deg rotation of this acoustic test section is possible which allows a sufficient examination of the sound field downstream of the TEGVs. During such a rotation, the mentioned struts keep their relative position to the measurement section.

Basically, this subsonic test rig is a scaled version of a real aero engine. The diameters are half of that of an engine, what means that the rotational speed has to be higher to achieve the same aerodynamical load. An important parameter is the stage loading parameter ψ which is defined as follows

$$\psi = \frac{\Delta h}{\frac{u^2}{2}} \quad (4.1)$$

With the circumferential velocity u of the rotor

$$u = \omega \cdot r \quad (4.2)$$

This parameter serves as a nondimensional parameter concerning the loading. Δh is the enthalpy difference upstream and downstream the rotor, ω is the angular frequency, and r is the radius. It can be seen, that with a decrease of the radius, the angular frequency has to be increased to achieve the same loading while keeping the circumferential velocity constant.

A more detailed description of the subsonic test turbine facility for aerodynamic, aeroacoustics, and aeroelastic investigations (STTF-AAAI) is given in Moser et al. [76] and Moser [77].

4.2 Operating Conditions and Stage Geometry

During this work, the noise certification point Approach (APP), which corresponds to the landing conditions of an aero engine, has been investigated. This point is selected because during this flight condition the noise pollution for people living close to an airport is enormous and therefore a noise reduction is terribly needed. The following Table 4.1 shows the operating point during this works' test campaign.

Table 4.1: Operating Point

Operating Point	
TEGV Reynolds number	~340000
Stage pressure ratio	1.16
Corrected speed	4042 rpm
Reduced mass flow rate	6.81 kg/s
Stage total inlet temperature	100 °C

Table 4.2 gives an overview of some details concerning the test rig geometry. Because of the use of an unshrouded rotor, a 1% tip gap with respect to the channel height is present, resulting in a tip leakage flow which has of course an influence onto the downstream vane row. Such a tip gap is uncommon for an aero engine but because the subsonic test rig is intended for doing mainly acoustic investigations, this type of rotor was chosen during the rig design process.

Table 4.2: Stage geometry details

		IGV	Stator	Rotor	TEGV
Blade/Vane count	-	83	96	72	15
Axial chord length	[mm]	20	17	23	100
Aspect ratio	-	4	4.71	3.48	0.8
Tip gap to blade height ratio	-	1.0%			
Hub to tip radius ratio	-	~2/3			

4.3 Turbine Exit Guide Vanes

In general, two different vane geometries have been investigated. The main geometry is the so-called Datum or Standard exit guide vane, which also served as a baseline for the investigations of resonator vanes and guide vanes with riblets applied on the suction side. The second main geometry is derived from the Standard TEC vane design and contains a 20 deg lean, what results in a reduction of the sound power level. Both baseline geometries have been already investigated successfully in other projects. See e.g. [78], [79], [36]. The following subsections present all investigated vane designs of this thesis concerning their difference in design.

For the sake of clarity, the next table shows an overview of the investigated setups concerning the use of Helmholtz absorbers in this work. It consists of the three different vane designs, the two different end wall designs (hard and soft), and different absorber neck diameters for both vanes and end walls. Each configuration should from now on be related to the letter in second line of Table 4.3. The stated diameter is related to the absorber neck diameter of either the Helmholtz vanes or the outer cassette of the soft end walls. Concerning the inner cassette, the diameter is kept constant at 3.5 mm to widen the frequency range of attenuation.

The coloured boxes in Table 4.3 indicate which vane and end wall design are combined in each setup. E.g. configuration (F) consists of the Helmholtz vane design with a neck diameter of 3.2 mm and of the hard end walls.

Table 4.3: Overview of investigated configurations

		Diameter [mm]	Configuration									
			A	B	C	D	E	F	G	H	I	J
Vane Design	Standard	-										
	taped											
	Helmholtz	3.2										
		3.4										
Leaned	-											
End Walls Design	Hard	-										
	Soft	3.5										
		3.8										
		4.2										

4.3.1 Standard and Helmholtz Vanes

This subsection is about the Standard TEC, which is derived from a state-of-the-art vane design of a commercial aero engine. Table 4.1 stated already the TEGV Reynolds number, which is calculated with the inlet Mach number and the axial chord length of this vane design.

Figure 4.2 shows the baseline vane of the Standard TEC, which should be referred to as Standard vane design from now on, on the left side and a vane including the Helmholtz absorber on the right side. This second design is named Helmholtz vane design. Both vane designs are identical from a geometrical point of view. Differences occur in the manufacturing process of both designs, having on the one side a milled Standard vane and on the other side an additive manufactured Helmholtz vane. Using this additive manufacturing process increases the surface roughness of the vanes. But this is wanted because a realistic manufacturing process, which can then also be used for real engine vanes, is required. The additive manufacturing process allows the inclusion of cavities inside the vane which is the main difference between those two vane designs. Due to these cavities and the bores located on the vane suction side, Helmholtz absorbers as described in section 2.2.2 could be realized. In total, 15 separated absorbers are implemented in the Helmholtz vane design.



Figure 4.2: Standard vane (left) and Helmholtz vane (right)

Table 4.4 presents the position of each absorber centre. The axial distance is measured from the vane LE and given in % regarding the chord length. Resonator line 1 is the closest to the leading edge. The radial position of each neck opening is stated in % of the span, starting at the inner duct casing.

The given axial position of resonator line 1 is due to the result of a project partner. They performed numerical simulations to find the highest pressure fluctuations at the vane surface.

Lines 2 and 3 are added to achieve a higher attenuation. The distances are realized due to the geometrical dimensions of the absorber cavities and the vane thickness.

Table 4.4: Absorber positions – Helmholtz vane

Resonator line	Axial distance from LE in % of chord length	Radial position from hub in % of span				
		1	2	3	4	5
1	16	18.75	33.75	48.75	63.75	78.75
2	25	26.25	41.25	56.25	71.25	86.25
3	34	18.75	33.75	48.75	63.75	78.75

Figure 4.3 shows a picture of a Helmholtz vane which was cut to see the inside structure of the printed volume end walls. It is visible, that the cavities have a very good circular shape without any edges (indicated by the yellow circle). This is important concerning the correct absorber eigenfrequency. The absorber neck was drilled after the manufacturing process to assure a smooth surface.



Figure 4.3: Cut of a Helmholtz vane

Concerning the Helmholtz vanes, two different diameters of the resonator neck have been investigated. A variation of this neck diameter should result in a variation of the absorber resonance frequency. To be sure about the influence of the vane surface roughness due to the manufacturing process, one test was also performed with closed absorber openings. Figure 4.4 shows on the left side again the Helmholtz vane and a fully equipped TEC on the right side.

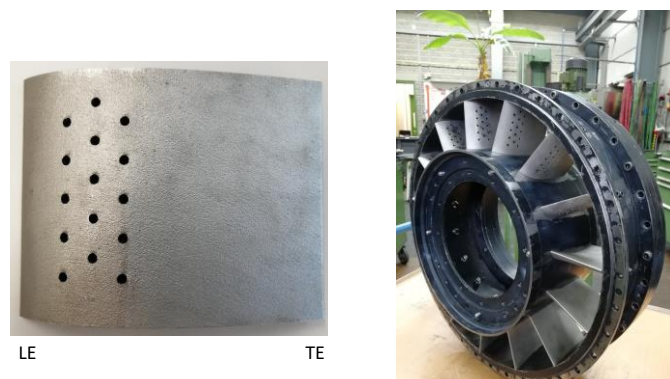


Figure 4.4: Helmholtz vane (left) and equipped TEC (right)

The geometrical details of the absorbers included in the Helmholtz vanes are presented in Table 4.5. The two values in the column of the neck diameter stand for two different setups.

Table 4.5: Geometrical details of the Helmholtz vane absorber

Neck diameter	Neck length	Cavity diameter	Cavity depth
[mm]			
3.2 / 3.4	2.7	7.8	6.2

These geometrical dimensions result in absorber resonance frequencies presented in Table 4.6, for both cases with and without Ma number influence, calculated according to equation (2.77). Comparing the calculated results with and without Ma number gives already an insight in how important it is to know first, if this correction is necessary, and second, which Ma number is predominant. A shift of almost 1000 Hz for all cases can be observed considering the Ma number or not.

Table 4.6: Calculated resonance frequencies with and without Ma number - Helmholtz vane

Setup	Neck diameter [mm]	Resonance frequency [Hz]	
		With Ma	Without Ma
(F)	3.2	5446	4612
(G)	3.4	5767	4864

4.3.2 Resonator Vanes

A second vane design based on the Standard vane and equipped with acoustic absorbers was also investigated during this thesis. The designing process of these vanes was done by a project partner. It is named Resonator vane design and consists of four separated cavities inside the vane connected to the environment via sixty openings, aligned in three rows, each. The resonator necks are again located at the vane suction side as already seen at the Helmholtz vane design. Having not only one opening per cavity is the main difference to the Helmholtz vanes. The second one is, that the bores are with 0.9 mm in diameter in the submillimetre area and therefore, such a system is declared as a microperforated panel absorber. This is a sub type of the classical Helmholtz absorber, which was already shown in Figure 2.7. Same as the Helmholtz vanes, also this design is additive manufactured.

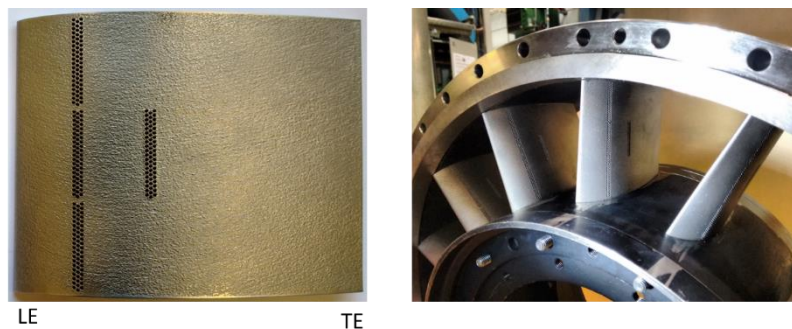


Figure 4.5: Resonator vane (left) and equipped TEC (right)

Figure 4.6 shows a cut through the CAD model of the resonator vane at midspan. On the right side of the figure, a zoom in of one absorber is depicted, indicating the cavity and three necks. The middle line of neck openings in the first resonator line has an axial distance of 16 % to the LE with respect to the chord length. In case of the second midspan cavity, an axial distance of 35 % is chosen. As already stated for the Helmholtz vane design, the position of the first cavity row is due to the result of a numerical simulation performed by a project partner.

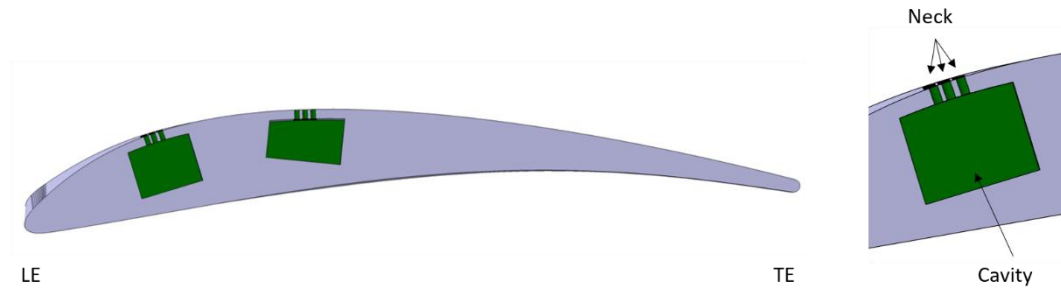


Figure 4.6: CAD cut of resonator vane

In Table 4.7, the geometrical details of the Resonator vane design concerning the included absorbers are given. The four resonator cavities are not equal in size, which is aimed to result in a more broadband effectiveness.

Table 4.7: Geometrical details of the Resonator vane absorber

	Cavity size [mm ³]	No. of openings per cavity	Neck diameter [mm]	Neck length [mm]
Hub	1300	60	0.9	1.2
Midspan	1345			
	1341			
Tip	1450			

4.3.3 Standard Vanes with Riblets

For these investigations, the basic Standard vane design is used as the carrier of the riblet foil, which is applied on the vanes suction side. Due to this application, the vane slightly thickens up. Consequently, a reference case with a smooth foil having the same thickness as the riblets valley is also investigated. In this baseline case, the vanes are fully covered with the smooth reference foil. Concerning the riblets case, the microstructure is only used on the vanes suction side. To ensure a uniform increase of the thickness over the whole vane surface and to avoid a forward-facing step in the vane leading edge area, a smooth foil was applied on the pressure side as well as on a small part of the suction side. On the latter one it is in the area from the vanes leading edge to the red line shown in Figure 4.7. The reason for this is that the turbulent boundary layer starts at this red line. To avoid edges on the vane LE, the smooth foil is one single piece covering the vane pressure side starting from the mentioned red line and ending at the trailing edge.

On the right side of Figure 4.7 a zoom-in onto the riblet geometry is shown. One can see that the investigated riblets are of trapezoid design with a tip to tip distance of 45 μm and an aspect ratio (AR) of 0.45. Additionally, a second foil with a rib tip distance of 90 μm and again an aspect ratio of 0.45 is investigated.

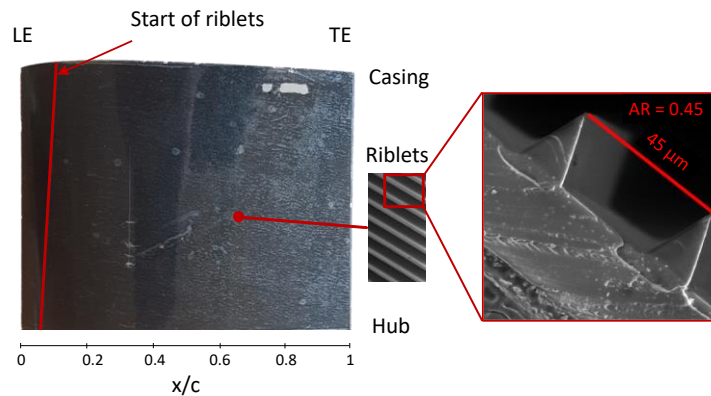


Figure 4.7: Riblets applied on a vane

The inclination of the riblet foil on the suction side is -10 deg, measured from a horizontal reference (see Figure 4.8). This angle is chosen by a project partner after running a CFD simulation with no foil on the vanes. The result of this simulation shows an inclination of the surface streamlines as it is depicted in Figure 4.8. Additionally, the ideal riblet size is indicated in this figure with the bar on its right side. It is clearly visible that the inclination as well as the ideal riblet size are changing over the whole vane surface.

The experimentally investigated riblets are chosen according to the most occurring inclination of the surface streamlines and the available riblet foil. The availability was dependent on the project partner, which had certain geometries manufactured regarding the tip to tip distance. The geometrical dimensions were uniform over the whole vane suction side.

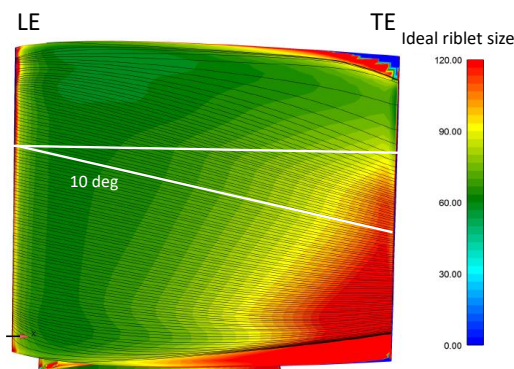


Figure 4.8: Ideal riblet size

4.3.4 Leaned Vanes

The second vane design besides the Standard vane and its derivatives is called Leaned vane design. It is an acoustically modified version of the Standard vane, with the design intent to reduce the overall sound power level downstream of a TEGV caused by the rotor stator interaction. A detailed illustration of this topic can be found in Broszat et al. [80]. Herein it is shown, that an inclination against the rotor wakes has the most positive impact onto the sound power level reduction. Therefore, the Leaned vanes have a 20 deg lean against the rotational direction of the rotor. The inclination of the rotor wake impinging the turbine exit vane leading edge at operating point approach is approximately 30 deg in rotational direction. An increased phase difference of the incoming wake between the inner and outer casing resulting of this raised difference of inclinations (wake and vane lean) is the reason for the reduced overall sound

power level. The vane profile itself as well as the vane count is the same as in the case of the Standard TEC.

Figure 4.9 shows a comparison between the CAD models of the Standard and the Leaned vane designs. The direction of view is aft looking forward and the rotor rotational direction is given with ω .

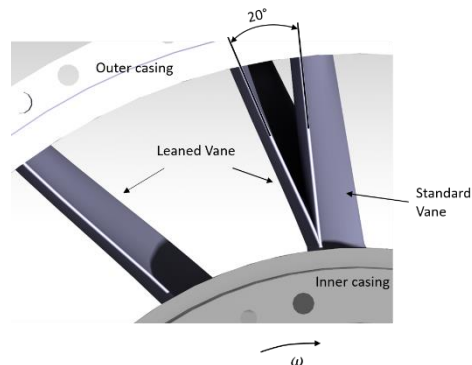


Figure 4.9: CAD comparison of Standard vane and Leaned vane

4.4 Soft End Walls

To increase the performance of noise attenuation with optimising a turbine exit casing, all the limited space has to be used. Therefore, also the available space in the passage between the exit guide vanes is equipped with lined elements. Changeable cassettes including Helmholtz absorbers are designed and manufactured with the same additive procedure as the Helmholtz vanes. In Figure 4.10, a CAD model of one vane passage including both cassettes can be seen. On the right side of the figure an additional zoom in on an inner cassette resonator is presented, indicating the absorber cavity and the neck. Again, all resonators are separated from each other and consisting of only one neck opening.

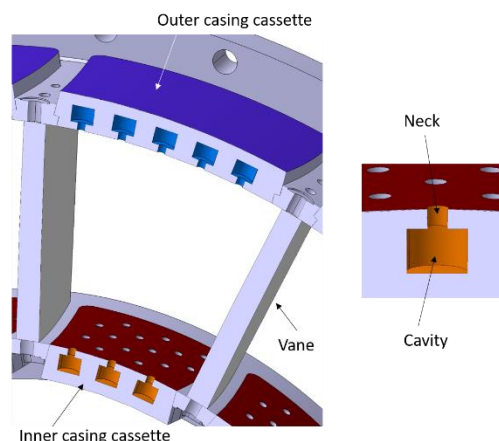


Figure 4.10: CAD model of the soft end walls

Figure 4.11 shows an example of the two cassettes which are used during the test runs, with the one for the inner casing on the left side and the one for the outer casing on the right side. The bent shape is due to the curvature of the vanes, which is considered to maximize the available space and hence the number of absorbers. The black line indicates the location of the TEGV leading edge.

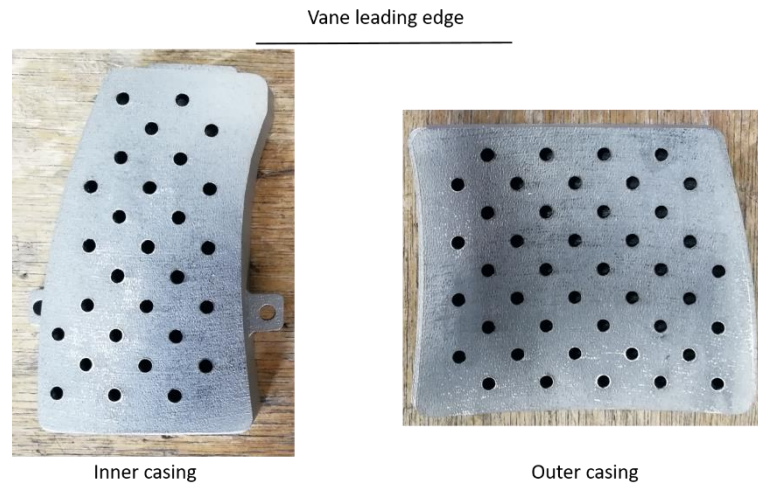


Figure 4.11: Soft end wall cassettes for inner (left) and outer casing (right)

In the following Table 4.8, all axial distances from the leading edge to each neck opening centre measured from the vane LE are given. The value is shown in % of the vane axial chord length. Resonator line 1 means, that this is the first line of openings with the same axial position downstream of the LE. The location in circumferential direction is chosen in a way, that with the needed geometry a maximum number of absorbers can be realized. To minimize the interaction of two neighbouring resonator lines in flow direction, a shift in circumferential direction is performed.

Table 4.8: Axial positions of absorbers – Soft end walls

Resonator line	Axial distance to LE in % of vane chord length	
	Inner casing	Outer casing
1	13.5	27.6
2	21	35.1
3	28.5	42.6
4	36	50.1
5	43.5	57.6
6	51	62.1
7	58.5	72.6
8	66	80.1
9	73.5	87.6
10	81	-
11	88.5	-

Table 4.9 gives an overview of the geometrical dimensions of the soft end walls absorber. The different values concerning the neck diameter belong to three different setups.

Table 4.9: Geometrical details of the soft end walls

Neck diameter	Neck length	Cavity diameter	Cavity depth
[mm]			
3.5 / 3.8 / 4.2	2.8	8.2	5.9

The corresponding resonance frequencies to these dimensions are stated in Table 4.10. Herein, both situations with and without a flow with a specific Mach number are stated (the used Mach number is corresponding to the one during the test runs in the STTF).

Table 4.10: Calculated resonance frequencies with and without Ma number – Soft end walls

Setup	Neck diameter [mm]	Resonance frequency [Hz]	
		With Ma	Without Ma
(B)	3.5	5641	4757
(C), (H), (J)	3.8	6098	5115
(D)	4.2	6706	5593

The purpose using changeable cassettes is to be able to easily unmount them and change the absorber resonant frequency by simply making a bigger neck diameter or manufacture new ones with a whole different geometry.

With these new casing parts, also the inner and outer rings are changed. Both are shown in the following figure with the inner ring on the left side and the outer one on the right side.



Figure 4.12: Inner (left) and outer (right) ring of the resonator TEC

A fully assembled TEC with the Standard vane design combined with the soft end walls is shown on the right side of Figure 4.13. Herein, also the fixation of the outer cassettes can be seen. While the inner ones are simply connected to the inner ring via screws, the outer soft end walls are hold in place by a flexible aluminium ring which can be tightened to ensure a fixed position.



Figure 4.13: Standard TEC with and without soft end walls

To ensure an exact positioning of the inner cassettes, a nose is added because a step as in the outer TEC ring to hold the cassettes is not possible. This positioning nose and the overlapping flaps which are used for mounting can be seen in Figure 4.14.

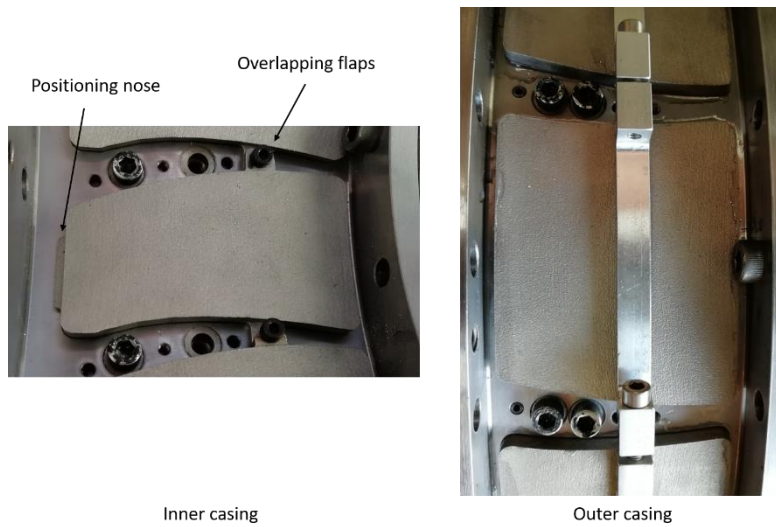


Figure 4.14: Mounting of the absorber cassettes

Figure 4.15 shows the combination of the Leaned vanes and the absorber cassettes. On the left side one can clearly see the lean of this vane design.



Figure 4.15: Leaned TEC with soft end walls

Concerning the mentioned idea of a maximum sound attenuation using Helmholtz absorbers in a turbine exit casing, a combination of the Helmholtz vanes with the soft end walls can be seen in the following picture. The zoom in on the left side shows the vanes as well as the outer end wall cassettes.



Figure 4.16: Helmholtz vanes with soft end walls

4.5 Impedance Tube

To be able to make acoustic pre-tests with different types of resonators, an impedance tube was built. Basically, it is a combination of a speaker on one end of a plastic pipe and a specimen on the other end. The specimen can be a soft end wall, a hard end wall, or any type of absorber. As a guideline, the work of Brunnader [81] was taken for building this small test rig. In general, such an impedance tube or also called Kundt's tube is built according to ISO 10534-1 and -2, in which two flush mounted microphones are used to investigate only plane acoustic waves. Concerning the problem of this thesis, a different solution had to be found because due to the high frequencies of interest, a test rig having only plane waves but can contain a whole absorber cassette in size was impossible. To realize plane waves for increasing frequencies, the cross sectional area needs to get smaller. Therefore, more microphones are needed to be able to investigate also higher order duct modes.

The used impedance tube includes eight condenser microphones (an explanation can be found in section 5.1) distributed uniformly around the pipe circumference in two different measurement planes. Each plane consists of four microphones, which are separated by an angle of 90 deg. The axial distance between the measurement planes is 20 mm, what ensures a maximum frequency that can be investigated of 8.5 kHz (at a temperature of 20°C). This limit is set due to the wavelength λ of this frequency according to the following equation, in which s stands for the axial distance between the two planes

$$s < \frac{\lambda}{2} \quad (4.3)$$

Another limitation is set by the cut-on frequency of certain duct modes according to the tube inner diameter. The following table gives these cut on frequencies for the respective (m, n) mode of the tube, considering an inner diameter of 0.1 m and a temperature of 20°C. With the realized arrangement of the microphones, no higher radial modes can be determined without performing a mode analysis procedure. This means, that starting at the cut on frequency of the mode (0,1), the measured signal cannot be investigated anymore using the simple post processing method described later. It should be mentioned, that no higher frequencies are needed because the frequency of interest in the subsonic test rig is about 5500 Hz. In this environment of a much higher temperature compared to room temperature and an additional influence of the flow Mach number, a downscaling of the absorber resonance frequency in case of the impedance tube tests is needed anyways.

Table 4.11: Cut-on frequencies of the impedance tube in [Hz]

		m			
		0	1	2	3
n	0	0	2011	3337	4590
	1	4186	5824	7326	8756

Figure 4.17 presents a sketch of the normal incident impedance tube test rig. The two measurement planes A and B, including four flush mounted microphones each, are indicated by the red arrows. A circumferential distribution of the microphones is depicted in the bottom left corner concerning measurement plane A.

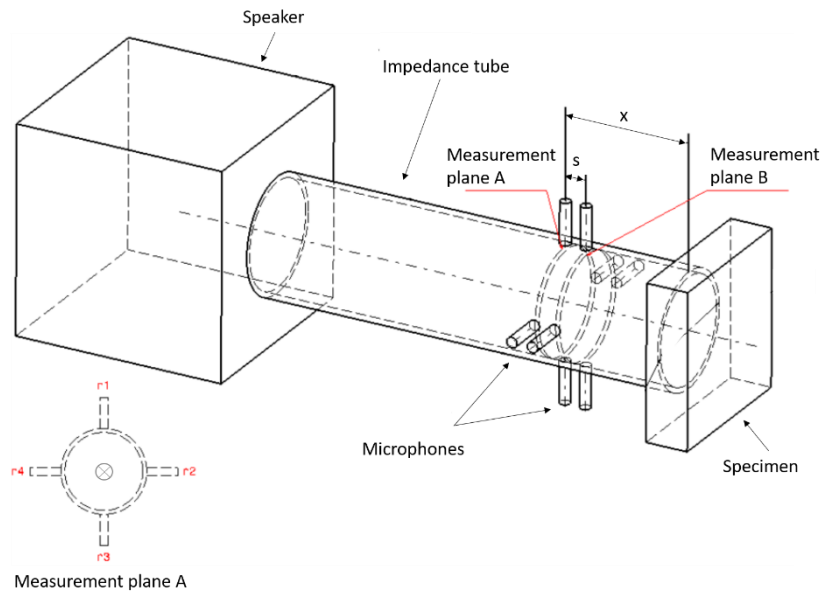


Figure 4.17: Sketch of impedance tube (adapted from [82])

As mentioned, the impedance tube according to ISO 10534-1 is working only with plane waves and hence only two microphones are needed. An extension of this 2-mic-method was performed in the work of Sanada [83], to be able to investigate also higher duct modes up to the cut-on of the first radial mode. In the work is stated that four measurement signals of measurement plane, as it is the case in the used impedance tube, can be summed up as follows

$$p_s = p(r_1) + p(r_2) + p(r_3) + p(r_4) = 4(A_{00}e^{-ik_0z} + B_{00}e^{ik_0z})e^{i\omega t} \quad (4.4)$$

By building this sum a filter effect is achieved, which cancels out the signals due to the higher order duct modes (1,0) and (2,0). Figure 4.18 shows the modes of a cylindrical duct and the measurement positions of the impedance tube. It can be seen, that the mode (1,0) has the same pressure amplitude at the measurement positions two and four but antiphase. Looking at mode (2,0), the measured pressures at neighbouring positions like one and two also have the same amplitude but are again antiphase. Due to this, a summation of the pressures in one measurement plane can filter the effects of higher order duct modes.

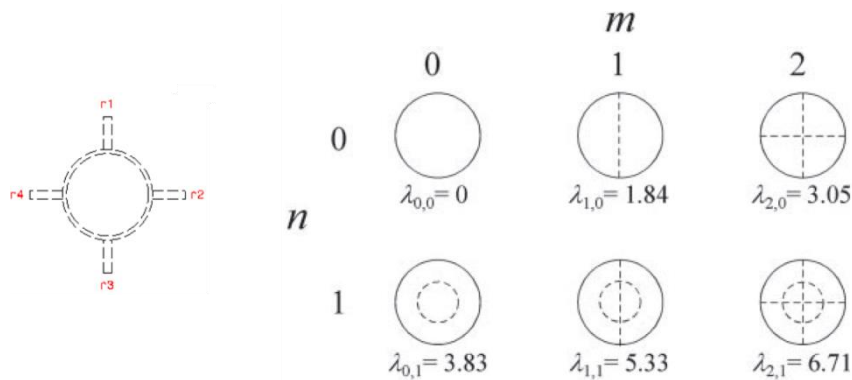


Figure 4.18: Acoustic mode shapes in a cylindrical duct and measurement positions in the impedance tube (adapted from [83])

With the summed signals of both measurement planes and after transforming them into the frequency domain, a frequency response function can be calculated according to the following equation

$$H = \frac{p_{sB}}{p_{sA}} \quad (4.5)$$

Afterwards, the normal incident reflection coefficient depending on the frequency can be evaluated as follows

$$R = \frac{H - e^{-i\alpha s}}{e^{i\alpha s} - H} e^{2i\alpha x} \quad (4.6)$$

Herein s is the axial distance between the two measurement planes, x is the axial distance between plane A and the specimen and α is the wave number according to equation (2.23).

A scattering of the sound at the specimen, from a normal incident wave to obliquely reflected instead of normally reflected ones, is neglected when using this measurement technique. But such a scattering does not occur if the spatial distribution of the specimen is uniform or the nonuniformity is small enough with respect to the wavelength.

Figure 4.19 shows a measurement result concerning the absolute value of the reflection coefficient over the frequency for a hard end wall test case. The vertical dotted lines indicate the cut on frequency of the respective mode order. This setup should have a theoretically value for the reflection coefficient of 1. The result shows a good accordance to this value, starting to deviate significantly after the cut-on frequency of the first radial mode (0,1). This is, as already mentioned above, due to the positioning of the microphones.

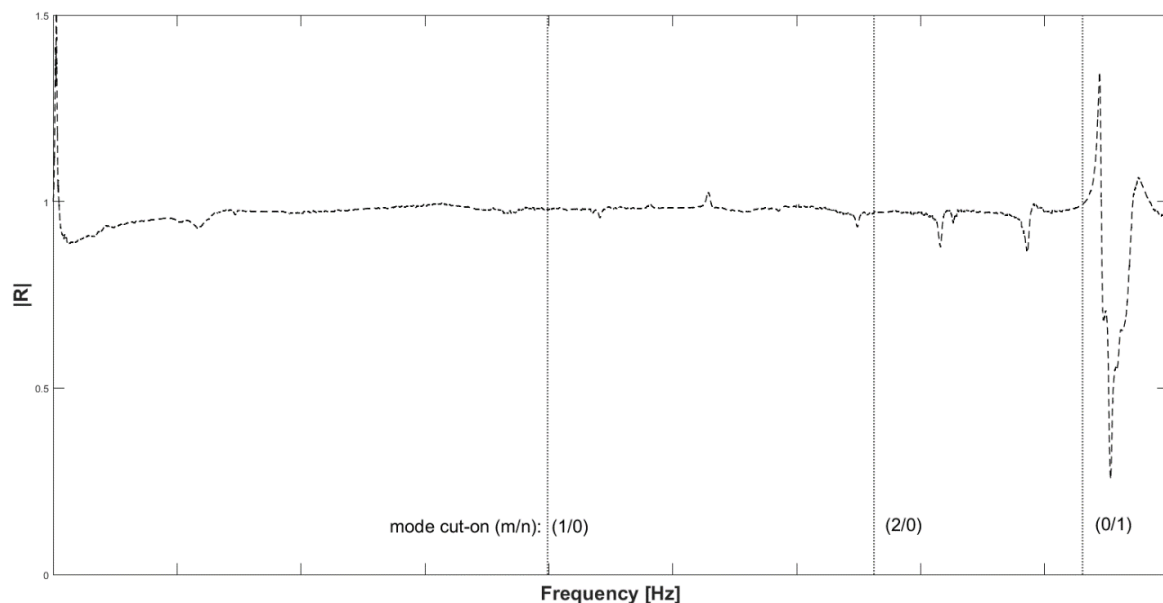


Figure 4.19: Reflection coefficient - Hard end wall

In Figure 4.20 the built and used impedance tube including the eight microphones can be seen, with the speaker on the right side and the specimen on the left side of the tube.

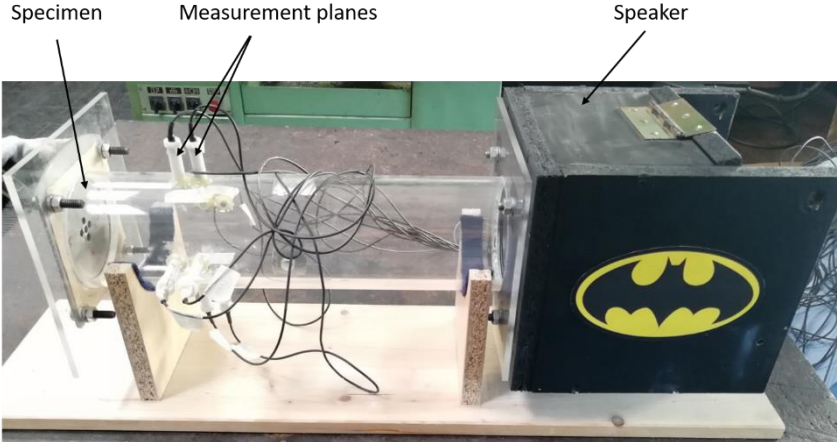


Figure 4.20: Used impedance tube

5 Measurement Setup

During this work a various number of different measurement techniques were used to fulfil the different measurement tasks. The following section provides a deeper insight into the techniques used for this thesis concerning the aeroacoustics as well as the aerodynamic investigations followed by a section about the measurement uncertainties and finally a section which deals with the post processing of the gained measurement data.

5.1 Acoustics

The main focus of this work is on the acoustical behaviour of the investigated setups. Therefore, a 360 deg rotatable acoustic measurement section is used. This section consists of six microphone plates in total, whereat two are used for this thesis. 12 high-precision prepolarized microphones can be applied in each microphone plate which results in 24 microphones in total. 12 are located on the inner and 12 on the outer casing. Condenser microphones (G.R.A.S. 40 BD ¼”) in combination with a G.R.A.S. 26AC preamplifier and a G.R.A.S. 12AN power module are used. Each microphone is flush mounted in the microphone plate. In order to obtain sufficient independent measurement data for further post processing (mode analysis), the test section is traversed 360 deg in circumferential direction with a step size of 2 deg between two following measurement positions. This results in 180 circumferential measurement positions and 4320 measurement points. Hence due to the Nyquist theorem a maximum circumferential mode order of $m = \pm 90$ can be evaluated.

All microphones are hold by steel cassettes which are fixed at the test rig. To avoid accidental ground, each microphone is covered by a white plastic bush. The axial distance between two microphones is 7.5 mm. As can be seen from Figure 5.1, in which the flow direction is indicated by the white arrow, two rows of microphones are realised for both cassettes to achieve a shorter axial distance between the microphones. The angle between the rows is 12deg.

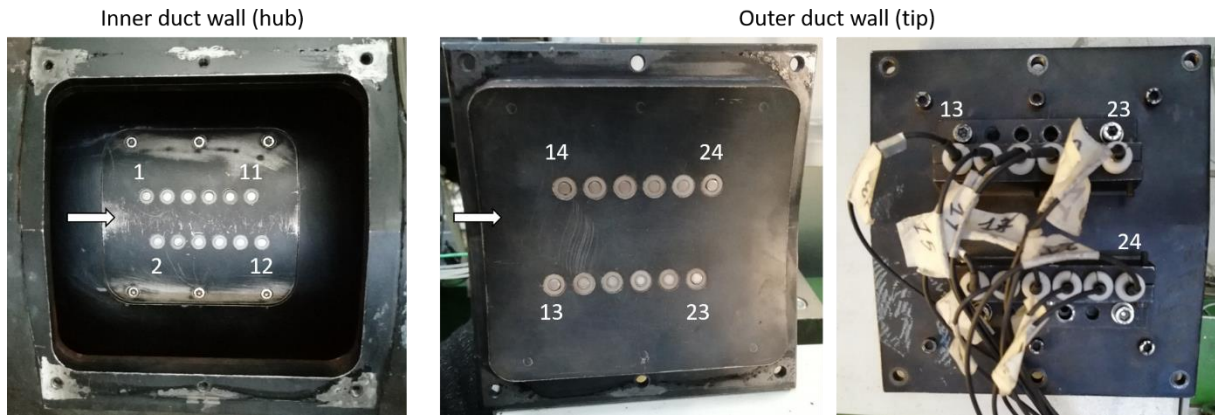


Figure 5.1: Microphones plates at hub (left) and tip (right)

The following table shows the location of the microphones with respect to the IGV leading edge. The microphone number corresponds to the one stated in Figure 5.1.

Table 5.1: Location of the microphones

Mic row	Distance between microphones and IGV leading edge [mm]											
	Microphone number (Hub / Tip)											
	1 / 13	2 / 14	3 / 15	4 / 16	5 / 17	6 / 18	7 / 19	8 / 20	9 / 21	10 / 22	11 / 23	12 / 24
A	508.5		523.5		538.5		553.5		568.5		583.5	
B		516.0		531.0		546.0		561.0		576.0		591.0

In addition, reference microphones upstream and downstream of the TEC are used. In case of the soft end walls investigations, a microphone is also flush mounted on the backside wall inside the cavity of an absorber. Figure 5.2 shows all three reference microphones and Figure 5.3 gives a look at the plastic bush of the cavity microphone.

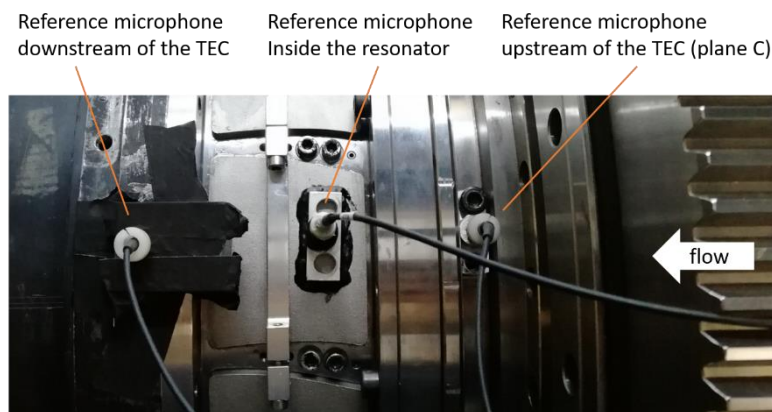


Figure 5.2: Locations of reference microphones

The used microphones are calibrated before each measurement using a G.R.A.S. 42AA pistonphone, which gives a discrete tone at 250Hz with an amplitude of 114dB.

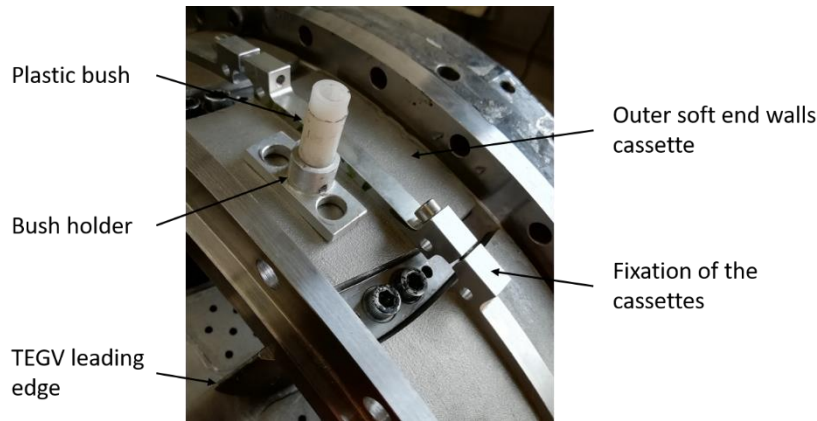


Figure 5.3: Mounting of the reference microphone inside the resonator

Data acquisition

The acquisition of the measured data is done by using a National Instruments PXI chassis including two high accuracy PXI 4498 data acquisition modules with a total number of 32 channels. The sampling rate of these modules is 204.8 kSamples/s. To transfer the measured data from the chassis via a fibre optic cable to a measurement PC, a PXIe8375 module is used.

More detailed information concerning the measurement setup in the acoustic test section can be found in the work of Selic [36].

5.2 Aerodynamics

During this work different methods for examining the aerodynamic behaviour of the investigated TECs are used. Flow fields of aerodynamic parameters are measured using an aerodynamic Five-Hole-Probe (FHP). Measurements concerning the total pressure distribution downstream of the TEGVs (vane wake) are done by using a probe based on a pitot tube. Additional visual investigations are done by performing oil flow visualisations. This section serves as a description of the mentioned measurement techniques.

5.2.1 Five – Hole – Probe

An aerodynamic five-hole-probe including a type K thermocouple is used to evaluate the flow fields up- and downstream of the investigated configurations. With this steady flow field measurement system, aerodynamic parameters like static and total pressure, static and total temperature, Mach number, pitch and yaw angle can be determined.

The used probe was manufactured and calibrated at the “Institut für Strahlantriebe und Turboarbeitsmaschinen” at the Rheinisch Westfälische Technische Hochschule Aachen and is shown in Figure 5.4. One can see the thermocouple on the bottom of the probe head. At the bottom of this figure, a sketch of the probe head is shown with an indication of the angle definition, the sign convention as well as the numbering of the bores (adapted from [84]).

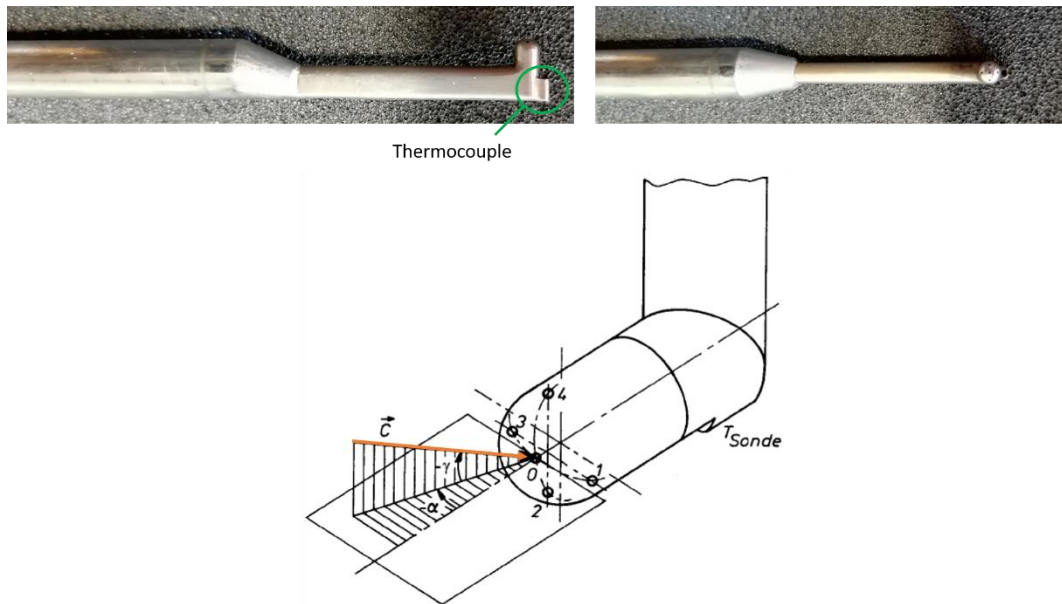


Figure 5.4: Five-hole-probe (top) and sketch of the probe head (bottom; adapted from [84])

With this thermocouple it is possible to evaluate, in combination with provided recovery factors, the static and total temperature as well as the flow velocity. Table 5.2 shows the calibration range of the used FHP.

Table 5.2: Calibration range of the five-hole-probe

Flow parameter	Minimum	Maximum	Step size
Mach number	0.1	0.8	0.1
Yaw Angle	-20	20	4
Pitch angle	-20	20	4

The measured data is evaluated according to the provided calibration reports of the RWTH Aachen [85] and [84]. Therefore, the following non-dimensional parameters are calculated with the five measured pressures:

- Mach number parameter

$$k_{Ma} = \frac{\Delta p}{p_0} \quad (5.1)$$

- Yaw angle parameter

$$k_\alpha = \frac{p_3 - p_1}{\Delta p} \quad (5.2)$$

- Pitch angle parameter

$$k_\gamma = \frac{p_4 - p_2}{\Delta p} \quad (5.3)$$

Δp is defined as follows

$$\Delta p = p_0 - \frac{p_1 + p_3}{2} \quad (5.4)$$

Using these parameters, the yaw angle α , pitch angle γ , Mach number Ma , recovery factor r , as well as parameters for the static k_{ps} and the total pressure k_{pt} can be calculated according to the multi-parameter approximation given in [85] and [84].

$$Y = \sum_{i=0}^l \sum_{j=0}^m \sum_{k=0}^n \delta_{ijk} c_{Y,ijk} k_{Ma}^i k_{\alpha}^j k_{\gamma}^k \quad (5.5)$$

$c_{Y,ijk}$ are the calibration coefficients and δ_{ijk} is the Kronecker delta

$$\delta_{ijk} = \begin{cases} 1 & \forall i + j + k \leq \max(l, m, n) \\ 0 & \forall i + j + k > \max(l, m, n) \end{cases} \quad (5.6)$$

To calculate the static and total pressure, two additional parameters are needed.

- Static pressure parameter

$$k_p = \frac{p_0 - p}{\Delta p} \quad (5.7)$$

- Total pressure parameter

$$k_{pt} = \frac{p_t - p_0}{\Delta p} \quad (5.8)$$

Although there are these parameters, a calculation of the static pressure is more accurate according to [85] and [84] using equation (5.9). The reason is, that the error by approximating the static pressure parameter k_p is higher than in case of the Mach number or the total pressure parameter k_{pt} and therefore, the static pressure is calculated according to the following equation.

$$p = \frac{p_t}{\left(1 + \frac{\kappa - 1}{2} Ma^2\right)^{\frac{\kappa}{\kappa - 1}}} \quad (5.9)$$

The included thermocouple gives the opportunity to measure the temperature T_{Probe} .

$$T_{Probe} = T + r \frac{c^2}{2c_p} = T \cdot \left(1 + r \frac{\kappa - 1}{2} Ma^2\right) \quad (5.10)$$

With this temperature, the Mach number and the recovery factor, it is possible to calculate the static as well as the total temperature and the flow velocity.

- Recovery factor

$$r = \frac{T_{Probe} - T}{T_t - T} \quad (5.11)$$

This recovery factor defines the captured part of the dynamic total temperature $\frac{c^2}{2c_p}$.

- Total temperature

$$T_t = T_{Probe} \left(\frac{1 + \frac{\kappa - 1}{2} Ma^2}{1 + r \frac{\kappa - 1}{2} Ma^2} \right) \quad (5.12)$$

- Static temperature

$$T = \frac{T_{Probe}}{1 + r \frac{\kappa - 1}{2} Ma^2} \quad (5.13)$$

The absolute velocity is then determined as follows

$$c = Ma\sqrt{\kappa RT} \quad (5.14)$$

Definition of the flow angles

A general description of the flow angles is shown in Figure 5.5. Herein, x is the axial direction pointing from the inlet to the outlet of the rest rig, r is the radial direction, and θ is the circumferential direction which has a positive direction if it is identical to the rotational direction of the rotor. The green arrow indicates the flow direction and the red arrows show the components according to the coordinate system.

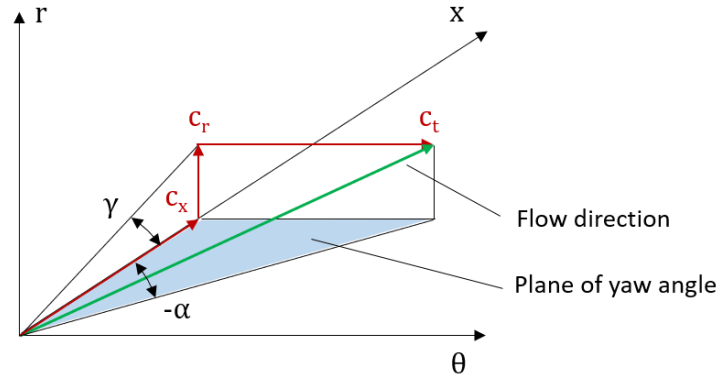


Figure 5.5: Definition of the flow angles

It can be seen, that the yaw angle is defined as

$$\tan \alpha = \frac{c_t}{c_x} \quad (5.15)$$

wherein c_t describes the flow component in tangential direction and c_x the component in axial direction which is perpendicular to the measurement plane. The definition for the sign of the yaw angle is linked to the rotational direction of the LPT rotor. If the flow component c_t

has the same direction as the rotor rotational direction, the yaw angle is positive as can be seen in the following figure

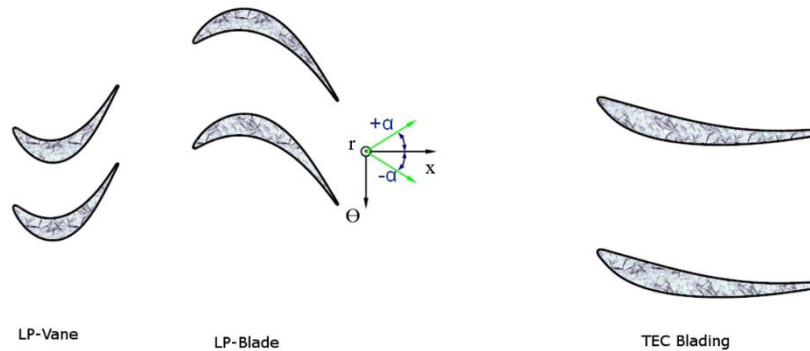


Figure 5.6: Definition of sign convention [36]

The definition of the pitch angle is as follows

$$\tan \gamma = \frac{c_r}{c_x} \quad (5.16)$$

c_r is the flow component in radial direction and has to point away from the machine axis, that means from hub to tip, to result in a positive sign for the pitch angle.

Measurement planes and grid

During this theses, two of the four possible measurement planes suitable for five-hole-probe measurements, which can be seen on the left side of Figure 5.7, are used. One plane is right downstream of the LPT rotor and named plane C and the second one is downstream of the turbine exit casing and named plane D (marked with red lines in Figure 5.7). With an axial distance of 60% related to the rotor blade chord length between the rotor blade trailing edge and plane C, the rotor exit conditions can be determined. Plane D is located 108 %, related to the TEGV chord length, downstream of the TEGV trailing edge. On the one hand measurements in this plane result in a flow field dominated by the exit guide vanes and hence give information about a possible change in each setup, and on the other hand the measured data is necessary for parameters needed concerning the acoustic evaluation (static pressure, static temperature, and Mach number).

On the right side of Figure 5.7 the measurement sectors for both planes are shown aft looking forward with exemplary measurement result.

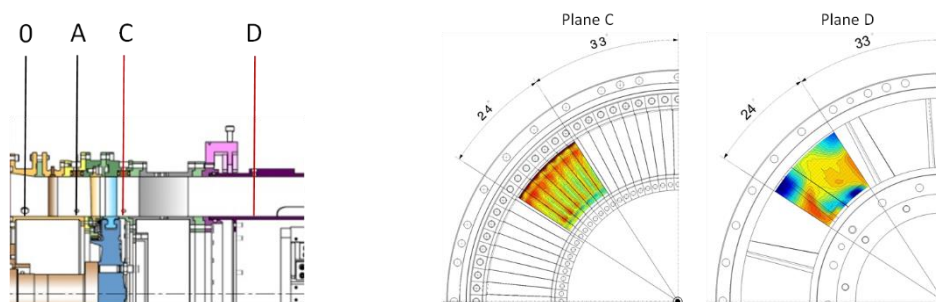


Figure 5.7: Measurement planes (left) and sectors (right)

The distance between two neighbouring measurement points in circumferential direction is 0.75 deg. This results in 21 circumferential and 33 radial measurement lines for both planes. Table 5.3 shows the radial measurement grid in percent of the channel height.

Table 5.3: Radial measurement points for the FHP in percent of the channel height

4.125	6.375	8.875	13.875	18.875	23.875	28.875
33.875	38.875	43.875	48.875	53.875	58.875	63.875
68.875	73.875	78.875	83.875	88.875	92.625	95.125

5.2.2 Trailing Edge Probe

For evaluating the TEGV wake directly downstream of the trailing edge, a second measurement system is used. It is the so-called trailing edge probe, which is a simple pitot tube. With this probe, the total pressure distribution downstream of the turbine exit casing can be measured with an axial distance of 0.3 mm between the TE and the probe head and therefore much closer compared with the five-hole-probe (see plane D in Figure 5.7). This short distance ensures, that the wake is not yet fully mixed out before reaching the probe inlet. An additional advantage with respect to the five-hole-probe is the smaller uncertainty concerning the post processing because only one measured total pressure is used without any approximation procedure. Figure 5.8 shows the probe inside the test rig.



Figure 5.8: Trailing edge probe inside the test rig

The probe is traversed in circumferential direction in a constant radial height of 30 % of the channel height. The measurement sector covers two TEC pitches with a step size of 0.2 deg between two neighbouring measurement points which results in 241 measurement points.

The radial height of 30 % is chosen, because former test runs showed that in this height the influence of the secondary flows is negligible. During the measurement the probe is not turned directly into the flow like the FHP but always keeps its alignment with the axis of the machine.

5.2.3 Oil Flow Visualization

This measurement technique is used to visualize the trajectories of the wall shear stress which is an indication of the flow close to the surface. Therefore, the investigated surfaces are covered with a mixture of motor oil and titanium oxide. For this work, the mixture is applied on the turbine exit guide vanes as well as on the end walls between the vanes (hub and tip). These oil flow visualizations are only used for the investigations concerning the riblets. In case

of the tested setups including resonators, no oil flow measurements are performed to avoid a change in the cavity size due to the intrusion of the oil mixture.

To avoid effects of the run up and shut down, these procedures are done as fast as possible.

5.3 Measurement Uncertainties

The used microphones are high precision condenser microphones which are made according to IEC 61094-4 requirements and defined as laboratory microphones (type 0 microphones). This extremely accurate type of microphone has a measurement uncertainty of ± 0.4 dB according to ANSI S1.4 [86]. The frequency response is linear from 10 Hz to 25 kHz and the sensitivity is 1.45 mV/Pa at 250 Hz.

The frequency response of the used preamplifier is from 2 kHz to 200 kHz (± 0.2 dB). It has a large dynamic range and a very low noise level.

Concerning the aerodynamic measurements, the system is made up by six multi-channel pressure transducers PSI 9016 with a total amount of 96 channels. The accuracy is 0.05 % full scale after a calibration of the manufacturer. The range of these modules is of 30 psi/ 2.068 bar.

Additionally, two National Instruments Field Point FP-TC-120 eight-channel thermocouple input modules and one FP-RTD-122 resistance thermometer input module are used.

Table 5.4 displays the measurement uncertainties (within a 95 % confidence interval) of the five-hole-probe measurements. These values are positive and negative deviations and contain the error due to the approximation, random error and the systematic error of the PSI Modules. The difference between the positive and the negative direction is a result of the multi-parameter approximation.

Table 5.4: Measurement uncertainties of the five-hole-probe

Mach number	+0.006	-0.003	[/]
Yaw Angle	+0.5	-0.08	[deg]
Total pressure	+3.3	-3.0	[mbar]
Static pressure	+5.3	-5.2	[mbar]

The accuracy of the trailing edge probe concerning the angle deviation is ± 1 deg due to the mounting procedure.

During a test run, the speed variations are kept below 0.2 % of the current operating speed. The measurement uncertainty of the temperature measurement is about ± 0.5 K.

5.4 Acoustic Post Processing

The measurement data obtained by the acoustic test runs need some post processing to receive the interesting parameters concerning the evaluation of the emitted noise. The post processing procedure consists of several steps which are:

- Adaptive resampling
- Phase averaging
- Fourier Transformation
- Azimuthal mode analysis
- Radial mode analysis and calculation of the modal sound power

5.4.1 Adaptive Resampling

The rotational speed during a test run is never ideally constant. Concerning the measurements performed for this thesis, a variation of the rotational speed with respect to the speed of the operating speed is smaller than $\pm 0.2\%$. To get an even distribution of samples per revolution, an adaptive resampling has to be done. Therefore, a trigger is needed which gives exactly one signal for each revolution of the test rig shaft. With this signal, it is possible to divide one revolution into a constant number of samples independent of the rotational speed. Using this new sampling frequency, the raw measurement signal can be resampled, and has furthermore to satisfy the following equation concerning the number of samples per revolution

$$nn = 2^k < \frac{f_s \cdot t}{n_{period}} \quad (5.17)$$

Herein, f_s is the sampling frequency, t is the measurement time and n_{period} is the number of revolutions during this measurement time. nn is the calculated number of samples per revolution in the resampled signal. The number of revolutions n_{period} is calculated as follows

$$n_{period} = \frac{n_{rpm}}{60} \cdot t \quad (5.18)$$

n_{rpm} is the rotational speed of the shaft in revolutions per minute.

5.4.2 Phase Averaging

After the adaptive resampling, the phase averaging is the next step in the post processing procedure. Herein, values of a flow parameter at an arbitrary position are averaged for a certain phase. That means, that all values with the same relative position between rotor and stator are averaged. This is performed for the acquired number of rotor revolutions and results in a phase averaged time signal for a single rotor revolution at each measurement point.

If a flow is characterised by a periodical fluctuation, the time dependent flow parameter can be split up into three components (“triple decomposition procedure”). The following equation shows these three major components of a measured signal:

$$p(t) = \bar{p} + \langle p(t) \rangle + p'(t) \quad (5.19)$$

Wherein $p(t)$ is the time dependent flow quantity, \bar{p} is the time averaged value of the fluid property, $\langle p(t) \rangle$ is the pure periodic component, and $p'(t)$ is the stochastic fluctuation of the

signal. The phase averaging procedure is performed, to remove these stochastic fluctuations of the signal which emerge from turbulence within the flow duct and are different for each rotor revolution. By averaging over a large enough number of revolutions, and therefore breaking it down to one single revolution, these stochastic fluctuations can be removed from the signal which results in a new signal

$$\tilde{p}(t) = \bar{p} + \langle p(t) \rangle \quad (5.20)$$

5.4.3 Azimuthal Mode Analysis (AMA)

Based on the modal analysis of a measured sound field, it is possible to determine the interactions inside a machine which are responsible for a certain sound. The theory of acoustic data analysis used during the present work is described well in the publications of Enghardt et al. [87] and [88].

A solution for the problem can be achieved looking at the following equation, which describes the pressure fluctuations p' in a cylindrical duct for a single annular frequency ω as a linear superposition of modal terms (see also Munjal [89])

$$p'(x, r, \theta, t) = \sum_{m=-\infty}^{\infty} \sum_{n=0}^{\infty} (A_{mn,f}^+ e^{ik_{mn}^+ x} + A_{mn,f}^- e^{ik_{mn}^- x}) f_{mn}(s_{mn} \frac{r}{R}) e^{im\theta} e^{-i\omega t} \quad (5.21)$$

Herein, A_{mn}^+ and A_{mn}^- are the complex amplitudes of the sound propagating in (+) and against (-) flow direction with the azimuthal mode order m and the radial mode order n . Each combination of the mode orders describes a characteristic pressure distribution. The corresponding axial wave numbers are written with k_{mn}^+ and k_{mn}^- (or also known as α_{mn}^+ and α_{mn}^-). f_{mn} is a shape factor which describes the radial distribution of the sound field in a duct. It consists of the solutions of the Bessel differential equation concerning acoustically hard walled boundary conditions and can be written as follows

$$f_{mn}(s_{mn} \frac{r}{R}) = \frac{1}{\sqrt{F_{mn}}} \left(J_m(s_{mn} \frac{r}{R}) + Q_{mn} Y_m(s_{mn} \frac{r}{R}) \right) \quad (5.22)$$

Herein, J_m is the Bessel function 1st kind and Y_m the Bessel function 2nd kind of a particular mode of m^{th} order. They are defined by the eigenvalues s_{mn} for hard-wall boundary conditions at the duct end walls and the hub-to-tip ratio $\frac{r}{R}$, with r being the inner duct radius and R the outer one. Q_{mn} is an eigenvector, which is zero for non-annular cylinders, and defined as follows

$$Q_{mn} = -\frac{J'_m(s_{mn} \frac{r}{R})}{Y'_m(s_{mn} \frac{r}{R})} \quad (5.23)$$

The normalisation factor F_{mn} transforms the orthogonal system into an orthonormal one

$$F_{mn} = \begin{cases} \frac{1}{2} \left[1 - \left(\frac{r}{R} \right)^2 \right], & m = n = 0 \\ \frac{1}{2} \left[\left(1 - \frac{m^2}{s_{mn}^2} \right) \hat{f}_{mn}^2(R) - \left[\left(\frac{r}{R} \right)^2 - \frac{m^2}{s_{mn}^2} \right] \hat{f}_{mn}^2 \left(\frac{r}{R} \right) \right], & \text{otherwise} \end{cases} \quad (5.24)$$

With

$$\hat{f}_{mn}(r) = J_m \left(s_{mn} \frac{r}{R} \right) + Q_{mn} Y_m \left(s_{mn} \frac{r}{R} \right) \quad (5.25)$$

The axial wave number for a mode (m, n) considering an axial mean flow was already stated in equation (2.35) in section 2.1.2 but should again be mentioned at this point

$$k_{mn}^{\pm} = \alpha_{mn}^{\pm} = \frac{k}{1 - Ma_x^2} \left[-Ma_x \pm \sqrt{1 - (1 - Ma_x^2) \left(\frac{s_{mn}}{kR} \right)^2} \right]$$

Wherein Ma_x is the axial Mach number and k is the wave number. The equation for the axial wave number is valid under the assumption of a swirl free flow. In reality, this assumption is not always true but experiments concerning the test rig used during this work showed, that the swirl component downstream of the turbine exit guide vanes is negligible.

The complex amplitudes in equation (5.21) can be determined by performing an azimuthal mode analysis onto a measured sound pressure. With this method, the amplitudes can be calculated for one certain frequency of interest. Each amplitude of a circumferential mode m can then be expressed like

$$A_m(x, r)_f = \sum_{n=0}^{\infty} (A_{mn,f}^+ e^{ik_{mn}^+ x} + A_{mn,f}^- e^{ik_{mn}^- x}) f_{mn} \left(s_{mn} \frac{r}{R} \right) \quad (5.26)$$

Substituting this equation into (5.21) leads to

$$p'(x, r, \theta, t) = \sum_{m=-\infty}^{\infty} A_m(x, r)_f e^{im\theta} e^{-i\omega t} \quad (5.27)$$

First, the measured signal is transformed from the time domain into the frequency domain for each microphone using a discrete Fourier transformation (DFT). The outcome is a complex sound pressure for all frequency components in the signal for a certain measurement position of a microphone with the coordinates x_0, r_0, θ_k . Taking a certain frequency of interest (in case of this thesis it is the 1st BPF) and performing a discrete Fourier transformation in the azimuthal direction leads to the complex amplitudes of this certain frequency for a given circumferential mode m [90], [91]

$$A_m(x_0, r_0)_f = \frac{1}{N_{\theta}} \sum_{k=1}^{N_{\theta}} p(x_0, r_0, \theta_k)_f e^{-im\theta_k} \quad (5.28)$$

In this equation, N_{θ} stands for the number of circumferential measurement points (or microphones) which are equally spaced in the circumferential direction.

The limit for the highest calculable mode order m_{max} is according to the Nyquist theorem

$$\frac{2\pi}{m_{max}} > 2\Delta\varphi = 2\left(\frac{2\pi}{N_\theta}\right) \rightarrow m_{max} < \frac{N_\theta}{2} \quad (5.29)$$

This means that the double of the spacing between two neighbouring microphones has to be smaller than the half of the azimuthal wavelength $\frac{2\pi}{m_{max}}$. Or in other words, the number of measurement points has to be bigger than the double of the highest mode order to be able to calculate the mode correctly.

5.4.4 Radial Mode Analysis (RMA)

An azimuthal mode analysis is not enough to get a full understanding of the sound field inside a duct. Therefore, also an analysis in the radial direction has to be done. Based on equation (5.26), a system of equations can be built

$$\mathbf{A}_m = \underline{\underline{W}}_m \mathbf{A}_{mn} \quad (5.30)$$

Herein, \mathbf{A}_m is a vector containing the solutions of the calculated complex amplitudes from the azimuthal mode (m, n) with a size of $N_x \cdot N_r \times 1$. N_x is the number of axial measurement positions and N_r of the radial positions. $\underline{\underline{W}}_m$ is a matrix with the size $N_x \cdot N_r \times 2 \cdot n_{max}$, containing the form factor f_{mn} , the axial wave number k_{mn}^\pm , and the axial position of each microphone as shown in the following equation

$$W_{mn} = f_{mn} e^{ik_{mn}^\pm x} \quad (5.31)$$

n_{max} is the maximum number of radial modes which are of interest for the investigation or which can be determined with the amount of used microphones. The vector \mathbf{A}_{mn} contains the amplitudes of the modes in and against flow direction and has the dimension $1 \times 2 \cdot n_{max}$.

To solve equation (5.30) for the radial amplitudes, a least-mean-squares fit (LSQR) is used during this thesis.

5.4.5 Calculation of the Modal Sound Power

With the solutions of the azimuthal and radial amplitudes, it is possible to determine the overall sound power level at a certain frequency using the following equation according to Morfey [92]

$$P_{mn}^\pm = \frac{\pi R^2 \alpha_{mn} (1 - M_x^2)^2}{\rho c (1 \mp \alpha_{mn} M_x)^2} |A_{mn}^\pm|^2 \quad (5.32)$$

Only cut on modes are investigated during this thesis because as explained in section 2.1.4 concerning the propagation of acoustic duct modes, also the sound power decays exponentially if the wave number is not a real number. This equation is valid to calculate the energy transported in the axial direction of a hard walled cylindrical duct, in and against the flow direction. There is no energy transport through the hard walls.

6 Results and Discussion

6.1 Pre-tests – Impedance - Tube

To verify the equation found in literature, and already described in section 2.2.2, concerning the resonance frequency of a Helmholtz absorber, an impedance tube is used. Therefore, the specimen is placed on the opposite end of the impedance tube with respect to the speaker. Experiments were taken at room temperature, which is of course much lower than the operating temperature in the test rig. The basic idea is to simply scale the frequency with the speed of sound which is a function of the temperature. This was already validated in the work of Kabral et al. [93] under no flow conditions.

Helmholtz vane

The reason for these measurements of single absorbers and not the whole vane is, that basic knowledge about the absorber behaviour should be gained. Additional tests are done by investigating only one absorber row. With using only the middle absorber row of the Helmholtz vane a normal incidence of the sound waves can be guaranteed which is the basis of the impedance tube and the post processing procedure. Due to the curvature of the vane, this would not be valid for the other two rows. A mounting of the vane is presented in Figure 6.1. On the left side of this figure, the three absorber rows and their numbering are shown. During the investigations, row number 2 is used. The middle and the right picture show the mounting of the vane on the impedance tube. Row number 1 and three are not only covered by a layer of two-component adhesive, which is on the same level as the metallic specimen holder.



Figure 6.1: Vane mount at the impedance tube

In Figure 6.2, a comparison between the hard wall configuration (dashed line) and an investigation of the Helmholtz vane with a neck diameter of 3.2 mm (solid line). In this investigation, all five neck openings of the second absorber row are open while the ones from the other two rows are closed. Depicted is the absolute value of the reflection coefficient over the frequency. The vertical dotted lines indicate the cut-on frequencies of higher order duct modes.

It can be seen, that the peaks of smaller reflection coefficients visible in the hard wall case are also recognizable in the configuration with the Helmholtz vane. The orange frames indicate peaks for both setups which have the same origin and therefore it is assumed, that this effect is resulting either from the test bench itself or the used white noise signal. The small shift in frequency between the peaks of the setups is caused by slightly different temperatures during the measurements.

The low value of the absolute reflection coefficient marked with the arrow is indicating the absorber resonance frequency. As mentioned in section 4.5, the used arrangement of the microphones does not allow an examination of radial modes. This is also visible when looking at the cut-on frequency of mode (0, 1). From this frequency on, the measurement cannot be interpreted anymore.

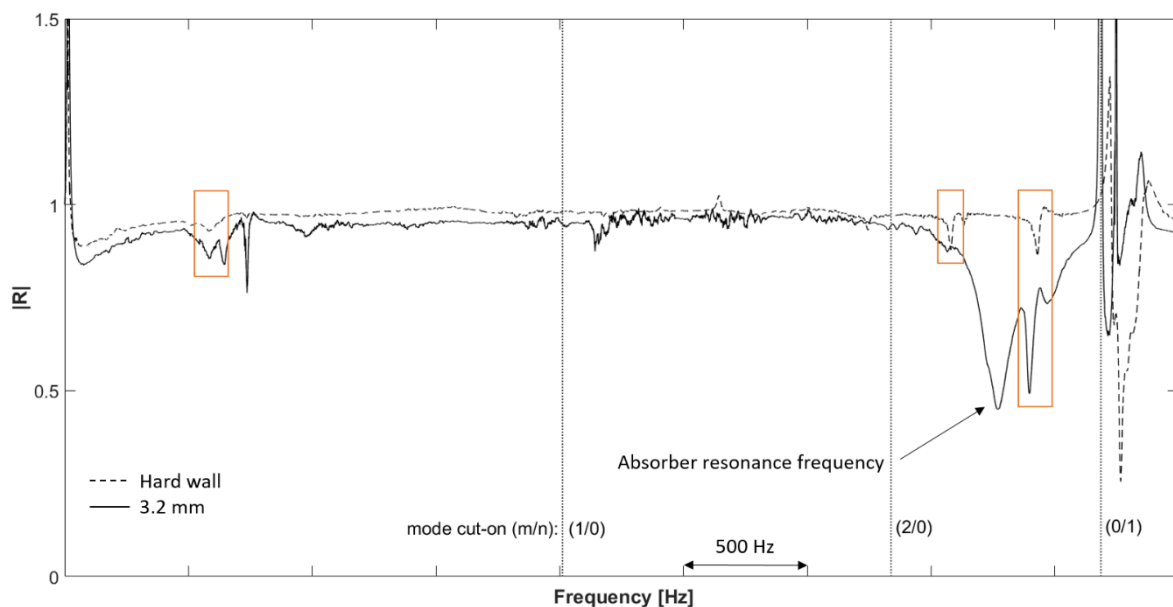


Figure 6.2: Comparison of hard wall and 3.2 mm neck diameter

Figure 6.3 shows the result of a series of tests concerning a changing absorber neck diameter in the frequency range of interest. Depicted is the absolute value of the reflection coefficient over the frequency. All five holes of the second absorber row are open during this investigation, while the other two rows are closed. The smallest diameter is 3.0 mm and the biggest one 3.5 mm with a step size of 0.1 mm.

One can clearly see that with increasing neck diameter, also the frequency at which the absorber is working best, is rising. Besides the difference in value of the calculated and measured resonance frequencies, the trend of an increase with a bigger diameter is according to the theory. It is also visible, that the two configurations having the biggest neck diameter (blue and red line) have also the lowest reflection coefficient and hence the highest absorption.

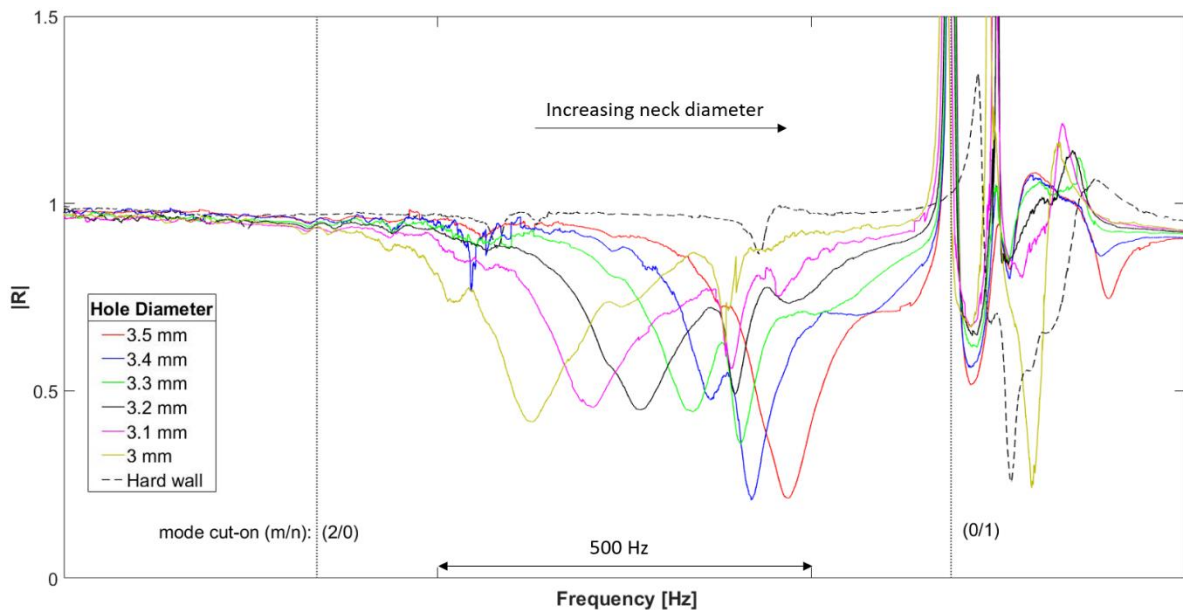


Figure 6.3: Test of Helmholtz vane with different absorber neck diameters

Figure 6.4 presents a comparison between the measurement results of the hard wall (back dashed line) and the configuration with two open holes (blue line) of one absorber row, with a neck diameter of 3.5 mm. All other neck openings are closed. Again, similarities which are unrelated to both setups are marked with the orange frames. The absorber resonance frequency is clearly visible and indicated by the black arrow.

Figure 6.5 shows again the distribution of the reflection coefficient over the frequency. In this investigation, the absorber neck diameter is kept constant at 3.5 mm but the number of open absorber necks of one row (again the second one) is increased. For all configurations, the influence of the measurement apparatus mentioned above is clearly visible.

It can be observed, that the frequency of maximum absorption is decreased with rising the number of open absorbers. It seems that this shift gets smaller the higher the number of open absorbers gets. The difference between one and two open necks is the highest within the whole measurement. Furthermore can be seen, that the value of the reflection coefficient gets smaller, and therefore the absorption higher, with an increasing number of open absorbers. Not much of a change is then observed between four and five open necks.

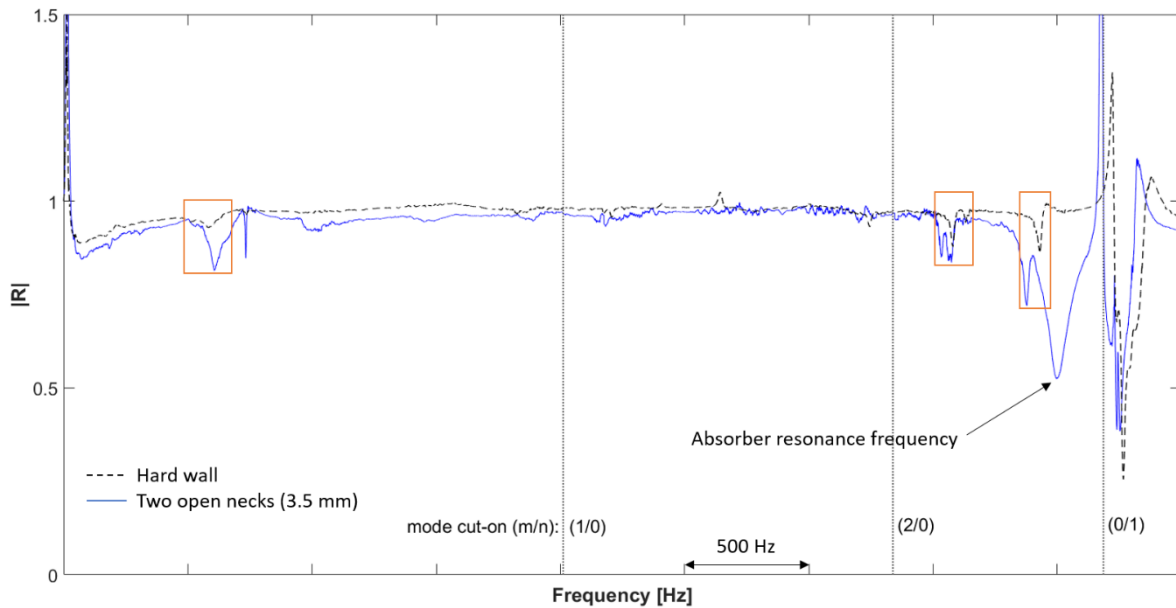


Figure 6.4: Comparison of hard wall and two open necks with 3.5 mm

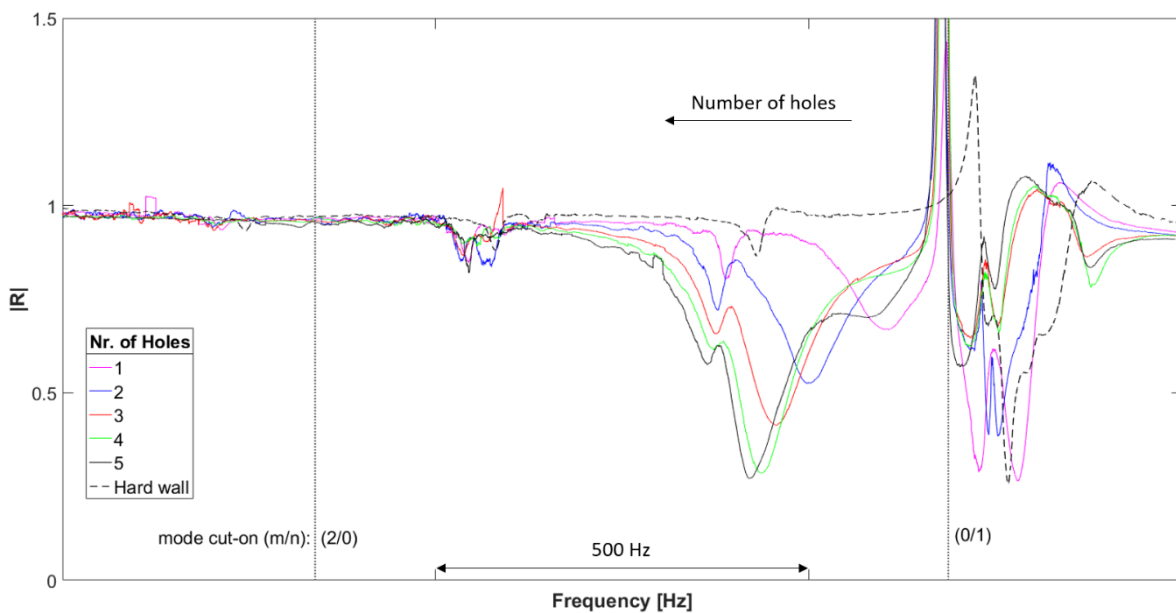


Figure 6.5: Test of Helmholtz vane with altering number of holes at diameter 3.5 mm

Following Table 6.1 shows a comparison between the measured and the calculated values of the resonance frequency depending on the different resonator neck diameters which are described above. Also stated in this table are the calculated values concerning the STTF temperature as well as the values including the flow Mach number. The first measurement is taken for one single open absorber neck, while the others of the same row are closed. The second measurement describes one open row, so all absorbers in a line are open. Concerning the measurements for one open absorber, a mean value for each diameter is shown because not every absorber gives the absolute same resonance frequency. This is presented in Figure 6.6 for a neck diameter of 3.5 mm. The results for each single open neck are indicated by the coloured lines and the absorber resonance frequencies are located inside the grey frame and shown by the vertical lines. In black, the result for all five open necks is shown.

Table 6.1: Comparison of measured and calculated resonance frequencies – Helmholtz vane

Neck diameter [mm]	Resonance frequency [Hz]					
	3.0	3.1	3.2	3.3	3.4	3.5
Calculated (tube)	3918	4031	4145	4258	4371	4485
Calculated (STTF)	4359	4486	4612	4738	4864	4990
Calculated with Ma (STTF)	5124	5285	5446	5607	5767	5927
Measured 1 neck	3746 ±40	3783 ±23	3873 ±18	3974 ±30	4028 ±31	4097 ±25
Deviation [%]	4.4	6.2	6.6	6.7	7.8	8.6
Scaled to STTF temperature	4143	4184	4283	4395	4454	4485
Measured 1 row	3625	3708	3772	3840	3919	3969
Deviation [%]	7.5	8.0	9.0	9.8	10.3	11.5
Scaled to STTF temperature	4009	4101	4171	4247	4334	4389

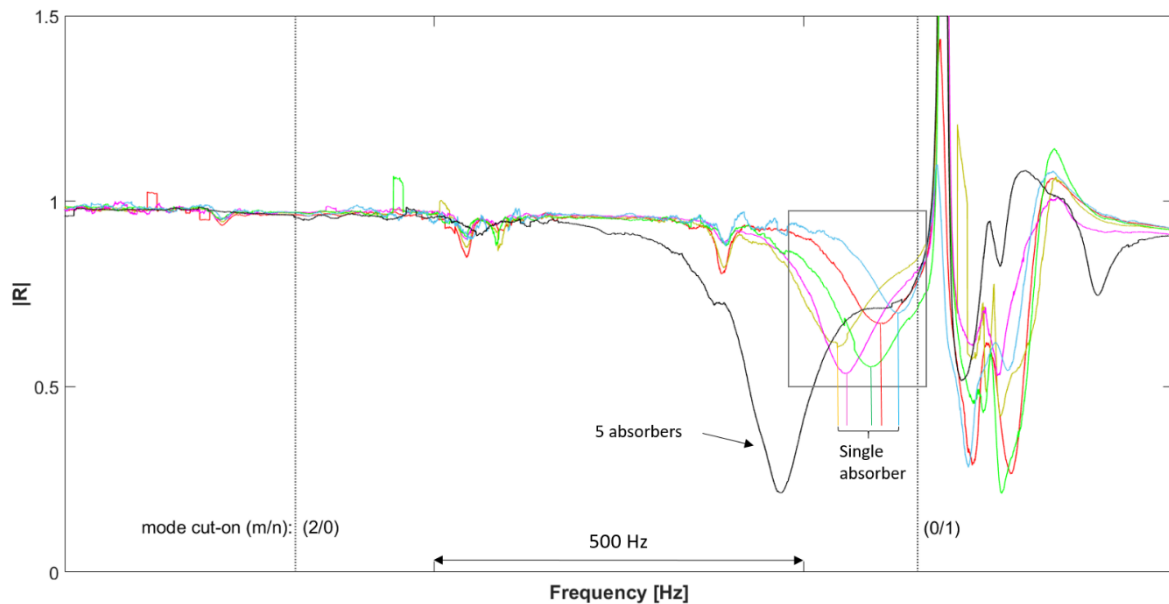


Figure 6.6: Comparison of the resonance frequency of single absorbers with 3.5 mm neck diameter

Baseline for the deviation in Table 6.1 is always the calculated value for the impedance tube according to equation (2.77). Below the deviations, also a scaling of the measured values to the STTF temperature without Mach number is presented.

The diameter was changed between 3.0 and 3.5 mm in steps of 0.1 mm. It can be seen, that the deviation is increasing with increasing neck diameter for both measurement campaigns. But with a maximum deviation of 8.6 % the results of the measurement with one open hole are comparable to deviations found in literature. Looking at the measurements for a full row of absorbers, the deviation gets bigger. In general, it can be noticed that the calculated frequency is always higher than the measured one.

The following figure depicts the distribution of the results stated in Table 6.1. Measurements taken with only one open neck are shown with the orange line and measurements taken for a whole row are indicated by the black line. Additionally, trend lines are included into the curves of the two measurement results, shown with the dashed lines. It can be seen, that the inclination

for both trend lines very similar but both are not as steep as the distribution of the calculated values (blue line).

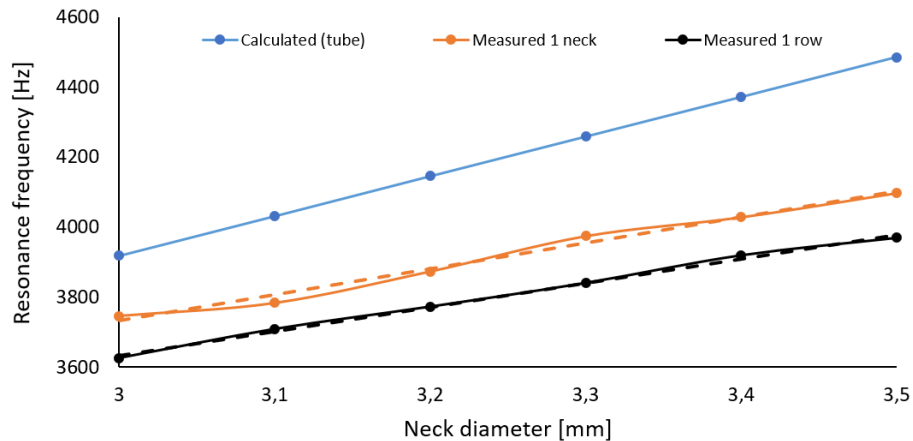


Figure 6.7: Distribution of resonance frequency over absorber neck diameter – Helmholtz vane

As mentioned above, using not only the middle absorber row of the Helmholtz vane is not guaranteeing a normal incidence of the soundwave onto the resonators of the outer two rows. Nevertheless, an additional measurement focusing on an altering number of absorber rows for a neck diameter of 3 mm is shown in Figure 6.9.

Figure 6.8 presents a comparison between the hard wall configuration (dashed line) and a test with the fully open absorber row nr. 1 (see Figure 6.1), indicated with the blue distribution. Again, the orange frames indicate similarities between both measurements which are not depending onto the investigated specimen.

Although row number 1 has no normal incidence to the soundwave, not much of a difference can be observed when comparing the result in this figure with the yellow distribution in Figure 6.3, showing the second row with the same neck diameter and normal incidence.

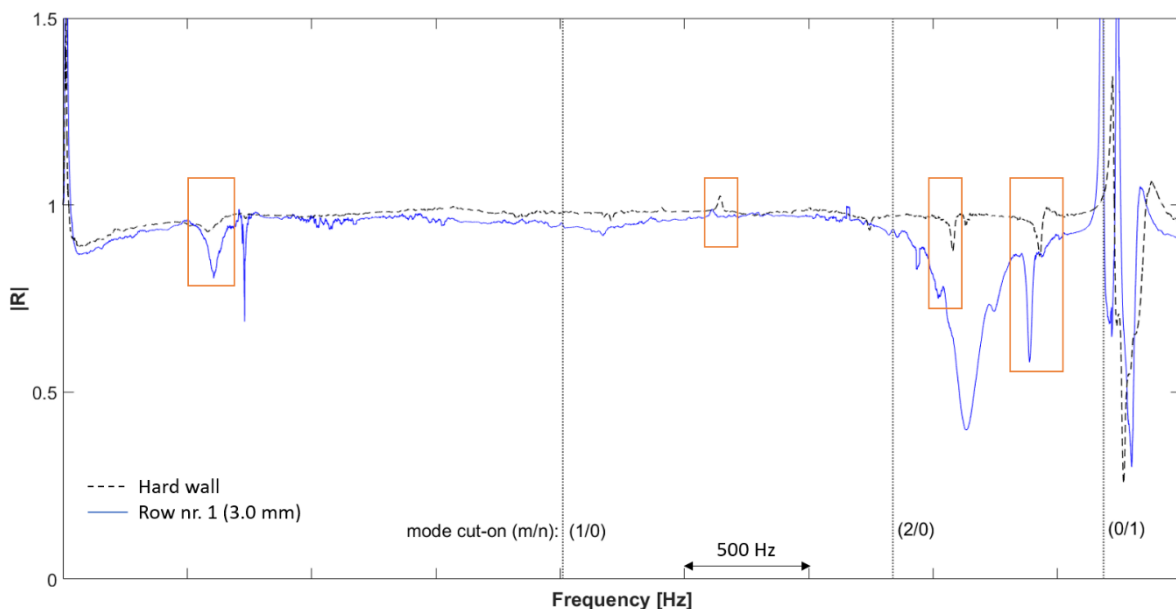


Figure 6.8: Comparison of hard wall and absorber row nr. 1 of the Helmholtz vane

Figure 6.9 shows the results of a different amount of fully open absorber rows in the frequency range of interest. A similar behaviour as seen in the investigations above concerning the decrease of resonance frequency with a rising number of open absorber necks can be

observed also in these investigations. Herein, the resonance frequency rises with the increasing number of used absorber rows.

In these experiments, the resonance frequency is not clearly visible because of all the additional peaks with low reflection coefficient. Besides this, again a clear shift to smaller reflection coefficients with higher number of open absorbers can be noticed. Using all three rows (green line), which is how the vanes are then mounted later in the TEC investigations, gives the lowest value of the reflection coefficient. It is also the lowest value of all measurements by nearly reaching zero reflection. There is not much of a difference combining row number 1 with number 2 or 3.

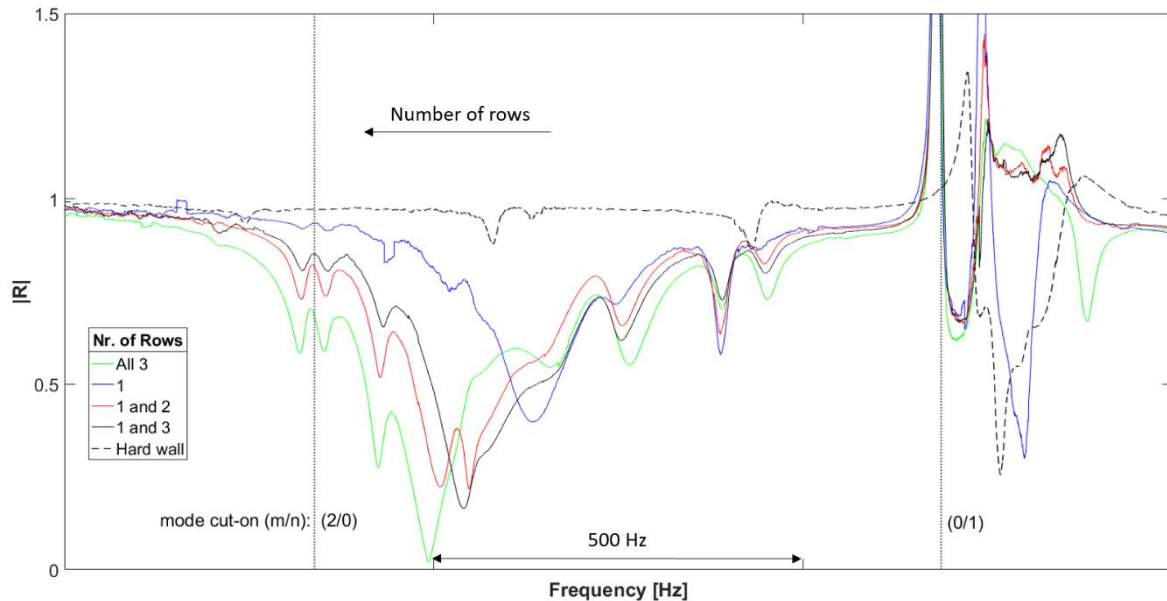


Figure 6.9: Test of Helmholtz vane with altering number of rows at neck diameter 3 mm

It seems, that from a certain number of open necks per row, no shift in the resonance frequency is happening anymore (see Figure 6.5). In the experiments conducted here, this number is assumed to be four for the investigated Helmholtz vane absorbers. When increasing the number of rows, this observation is not valid any longer.

Soft end wall

In this section, the results for the inner cassette of the soft end walls is presented. The tests are the same as shown in the section before. Therefore, only the concluding results are depicted. It is assumed, that the behaviour of the absorbers included into outer cassette of the soft end walls is the same as for the inner one because for the absorbers are identical for both cases.

The same behaviour as observed in case of the Helmholtz vanes can be identified here but with a smaller difference between the values of one measured open neck and one measured row compared to the case of the vane.

Table 6.2: Comparison of measured and calculated resonance frequencies – Soft end wall

Neck Diameter [mm]	Resonance frequency [Hz]					
	3.1	3.2	3.3	3.4	3.5	3.6
Calculated (tube)	3905	4014	4124	4233	4342	4450
Calculated (STTF)	4279	4399	4518	4639	4757	4876
Calculated with Ma (STTF)	5031	5184	5337	5489	5641	5793
Measured 1 neck	3660 ±24	3701 ±10	3831 ±20	3860 ±17	3882 ±3	3900 ±15
Deviation [%]	6.3	7.8	7.1	8.8	10.6	12.4
Scaled to STTF temperature	4010	4055	4198	4230	4254	4273
Measured 1 row	3625	3708	3772	3840	3919	3969
Deviation [%]	7.2	7.6	8.5	9.3	9.7	10.8
Scaled to STTF temperature	3974	4065	4135	4209	4296	4351

The following figure shows the distribution of the resonance frequency over the absorber neck diameter of the values from the table above. The orange dashed line indicates the trend line of the measurement taken for a single open neck. In this figure, the distributions of the measurement results, both for one open neck and for one row, are almost identical in values with only minor differences. Such a result can be expected according to the theory, but it is different to the one observed in case of the Helmholtz vanes. There, a bigger difference between the two measurements is visible. The only bigger difference between the absorbers included in the vanes to the ones included in the end walls is the cavity depth, which is deeper in case of the end walls.

It is visible, that there is again a large difference between the calculated and measured values as already seen in case of the Helmholtz vane investigations and that the inclinations comparing calculated and measured results are slightly different. This change in inclination can only mean, that one of the parameters (for example the end correction) in equation (2.77) has a different influence onto the resonance frequency in case of this normal incident measurements compared to the theory.

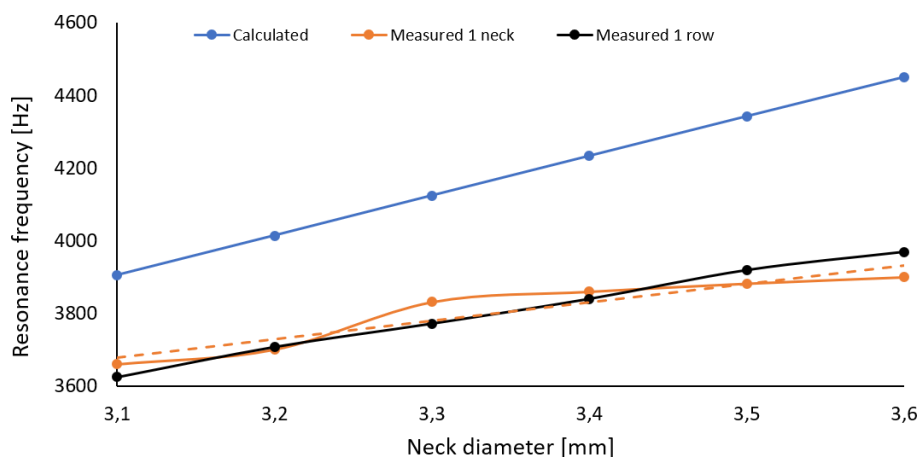


Figure 6.10: Distribution of resonance frequency over absorber neck diameter – Soft end wall

Resonator vane

This section is about the Resonator vane measurements in the impedance tube. Figure 6.11 presents the vane mount at the impedance tube on the right side and the investigated resonator cavities on the left side. Due to the vane curvature, only the part with the three resonator cavities is investigated to assure a normal incident of the sound wave onto the vane surface.

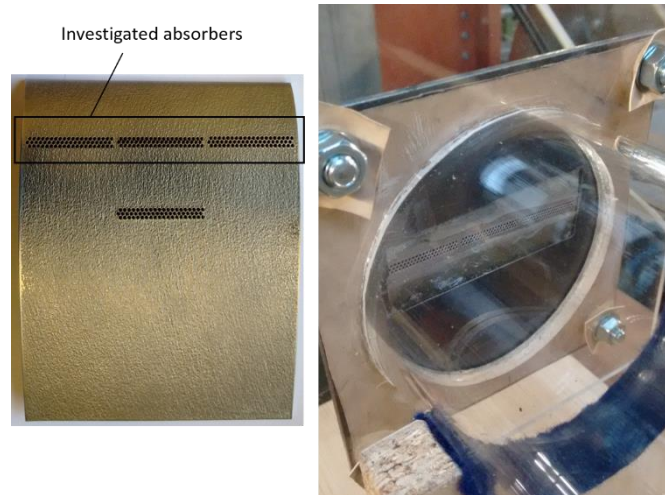


Figure 6.11: Resonator vane mount

Because the neck diameter is 0.88 mm, only investigations on a varying number of open absorber neck rows per cavity and no single necks are done. Figure 6.12 shows a comparison of the hard wall configuration (black dashed line) and the case of using only one row of open necks at each resonator cavity (yellow line). As already seen before for the Helmholtz vanes, also here similarities between the setups occur which are not related to them (marked with the black frames). It can be seen, that there is a reduction of the reflection coefficient over a wide frequency range using the Resonator vane. This range is also wider compared with the results of the Helmholtz vane. A reason could be, that here there is not only one neck per cavity but multiple ones. This is maybe changing the effect of the resonator itself.

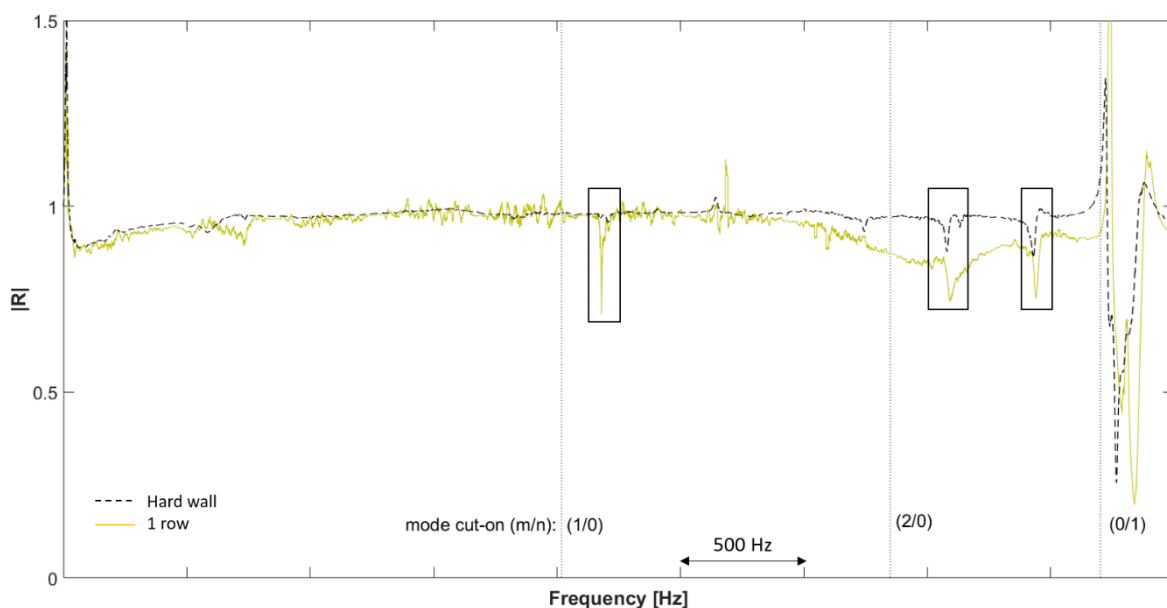


Figure 6.12: Comparison hard wall configuration and 1 row from Resonator vane

In the following Figure 6.13, a comparison between an altering number of open absorber neck rows per cavity is shown in the frequency range of interest. It can be seen, that the correct absorber resonance frequency can't be distinguished with this result, especially in the case of all three open rows. But what can be observed is, that the resonance frequency is rising with an increasing number of open absorber necks. This behaviour is also according to the theory. It should be mentioned that it is not comparable with the result seen for the Helmholtz vane, for which a rising number of open necks leads to a decrease of the resonance frequency. There, each cavity had its own neck opening and therefore the behaviour is different.

Figure 6.13 shows also, that with an increase of the rows the result gets more chaotic. Only the result for one open row can be interpreted. It is assumed, that a scattering of the incident wave due to the high number of very small holes is the reason for this behaviour. The black dash-dotted line is indicating the assumed shift in the resonance frequency for each case, resulting in an almost same offset between two following setups. This result indicates, that the resonance frequency is increasing with a higher number of open holes. Also Liu et al. [94] stated in their work, that an increase of the porosity shifts the resonance frequency to higher values but also the bandwidth of absorption grows when investigating a microperforated panel absorber compared to a Helmholtz absorber.

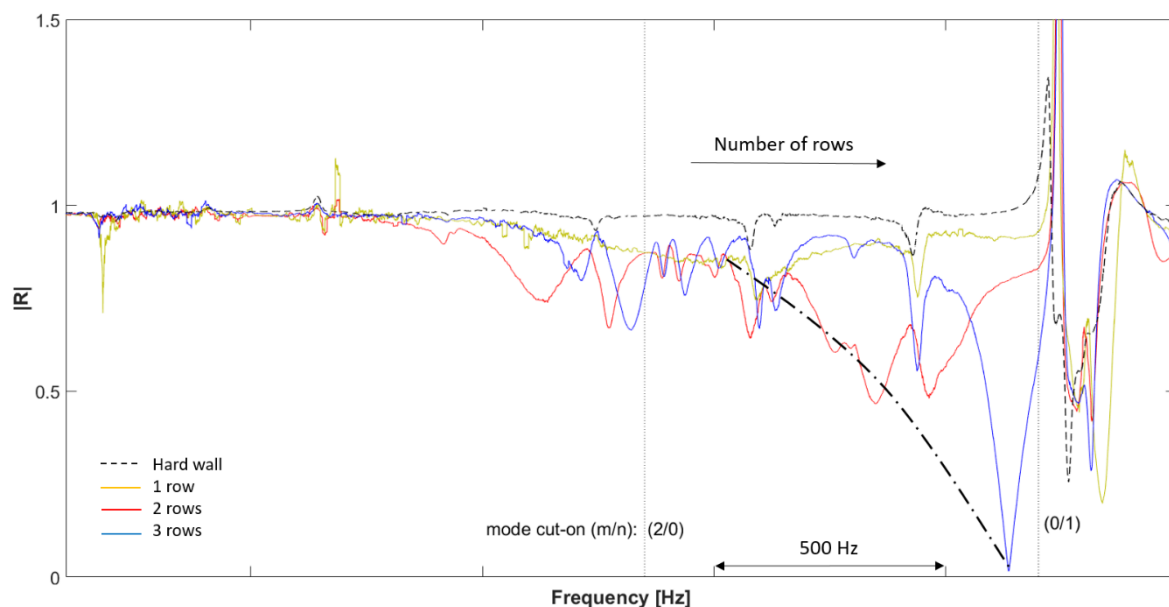


Figure 6.13: Comparison of different number of open absorber rows of the Resonator vane

According to the procedure described in section 2.2.2 concerning the microperforated panel absorber, the absorption coefficient of the investigated Resonator vane in case of a normal incident sound wave should have the theoretically distribution shown in Figure 6.14. In this figure, only the frequency range of interest concerning the test rig investigations is presented. The broadband absorption of this type of absorber can be seen clearly. This behaviour looks very similar to the one observed for the one row measurement, but the frequency range is different. It is possible, that in case of the measurements, the range is also extended to higher frequencies but not visible due to the possible resolution with the used microphones.

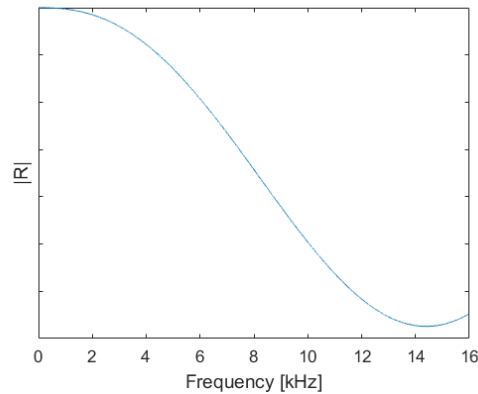


Figure 6.14: Theoretical normal incident reflection coefficient Resonator vane

During this thesis, I have supervised the master thesis of Barro Savonuzzi [95], which dealt amongst others with investigations onto this vane design. There it could also be seen, that a calculated resonance frequency did not fit to the experimental results obtained using an impedance pipe (different to the one used here) with normal wave incidence as well as tests performed having the Resonator vane mounted as a side branch absorber. With the latter one, the transmission loss was calculated with microphones located in front of and behind the lined section. These experiments showed different frequencies of the minimum reflection coefficient and transmission loss respectively, which were both far away from the intended resonance frequency desired by the project partners design.

After the stated experiments, a reference point concerning the deviation of resonance frequency with respect to the calculated one could be done. This is important, because the same absorbers are used than later in the test rig. The only unknown thing at this point is the change of the resonance frequency in presence of a grazing incident of the acoustic wave and an additional mean flow. This problem is not clearly solved in literature.

6.2 Test Rig Investigations

The following sections are about testing the different configurations including absorbers in either the guide vanes or the end walls as well as the riblet foil applied on the suction side of the TEGVs.

For a better comparison concerning the acoustic performance of each setup, the frequency spectra shown in this section are limited to the range of 2 – 10 kHz, as the orange frame indicates in the following figure. The respective hard end walls baseline setup concerning the investigations on absorbers is always indicated by a black line and the alternating configurations using either soft end walls, Helmholtz vanes, or a combination of both is depicted by the red line.

In this exemplary figure, also the target frequency to reduce, the first blade passing frequency, is indicated with 1st BPF. Next to it, and marked with VF, is a vibration frequency which can be related to a eigenfrequency of the used rotor disc (see Schönleitner [96]).

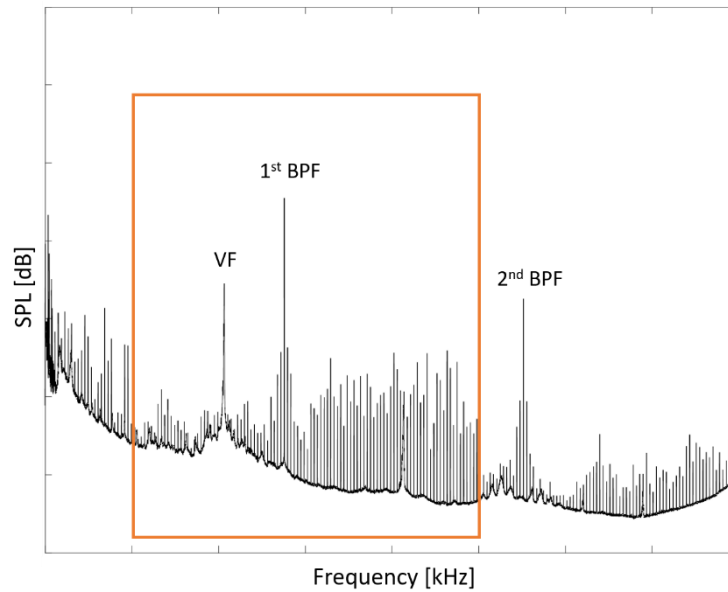


Figure 6.15: Frequency spectra with investigated area

In the comparisons of the overall PWL regarding the cut-on circumferential modes m , summed up over all relevant radial modes n , the amplitude of a propagation in and against the flow direction is shown. Bright colours indicate a propagation in flow direction and dark ones against. Orange shows the airfoil interaction modes of the examined turbine stage, and blue depicts the scattered interaction modes at the turbine exit casing. White and grey bars show modes, which can't be clearly related to such interactions or their scattering. Figure 6.16 should serve as an example for this interpretation.

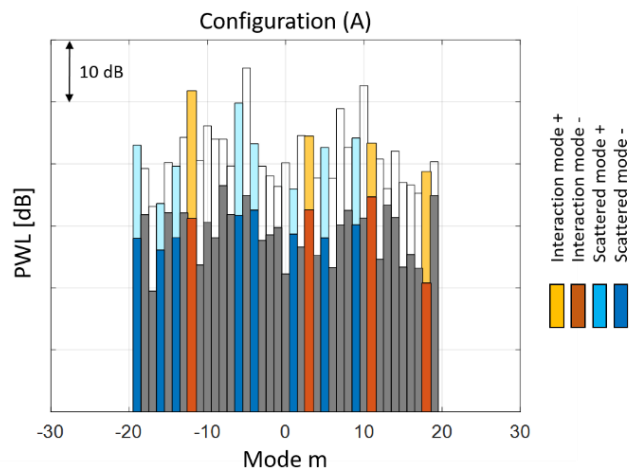


Figure 6.16: Example for overall PWL

The mentioned airfoil interaction modes and their scattered modes, visible in Figure 6.16, are stated in Table 6.3 with respect to their origin. Although the rotor – stator interaction mode $m = 24$ is cut-off in the present investigations, its scattered modes are not. Due to the fact that the energy of the mode is not totally vanished when it reaches the TEC, it is assumed that there is still some impact from it and its scattered modes onto the total sound field.

Table 6.3: Airfoil interaction modes and their scattered modes on the TEC

	IGV-Rotor	Rotor-Stator	Rotor-TEC
Interaction mode	11	24	-12, 3, 18
Scattered modes at TEC	-19, -4	-6, 9	-16, -14, 1, 5

The table presented at the beginning of section 4.3 describing the naming of the different investigated setups having Helmholtz absorber included should be shown again at this point. As mentioned, the coloured boxes indicate which vane and end wall design are combined in each setup. E.g. configuration (F) consists of the Helmholtz vane design with a neck diameter of 3.2 mm and of the hard end walls.

		Diameter [mm]	Configuration									
			A	B	C	D	E	F	G	H	I	J
Vane Design	Standard	-	■	■	■	■						
	Helmholtz	taped					■					
		3.2						■				
		3.4							■	■		
	Leaned	-								■	■	
End Walls Design	Hard	-	■				■	■	■		■	
		3.5		■								
	Soft	3.8			■					■		■
		4.2				■						

Besides the aeroacoustical comparison between the various configurations, also aerodynamical investigations are done to see if there is an impact onto the aerodynamical performance of a setup when changing the surface structure. On the one hand by including openings into vanes and end walls and on the other hand by applying a riblet structure onto the vane suction side surface. The following part should be firstly an introduction into the performed examinations and secondly a general description of the flow effects which could be observed during this thesis by using the already explained aerodynamical five-hole-probe.

Therefore, Figure 6.17 shows an exemplary result of the hard wall baseline configuration (A) including Standard vanes. On the left side of this figure, the total pressure downstream of the investigated vane row normalized by the stage inlet total pressure is depicted, followed by the flow Mach number in the middle, and the yaw angle on the right side. All plots indicate the radial distribution from circumferentially mass averaged values of the whole measurement sector, over the relative channel height. The bars in the bottom region of each plot give the scale of the shown parameter.

The decrease visible in the normalized total pressure as well as in the Mach number at the outer and the inner casing, with respect to the core flow, can be connected to the strong secondary flow effects in the vane passage. At the outer casing, also the rotor tip leakage flow has an impact. From the yaw angle distribution, it can be determined that there is not much of a swirl left in the flow downstream of the TEC.

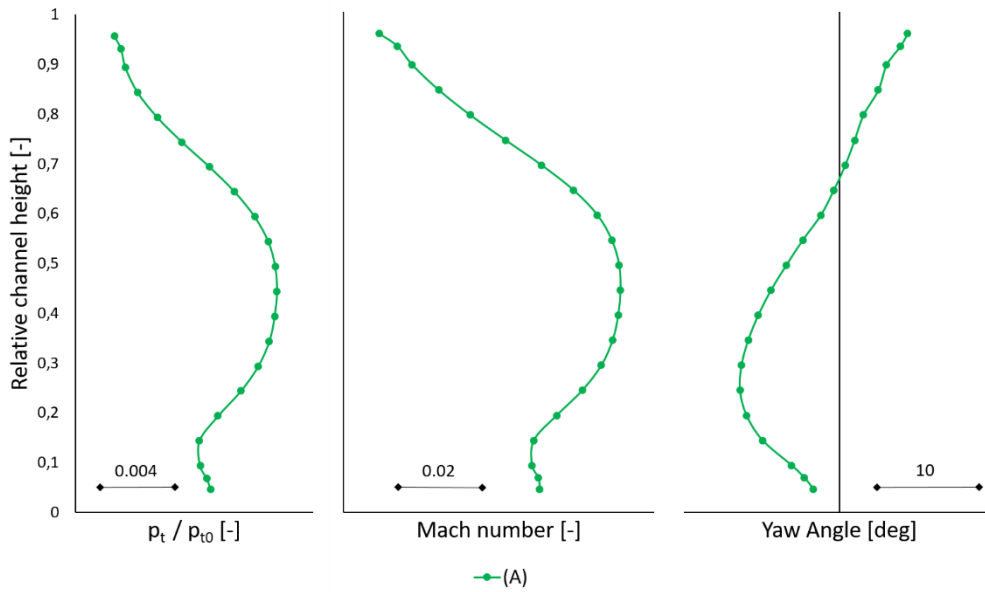


Figure 6.17: Visualisation example of aerodynamical parameters

In addition to the radial distributions, the whole measured flow field downstream of the TEC for the normalized total pressure and the yaw angle are shown for all configurations. In those aft looking forward plots, one can identify secondary flow effects. Again, as an example, the results for the baseline setup (A) are shown at the top of following Figure 6.18, and results of configuration (I) including the Leaned vane design are depicted at the bottom.

The vane wake is indicated by the black dashed lines with the vane pressure side on the right, and the suction side on the left side of the line. Concerning configuration (A) four vortices, which could be clearly identified, are represented by the white arrows and marked with the roman numbers I, II, III and IV. The wake is clearly skewed, which is the outcome of the presence of the vortices.

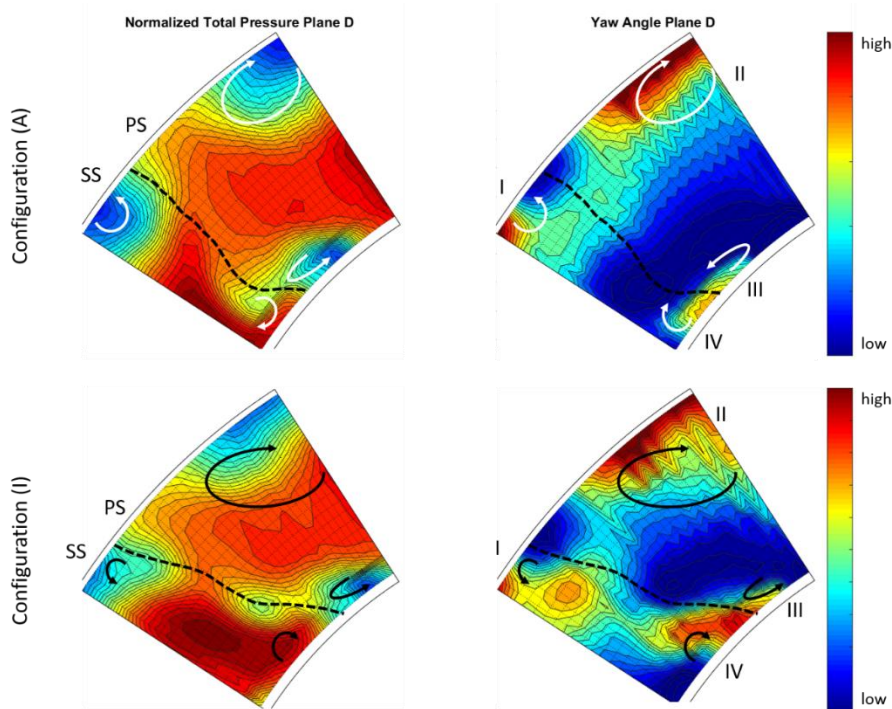


Figure 6.18: Examples of the flow fields downstream of the TEC

Vortex I, located on the outer casing, is rotating in counter clockwise direction and results from a separation on the vane suction side. The clockwise rotating vortex II, also located in the outer casing area, is the biggest vortex and results from a separation on the vane pressure side. This vortex is additionally shifted in the direction of the neighbouring vane suction side due to the secondary flow effects at the tip. In other words, the upper passage vortex (UPV), resulting from the pressure gradient between the two vane sides, is merging with the separation to one big vortex II. Vortex III, located on the inner casing, is again rotating in counter clockwise direction. It is assumed that this flow structure is resulting from the pressure gradient on the hub end wall. Therefore, this vortex is the secondary flow effect called lower passage vortex (LPV). Vortex IV is assumed to be a corner vortex located at the sharp intersection between the vane suction side and the inner casing. It is counter rotating with respect to the LPV.

When looking at setup (I) at the bottom of Figure 6.18, four vortices could be identified indicated by the black arrows and marked again with the roman numbers I, II, III, and IV. All four vortices are the same ones as already described above for configuration (A).

The vane wake, again indicated with the black dashed line, is clearly inclined to the left, and therefore against the rotor rotational direction, due to the intended lean of the vanes.

In the upcoming sections, all configurations are investigated by showing the aerodynamical parameters described above. It should always be referred to this description and therefore no arrows for the vortices are included in the upcoming figures, but the regions are marked with the above mentioned roman numbers.

6.2.1 Helmholtz Vanes

The first section is about the use of the Helmholtz vanes and hard end walls. Two different versions of this vane design are investigated, with the difference being the diameter of the absorber neck. To see if there is an influence of the rougher surfaces, with respect to the smooth one from the Standard vane design, due to the additive manufacturing process, another setup with taped absorbers is also investigated.

Acoustics

Configuration (E) – taped openings

First, the configuration (E) containing the taped Helmholtz vanes and hard end walls is compared with the baseline configuration (A) using Standard vanes and hard end walls as well. Figure 6.19 shows the sound pressure level distribution over the chosen frequency range for configuration (A) with the black line and for setup (E) with the red line. It can be seen that the Helmholtz vane design has a reduced background noise over a large frequency range. This background noise does not result from the measurement system but is mainly flow noise. But on the other hand, there is an increase in almost every peak of the spectrum.

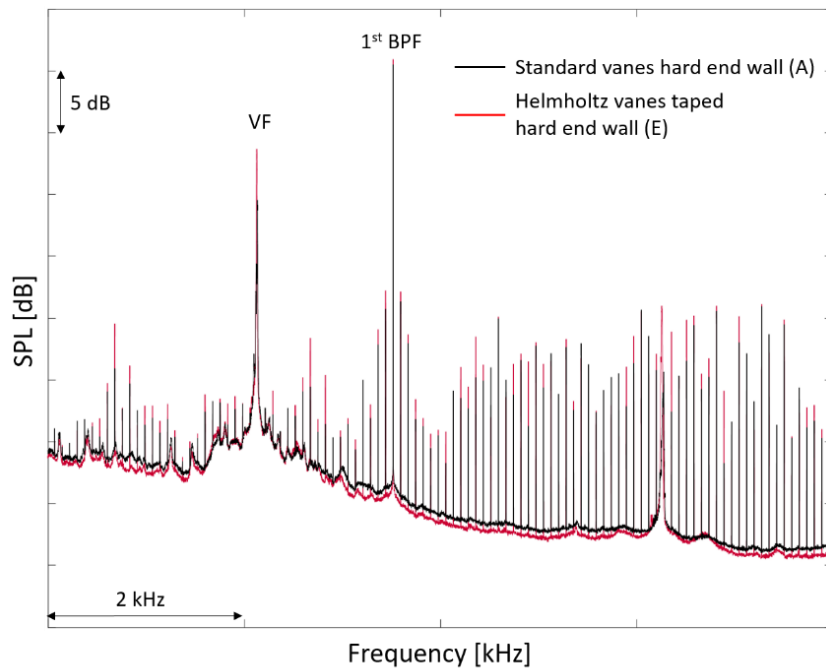


Figure 6.19: Frequency spectra - Configurations (A) and (E)

The following figure shows a comparison between both setups concerning the overall PWL for each circumferential mode order m as a sum of all radial modes n , which can be determined with the used measurement system. It is visible, that there are no big changes concerning the interactions as well as their scattered modes, besides for $m = -19$ showing a 4.5 dB, and $m = -16$ a 4.4 dB reduction for configuration (E).

The overall sound power level of all cut-on modes shows a reduction of 0.4 dB in flow direction, which is in the measurement uncertainty of a microphone and can therefore be neglected, and an increase of 1.1 dB against flow direction concerning configuration (E).

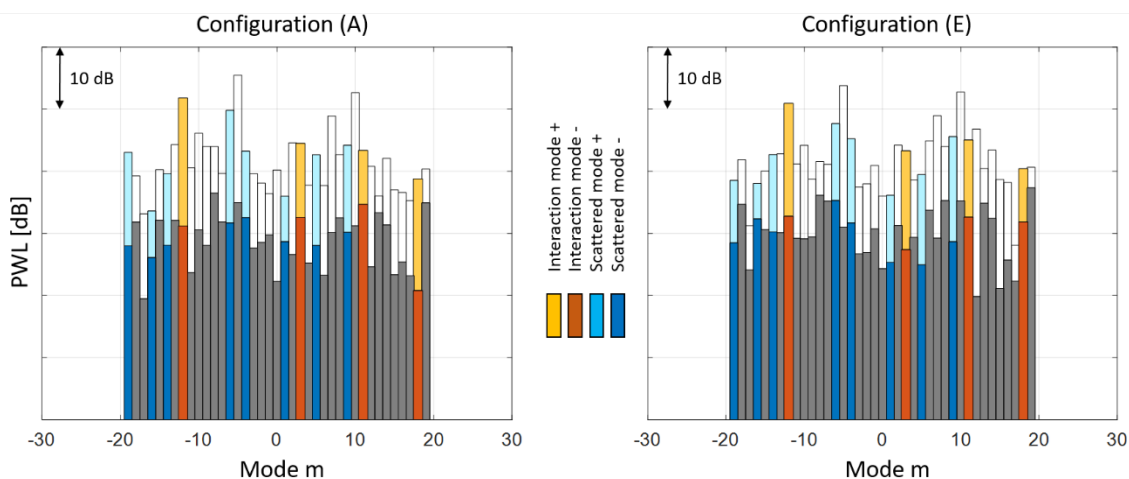


Figure 6.20: Overall PWL comparison - Configurations (A) and (E)

Configuration (F) – 3.2 mm absorber neck diameter

The next comparison is between configuration (A) and (F), which has the smaller of the two different absorber neck diameters concerning the Helmholtz vane investigations. Figure 6.21 shows the SPL over the frequency. Again, the background noise is reduced using the additive

manufacture vanes, as it can also be seen in the comparison of configuration (A) and (E). With open absorber holes, this setup achieves also a SPL reduction for many peaks at different frequencies. But there is no reduction as could be assumed due to the underlying theory of this type of absorber.

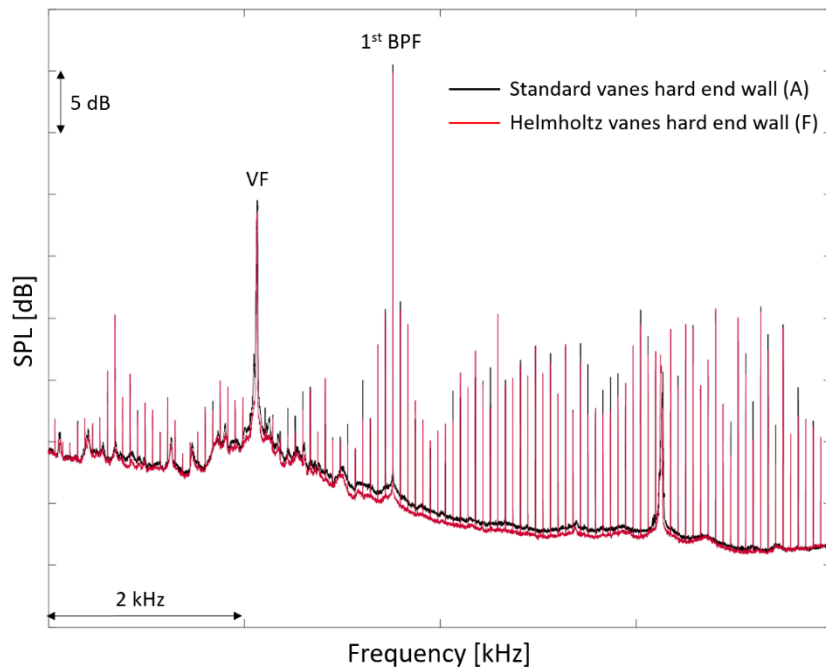


Figure 6.21: Frequency spectra - Configurations (A) and (F)

In Figure 6.22, a comparison of the overall sound power level for all cut-on modes is presented. It is visible, that the dominant mode $m = -10$ is reduced by about 3 dB using configuration (F). The rotor – TEC interaction modes are almost constant but the resulting scattered mode $m = 5$ shows a reduction of 9 dB in flow direction. With $m = -19$ and $m = 9$, also two other scattered modes show a reduction of 5.2 dB and 6.8 dB respectively, both travelling in flow direction. The interaction modes themselves have besides a decrease of 2.3 dB for mode $m = 3$ not much of a change.

With this configuration (F), a reduction of the overall sound power level for a propagation in flow direction of 1.4 dB compared with configuration (A) can be achieved. The one propagating against the flow direction stays constant.

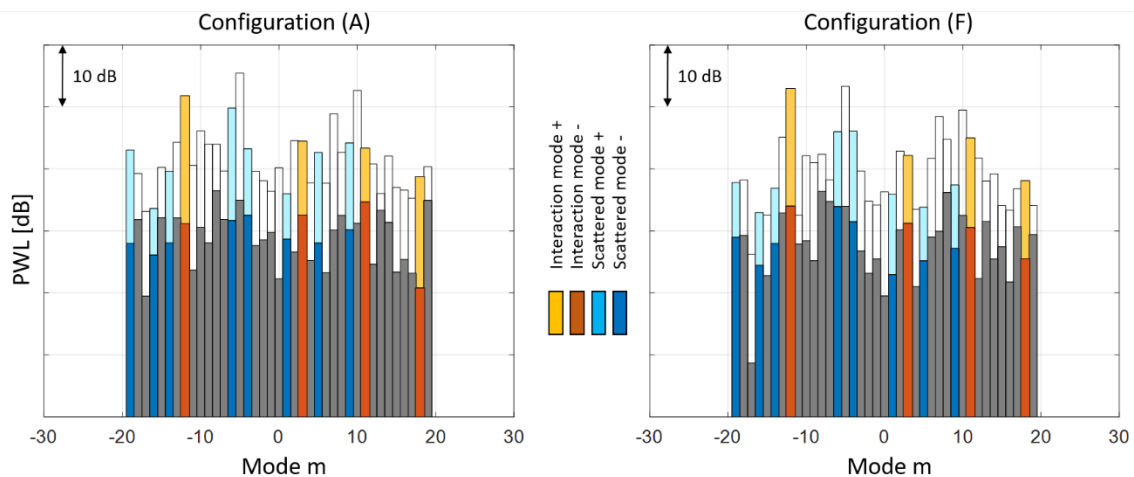


Figure 6.22: Overall PWL comparison - Configurations (A) and (F)

Configuration (G) – 3.4 mm absorber neck diameter

Figure 6.23 shows the comparison of configuration (A) and the Helmholtz vane setup with the bigger of the two investigated neck diameters (G). Both cases are again with hard end walls. There is still the reduction of the background noise as seen in the two comparisons above and again also a reduction of the peaks as seen in case of setup (F).

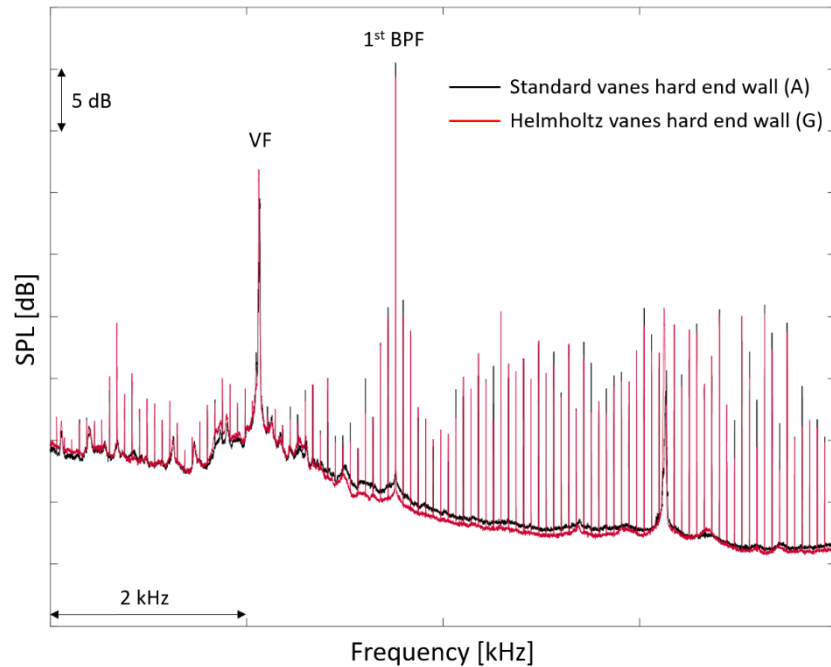


Figure 6.23: Frequency spectra - Configurations (A) and (G)

A comparison of the overall PWL is given in Figure 6.24. Mode $m = 5$ (scattered rotor – TEC interaction) shows with a reduction of 11 dB (propagating in flow direction) for configuration (G) again the highest change. The dominant mode $m = 10$ is reduced by 4.2 dB in flow direction. The interaction modes show, besides an increase of mode $m = 11$ of 3.7 dB, no significant change comparing those two configurations. Concerning the scattered modes, a reduction for $m = -19$ and $m = -6$ of 4.2 dB in both cases, and a decrease of 5.3 dB for mode $m = 9$ is achieved.

The difference between those two setups concerning the sound power level is 1.6 dB in and 0.9 dB against the flow direction with achieving the reduction using the Helmholtz vanes design.

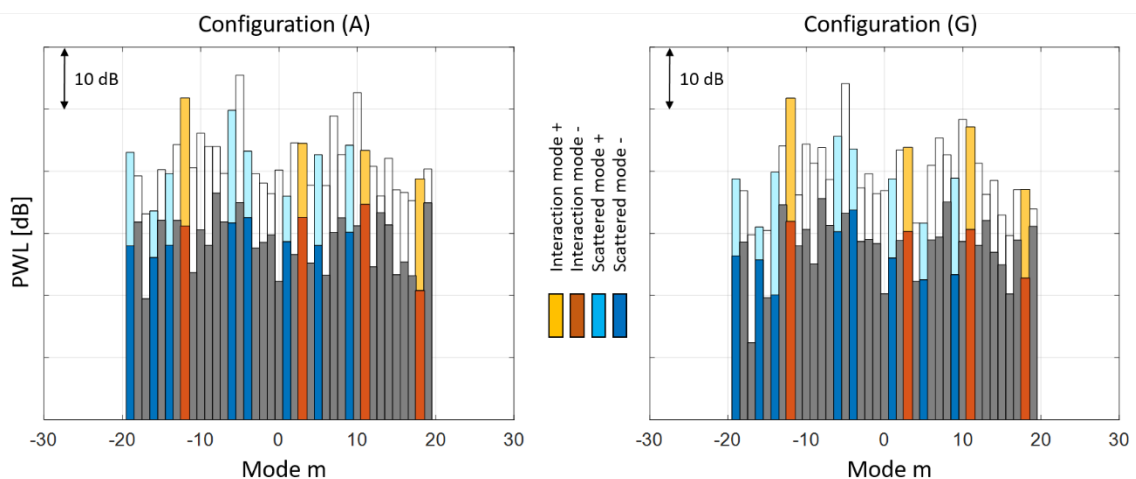


Figure 6.24: Overall PWL comparison - Configurations (A) and (G)

Aerodynamics

In this section, a comparison between the setups concerning some aerodynamical parameters is done. Figure 6.25 depicts all three configurations with the combination of Helmholtz vanes and hard end walls ((E), (F), (G)) as well as the baseline setup (A) having the Standard vanes and the hard end walls as well. On the left side, the total pressure measured downstream of the vanes normalized by the total pressure at stage inlet is shown over the relative channel height. In the middle, the Mach number distribution is given, followed by the yaw angle on the right side of the figure. Each dot in the distributions represents a circumferentially mass averaged value of the measured flow field.

The scale in all three parameter plots indicates that the differences between the configurations are very small. Also the shape of all radial distributions are very similar. The only obvious difference can be detected when looking at the hub region of the normalized total pressure. Herein, configuration (E) shows a small deviation at the measurement point closest to the inner casing.

Setup (A) indicates a stronger lean to smaller values starting at about 40% of the relative channel height, looking at the normalized total pressure and the Mach number, with respect to the other three configurations. But with a maximum difference of 0.002 in the normalized total pressure between setup (A) and (E) at the very last point closest to the tip, this deviation can be neglected.

In general, it can be said, that the configurations without openings in the vane surface (baseline (A) and setup (E) with taped openings) have higher values of normalized total pressure over the whole radial height. This indicates, that the aerodynamical losses are higher in case of the setups including absorbers if it is assumed that the total pressure upstream of the vane row is identical for all cases. An assumption like this can be made, because the operating point was always set identical. But anyway, the difference is so small, that this can be neglected.

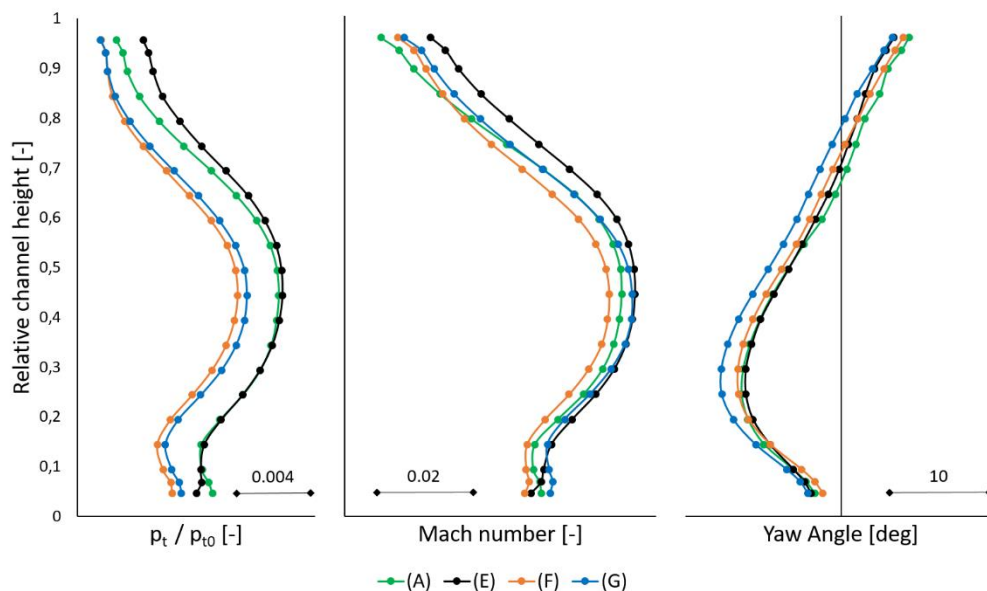


Figure 6.25: Aerodynamical comparison - Configurations (A), (E), (F), and (G)

Figure 6.26 presents a comparison of the aerodynamical parameters total pressure normalized by the total pressure at stage inlet at the top, and the yaw angle at the bottom. On the very left side the baseline configuration (A) is depicted, followed by three setups combining Helmholtz vanes and hard end walls. As could already be seen in Figure 6.25, the overall level in normalized total pressure is higher for the configurations (A) and (E) compared to (F) and (G). The three areas of low normalized total pressure, marked with I, II, and III, have a larger extension in the cases (F) and (G). Concerning area I, which is at the intersection of the vane

suction side and the outer casing, an extension in radial direction following the vane SS pointing towards the centre of the channel height can be observed. Area III of low level normalized total pressure located at the hub has a slightly lower level for the configurations (F) and (G).

The measured flow fields concerning the yaw angle are all very similar. No changes due to the different surfaces can be detected in these measurement results.

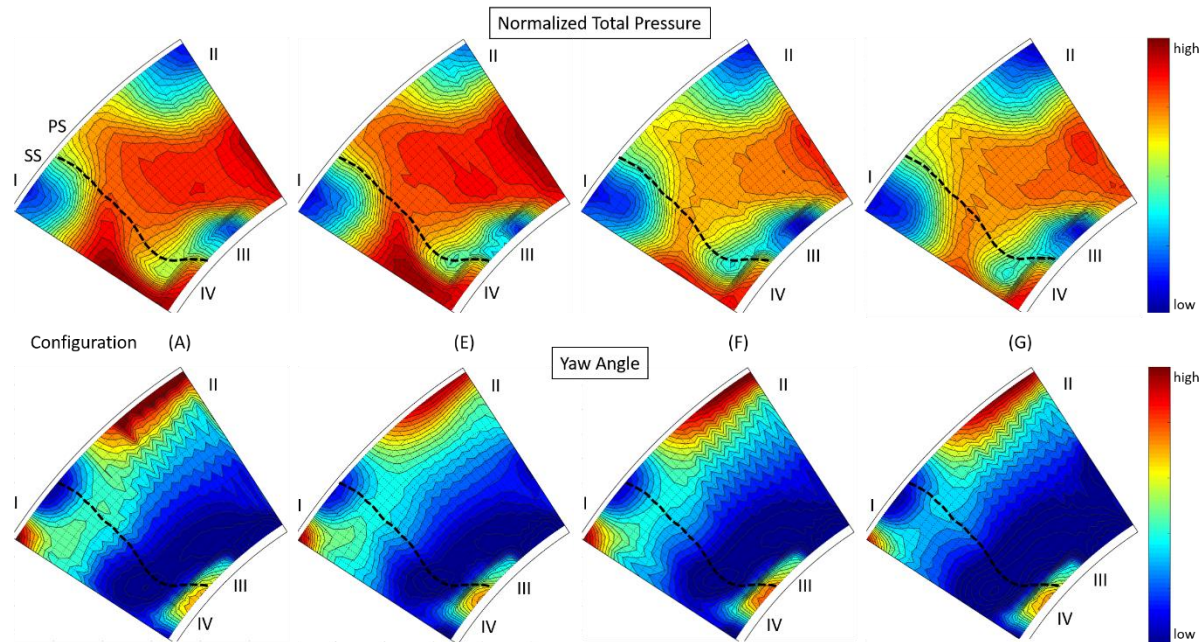


Figure 6.26: Aerodynamical flow fields – Configurations (A), (E), (F), and (G)

Figure 6.27 shows a comparison of two results obtained by using the trailing edge probe in an axial distance of 0.3% (related to the vane chord length) downstream of the vane TE. The total pressure in each measurement point is normalized by the averaged value of the whole circumferential measurement line.

The blue coloured distribution indicates the result of a measurement in the usual channel height of 30% and the green line gives the normalized total pressure at a channel height of 34%. Two heights were measured to see if the openings in the vane surface have an influence onto the wake. Both relative channel heights are marked with black dashed lines in Figure 6.28. It can be seen that the 30% line is in-between of two radially spaced openings and the one at 34% is directly downstream of two in axially direction shifted absorber necks.

Coming back to Figure 6.27, no difference in shape between both results can be detected except the small area at the slope on the suction side. It seems, that the wake there is a little bit wider in case of the measurement at 34 % relative channel height, and therefore directly downstream of a neck opening.

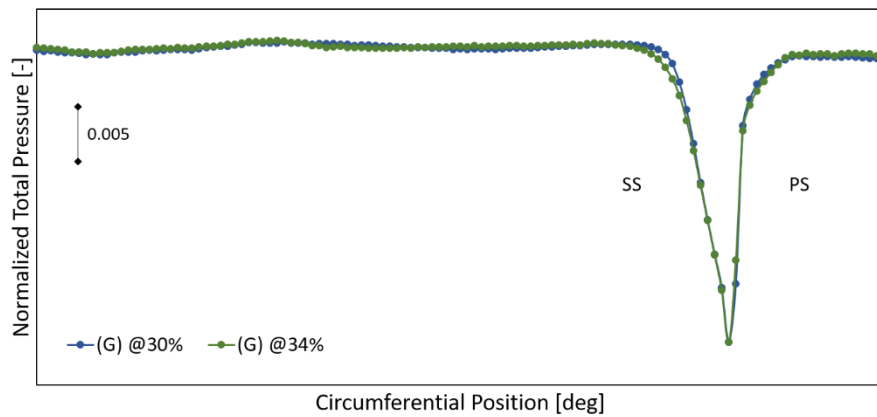


Figure 6.27: Comparison of vane wake measurements – Helmholtz vane design

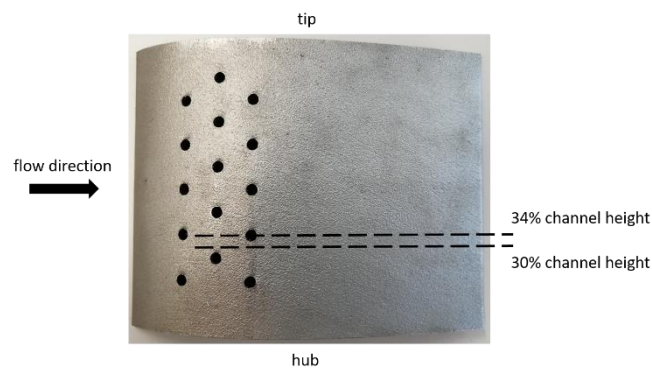


Figure 6.28: Helmholtz vane with markers for channel height

Determining the aerodynamic parameters for both measurements concerning the equation given in Schobeiri and John [34] leads to an increased wake width (7.7 %) as well as momentum thickness (12.9 %) in case of the measurement at 34 % relative channel height. These results and the one calculated only for the vane suction side are presented in Table 6.4. No results of the pressure side are stated here, because the normalized total pressure distributions on this vane side are congruent. It is visible, that the parameters have an increase on the suction side for the 34 % measurement. This is in accordance with the distribution shown above. With these results it can be said, that the neck openings slightly influence the vane wake.

Table 6.4: Aerodynamic parameters – Helmholtz vane

	Configuration		Change in [%]
	(G) at 30%	(G) at 34%	
Wake width (total) [m]	0.00262	0.00282	7.7
Wake width (SS) [m]	0.00137	0.00155	12.9
Momentum thickness (total) [m]	0.00121	0.00133	10.5
Momentum thickness (SS) [m]	0.00079	0.00086	7.9

Comparison

It can be observed, that for all investigated setups in this section, a broadband reduction of the background noise could be achieved. It is assumed, that this is due to a similar effect as explained theoretically in section 2.4 dealing with the ability of riblets to hinder velocity fluctuations in crossflow direction and therefore to be able to suppress the noise generated by

these fluctuations. The reason for this assumption can be seen in Figure 6.29, where a zoom in of a Helmholtz vane using a microscope is shown. Due to the manufacturing process, which is melting metal powder layer after layer, a directed roughness can be observed on the vane surface (indicated by the yellow dashed lines). This is similar to the geometry of riblets, but bigger in size. Comparing this figure with Figure 4.8 showing the ideal riblets size, it can be observed that the inclination of the roughness corresponds very well to the surface streamlines. It is therefore assumed, that also this directed roughness is somehow guiding the flow on the surface and hampers the velocity fluctuations perpendicular to the flow direction. Hence, this hindering results in a reduction of the background noise. The most important evidence is that this reduction is also visible in the case of taped absorber necks and therefore the resonators can be excluded as a contributor to this SPL decrease.

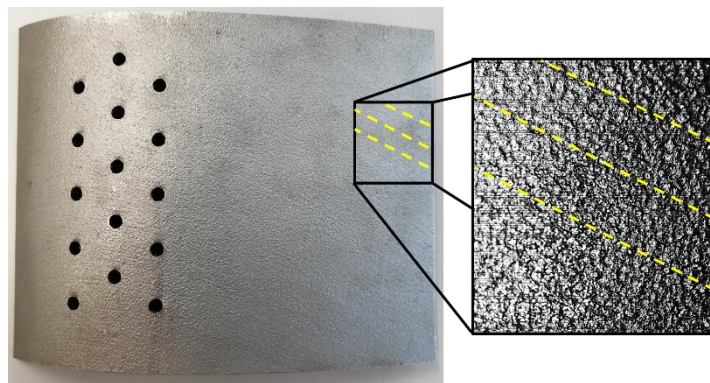


Figure 6.29: Helmholtz vane and zoom in for roughness visualisation

A direct comparison concerning the change in sound power level for a propagation in flow direction for all cut-on mode is depicted in Figure 6.30. In this figure, all configurations combining hard end walls and Helmholtz vanes are compared with the respective hard walled baseline setup. The majority of modes show a decreased sound power level for all cases except configuration (E) having the taped absorber openings. Important interaction modes are indicated by the arrows also showing which interaction it is: R – T is rotor – TEC, R – S means rotor stator interaction.

The highest reduction with 11 dB using configuration (G) could be achieved at mode $m = 5$, which is a scattered rotor – TEC interaction. But also setup (F) has with 8.8 dB a significant reduction concerning this mode. Also mode $m = -15$ shows a large reduction for these two setups. This mode cannot be related to any interaction or scattered mode.

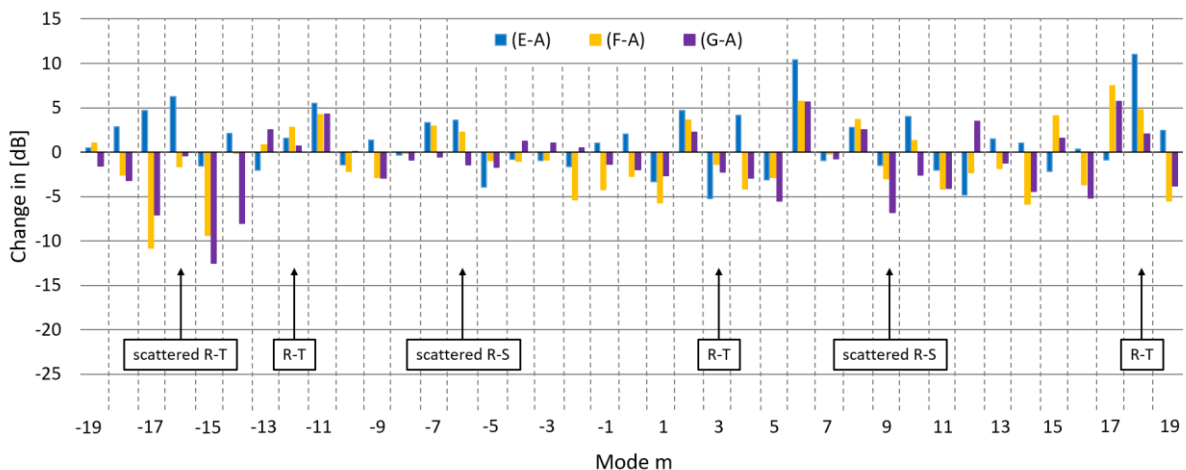


Figure 6.30: PWL^+ change of cut-on modes – Helmholtz vanes

The same comparison as above is given in Figure 6.31 with the focus on a wave propagation direction against the flow direction. Mode $m = 18$, which is a rotor – TEC interaction mode, has increased for all three setups with respect to the baseline configuration. The highest increase is detected for the taped case. But it is also noticeable, that the increase gets smaller with rising absorber neck diameter. Also the modes $m = -11$ and $m = 6$ have increased for all configurations. These two modes cannot be connected to a vane blade interaction.

Looking at the modes $m = -17$ and $m = -15$, a significant reduction can be identified for the setups (F) and (G). But again, these modes cannot be linked to a vane blade interaction.

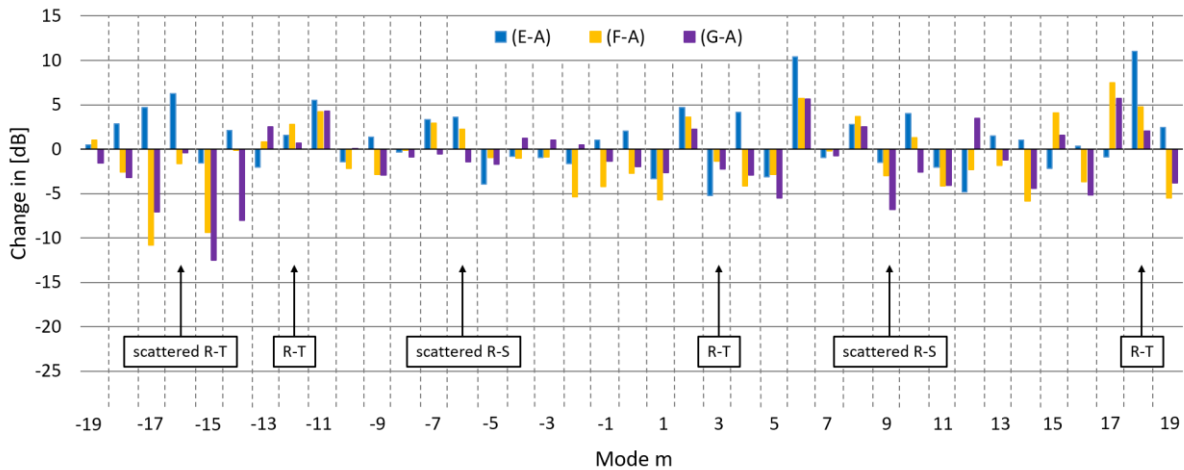


Figure 6.31: PWL change of cut-on modes – Helmholtz vanes

Comparing the reduction of both propagation directions it can be seen, that there is in general a higher decrease of the modes if the propagation direction is equal to the flow direction.

Interestingly, all configurations show a significant increase of the PWL in as well as against flow direction for the mode $m = 6$. This mode is not related to any vane blade interaction.

A possible reason for the increase in the rotor – TEC interaction modes observed in the two upper figures is the location where the rotor wake is impinging the TEGV suction side. This wake – vane impingement is the cause of these interaction modes. From Figure 6.32 it can be seen, that the rotor wake (taken at midspan), indicated by the red lines, has the first contact with the TEGV in the region of the absorber neck openings. The location of the openings is presented in % of the vane chord length and shown with the vertical black lines. This interaction between the wake and the roughness due to the openings could be the reason for the increase of the interaction modes because a “rougher surface” is noisier compared to a smooth one (see also [97]).

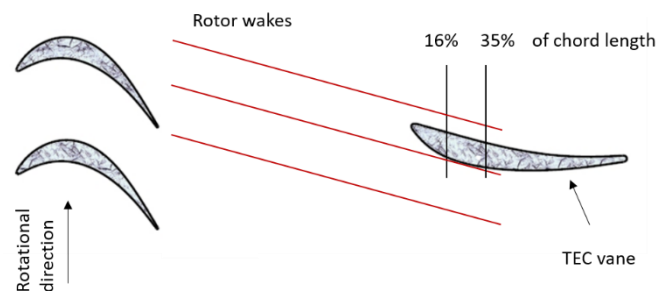


Figure 6.32: Rotor wake impinging TEGV

6.2.2 Soft End Walls

This section is about the use of soft end walls in combination with different vane designs. In total, three different configurations are investigated concerning the absorber neck diameter of the outside casing cassette while the diameter of the inside cassette is kept constant. The reason doing so is to increase the absorption band width. In general, the design for both absorbers, inside and outside casing, is the same and similar in shape to the one included into the Helmholtz vanes.

A green line in each comparison of the frequency spectra indicates the signal of the reference microphone flush mounted on the back wall of one resonator cavity. The maximum value in the signal indicates the highest pressure inside the cavity and therefore the absorber resonance frequency. An additional small peak can be seen in the signal, which is due to the high vibration frequency of the test rig and hence is not related to the resonator performance.

6.2.2.1 Standard Vanes

First, the combination of the state-of-the-art vane design and the soft end walls is shown. It is compared with the baseline hard end walls setup, including the same vane design.

Acoustics

Configuration (B) – 3.5 mm absorber neck diameter

In the following figure, a comparison of the frequency spectra for both configurations (A) and (B) is shown. It can be clearly seen, that there is a SPL reduction in the frequency range between the vibration frequency and the 1st BPF. Many of the peaks in this about 2 kHz wide range are decreased down to the background noise level. A SPL peak reduction at the frequency of interest (1st BPF) of 1.9 dB is achieved. The maximum of the reference microphone signal is at 4408 Hz, which corresponds quite well to both, the frequency which is achieved by scaling the normal incidence result of the impedance tube for this diameter to the STTF temperature as well as the calculated one without Mach number (stated in Table 6.2 in section 6.1). It seems according to this, that there is no effect due to the Mach number.

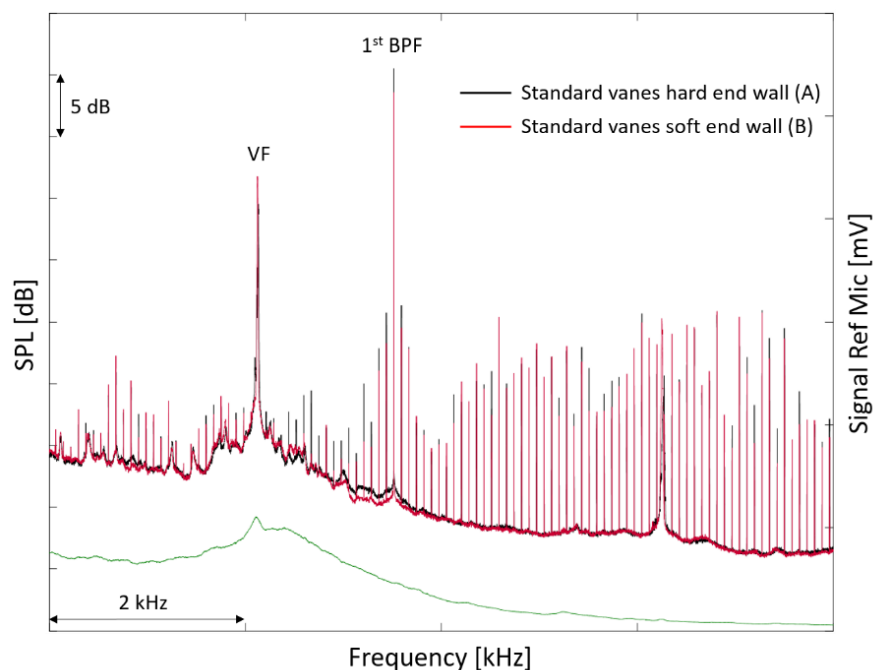


Figure 6.33: Frequency spectra - Configurations (A) and (B)

Figure 6.34 shows the change in overall PWL of all cut-on modes. The highest reduction is at the rotor – TEC interaction mode $m = 18$ with a value of 16.8 dB for the propagation direction equal to the flow direction and 18.3 dB against it. Also the scattered mode $m = -16$ resulting from the rotor – TEC interaction has a high reduction of 9.6 dB in flow direction as well. Mode $m = 5$ shows an increase of 5 dB for configuration (B) and $m = -6$ (one of the dominant modes) and $m = 9$ a decrease in flow direction of 7.8 dB and 9.5 dB respectively (both are rotor – stator interaction modes). Mode $m = 10$, which is one of the dominant modes, is decreased by 2.8 dB in flow direction.

The decrease of the overall PWL including all cut-on modes is 2.3 dB for a propagation in flow direction and 1.9 dB against it.

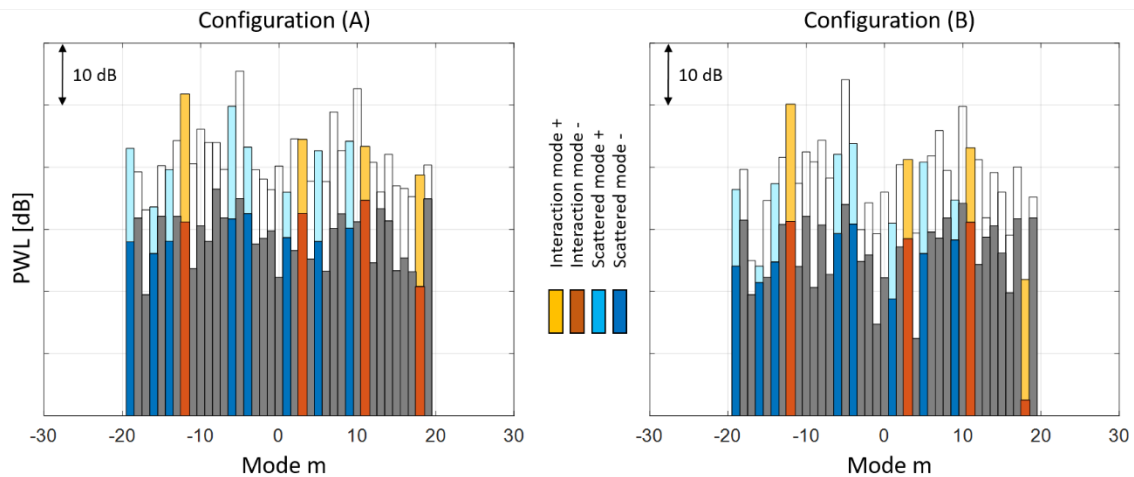


Figure 6.34: Overall PWL comparison - Configurations (A) and (B)

Configuration (C) – 3.8 mm absorber neck diameter

The following comparison is of the configurations (A) and (C). Setup (C) consists of a larger absorber neck diameter compared to configuration (B). This can also be seen when evaluating the reference microphone signal in Figure 6.35, where the maximum is shifted to a higher frequency compared to Figure 6.33. This could be expected due to the theory on which the absorbers are based on. The SPL peak reduction in the same frequency range between the VF peak and the 1st BPF peak can be identified as for configuration (B).

A peak reduction at the 1st BPF of 2.4 dB is achieved, which is higher than for setup (B). It is assumed that this is due to the closer maximum absorption frequency of the absorber and the frequency of interest.

Due to the location of the maximum reference microphone signal and the result obtained for the absorber neck diameter of 3.5 mm, another impedance tube test with a single open neck tube having a diameter of 3.8 mm is done. This results in a resonance frequency of 4144 Hz. Scaling this frequency to the STTF temperature and no flow gives an absorber resonance at 4876 Hz. The calculated value in the test rig without Mach number is 5115 Hz. Comparing the value the maximum of the signal shown in Figure 6.35, which is at 4876 Hz, it can be seen that it is again located between the two mentioned values without Mach number. This could also be observed in the case of the absorber neck diameter of 3.5 mm. Therefore it is assumed, that the resonance frequency is not or only very little affected by the flow Mach number present in the STTF.

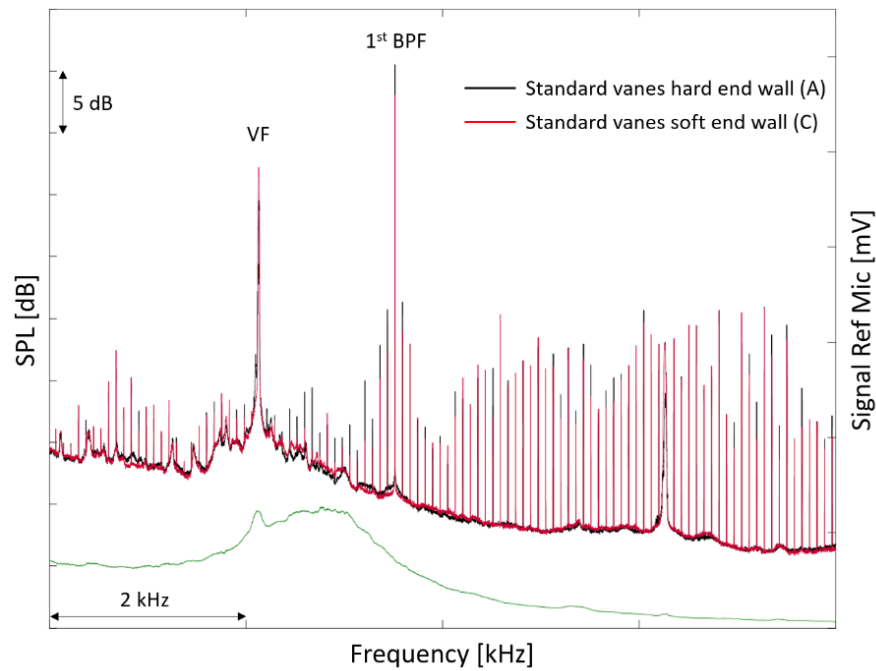


Figure 6.35: Frequency spectra - Configurations (A) and (C)

Equal to configuration (B), also setup (C) results with a value of 12.1 dB in flow direction and 10.4 dB against it in a very high reduction of the interaction mode $m = 18$. Also the scattered mode $m = -6$, which is one of the most dominant modes, has with 5.6 and 8.6 dB in and against flow direction a significant decrease. With a reduction of 14.8 dB propagating in flow direction, the scattered stator – rotor interaction $m = 9$ has the highest one of the modes related to airfoil interactions. The second most dominant mode $m = 10$ results in a 3.8 dB lower value in case of a propagation in flow direction and 3.1 dB against it.

The reduction in overall PWL including all cut-on modes is 2.2 dB for the propagation equal to the flow direction and 2.3 dB against flow direction using configuration (C).

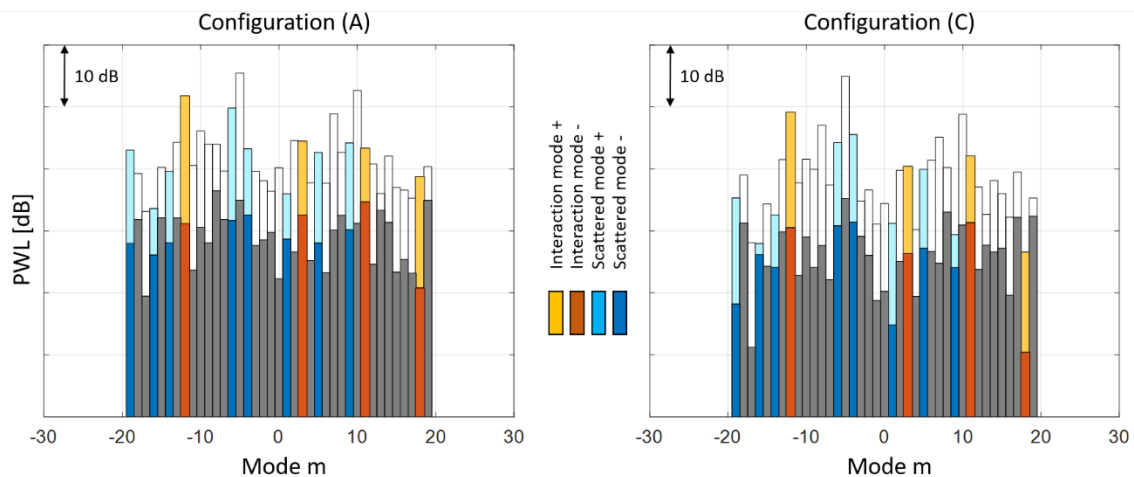


Figure 6.36: Overall PWL comparison - Configurations (A) and (C)

Configuration (D) – 4.2 mm absorber neck diameter

The last comparison of this section is between configuration (A) and setup (D), which is the configuration with the biggest absorber neck diameter investigated in this work. This diameter

is chosen because of the results observed concerning the influence of the flow Mach number onto the resonance frequency. With this diameter, a theoretical resonance frequency of 5593 Hz should be achieved.

Figure 6.37 shows the comparison of the frequency spectra, including also the signal of the reference microphone indicated with the green line. It is again visible, that the resonance frequency is shifted to a higher value due to the increase of the neck diameter. The maximum of the signal is now located at 5445 Hz, which is in the direct vicinity of the frequency of interest. This location also confirms the assumption of not taking the Mach number into account when calculation the absorber resonance in case of a use in the STTF. As seen in the two setups before, the same frequency range between the VF and the 1st BPF concerning a significant peak reduction is visible.

A negative aspect of this configuration is the increase of the background noise in a frequency range of about 3 kHz, with the maximum at the absorber resonance frequency. This behaviour is not observed in any other configuration. In the work of Golliard and Bruggeman [98] they mention, that under certain circumstances, a tonal noise, a broadband noise, or a combination of both can be excited by a flow over a cavity. It is assumed, that the combination of the flow velocity over the opening and the size of the neck diameter is the forcing of this observed increase. But although there is this less advantageous effect, a significant reduction of the peak SPL can be identified. Concerning the target frequency peak, a reduction of 2.5 dB is achieved by using configuration (D).

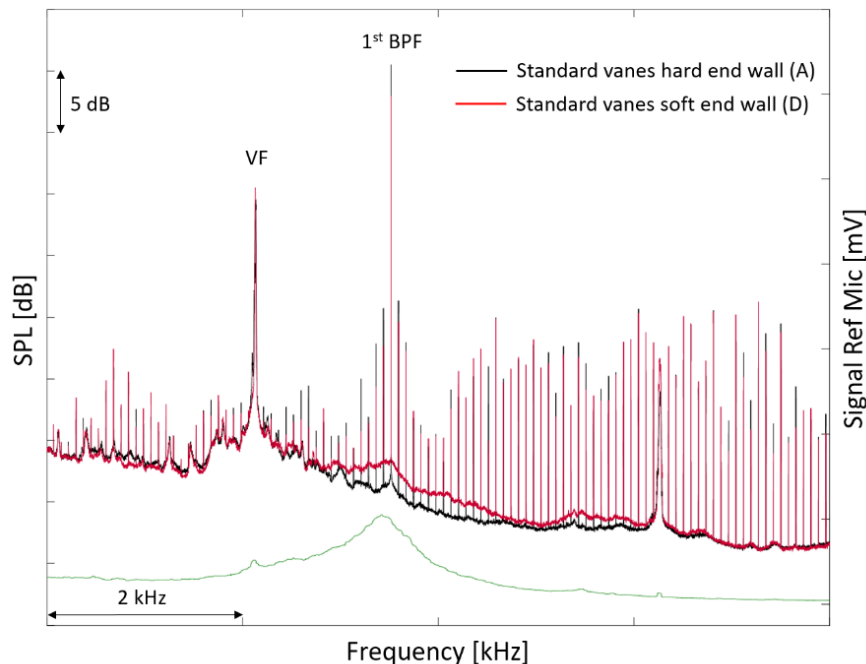


Figure 6.37: Frequency spectra - Configurations (A) and (D)

Figure 6.38 shows the comparison of the overall PWL for each cut-on mode. In case of configuration (D), no significant reduction for mode $m = 18$, as it was observed for the other configurations using soft end walls, can be identified. The other rotor – TEC interaction $m = -12$ on the hand, shows a reduction of 4 dB in flow direction. In the investigated case, this is also one of the most dominant modes and therefore a reduction there has a much higher impact onto the overall PWL reduction. Another dominant mode is the scattered mode $m = -6$, which is reduced by a value of 6.1 dB in and 3 dB against the flow direction.

The maximum reduction of a mode related to the airfoil interactions is achieved for the scattered mode $m = -14$, with a decrease of 12.6 dB in flow direction and 16 dB against it. This is the highest observed reduction for this mode of all investigated setups. The second

highest decrease related to interaction modes is at the scattered rotor – TEC interaction mode $m = 5$. It is with a reduction of 9.7 dB in flow direction another significant one. A high reduction, with 7.6 dB in flow direction, can be seen for the second most dominant mode within all cut-on modes $m = 10$. For the other propagation direction, a reduction of 6.4 dB could be achieved.

The overall PWL including all cut-on modes is decreased by 2.3 dB for soundwaves propagating in flow direction and by 1.6 dB propagating against flow direction, using configuration (D).

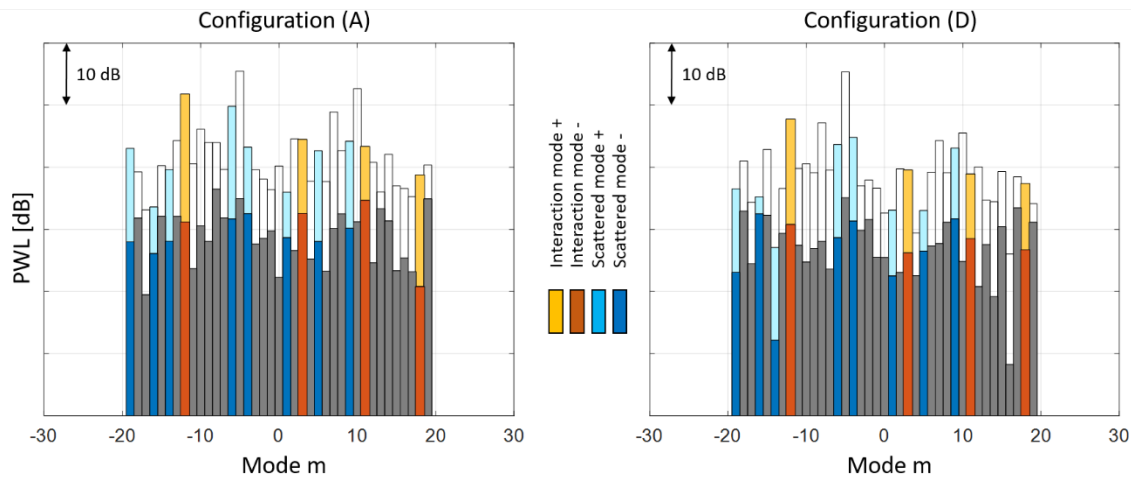


Figure 6.38: Overall PWL comparison - Configurations (A) and (D)

Comparison

The results show that the frequency of interest has a peak reduction in each investigation, rising with increasing neck diameter. This indicates, that although the peak reduction ability of a Helmholtz absorber flattens due to grazing mean flow (see Figure 3.1 in section 3.1, taken from Selamet [52]), it is important to have the absorber resonance frequency as close as possible at the target frequency concerning a reduction.

Figure 6.39 shows a direct comparison of all cut-on modes for the three configurations discussed in this section, concerning the change in sound power level with the propagation direction equal to the flow direction. A negative value indicates a reduction of the PWL using the treated end walls. It can be seen, that especially for the configurations (B) and (C), almost each mode has a reduction compared to the baseline setup (A). Setup (D) shows a small increase at the modes $m = -15, -16, -17, -18$. All configurations have an increase at the modes $m = 6, 17$.

The reduction at mode $m = -14$ is rising with increasing neck diameter from 2.2 dB for configuration (B), over 7 dB using configuration (C), up to 12.6 dB for configuration (D). The same behaviour can be observed by looking onto mode $m = 0$, with a reduction between 4.2 dB and 7.6 dB using a configuration with treated end walls. The most dominant mode $m = -5$ is almost constant for all setups and the second most dominant one $m = 10$ is decreasing in the same manner as seen for mode $m = -14$ and $m = 0$. The values of reduction increase from 2.8 dB (configuration (B)) up to 7.1 dB (configuration (D)).

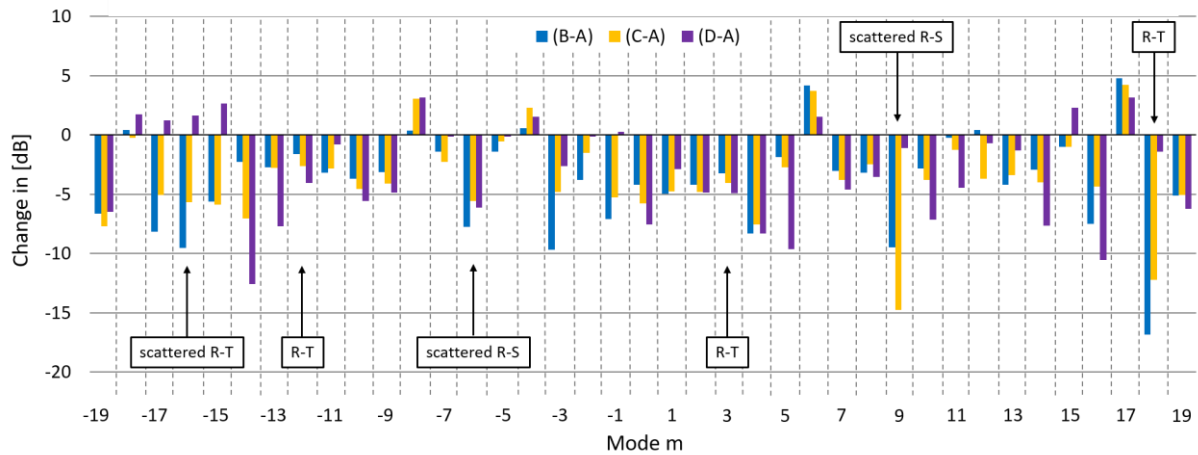


Figure 6.39: PWL^+ change of cut-on modes – Configurations (B), (C), and (D)

Figure 6.40 gives an overview of the changes in PWL concerning the propagation against the flow direction. Also here, configuration (D) shows a high increase at modes $m = -16, -17, -18$. In addition, the modes $m = 15, 17, 18$ are increased for this direction of propagation. There is again an increase at mode $m = 6$ for all three setups including the Helmholtz absorbers in the end walls, as already seen for the propagation in flow direction.

The scattered rotor – TEC interaction mode $m = -14$ has a similar PWL reduction as already seen for the propagation in flow direction. It is increasing with growing neck diameter, from 4 dB using configuration (B) up to 15.9 dB in case of setup (D).

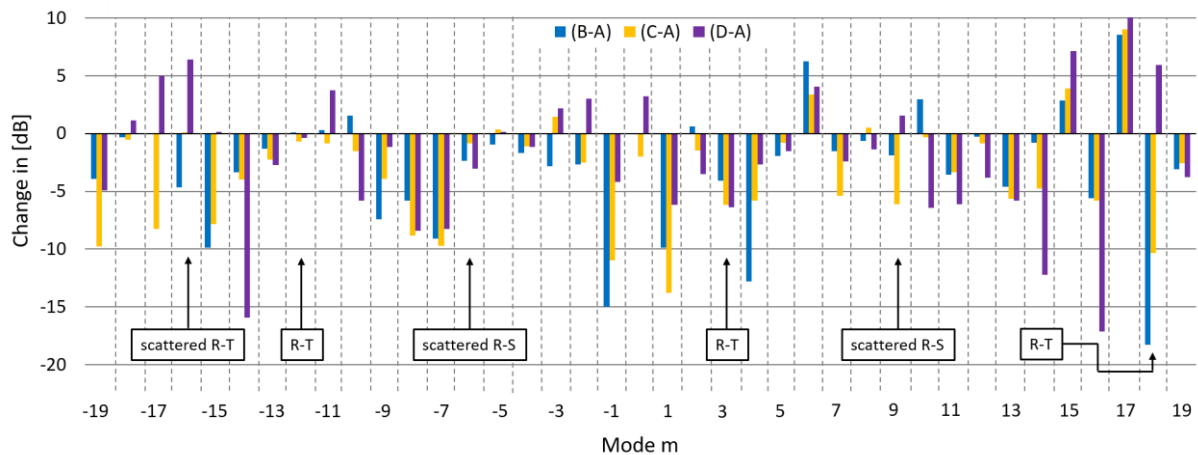


Figure 6.40: PWL^- change of cut-on modes – Configurations (B), (C), and (D)

Aerodynamics

The following Figure 6.41 shows again the distribution of the three aerodynamical parameters total pressure downstream of the TEC related to the stage inlet total pressure, Mach number, and yaw angle. All values are circumferentially mass averaged and each parameter is drawn over the relative channel height.

Mach number as well as normalized total pressure distributions give not much of a difference between all setups. Solely the baseline configuration (A) shows again a stronger lean to smaller values with respect to the other cases, as was already observed in Figure 6.25 dealing with the configurations using Helmholtz vanes.

Concerning the yaw angle distribution, a shift towards more negative values at the outer casing and a shift to more positive values on the inner casing can be identified for the setup (C). The reason for this is due to a measurement error in an area which can be identified with the

white zone in Figure 6.42. As can be seen, a large area of high yaw angle, visible in the other configurations, is missing in the tip region and therefore the averaged values are lower. In the hub region, a large area of low values is missing. These missing values have not such a big influence in the remaining area away from the tip and the hub regions because there they are almost constant over a circumferential measurement line (again comparing with the other three configurations shown in the same figure).

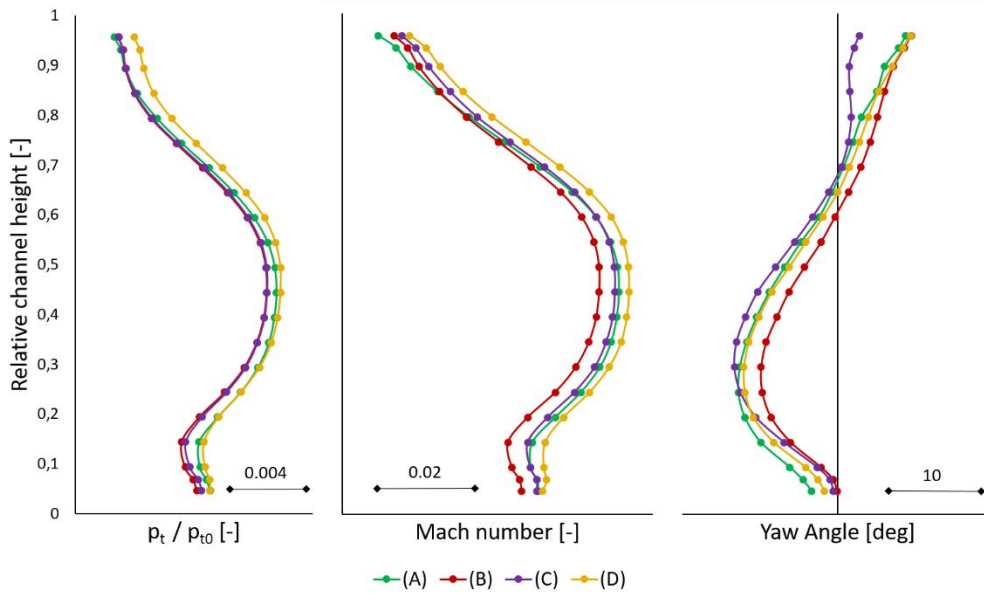


Figure 6.41: Aerodynamical comparison - Configurations (A), (B), (C), and (D)

Figure 6.42 shows the comparison of the measured flow fields for all four configurations. The wake is indicated with the black dashed line having the vane suction side on the left, and the pressure side on the right. As already mentioned above, the white zone of yaw angle for configuration (C) is due to a measurement error and therefore the values are not depicted here.

No big difference concerning the normalized total pressure can be identified for the examined cases. The yaw angle of setup (B) shows higher values on the whole vane suction side compared to all other setups depicted here.

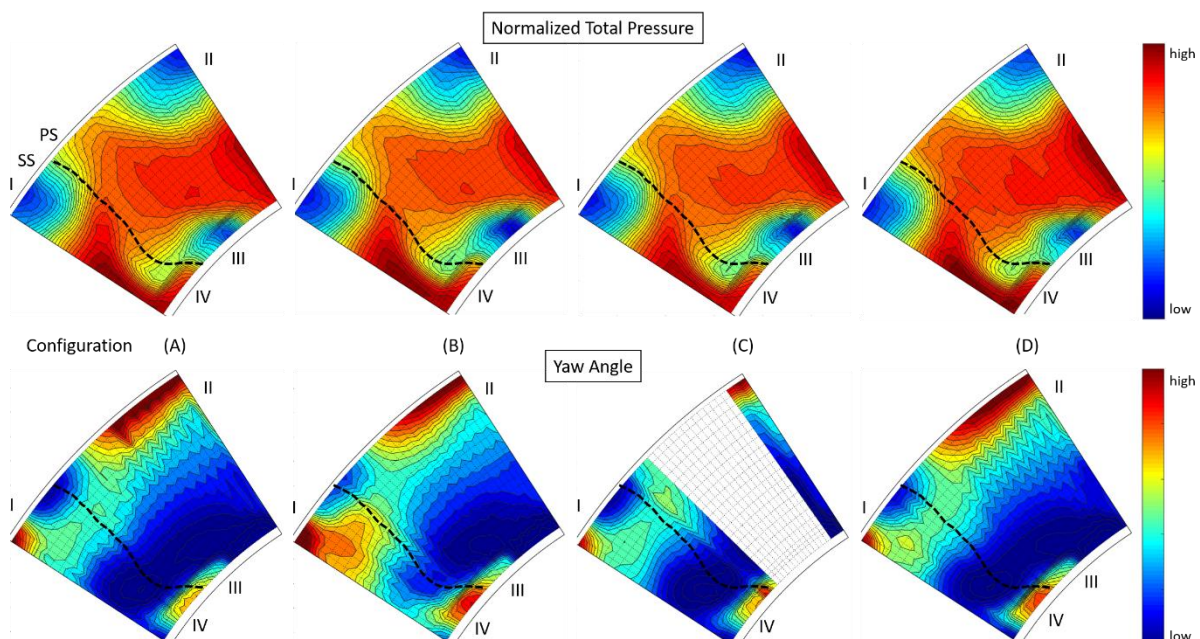


Figure 6.42: Aerodynamical flow fields – Configurations (A), (B), (C), and (D)

6.2.2.2 Leaned Vanes

This section is about the combination of the Leaned vane design and the soft end walls with the second biggest diameter (configuration (J)). The results are compared with the respective hard end walls setup (I).

Acoustics

Figure 6.43 shows the comparison of the baseline configuration (I) indicated in black and (J) in red. The green line is again the reference microphone signal placed inside the absorber cavity. It is clearly visible, that in the frequency range where the reference microphone signal has its maximum, also the noise attenuation is the highest. Peaks in a frequency width of around 1.5 kHz are reduced almost down to the background noise level. The second small peak of the signal is due to the response onto the vibration peak and is unrelated to the absorber performance.

Additionally, a reduction outside of this frequency range can be identified, with a reduction of the target frequency (1st BPF) of 2 dB.

In the vicinity of the vibration frequency peak and its first harmonic, a decrease in SPL of the background noise can be identified. This result is not observed for any other configuration throughout this thesis.

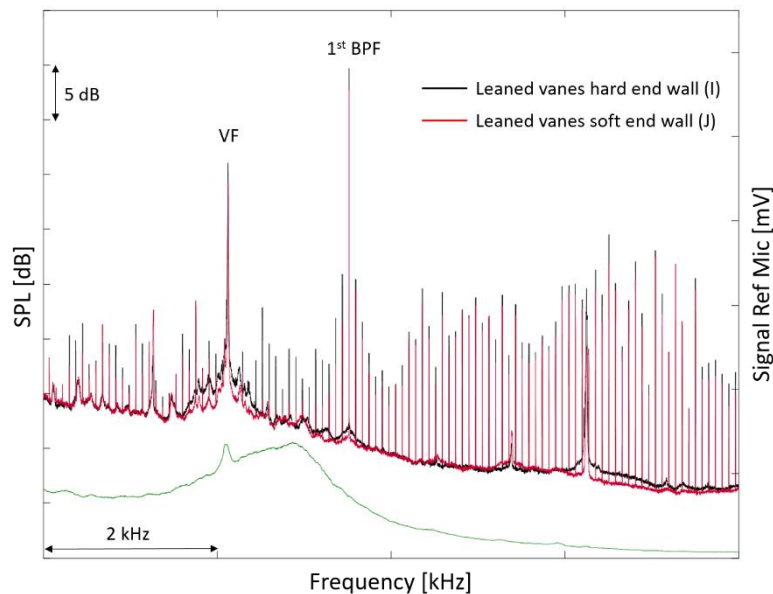


Figure 6.43: Frequency spectra - Configurations (I) and (J)

Figure 6.44 shows the overall PWL for both cases in and against flow direction. Only the rotor – TEC interaction mode $m = 3$ has a reduction of 3 dB in flow direction and 6 dB against it, while the two others ($m = -12$ and $m = 18$) are constant. The highest reduction is caused at scattered modes especially at mode $m = -16$ with -15.6 dB in flow direction and 12.6 dB in the opposing direction using soft end walls.

It can be seen, that there is a change in the dominant modes using Leaned vanes compared to the Standard vanes. Mode $m = -5$ is no longer the most dominant mode but changed now with $m = 10$ concerning this contribution. This is due to a reduction by 8 dB in flow direction when using the Leaned vanes design compared to the Standard design. As a reason for this, a change in the mode scattering due to the lean of the vane, compared to the Standard vanes, can be addressed.

Both mentioned modes show an increase in flow direction of 3.8 and 1.4 dB respectively when using setup (J) with respect to (I). Nevertheless, comparing the overall sound power level

of both configurations, a decrease of setup (J) by 0.9 dB in flow direction and 2.7 dB against flow direction could be achieved.

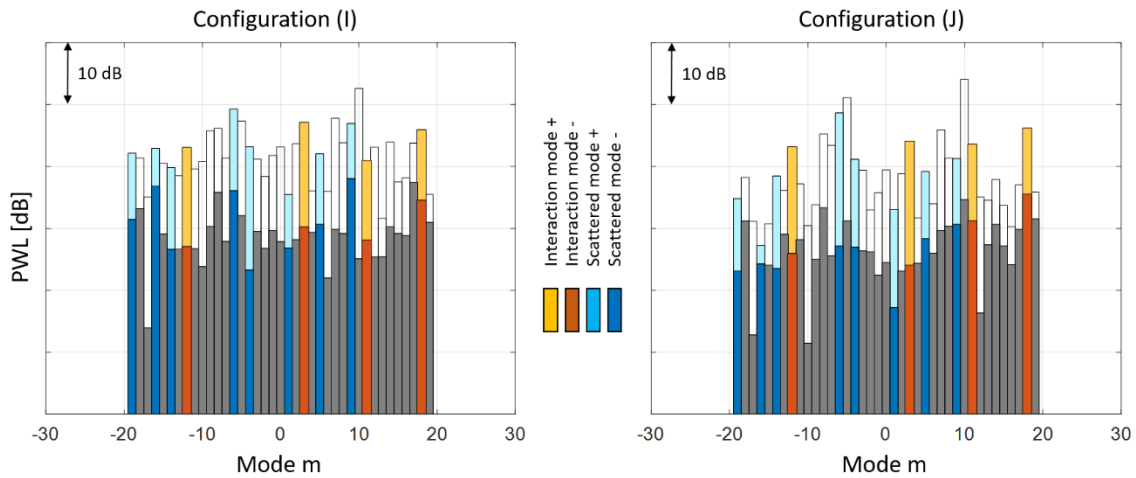


Figure 6.44: Overall PWL comparison - Configurations (I) and (J)

Figure 6.45 gives a direct comparison between the two setups (I) and (J) concerning the sound power level change in and against flow direction of all cut-on modes. The negative values indicate a reduction of the PWL when using the configuration including the soft end walls. It is clearly visible, that the majority of cut-on modes could be reduced concerning their sound pressure level. Solely mode $m = 10$ shows a high increase of almost 10 dB, investigating the propagation direction against the flow direction.

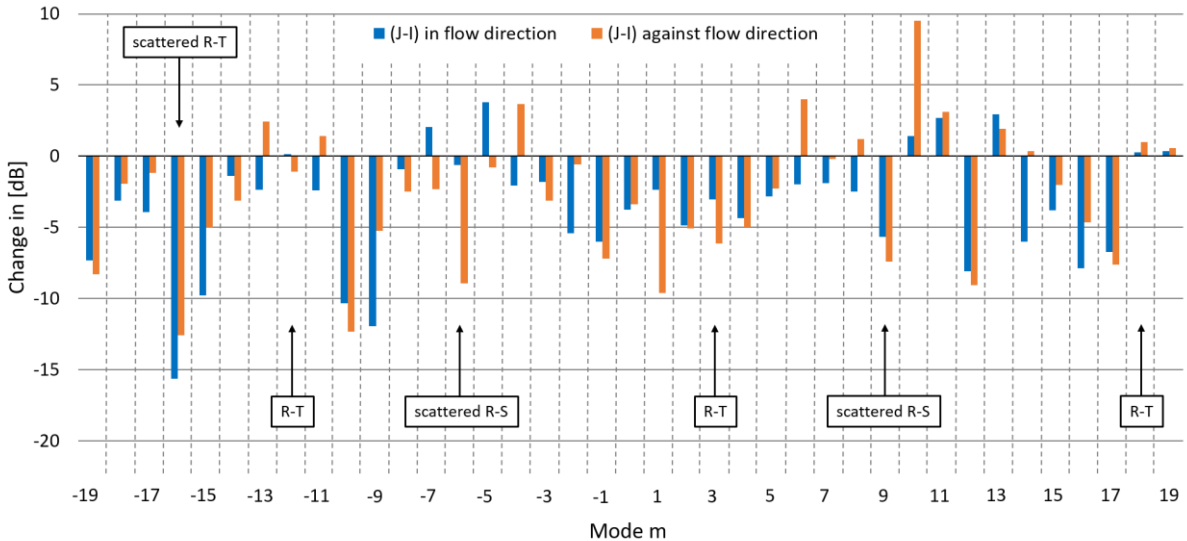


Figure 6.45: PWL[±] change of cut-on modes – Configuration (I)

Aerodynamics

A comparison of aerodynamical parameters downstream of the TEC is shown in Figure 6.46 between the reference setup (I) in green and the configuration (J) in black.

It can be clearly seen, that both setups are identical in case of the normalized total pressure as well as in Mach number distribution. Both configurations are congruent over the whole relative channel height. The yaw angle shows only minor differences between the two setups, especially in the region from 20 up to 80% of the flow channel, with a maximum deviation of

2 deg. This is due to the measurement uncertainty of the used probe traverse. These results indicate, that there is no change due to the use of the absorbers included into the duct end walls, which can be detected using a FHP.

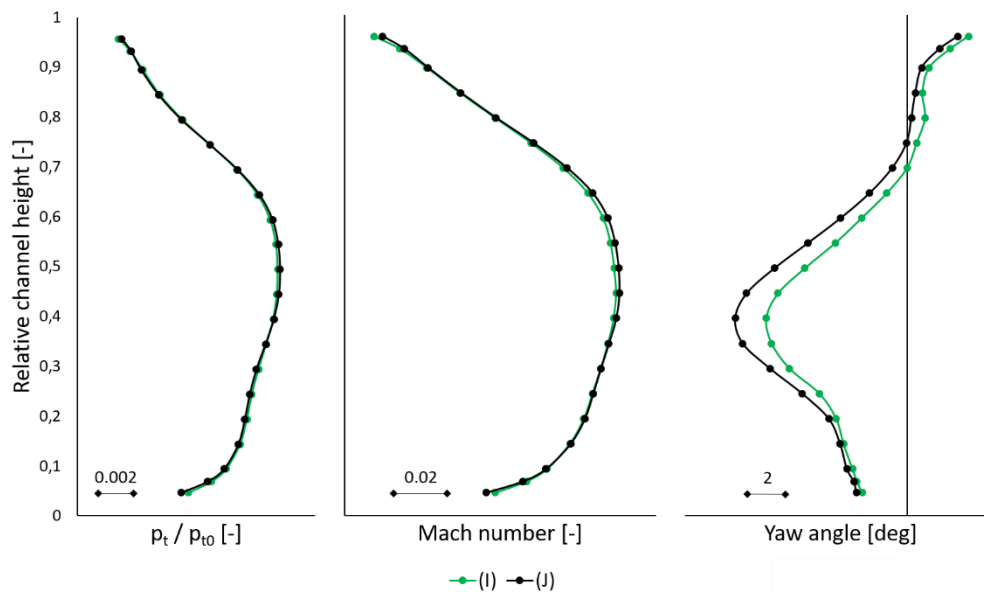


Figure 6.46: Aerodynamical comparison - Configuration (I) and (J)

In the following figure, the aerodynamical parameters total pressure normalized by the total pressure at stage inlet and the yaw angle of the whole measured flow field can be seen. The vane wake is indicated by the black dashed line and one can clearly see the strong lean against the rotor rotational direction. On the vane pressure side and marked with III, a region with low normalized total pressure can be identified, which is due to the cross passage flow on the inner duct casing. The upper casing is again dominated by the low normalized total pressure due to the upper passage vortex marked with II.

From the yaw angle it can be seen, that there is a migration of fluid on the suction side of the vane from the outer casing into midspan direction (indicated by the positive values close to mark I). This is a result from the superposition of the impact by the rotor tip leakage flow (migration of fluid from the vane pressure side to the suction side on the outer casing), the upper passage vortex and the pressure gradient due to the vane lean. (see also Selic [36])

As already observed in the results of the other investigated configurations, no big differences between the reference setup (I) and the configuration including soft end walls (J) can be identified. Both look almost identical in shape and level.

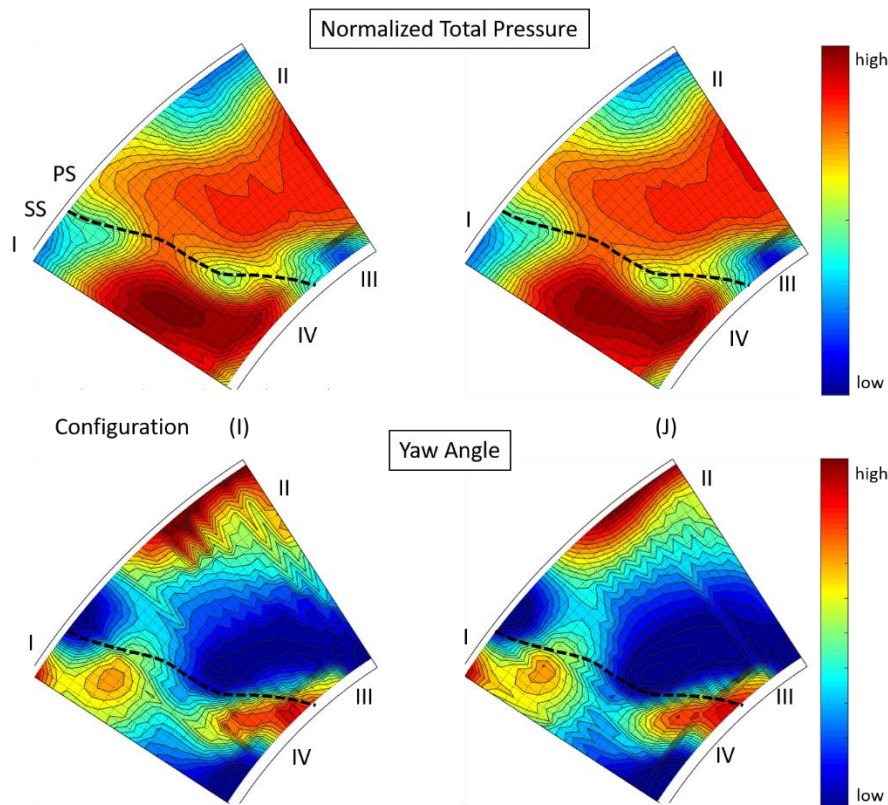


Figure 6.47: Aerodynamical flow fields – Leaned vane design

6.2.3 Combination of Helmholtz Vanes and Soft End Walls

For a maximum noise attenuation, as much surface as possible, should be covered with acoustic liners. Therefore, a combination of both, the soft end walls and the Helmholtz vanes is also investigated.

Acoustics

Figure 6.48 shows the comparison of the frequency spectra concerning configurations (A) and (H). As seen also with the soft end walls combined with hard wall vane designs, there is a region of SPL reduction close to the target frequency. This is now added up with the peak reduction using the Helmholtz vanes.

It is also visible, that the reduction of the background noise when using those Helmholtz vanes is not happening anymore like it could be seen in section 6.2.1. This was already observed in the studied cases using only the soft end walls in section 6.2.2. It is assumed now that the lined end walls cancel out this effect. But they also don't worsen the background noise level. The peak reduction at the frequency of interest (1st BPF) is 2.9 dB and therefore a significant improvement. It is the highest change concerning the peak value of all investigated setups within this thesis.

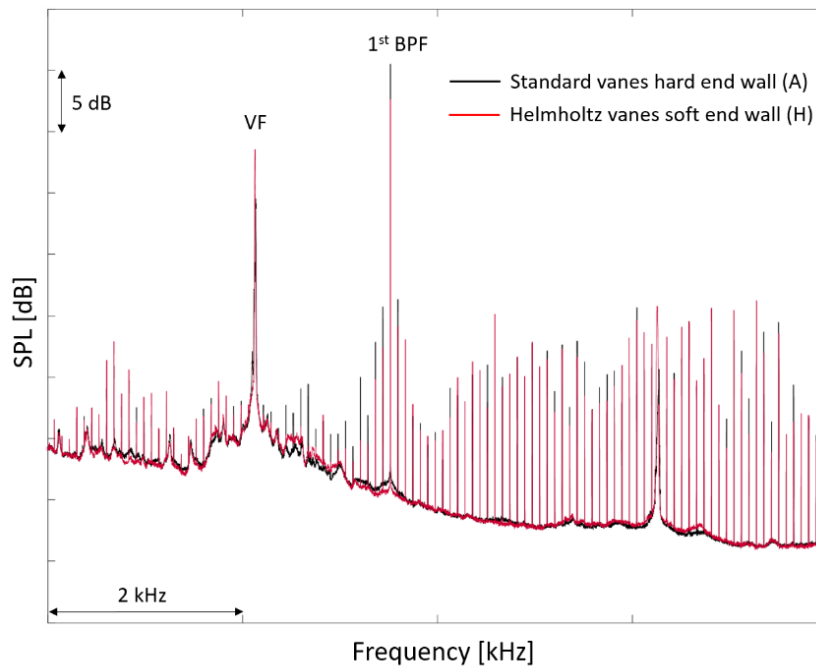


Figure 6.48: Frequency spectra - Configurations (A) and (H)

Figure 6.49 depicts the comparison of the overall PWL concerning all cut-on modes. It can already be seen that a lot of mode amplitudes are changed. As already examined in the comparisons concerning configurations using Helmholtz vanes (see section 6.2.1), also here mode $m = 5$ has with a reduction of 11.5 dB in flow direction the highest one amongst all others. It is followed by the scattered mode $m = -19$ with a decrease of 10.8 dB again in flow direction. Also the other scattered rotor – TEC interactions show a high decrease between 5 and 9.6 dB. Concerning the interaction modes themselves, only $m = 18$ and $m = 11$ have a significant reduction with 7.7 dB and 4.8 dB in flow direction and 7 dB and 5.3 dB against flow direction respectively. The scattered modes $m = -6, 9$ resulting from the rotor – stator interactions are decreased by 7.4 and 9.4 dB in flow direction. Mode $m = 10$ with the second highest contribution to the overall PWL is decreased by a value of 5.3 dB in flow direction and 2 dB against it.

The overall PWL including all cut-on modes is reduced by 2.3 dB for both, the sound waves propagating in and against flow direction.

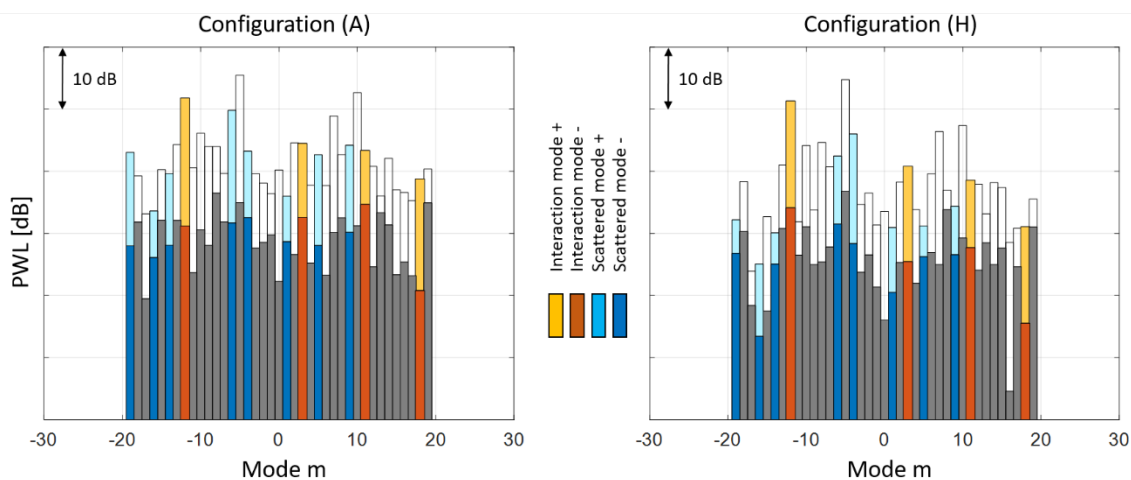


Figure 6.49: Overall PWL comparison - Configurations (A) and (H)

A direct comparison of the sound power level for each mode order m between the two configurations is given in Figure 6.50. It shows the difference in dB for all cut-on modes in flow direction, indicated by the blue bars, as well as against flow direction, depicted by the orange bars. Herein, the positive effect of using Helmholtz absorbers can be clearly seen. Only few modes show an increase using the absorbers compared to the hard wall reference setup, mainly against the flow direction.

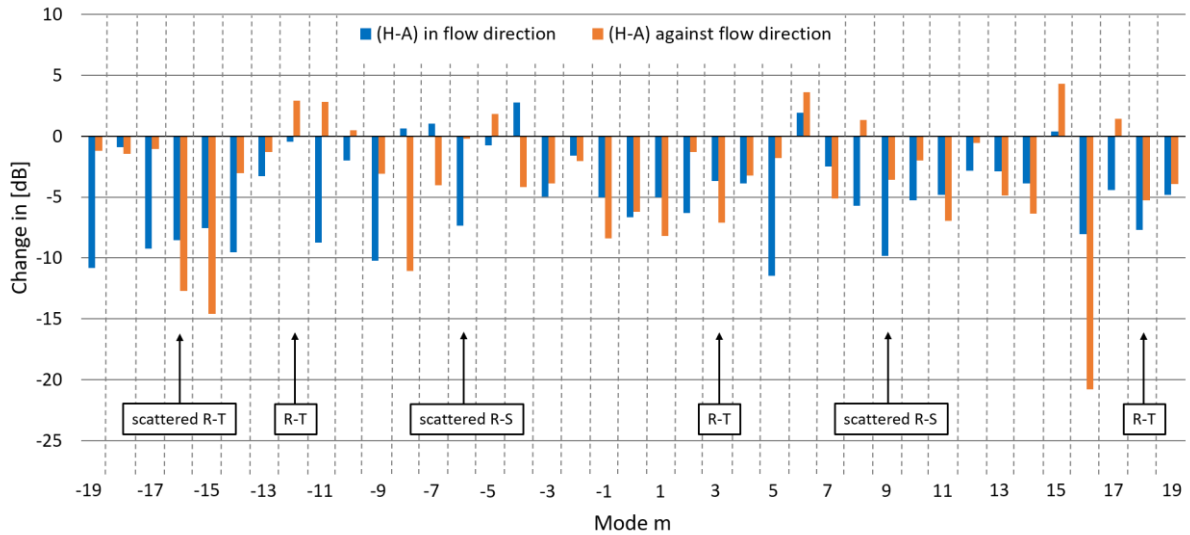


Figure 6.50: PWL^{\pm} change of cut-on modes – Configuration (H)

Aerodynamics

In Figure 6.51, the aerodynamical comparison of both setups can be seen. All dots represent circumferentially mass averaged values.

In the normalized total pressure as well as in the Mach number distribution, the deviation of the baseline configuration (A) close to the hub can be again identified as already seen in Figure 6.25 showing the comparison of all the setups using Helmholtz vanes.

The yaw angle plot indicates a small difference in the region starting at about 50% relative channel height up to the outer casing.

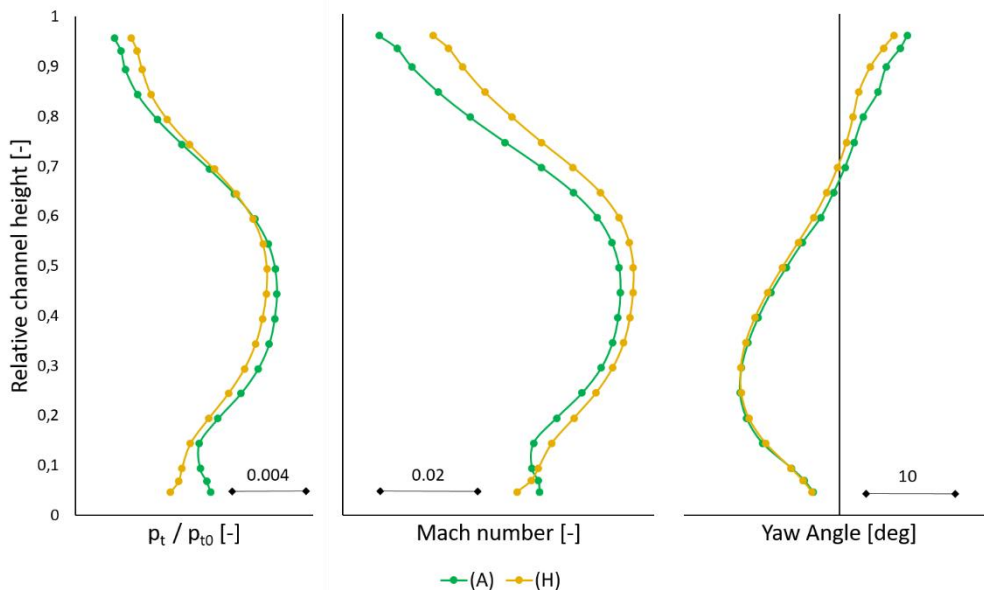


Figure 6.51: Aerodynamical comparison - Configurations (A) and (H)

The results of the measured flow fields of the normalized total pressure and the yaw angle can be seen in Figure 6.52. From a shape point of view, there is almost no difference between these two cases. Area I shows a slightly lower normalized total pressure concerning configuration (A). In zone II, the normalized total pressure shows higher values for setup (A) with respect to (H). The main difference can be seen when comparing the area between the markers III and IV directly at the intersection of the vane wake and the inner casing. Here setup (H) indicates an additional zone of lower total pressure, following the indicated wake.

The yaw angle is almost identical except in area IV, which is a little bit smaller in circumferential direction in case of configuration (H).

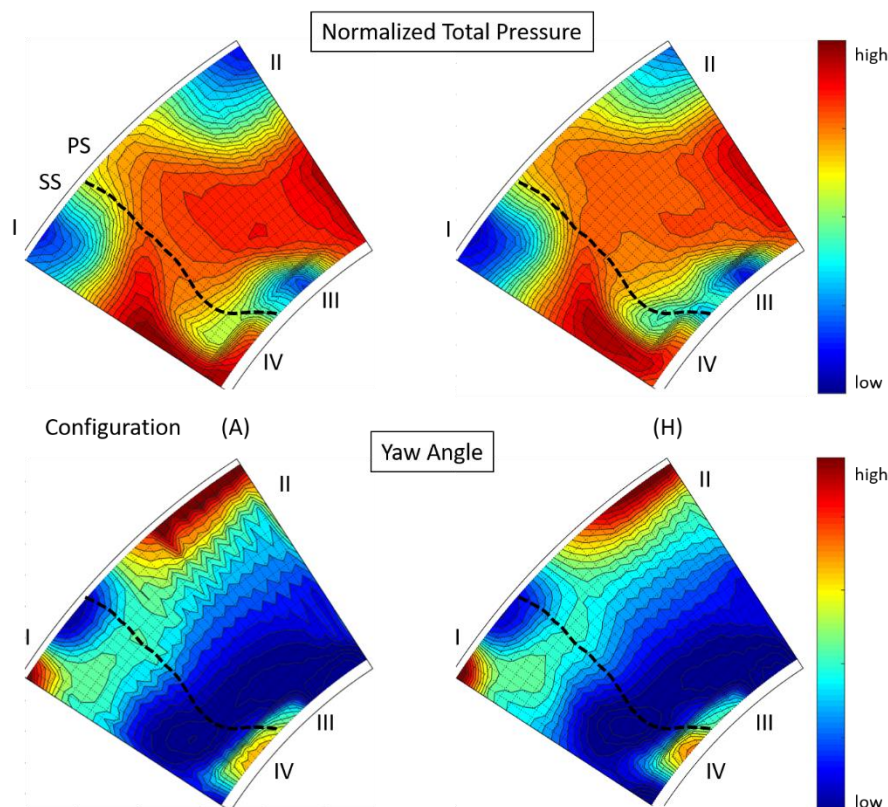


Figure 6.52: Aerodynamical flow fields – Configurations (A) and (H)

It can be concluded, that there is no obvious change of the flow field due to the presence of openings in the duct end walls and vane suction surface, which can be identified with the used measurement probe.

6.2.4 Resonator Vanes

This section is about the second vane design including acoustic absorbers combined with acoustically hard end walls.

Acoustics

In Figure 6.53, the two frequency spectra of the hard end wall baseline configuration (A) and the one with the Resonator vanes (K) are shown. It is visible, that there is again the broadband reduction of the background noise in the same area as already observed for the configurations using the Helmholtz vanes. It is again assumed, that this reduction is due to the

directed roughness of the vane surface due to the additive manufacturing process. Additionally, there is a decrease in SPL at many peaks over a wide frequency range. This reduction is according the theory behind this kind of absorber, to reduce noise over a wide range. The reduction at the frequency of interest is 1.1 dB in case of configuration (K). Nevertheless, an increase of the broadband noise in the vicinity of the vibration frequency and its second harmonic can be identified. According to [96] this vibration frequency is an eigenfrequency of the used rotor disc. It is assumed, that the observed increase is due to an interaction between the aerodynamics and acoustics.

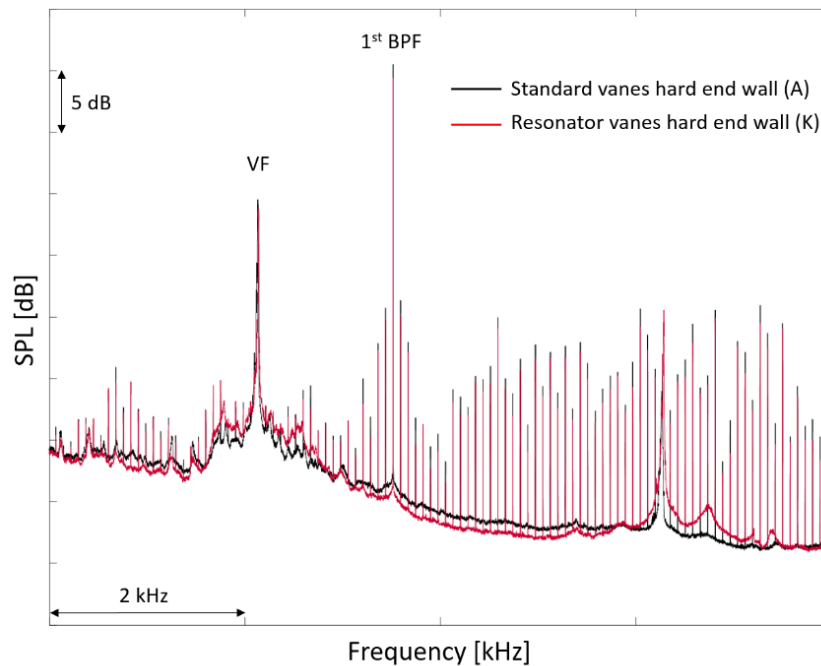


Figure 6.53: Frequency spectra - Configurations (A) and (K)

A comparison of the sound power level concerning all cut-on modes in Figure 6.54 shows the highest reduction at the scattered mode $m = -16$, with 9.5 dB in flow direction. All other modes of interest show also a decrease of the sound power level, besides the rotor – TEC interaction mode $m = 18$. This mode has increased by 4.6 dB in flow direction and by even 12.4 dB in the opposing one using configuration (K). One of the dominant modes, $m = 10$ which is not related to an interaction, decreased by 3.8 dB in flow direction. Also mode $m = -6$ which is another dominating one achieved a reduction of 5.3 dB in flow direction but an increase of 2.7 dB against the flow direction.

The overall PWL including all cut-on modes is decreases by 1.9 dB concerning the propagation direction in flow direction and does not change against flow direction for the acoustically treated setup (K).

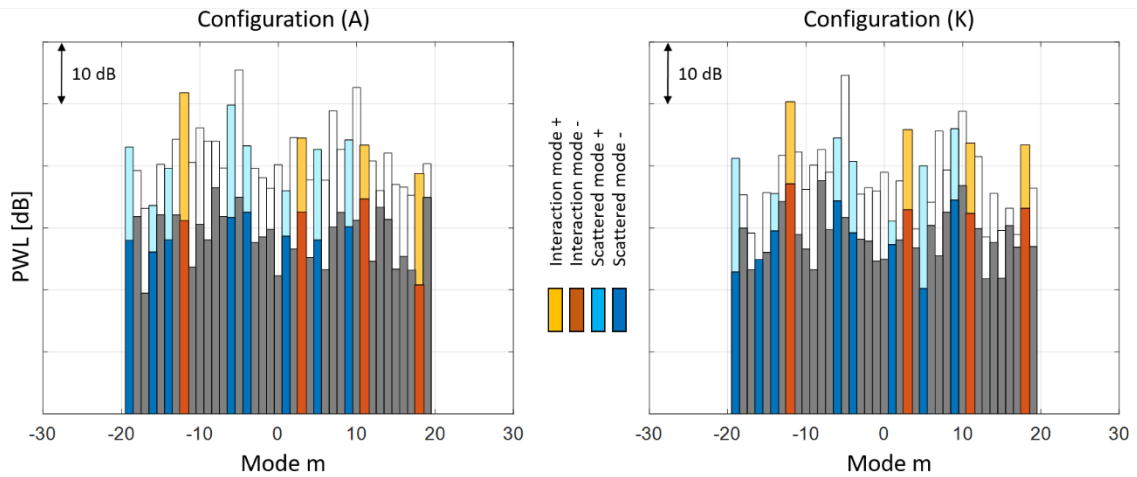


Figure 6.54: Overall PWL comparison - Configurations (A) and (K)

The following figure gives a direct comparison of the PWL in (blue bars) and against flow direction (orange bars) of the two configurations. It can be seen, that in case of the propagation against flow direction, many modes have an increase concerning setup (K) with respect to the baseline configuration (A). Especially the rotor – TEC interaction mode $m = 18$ has with 12 dB a significant rise propagating against the flow direction but also an increase in flow direction. Also the configurations (D) and (E) showed an increase at this crucial mode, for a wave propagation against the flow direction. With a small increase at mode $m = 3$ in flow direction and with 6 dB another one against flow direction for mode $m = -12$, all three rotor – TEC interaction modes have a more or less significant rise using this configuration (K). It is again because of the impingement of the rotor wake on the TEGV surface at the location of the neck openings (see section 6.2.1). Still, the decrease achieved at the other acoustic modes results in the already mentioned reduction of the total sound power level of 1.9 dB in flow direction. It is assumed that especially the reduction of mode $m = 10$ is the reason for this result, because it is one of the dominant modes as could be seen in Figure 6.54.

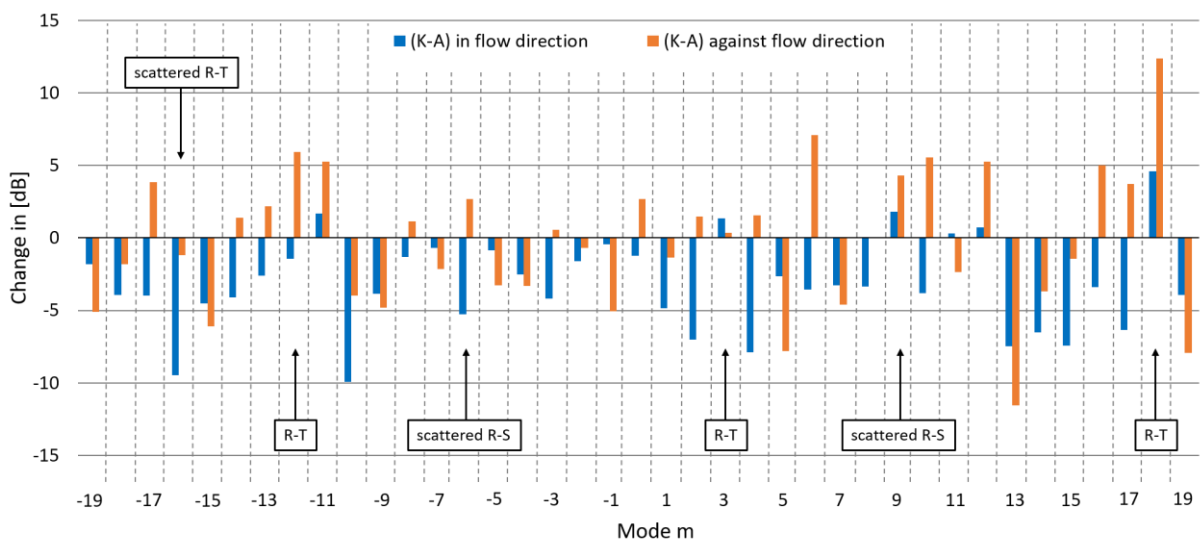


Figure 6.55: PWL^{\pm} change of cut-on modes – Configuration (K)

Aerodynamics

Figure 6.56 shows once more the circumferentially mass averaged radial distributions of the already known aerodynamical parameters. Both presented setups are again of good accordance for all three parameters. With a maximum difference of 0.002 concerning the normalized total pressure, this deviation can be neglected as well as the one for the Mach number distribution (maximum difference of 0.007). Concerning the yaw angle, a maximum deviation of 1.6 deg can be identified, which can be a result of setting the FHP and its uncertainty.

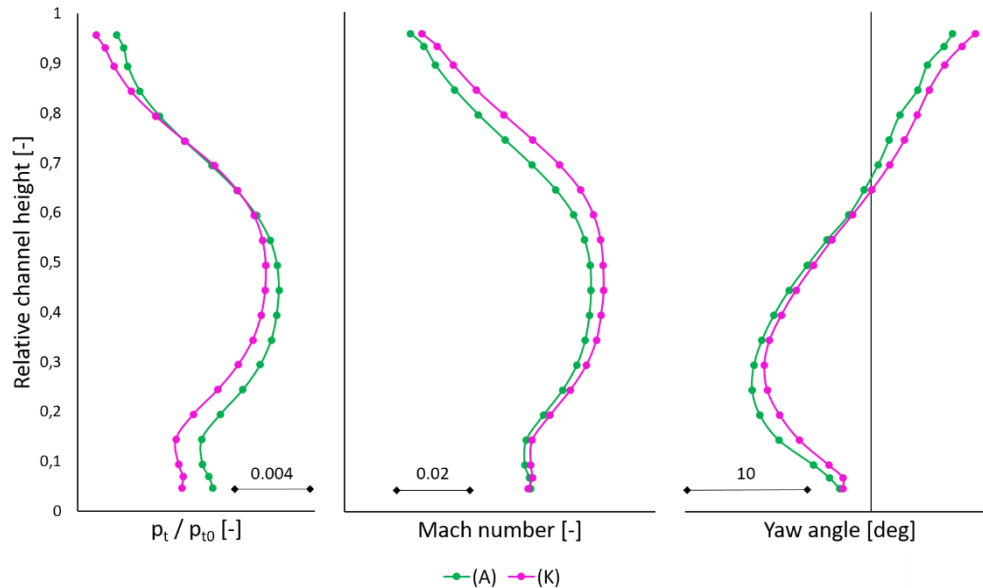


Figure 6.56: Aerodynamical comparison - Configurations (A) and (K)

The measured flow field of the normalized total pressure and the yaw angle for both configurations can be seen in Figure 6.57. Also here, no big changes between the two setups can be identified.

Area I at the outer casing has a lower level of total pressure in case of configuration (A) but is a little bit larger in circumferential direction compared to setup (K). The zone at the inner casing marked with III shows a higher level and a bigger extension in circumferential direction concerning configuration (K).

Looking at the yaw angle, the only difference can be identified close to area I at the intersection of the vane and the outer casing. This area shows a lower level for configuration (A).

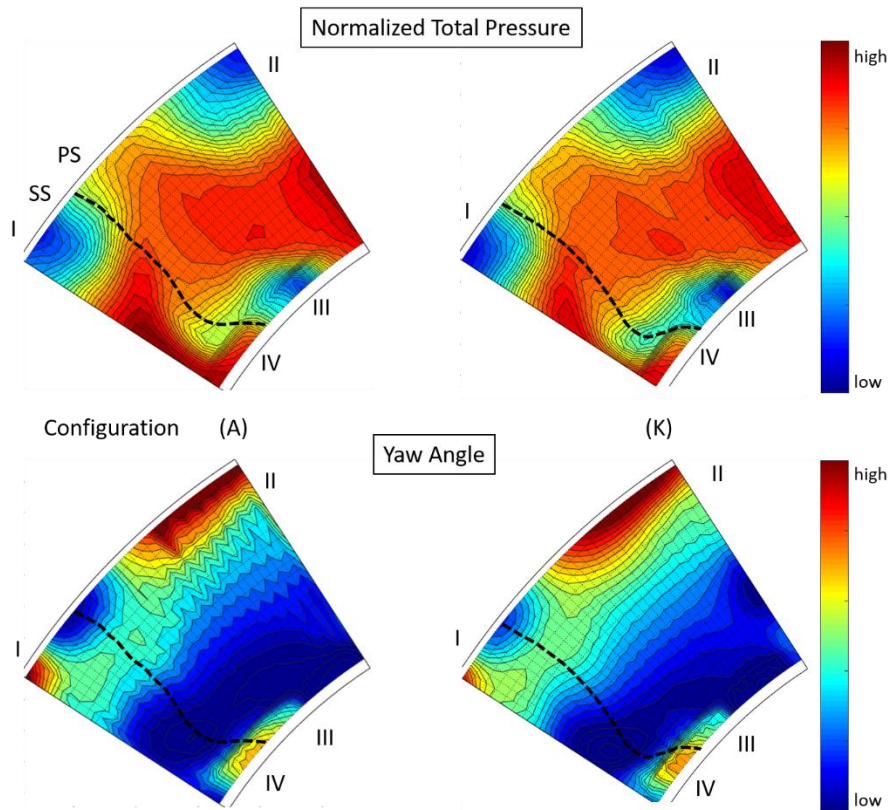


Figure 6.57: Aerodynamical flow fields – Configurations (A) and (K)

Figure 6.58 gives a comparison of the wake profile measurements between the configurations (A), (G), and (H), taken directly downstream of the vane trailing edge. So the baseline setup, the one including Helmholtz vanes combined with hard end walls, and the Resonator vanes. It can be seen, that the baseline configuration (A) has a little bit lower normalized total pressure minimum with respect to the other two cases. While the pressure side distribution is almost identical, a difference can be detected on the suction side slope. Both configurations including the additive manufactured vane designs show a kink close to the minimum in total pressure resulting in a flatter slope compared to the one of configuration (A).

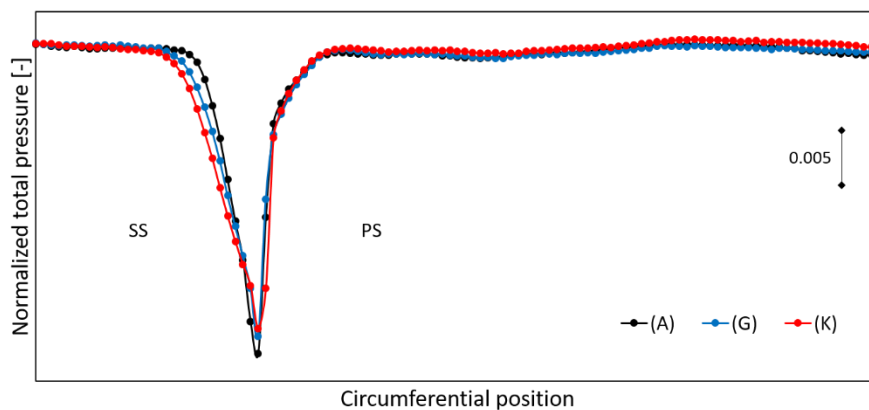


Figure 6.58: Comparison of vane wake measurements - Configurations (A), (G), and (K)

The following Table 6.5 gives a comparison of the aerodynamical parameters wake width, momentum thickness, energy thickness, and displacement thickness for the setups (A), (G), and (K). The parameters are obtained by evaluating the vane wake measurement according to the procedure from Schobeiri and John [34] explained in section 2.3.3. Both vane designs (G) and

(K) having openings in the vane suction side show an increase of the wake width with respect to the baseline configuration (A). A reason for this could be the higher surface roughness of both designs due to the manufacturing process. Also Zhang et al. [99] showed an increase of the wake width with an increase of the surface roughness on a turbine vane.

Table 6.5: Aerodynamic parameters - Configurations (A), (G), and (K)

	Configuration			Change to (A) in [%]	
	(A)	(G)	(K)	(G)	(K)
Wake width [m]	0.00294	0.00298	0.00347	1.4	18.0
Momentum thickness [m]	0.00112	0.00146	0.00153	30.4	36.6
Energy thickness [m]	0.00192	0.00249	0.00252	29.7	31.3
Displacement thickness [m]	0.00165	0.00256	0.00281	55.2	70.3

6.2.5 Acoustical Comparison of Lined Configurations

In this section, an overall acoustical comparison between all configurations including acoustic liners is presented. First, a comparison of the attenuation potential of the airfoil interaction modes and their scatter modes is shown because these are the most interesting ones concerning a change of the turbine exit casing. Each shown circumferential mode is given the sum of all radial modes. Secondly, a closer investigation concerning a change of the overall PWL focused on the mode spinning direction is done. Both examinations are performed for a propagation direction in and against the flow direction separately.

Airfoil interaction modes and their scattered modes

Figure 6.59 gives an overview of the PWL change in flow direction of the mentioned modes. All setups with included acoustic liners, excluding the ones with Leaned vanes which are shown later, are compared with the respective baseline design (A). It can be seen, that almost all modes are significantly reduced with the presence of a lined section. Especially the rotor – TEC interaction mode $m = 18$ and the scattered rotor – stator interaction $m = 9$ show a high potential in decreasing the PWL by using soft end walls (configurations (B), (C), and (H)). It can also be seen, that the attenuation of the modes follows a parabolic pattern with the maxima located at the highest order modes. Such an effect is also mentioned in the work of Motsinger and Kraft [100], in which they state the higher propagation angle between the wave front and the duct axis of higher order modes as a reason for this behaviour. This higher angle leads to an increased number of impingements between the acoustic wave and the treated duct walls and hence to a reduction of the acoustic power with each impact. Also [15] stated that the attenuation is different for each mode. They mentioned that, the higher the order, either radial or azimuthal, the higher the attenuation gets. The reason is that at higher modes the energy is concentrated close to the wall and therefore in the vicinity of the duct treating.

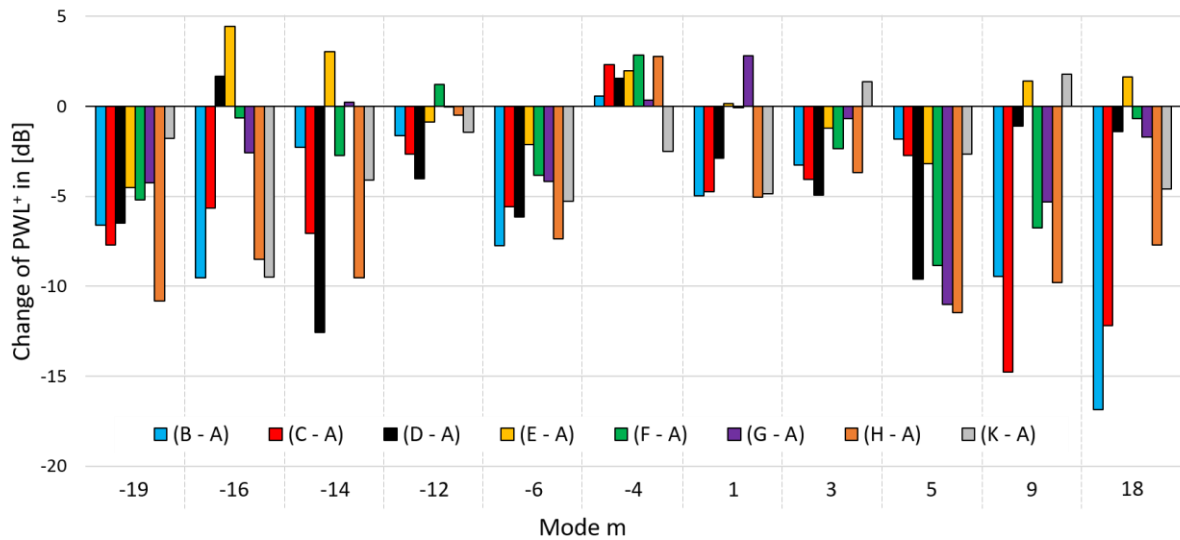


Figure 6.59: PWL⁺ change of interaction modes and their scatted modes – Standard, Helmholtz, and Resonator vane designs

Figure 6.60 presents the same results as above but concerning a wave propagation direction against the flow direction. Again, the mode $m = 18$ shows a high decrease for the setups with the soft end walls. On the other hand, configurations including absorber vanes depict a significant increase of the PWL at this mode. But it can also be seen that this increase shows an inverse behaviour to the diameter of the absorber neck. Configuration (K) with the smallest diameter (<1 mm) depicts the highest rise in sound power level at mode $m = 18$. The modes $m = 5$ and $m = -19$, which had a significant decrease for all configurations at a propagation direction equal to the flow direction, show now only small reductions.

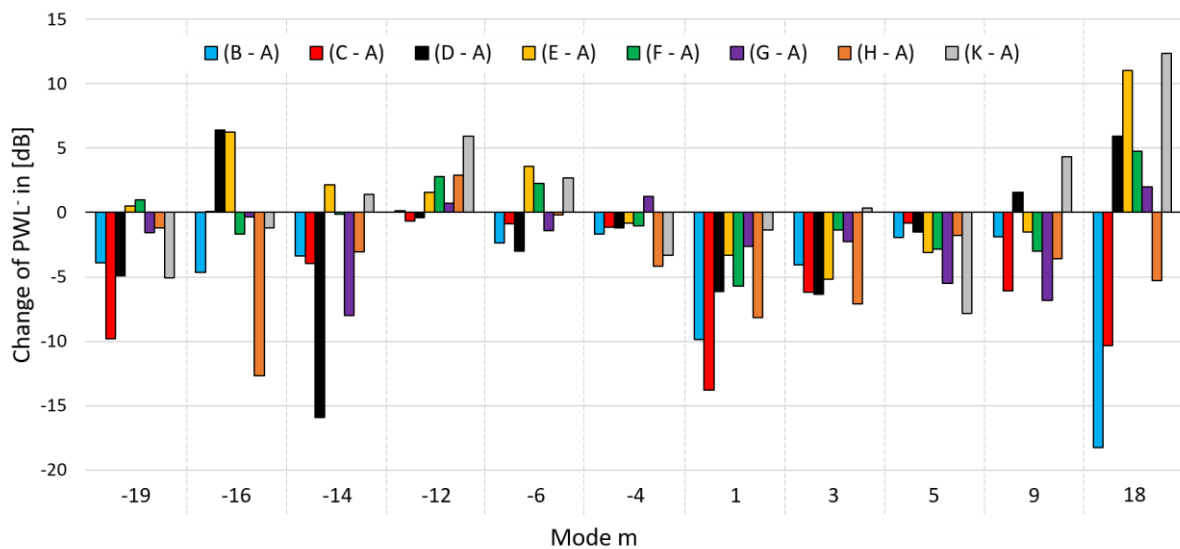


Figure 6.60: PWL⁻ change of interaction modes and their scatted modes – Standard, Helmholtz, and Resonator vane designs

Figure 6.61 presents three different comparisons concerning setups including the Leaned vane design. The comparison (I-A) gives the change between the two baseline hard end walls configurations of the Standard and Leaned vane designs with the green bars. Blue bars indicate the comparison of the configurations (J) and (A), and the red bars show a direct comparison of the two investigated setups (I) and (J) using the Leaned vane design.

Comparing the two hard end wall configurations with different vane designs (I-A), it can be seen that there is a huge increase of the PWL for mode $m = -16$ as well as for $m = 18$. Mode $m = 18$ is a rotor – TEC interaction and $m = -16$ is the result of this mode scattered on the TEC again. The same result was also obtained by Broszat et al. [80]. Another rise of the PWL happens for the modes $m = 3$ and $m = 9$. Although these modes are increased, the overall PWL including all cut-on modes is decreased by 1.3 dB in flow. This can be explained by knowing that mode $m = -12$ is a dominant mode which can be reduced by 8.7 dB.

Comparing the configurations (A) and (J), the increase at mode $m = 18$ can be again identified. The one at its scattered mode $m = -16$ is not visible anymore but decreased instead by 6.3 dB.

The most important comparison is now the one between the Leaned vane design combined with the hard end walls (I) and the configuration including the soft end walls (J). There, no change concerning the rotor – TEC interaction mode $m = -12$ and $m = 18$ is visible, but a large reduction for the scattered mode $m = -16$ with a change of 15.6 dB using the soft end walls.

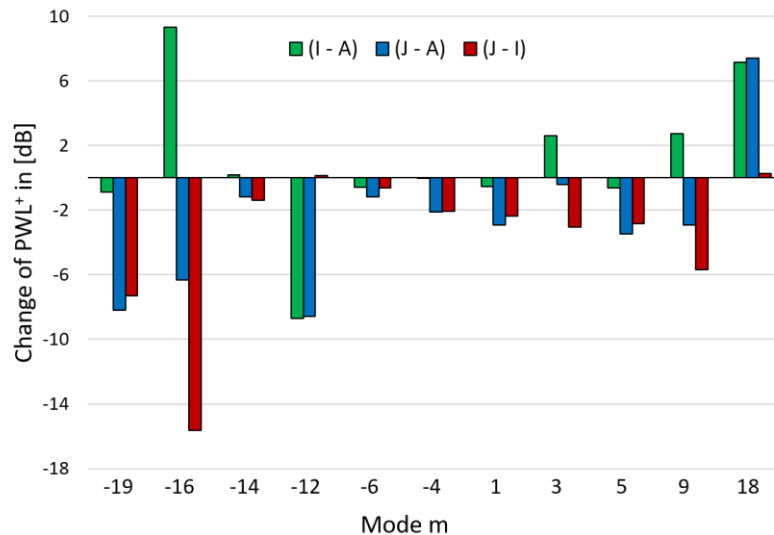


Figure 6.61: PWL⁺ change of interaction modes and their scattered modes – Leaned vane design

Same investigations are done now for the propagation direction against the flow direction. The obtained outcomes are shown in Figure 6.62. Also for this propagation direction, using the Leaned vanes with hard end walls results in a very high increase for the rotor – TEC interaction $m = 18$ and the scattered mode $m = -16$ compared to the baseline setup (A). Also the presence of the soft end walls does not change this behaviour for the interaction mode but improves the results of the scattered mode. What can also be seen from this figure is that, combining the Leaned vane design with the soft end walls (J) has a high impact onto waves propagating against the flow direction. Almost all plotted modes are significantly decreased in PWL compared to the respective hard wall setup (I). The highest is like in the case of propagation in flow direction mode $m = -16$ with a reduction of 12.6 dB.

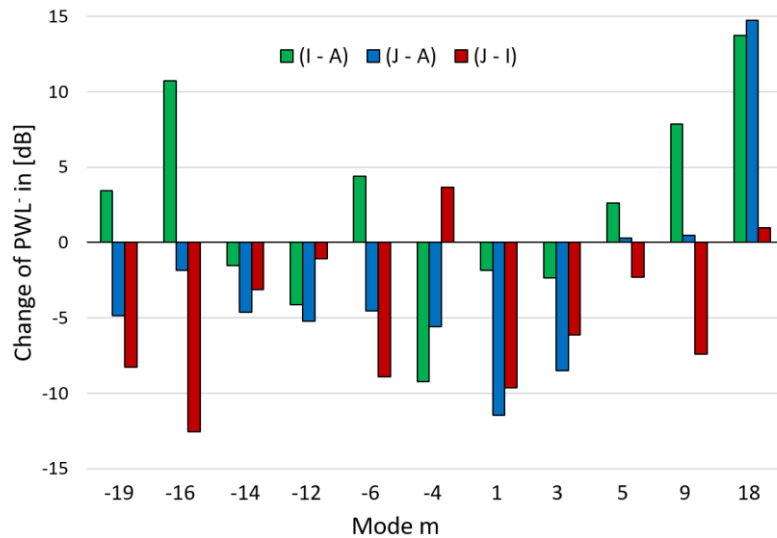


Figure 6.62: PWL change of interaction modes and their scatted modes – Leaned vane design

As mentioned above, the rotor –TEC interaction mode $m = 18$ is increased while the other interaction mode $m = -12$ is decreased by using the Leaned vane design. The intended idea of these Leaned vanes is to reduce the overall noise emitted at this interaction, which consists of the modes $m = -12, 3, 18$, with respect to the Standard vane design. On the left side of Figure 6.63 the PWL of configuration (A) including the Standard vanes for each cut-on mode order m is shown. The black arrows indicate the three interaction modes of the rotor – TEC interaction. It can be seen, that $m = -12$ is the dominant one within those three modes. Elhadidi and Atassi [101] stated in their work, that a variation in the radial phase of the disturbance with respect to the vane LE, which is the basic idea of a vane lean, is exciting higher order duct modes. This is also assumed here in case of the interaction modes. As can be seen on the right side of Figure 6.63, the PWL of mode $m = 3$ is rising with an increasing radial mode order n using configuration (I) compared to setup (A). Also mode $m = 18$ shows an increased value (higher n modes are cut-off). Additionally, both modes $m = 3$ and 18 have the same spinning direction as the lean direction of the exit guide vanes. On the other hand, it can be observed that in case of the dominant mode $m = -12$ the noise reduction is even higher with a higher order of n .

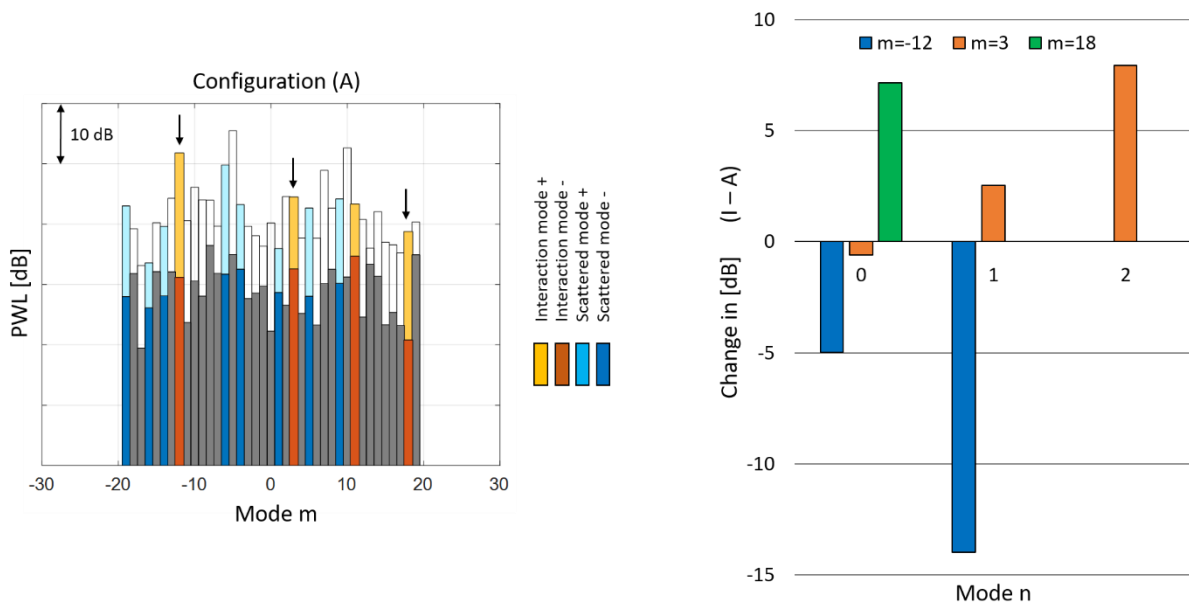


Figure 6.63: Change of rotor - TEC interaction modes - Configuration (A) and (I)

Spinning direction of cut-on modes

Another point that should be investigated here is the influence of a lined section onto the acoustic modes with respect to their spinning direction. In this thesis, modes which have a positive sign are counter rotating with the rotor rotational direction and modes with a negative sign are co-rotating (see also Simonassi et al. [102]). The mode $m = 0$ is a plane wave mode and has therefore no rotation.

Figure 6.64 presents the change of the overall sound power level in flow direction split up into the modes with a positive and a negative spinning direction as well as the 0 mode. Each setup is related to the baseline configuration (A).

All setups having open absorber necks, have a higher reduction of the positive spinning modes compared to the positive ones (setup (E) has the taped openings). Nevertheless, the 0 mode shows the highest reduction of the PWL in flow direction for all investigated setups.

Concerning the use of soft end walls, a rise of the attenuation potential can be identified with increasing the absorber neck diameter for both, the counter rotating modes and the 0 mode. The same behaviour is valid for the Helmholtz vanes concerning the positive modes. Configuration (E) having the taped resonator openings, has an increase of the PWL^+ concerning the counter rotating modes. It is assumed now, that the lined section as well as the Helmholtz vanes have a higher impact onto the modes with a spinning direction opposing the one of the LPT rotor. Serrano and Torres [54] also stated a higher impact of absorbers located on the suction side of outlet guide vanes onto counter rotating modes.

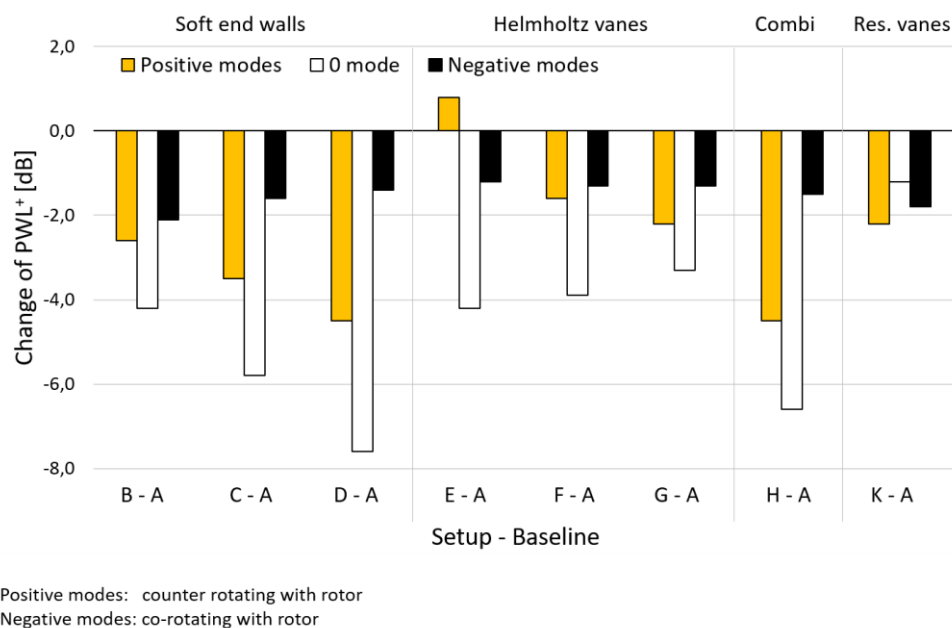


Figure 6.64: PWL^+ change regarding the mode spinning direction – Standard, Helmholtz, and Resonator vane designs

Taking also a look onto the propagation direction against the flow direction, a similar behaviour can be seen at least for the setups including the Helmholtz vanes with open necks. Again, the 0 mode has the highest attenuation, followed by the counter rotating modes. The co-rotating modes have the smallest PWL^- reduction. Concerning the configurations having soft end walls, the results look a little different. In the cases (B) and (C), the negative rotating modes have a higher decrease compared to the positive ones as well as the 0 mode. Configuration (D), which showed an increase of the broadband noise, has an increased 0 mode compared to the baseline setup. But also setup (K) including the Resonator vanes and setup (E) with the closed absorber necks have a significant increase of the 0 mode as well as a rise of the positive and the negative spinning modes with respect to the baseline setup.

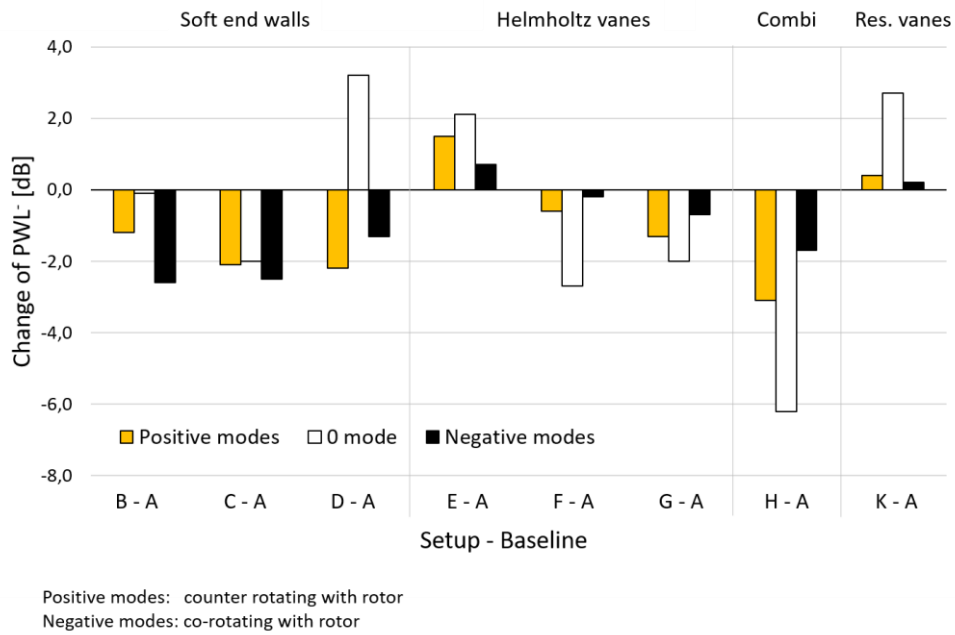


Figure 6.65: PWL⁻ change regarding the mode spinning direction – Standard, Helmholtz, and Resonator vane designs

The same examinations as above are now stated for the setups with the Leaned vane design, starting with the wave propagation direction equal to the flow direction. Both configurations are compared with the baseline setup (A) and with each other. As expected from the design intent of this vane configuration (reducing the rotor – TEC interaction), both Leaned vane setups show a decrease of the co-rotating (negative) modes with a maximum value of almost 4 dB in case of configuration (J). As mentioned before, the negative mode $m = -12$ is the dominant one within the interaction modes and can be reduced significantly with this vane design. The 0 mode on the other hand is significantly increased for setup (I) compared to setup (A). By comparing the configurations (I) and (J) it is visible, that the 0 mode receives the highest PWL⁺ reduction using the soft end wall configuration. The spinning modes have an almost identical attenuation independent from the rotational direction.

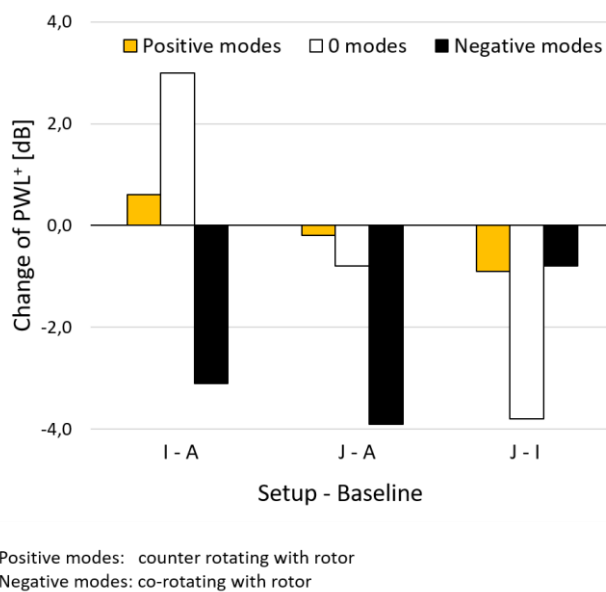


Figure 6.66: PWL⁺ change regarding the mode spinning direction – Leaned vane design

The results of the propagation against the flow direction is depicted in Figure 6.67. It is visible, that the 0 mode has again a much higher value, as already seen above, for setup (I) with the Leaned vanes compared to the baseline setup (A) including the Standard vanes. With the soft end walls used in configuration (J) a reduction of the PWL level for both spinning directions can be achieved especially for the negative ones when comparing it also with setup (A).

A direct comparison of the two Leaned vane setups results in a better acoustical performance when including liners in the duct end walls. Herein, all three examined mode types receive a significant reduction with respect to the hard wall setup. This result is comparable with the one observed in the opposite propagation direction.

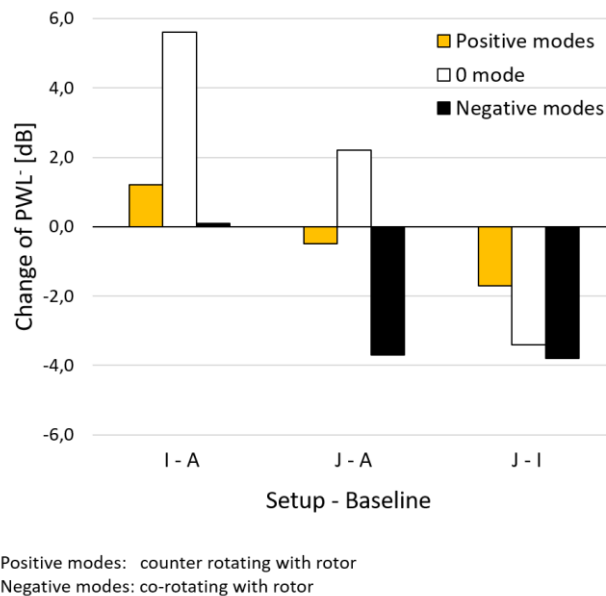


Figure 6.67: PWL change regarding the mode spinning direction – Leaned vane design

These investigations showed that for a wave propagation direction against the flow direction, the co-rotating (negative) modes, with respect to the rotor rotational direction, can be attenuated better than the counter rotating (positive) ones using setups with a soft duct end wall. In flow direction it is the other way around.

In case of having Helmholtz absorbers implemented in the suction side of a vane, the result is different. Here a better PWL reduction can be achieved for counter rotating modes independently of the propagation direction. But the highest attenuation is always at the 0 mode.

The following table gives the obtained results shown in the figures above, indicating the sound power level change in [dB] values for all setups including acoustic liners. Herein, the baseline value is subtracted from each acoustically treated setup.

Table 6.6: Change of PWL[±] - Spinning modes

In flow direction	Setup	(B)	(C)	(D)	(E)	(F)	(G)	(H)	(K)	(I - A)	(J - A)	(J - I)	
	Change to setup (A) in [dB]												
Positive modes		-2.6	-3.5	-4.5	0.8	-1.6	-2.2	-4.5	-2.2		0.6	-0.2	-0.9
0 mode		-4.2	-5.8	-7.6	-4.2	-3.9	-3.3	-6.6	-1.2		3.0	-0.8	-3.8
Negative modes		-2.1	-1.6	-1.4	-1.2	-1.3	-1.3	-1.5	-1.8		-3.1	-3.9	-0.8

Against flow direction	Setup	(B)	(C)	(D)	(E)	(F)	(G)	(H)	(K)	(I - A)	(J - A)	(J - I)	
	Change to setup (A) in [dB]												
Positive modes		-1.2	-2.1	-2.2	1.5	-0.6	-1.3	-3.1	0.4		1.2	-0.5	-1.7
0 mode		-0.1	-2.0	3.2	2.1	-2.7	-2.0	-6.2	2.7		5.6	2.2	-3.4
Negative modes		-2.6	-2.5	-1.3	0.7	-0.2	-0.7	-1.7	0.2		0.1	-3.7	-3.8

6.2.6 Riblets

This section is about the grooved microstructure applied on the turbine exit guide vanes suction side to achieve a reduction of the broadband noise generated by turbulent flow as explained in section 2.4.2. During this work, three different foils applied on the Standard vanes are investigated. First, a smooth foil was applied to result in the same vane thickness as with riblets. This setup serves as a reference case and is named configuration (L). The other two foils are riblets with two different geometry details.

From now on, the case with the smaller tip to tip distance and riblets height is referred to as configuration (M), and the setup with the bigger geometry is configuration (N).

Acoustics

Figure 6.68 shows a comparison of the SPL over frequency for all three investigated setups concerning riblets. Black indicates the reference case, orange configuration (M), and blue gives the measurement results for configuration (N). It can be seen, that there is not much of a difference comparing both riblet cases. It is different doing a comparison with the reference case, wherein two larger regions of decreased SPL can be identified when using the grooved structure. The first one is in the area around the second harmonic of the vibration frequency (2nd VF), and the second region starts close to the 2nd BPF and extends until the end of the shown frequency range.

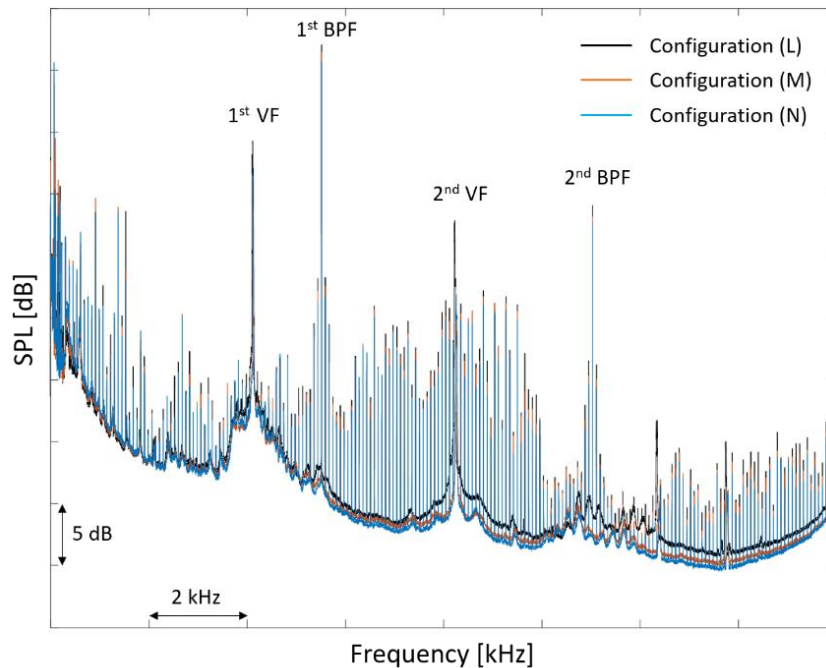


Figure 6.68: Frequency spectra – Configurations (L), (M), and (N)

To give a clearer insight into the change between the reference case and the riblets, Figure 6.69 contains a difference of the SPL for every frequency is shown additionally to the frequency spectra of configurations (L) and (M). Black indicates configuration (L), red configuration (M) and in green, the SPL difference between those two cases is shown. The dashed black horizontal line depicts zero difference. Values above this line are an increase concerning the SPL of the riblet case, and values below the line show a decrease. This difference is only concerning the background noise and excludes the peaks to show the change related to the different surface as explained in 2.4. The procedure is described in the annex section 12.4.

Starting at 2 kHz, a reduction of the background noise for configuration (M) can be identified. The biggest differences are in the vicinity of 8 kHz and 12 kHz with a maximum decrease of 1.6 dB at both frequencies. At frequencies higher than 12 kHz, an almost constant reduction with a minimum of 0.7 dB is observed. It is assumed, that this high frequency reduction is due a reduction of the Reynolds stresses using the guiding microstructure. A decrease of these stresses goes hand in hand with a reduction of the drag. Skudrzyk and Haddle [41] mentioned in their work, that a reduction of the drag is correspondent to a decrease of the high-frequency flow noise.

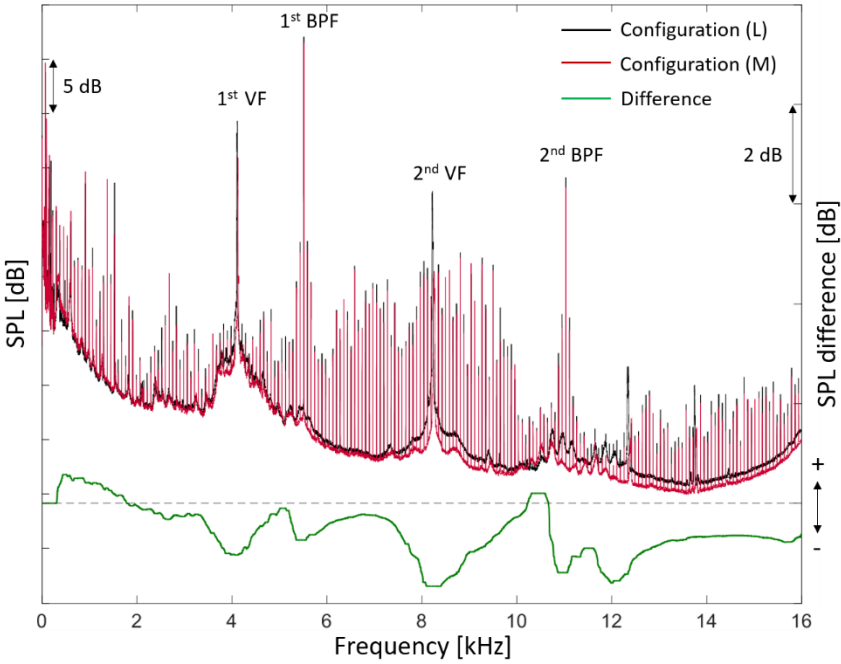


Figure 6.69: Frequency spectra of Configurations (L) and (M)

A very similar result can be seen when looking at Figure 6.70, which shows a comparison of the configurations (L) and (N). As mentioned, the second configuration has slightly bigger riblets dimensions compared to configuration (M). Starting again at 2 kHz, as in case of the other riblet setup above, a reduction of the SPL using riblets can be observed over the whole frequency range. The two areas of maximum reduction are again at 8 kHz and at 12 kHz, with a drop of 1.8 dB and almost 2 dB respectively. The decrease is again connected with the decrease of the turbulent boundary layer noise. In total, the broadband noise reduction is higher using configuration (N) compared with setup (M).

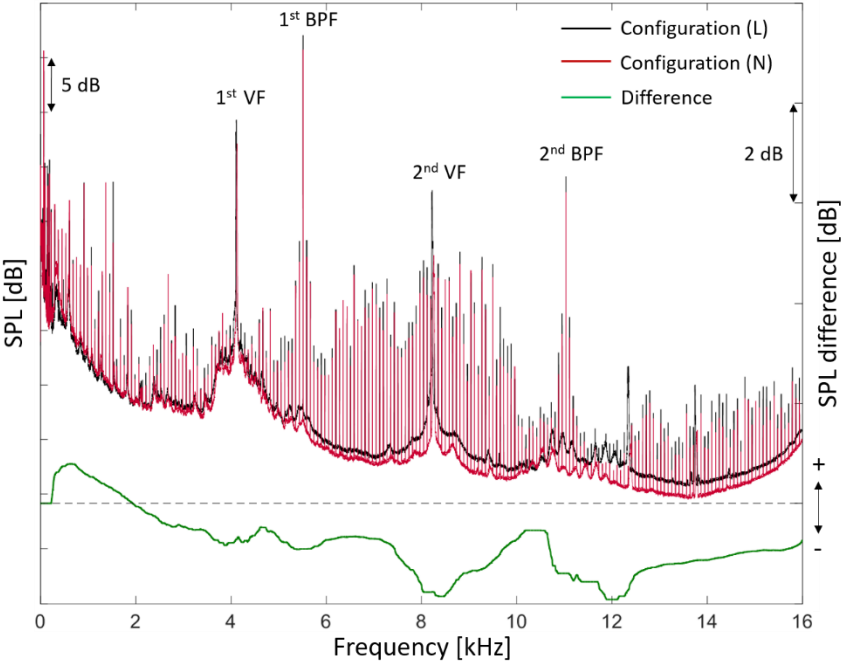


Figure 6.70: Frequency spectra of configurations (L) and (N)

A comparison regarding the overall sound power level in and against flow direction for all three setups is given in Figure 6.71. It is visible, that the reduction in flow direction as well as the increase against flow direction have a stepped characteristic but with opposite directions. A decrease of the overall PWL with a propagation direction in flow direction is coupled with an increase concerning the opposing direction.

With configuration (M), a reduction of 1 dB in flow direction could be achieved with respect to the reference setup (L). On the other hand, an increase of 0.9 dB can be observed against the flow direction. Comparing configurations (N) and (L), a decrease of 2 dB in flow direction and an increase of 1.3 dB against flow direction can be seen.

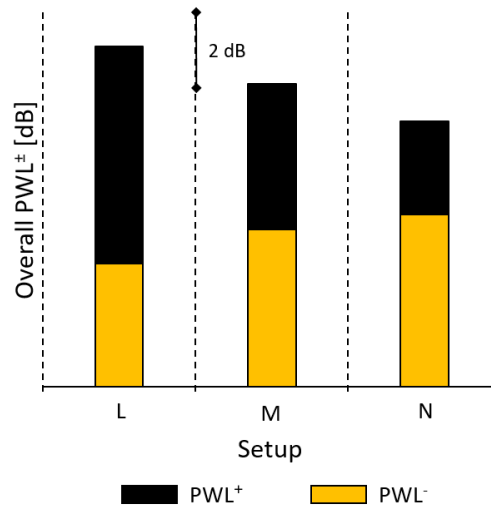


Figure 6.71: Overall PWL[±] – Configurations (L), (M), and (N)

Aerodynamics

In this section, a comparison of the aerodynamical behaviour of the configurations (L), (M) and (N) is done for both the rotor exit and the TEC exit measurement plane. Three parameters are compared, namely the total pressure normalized with the total pressure at the stage inlet, the Mach number, and the yaw angle. Different to the other sections, in this one also flow parameters downstream of the LPT rotor are shown. This is done to see if there is an upstream effect of the riblet structure.

Rotor – Exit flow

Figure 6.72 shows the radial distribution of the mass averaged rotor exit flow parameters. Black indicates the reference setup (L), orange the configuration (M), and blue the configuration (N). The total pressure distribution on the left side shows for all three configurations a very good accordance with only a small difference on the outer casing. This drop in total pressure is due to the tip leakage vortex caused by the flow over the unshrouded rotor and the rise to higher values on the very tip is due to the jet over the rotor tip gap. The slightly higher values around 10% of the relative channel height is due to the hub leakage flow of the upstream located inlet guide vanes as well as due to the secondary flow which result from the upstream stator, the rotor itself, and an interaction of both vane rows (more information concerning the rotor used in this work can be found in Selic et al. [74]). The same effects can also be seen in the Mach number distribution in the middle of Figure 6.72. Besides that, a difference between the three cases is visible, with a lower velocity for both riblet configurations compared to the reference setup. But according to the small values in difference (maximum

0.02), this can be neglected. The yaw angle on the right side is again of good accordance for all investigations. With these results it can be said, that the operating point was set identical for all three cases and that according to this rotor exit flow results, no upstream effect of the riblets could be measured.

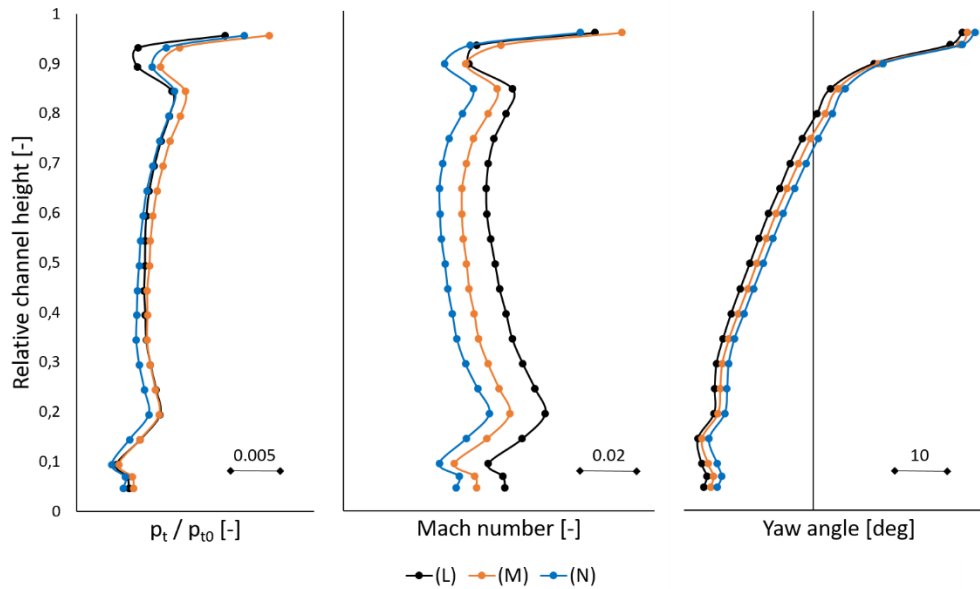


Figure 6.72: Aerodynamical comparisons – Rotor-exit – Configurations (L), (M), and (N)

In Figure 6.73 the corresponding flow fields of normalized total pressure and yaw angle of the explained radial distributions are shown. Vane wakes from the upstream located LPT stator are indicated by the black dashed lines with the pressure side on the left and the suction side on the right side. The rotational direction of the rotor is given with ω in the plot on the top left side. This flow field is also divided into four sectors indicated by the red lines extending over the whole circumferential direction and marked with roman numbers I, II, III, and IV. Sector I is dominated by the jet caused by the tip gap which can also be identified due to the very high values of yaw angle. In sector II, the tip leakage flow is visible again indicated by the high values of yaw angle. The area at the very hub, which is marked with IV is dominated by secondary flow effects.

As could already be seen in the radial distributions, no big differences are visible. The small shift in circumferential direction of the reference setup (L) is assumed to be caused by the mounting of the used probe. Concerning configuration (M), the sectors I and II have higher values than it is the case for the other two setups.

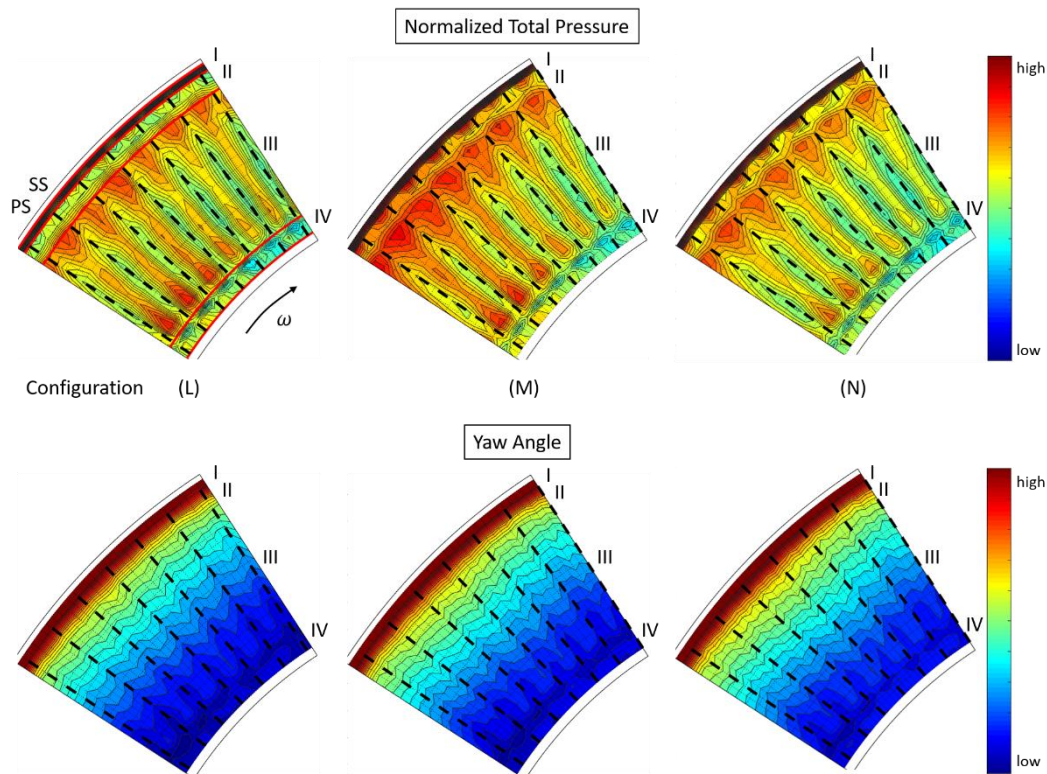


Figure 6.73: Aerodynamical flow fields – Rotor exit – Configurations (L) (M) and (N)

TEC – Exit flow

The parameters for the TEC exit flow are depicted in Figure 6.74. Again, the normalized total pressure distributions show a similar behaviour for all three cases over the whole radial channel height. The Mach number gives lower values for the two designs (M) and (N) compared to the reference case (L) but the distributions are almost identical for the two riblet cases. Knowing that the investigated vane row is diffusing, the lower Mach number of both Riblet designs would indicate a better performance using them. But again, as mentioned above, the difference is so small that it can be neglected. Concerning the yaw angle, a shift to more positive values for the setups having riblets in the area between 20 and 80 % of the relative channel height can be seen. Especially for configuration (N), this shift is well observed. Configuration (M) is additionally shifted to more positive values in each radial averaged measurement point but has the same shape in the midspan region as setup (N). It is assumed, that this additional parallel offset of configuration (M) with respect to (N) is due to the setting of the probe. An oilflow visualization showed a separation at the trailing edge of the reference case (L) but none for the riblets setup (M) in exactly this area of shifted yaw angle. Both oilflow visualisations can be seen in Figure 6.75, wherein the position of the separation is indicated with the black frame. It is assumed, that the cancellation of this separation when using riblets is the cause of the more positive values between 20 and 80% channel height in the measured yaw angle.

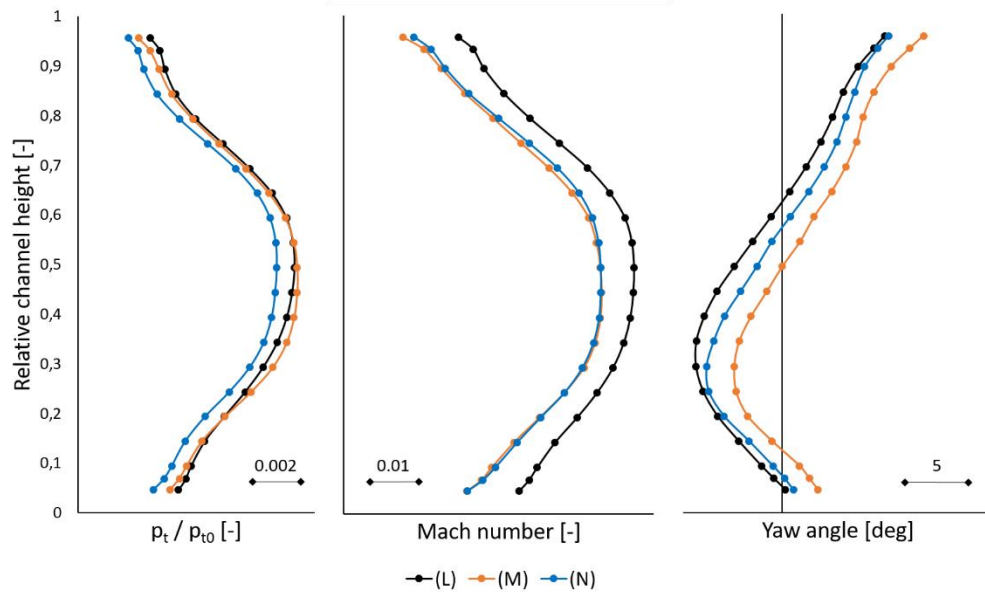


Figure 6.74: Aerodynamical comparisons – TEC-exit – Configurations (L), (M), and (N)

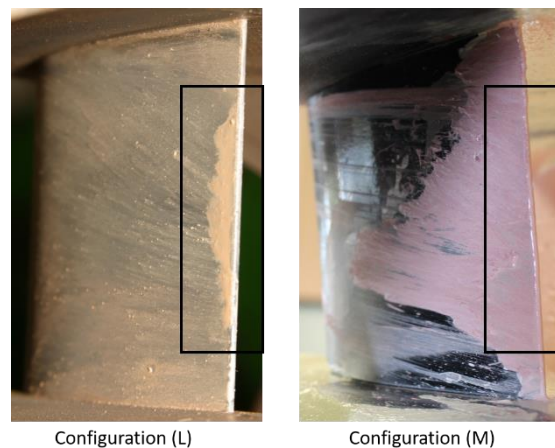


Figure 6.75: Oilflow visualizations – Vane suction side – Configurations (L) and (M)

In Figure 6.76, the corresponding flow fields with respect to the radial distributions are given for all three setups. The region marked with II in the normalized total pressure of setup (M), which is due to the UPV, has a higher level compared with the other two configurations.

The yaw angle of setup (M) shows higher values in the whole sector. Especially the regions marked with I (at the outer casing) and IV (at the inner casing) are more pronounced in this setup. Configuration (L) and (N) are very similar, which could already be seen in the radial distributions.

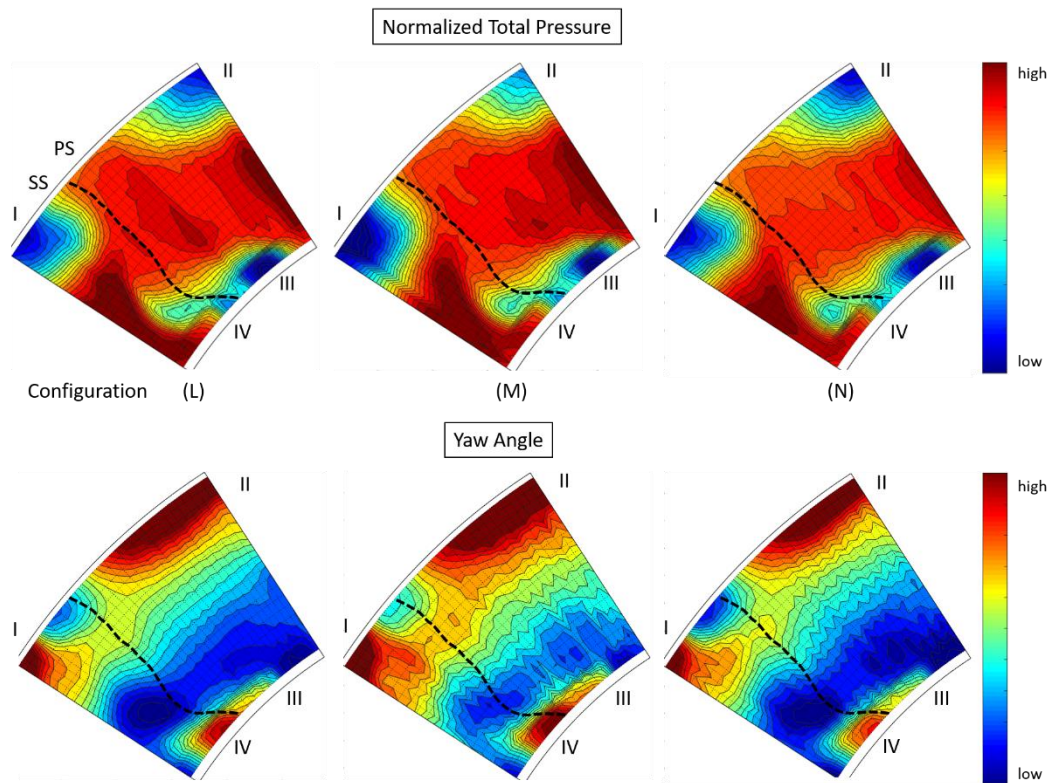


Figure 6.76: Aerodynamic flow fields of the reference setup (L) and configurations (M) and (N) – TEC exit

The following figure shows four different pictures of two different oilflow visualization test runs. Pictures 1, 2, and 3 result from a test run with configuration (M) and picture 4 shows the result of the reference configuration (L). The red line marked with [A] depicts the location of the riblets starting point on the suction side surface.

Pictures 1 and 4 show the same behaviour of the flow, marked with [E] and [C] respectively. Streamlines move from the outer casing radially inwards the closer they get to the vane trailing edge. Whereas in picture 2 the flow is following the riblets inclination perfectly, which is indicated by the orange lines marked with [B]. Picture 1, where the viscosity of the oilflow was higher compared to the result in picture 2, shows no such behaviour what confirms, that riblets are only influencing the inner boundary layer. The oil in picture 4 has the same viscosity as the one in picture 2. Herein the streamlines, indicated by white lines and marked with [C], are skewed to midspan in direction of the vane TE, which is a result of the presence of secondary flow effects. Picture 2 shows on the other side, that when riblets are used, the streamlines are clearly parallel.

In picture 3 and marked with [D], a separation on the pressure side of the vane can be seen, which results of the wrong incident of the flow in the tip region due to the tip leakage flow over the rotor. This structure is visible for both configurations, with and without riblets (see Figure 6.79). The result due to the wrong incident is also shown in Selic [36].

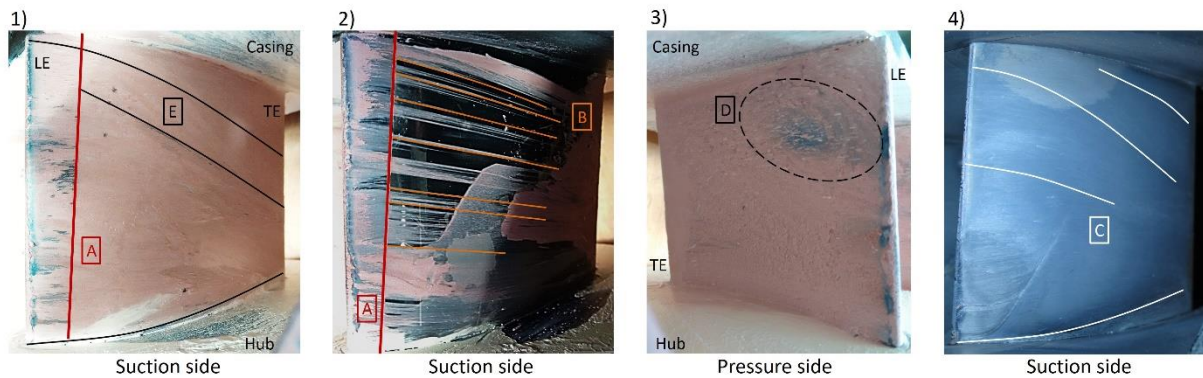


Figure 6.77: Oilflow visualisations - Configurations (M) (1, 2, and 3) and (L) (4)

The results of the vane wake measurements are presented in Figure 6.78, which shows the total pressure downstream of the trailing edge normalized by the averaged total pressure concerning each measurement on the ordinate, and the circumferential measurement position on the abscissa. The vanes pressure side (PS) is located on the right side of the total pressure minimum and the suction side (SS) on the left side. This clearly visible minimum indicates the location of the wake. It can be seen, that both designs having riblets on their vane suction side show a higher total pressure in the wake centre compared to the one without. In general, all three setups are similar in shape except the regions of wake start and end.

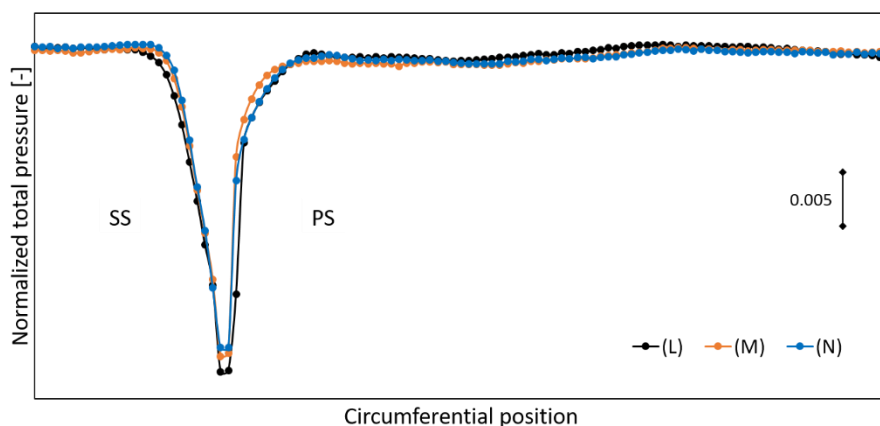


Figure 6.78: Vane wake measurements results - Configurations (L), (M), and (N)

With the procedure of Schobeiri and John [34] explained in section 2.3.3, the wakes could be evaluated, and the results are shown in Table 6.7. It can be seen, that for both riblet configurations all four parameters are decreased compared to the reference case (L). There is a reduction of the wake width as well as the momentum thickness of around 19 % for both parameters in case of setup (M). Concerning configuration (N), using the bigger riblets geometry, this reduction is 5.6 % and 3.8 % respectively.

A comparison of the two riblet setups (M) and (N) shows, that configuration (M) has a higher reduction for each parameter with respect to the reference configuration. This indicates, that the smaller riblet size fits better to the operating conditions of the test turbine.

Table 6.7: Results of wake measurements - Configurations (L), (M), and (N)

	Configuration			Change to (L) in [%]	
	(L)	(M)	(N)	(M)	(N)
Wake width [m]	0.00337	0.00271	0.00318	-19.6	-5.6
Momentum thickness [m]	0.00132	0.00107	0.00127	-18.9	-3.8
Energy thickness [m]	0.00256	0.00178	0.00217	-30.5	-15.2
Displacement thickness [m]	0.00223	0.00215	0.00222	-3.6	-0.4

The following table shows the values for the shape factor on both, vane suction and pressure side, of the three configurations according to equation (2.92) stated in section 2.3.3.

Concerning the suction side, all three setups have values either in the range according to literature for a turbulent boundary layer (value between 1.3-1.4) or close to it. The separation mentioned above on the suction side of the reference setup is not visible in these values, because the measurement is taken at the border of this separation.

When looking on the vane pressure side, a different result can be observed. Configuration (M) is with a value of 3.12 very close to the stated one of 4, which indicates a separation (according to [35]). Such a high value can't be seen in the other two cases. Comparing this result now with the oilflow visualization shown in Figure 6.79, it gets clear that there is a separation (indicated by the black frame) for setup (M) but none in case of the reference setup (L).

Table 6.8: Shape factor – Configurations (L), (M), and (N)

		Configuration		
		L	M	N
Shape factor	Suction side	1.36	1.22	1.44
	Pressure side	1.99	3.12	2.02

In the following figures, the impact of the wrong incident on the exit guide vanes as mentioned above can be seen. Both vanes show a vortical structure close to the outer casing at the leading edge indicated by the dashed elliptical line.

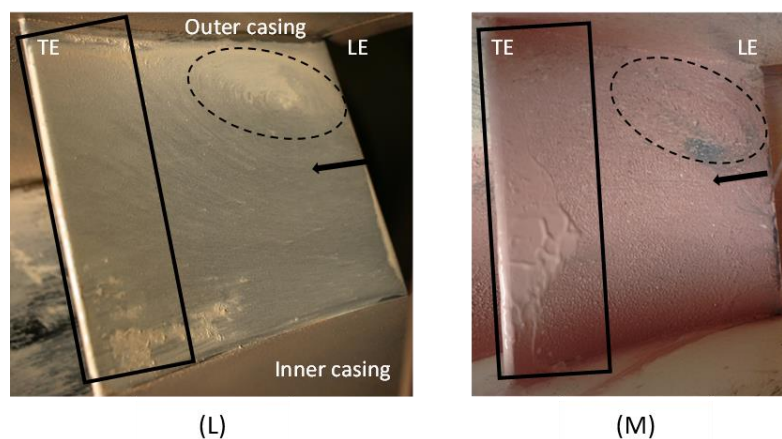


Figure 6.79: Oilflow visualizations – Pressure side – Configurations (L) and (M)

Overall can be said, that the goal of reducing the sound power level by the setups investigated within this section has been successfully achieved. Both basic ideas, implementing acoustical liners in vanes and/or side walls of the turbine exit casing as well as using riblets on the suction surface of the turbine exit guide vanes, showed a decreased noise level when using them compared to the respective state of the art configuration.

7 Conclusions

A series of different ways to reduce the noise emitted by a low pressure turbine have been presented in this thesis. Experiments have been performed under engine representative operating conditions in a 1 ½ stage low pressure test turbine located at the Institute for Thermal Turbomachines and Machine Dynamics at Graz University of Technology. Noise reduction mechanisms have been applied with the focus on the turbine exit casing, treating the turbine exit guide vanes as well as the inner and outer end walls of the flow duct. Not only the results concerning the acoustics but also the change in aerodynamical performance using these noise suppression devices has been investigated. As operating point, the noise certification point approach has been selected because the impact of an aero engine onto the environment of an airport is very high during this flight attitude.

In total, 14 different setups have been investigated during this work with the main focus on the noise suppression potential of each configuration. Four different exit guide vane designs have been combined with diverse inner and outer duct treatments. The majority of setups included so-called Helmholtz absorbers integrated in vanes or duct end walls. The second investigated mechanism has been the use of a grooved microstructure called riblets, applied on the suction side of the turbine exit guide vanes.

The mentioned Helmholtz absorbers located in the duct end walls have been combined with three different vane designs. Firstly, Standard vanes, which have an engine realistic design, secondly Helmholtz vanes, which have the same geometry as the Standard vanes but also absorbers included internally, and thirdly Leaned vanes, which are derived from the Standard vane design having a lean against the rotor rotational direction to reduce the interaction noise. The fourth vane design is called Resonator vane and has also the same geometry as the Standard vane design but include a different type of Helmholtz absorber with respect to the one of the Helmholtz vanes as well as the end walls. Concerning the riblets, again the Standard vane design has been chosen as the vane design of interest.

Table 7.1 presents the calculated resonance frequencies of the soft end walls as already seen in Table 4.10, but with an extension concerning the measured maximum frequency inside the absorber during the STTF test run. It seems that although there is a mean flow with a certain Mach number, it is not affecting the absorber resonance frequency or only little. The values calculated without Mach number fit very well to the measured ones. Bell et al. [53] mentioned

in his work, that a mass end correction due to a flow Mach number is needed starting with 0.24 upwards. In the case of the performed investigations during this thesis, the mean flow Mach number had a value of 0.19 and therefore it can be assumed that it has negligible influence.

Table 7.1: Calculated and measured resonance frequencies of soft end walls

Setup	Neck diameter [mm]	Resonance frequency [Hz]		Measured inside resonator
		With Ma	Without Ma	
(B)	3.5	5641	4757	4408
(C), (H), (J)	3.8	6098	5115	4876
(D)	4.2	6706	5593	5445

Figure 7.1 shows a comparison of all investigated setups concerning their sound power level at the first blade passing frequency, which is the dominant frequency of the machine and therefore the one of interest. The grey bars indicate the setups with hard end walls, the chequered ones are a combination with soft end walls (absorbers included in the duct walls between the vanes), and the striped ones depict the setups with riblets. Having different bars inside one setup group means, that the neck diameter of the absorber, and therefore its resonance frequency, are altered. Below each bar at the very bottom of the figure, the absorber neck diameter of each configuration is stated. The ability of noise reduction can be clearly seen when using acoustically treated setups. It is also visible, that absorbers included in the duct end walls have a higher impact onto the noise reduction compared with the ones included in the vane itself. The highest reduction with almost 3 dB could be achieved with setup (H), which is the combination of the Helmholtz vanes (\varnothing 3.2 mm) and the soft end walls (\varnothing 3.8 mm). With only soft end walls, in case of the Standard vanes a PWL reduction of 2.6 dB and combined with the Leaned vanes 2.1 dB could be achieved. Also the riblets have with a maximum decrease of 1.3 dB a remarkable impact onto noise suppression at the first blade passing frequency.

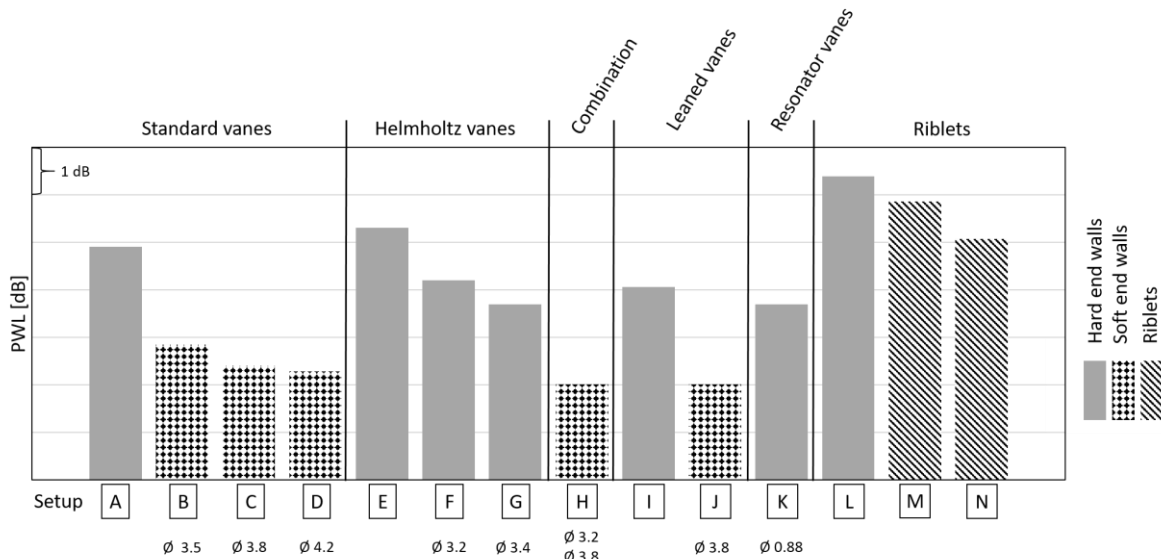


Figure 7.1: Sound power level at 1st BPF for all investigated configurations

In Figure 7.2, a comparison of the overall sound power level in (black bars) and against (yellow bars) flow direction for all investigated configurations can be seen. And as already observed for the PWL at the 1st BPF, also here a significant decrease when using acoustically treated elements is visible. Again, setup (H) has with 2.3 dB in as well as against the flow direction the highest reduction. But also configurations (B) and (D), having two different absorber neck diameters, have the same 2.3 dB decrease looking at the overall PWL in flow

direction and 1.9 dB and 1.6 dB against flow direction respectively. Concerning the Leaned vane design, a reduction of about 1 dB in flow direction and 2.7 against it could be observed when investigating setup (J) including the soft end walls. The Resonator vane configuration (K) showed a reduction of 1.9 dB in flow direction and no change against it. The riblets setup achieve a maximum reduction using configuration (N) of 2 dB in flow direction but an increase of 1.3 dB looking at the propagation direction against the flow direction.

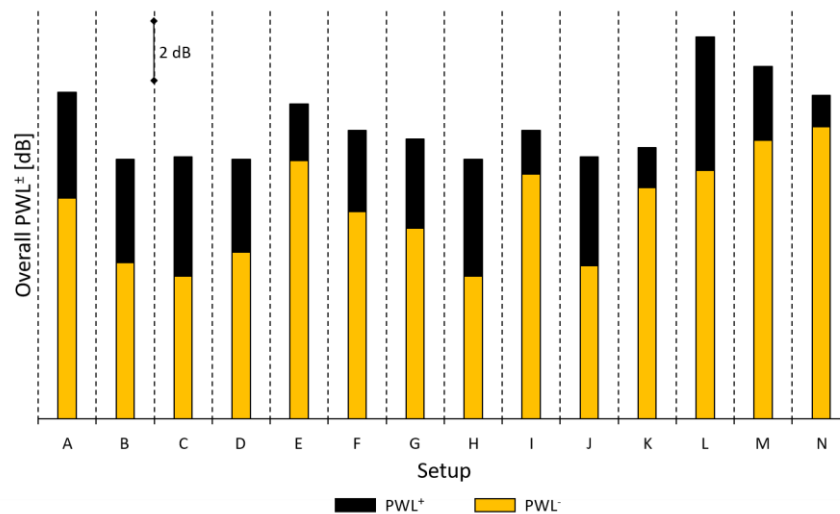


Figure 7.2: Overall PWL comparison in and against flow direction – All configurations

Aerodynamical data of all setups have been investigated as well concerning a change in performance of the LPT stage. The only change when using the Helmholtz vanes or Resonator vanes is an increase of the vane wake width, which is assumed to result from the rougher surface due to the manufacturing procedure of the vanes.

Riblets on the other hand, even improve the aerodynamical performance of the Standard vane design when applied on their suction side surface. The vane wake width could be significantly reduced with a value of 19.6 % using configuration (M) and 5.6 % with setup (N).

Another key fact of the shown investigations is the used material. It can also withstand the high temperatures in a commercial LPT exit casing. Also Broszat et al. [56] tested acoustic liner in the same test rig which was also used during this thesis. There, a honeycomb and a porous material were jointed adhesively. Due to the glue, an application in an aero engine is not thinkable. This challenge is passed when manufacturing the liners additive as one single piece like it was done within this thesis.

The present work shows the beneficial effect on the emitted LPT noise which can be achieved by optimizing the turbine exit casing by inserting acoustic liners in the turbine exit guide vanes as well as in the duct end walls between the vanes. Hence, the evaluated experimental results during this thesis could be a contribution to achieve noise certification limits of future aero engines.

Outlook

As could be seen in the above sections, a significant reduction of the sound power level at a certain frequency can be achieved by using acoustic liners consisting of Helmholtz absorbers. To even increase the usability of such an acoustic lining concerning their attenuation potential over a wider frequency range, further steps have to be taken. For example, the noise emissions of an aero engine at approach and take off are both crucial to the environment but are two totally different operating points. To be able to suppress the dominating frequency (blade passing frequency) at both points, a simple Helmholtz absorber cannot be used anymore. Therefore, a tuneable absorber by changing the cavity size could be taken into account to cover more than only one of these frequencies and hence increase the overall noise attenuation potential of the whole device.

One could also think about the use of a more difficult lining in terms of geometry as for example a non-axisymmetric cavity with respect to the neck opening which results in a second resonance frequency (see [103]). Another possibility is to increase the complexity of an absorber to a two-degree-of freedom system by combining two absorbers connected in series (see [104]) or by including a vibrating membrane and split one cavity into two (see [105]). The problem of those mentioned possibilities is the difficulty in terms of realising the wanted resonant frequencies as well as having enough space to attach them. Additionally, the stated literature always investigated plane waves and no higher order duct modes.

8 Publications

8.1 Journal Publications

2020

Manuel Zenz, Loris Simonassi, Philipp Bruckner, Simon Pramstrahler, Franz Heitmeir, and Andreas Marn, “*Noise Attenuation Potential Using Helmholtz Absorbers Integrated in Low Pressure Turbine Exit Guide Vanes and Turbine Exit Casing End Walls*”, Suggested for Journal of Turbomachinery

2019

Simonassi, L., **Zenz, M.**, Zerobin, S., Selic, T., Heitmeir, F., and Marn, A., “*On the Influence of Different Exit Casing Designs onto the Unsteady Flow Field Downstream of a Low Pressure Turbine Rotor*”, Journal of Turbomachinery, Vol. 141, April 2019

2017

F. Schönleitner, T. Selic, **M. Zenz**, F. Heitmeir, and A. Marn, “*On the Influence of a Five-Hole-Probe on the Vibration Characteristics of a Low Pressure Turbine Rotor while Performing Aerodynamic Measurements*”, Technische Mechanik Vol. 37 No. 2-5 (2017)

8.2 Conference Publications

2020

Manuel Zenz, Loris Simonassi, Philipp Bruckner, Simon Pramstrahler, Franz Heitmeir, and Andreas Marn, “*Noise Attenuation Potential Using Helmholtz Absorbers Integrated in Low Pressure Turbine Exit Guide Vanes and Turbine Exit Casing End Walls*”, Accepted for ASME Turbo Expo, June 2020, London, United Kingdom

Simonassi L., **Zenz M.**, Bruckner P., Pramstrahler S., Heitmeir F., and Marn A., “*Experimental Study on the Effect of Clocking on the Propagation of Inflow Pressure*”

Distortions in a Low Pressure Turbine Stage”, Proceeding of ASME Turbo Expo, June 2020, London, United Kingdom

2019

Zenz, M., Hafizovic, A., Simonassi, L., Leitl, P., Heitmeir, F., and Marn, A., “*Aeroacoustical and Aerodynamical Investigations of Riblets Applied on Low Pressure Turbine Exit Guide Vanes for two Different Operating Points*”, Proceeding of ASME Turbo Expo, June 2019, Phoenix, Arizona, USA

Simonassi, L., **Zenz, M.**, Bruckner, P., Heitmeir, F., Marn, A., “*Aeroelastic and Aerodynamic Investigation on a Low Pressure Turbine Under the Influence of Circumferential Inlet Distortion*”, Proceeding of ASME Turbo Expo, June 2019, Phoenix, Arizona, USA

Zenz, M., Hafizovic, A., Simonassi, L., Leitl, P., Benauer, R., Heitmeir, F., and Marn, A., “*Aerodynamical and Aeroelastic Investigations of a Riblet Design Applied on the Surface of Turbine Exit Guide Vanes of a Low Pressure Turbine*”, Proceeding of 13th European Conference of Turbomachinery, Fluid Dynamics, and Thermodynamics, April 2019, Lausanne, Switzerland

Simonassi, L., Benauer, R., **Zenz, M.**, Leitl, P., Heitmeir, F., Marn, A., “*Numerical and Experimental Study of the Aerodynamic and Aeroelastic Performance of a Low Pressure Turbine*”, Proceeding of 13th European Conference of Turbomachinery, Fluid Dynamics, and Thermodynamics, April 2019, Lausanne, Switzerland

2018

Simonassi, L., **Zenz, M.**, Zerobin, S., Selic, T., Heitmeir, F., and Marn, A., “*On the Influence of Different Exit Casing Designs onto the Unsteady Flow Field Downstream of a Low Pressure Turbine Rotor*”, Proceeding of ASME Turbo Expo, June 2018, Oslo, Norway

2017

Zenz, M., Schönleitner, F., Simonassi, L., Bauinger, S., Broszat, D., Heitmeir F., and Marn, A., “*Experimental Determination of the Effectiveness of a Sound Absorbing Turbine Exit Casing*”, Proceeding of 12th European Conference of Turbomachinery, Fluid Dynamics, and Thermodynamics, April 2017, Stockholm, Sweden

9 List of Figures

Figure 1.1: Noise sources of a modern airplane (taken from [2])	1
Figure 1.2: History of aircraft noise reduction (adapted from [2])	2
Figure 1.3: Modern high-bypass turbofan engine Trent 7000 (adapted from [3]).....	3
Figure 1.4: Modern geared turbofan PW1100G (adapted from [4])	3
Figure 1.5: Comparison of a geared turbofan (top) and a conventional turbofan (bottom) (adapted from [5])	4
Figure 1.6: Acoustic liners at the inlet of an Airbus A380 (adapted from [6]).....	4
Figure 1.7: Possible locations for acoustic liners (adapted from [7])	5
Figure 1.8: Contributors to aircraft noise (adapted from [9])	5
Figure 1.9: Example of a noise spectrum from a low bypass ratio engine (adapted from [7])...6	
Figure 2.1: Bessel functions of the first (top) and second (bottom) kind for modes [0,5]	11
Figure 2.2: Examples of sound pressure distributions in a cylindrical duct (taken from [11]) 13	
Figure 2.3: Diameter discontinuity (adapted from [14])	17
Figure 2.4: Transmitted and reflected waves due to impedance discontinuities in a duct	20
Figure 2.5: Hard and soft wall conditions - Standing wave (taken from [18]).....	22
Figure 2.6: Schematic sketch of porous absorbers	22
Figure 2.7: Schematic sketch of resonant absorbers	23
Figure 2.8: Substituted systems of resonant absorbers.....	23
Figure 2.9: Absorption characteristics (adapted from [18])	24
Figure 2.10: Helmholtz absorber as a spring mass system	24
Figure 2.11: Secondary flows (taken from [27]).....	29
Figure 2.12: Secondary flow origin (adapted from [7])	29
Figure 2.13: Vortices downstream a vane passage (adapted from [28])	30
Figure 2.14: Secondary flow structures in a turbine vane passage (adapted from [29])	31
Figure 2.15: Origin of the tip leakage vortex (adapted from [7])	31
Figure 2.16: Origin of the trailing edge wake (adapted from [7]).....	32
Figure 2.17: Streamwise components needed to analyse the trailing edge wake (adapted from [34])	32
Figure 2.18: Shape factor distribution on a flat plate (taken from [35])	34
Figure 2.19: Evolution from shark skin to riblet foil (taken from [38]).....	35
Figure 2.20: Boundary layer types	35
Figure 2.21: Riblets theory – Mechanism one (adapted from Hafizovic [39]).....	36

Figure 2.22: Riblets theory – Mechanism two (adapted from [40]).....	37
Figure 2.23: Definition of aircraft noise certification points	40
Figure 3.1: Shift of resonance frequency due to grazing Ma number (taken from [52])	42
Figure 3.2: Effectiveness of different riblet geometries (taken from [57])	44
Figure 4.1: Experimental facility STTF-AAAI.....	47
Figure 4.2: Standard vane (left) and Helmholtz vane (right).....	50
Figure 4.3: Cut of a Helmholtz vane	51
Figure 4.4: Helmholtz vane (left) and equipped TEC (right)	51
Figure 4.5: Resonator vane (left) and equipped TEC (right).....	52
Figure 4.6: CAD cut of resonator vane.....	53
Figure 4.7: Riblets applied on a vane	54
Figure 4.8: Ideal riblet size	54
Figure 4.9: CAD comparison of Standard vane and Leaned vane	55
Figure 4.10: CAD model of the soft end walls	55
Figure 4.11: Soft end wall cassettes for inner (left) and outer casing (right)	56
Figure 4.12: Inner (left) and outer (right) ring of the resonator TEC.....	57
Figure 4.13: Standard TEC with and without soft end walls.....	57
Figure 4.14: Mounting of the absorber cassettes	58
Figure 4.15: Leaned TEC with soft end walls	58
Figure 4.16: Helmholtz vanes with soft end walls	58
Figure 4.17: Sketch of impedance tube (adapted from [82])	60
Figure 4.18: Acoustic mode shapes in a cylindrical duct and measurement positions in the impedance tube (adapted from [83])	60
Figure 4.19: Reflection coefficient - Hard end wall.....	61
Figure 4.20: Used impedance tube	62
Figure 5.1: Microphones plates at hub (left) and tip (right)	64
Figure 5.2: Locations of reference microphones.....	64
Figure 5.3: Mounting of the reference microphone inside the resonator	65
Figure 5.4: Five-hole-probe (top) and sketch of the probe head (bottom; adapted from [84]).	66
Figure 5.5: Definition of the flow angles.....	68
Figure 5.6: Definition of sign convention [36]	69
Figure 5.7: Measurement planes (left) and sectors (right).....	69
Figure 5.8: Trailing edge probe inside the test rig	70
Figure 6.1: Vane mount at the impedance tube.....	77
Figure 6.2: Comparison of hard wall and 3.2 mm neck diameter.....	77
Figure 6.3: Test of Helmholtz vane with different absorber neck diameters	78
Figure 6.4: Comparison of hard wall and two open necks with 3.5 mm.....	79
Figure 6.5: Test of Helmholtz vane with altering number of holes at diameter 3.5 mm	79
Figure 6.6: Comparison of the resonance frequency of single absorbers with 3.5 mm neck diameter	80
Figure 6.7: Distribution of resonance frequency over absorber neck diameter – Helmholtz vane	81
Figure 6.8: Comparison of hard wall and absorber row nr. 1 of the Helmholtz vane.....	81
Figure 6.9: Test of Helmholtz vane with altering number of rows at neck diameter 3 mm.....	82
Figure 6.10: Distribution of resonance frequency over absorber neck diameter – Soft end wall	83
Figure 6.11: Resonator vane mount	84
Figure 6.12: Comparison hard wall configuration and 1 row from Resonator vane.....	84
Figure 6.13: Comparison of different number of open absorber rows of the Resonator vane .	85
Figure 6.14: Theoretical normal incident reflection coefficient Resonator vane.....	86
Figure 6.15: Frequency spectra with investigated area	87

Figure 6.16: Example for overall PWL	87
Figure 6.17: Visualisation example of aerodynamical parameters	89
Figure 6.18: Examples of the flow fields downstream of the TEC.....	89
Figure 6.19: Frequency spectra - Configurations (A) and (E).....	91
Figure 6.20: Overall PWL comparison - Configurations (A) and (E).....	91
Figure 6.21: Frequency spectra - Configurations (A) and (F)	92
Figure 6.22: Overall PWL comparison - Configurations (A) and (F).....	92
Figure 6.23: Frequency spectra - Configurations (A) and (G).....	93
Figure 6.24: Overall PWL comparison - Configurations (A) and (G).....	93
Figure 6.25: Aerodynamical comparison - Configurations (A), (E), (F), and (G).....	94
Figure 6.26: Aerodynamical flow fields – Configurations (A), (E), (F), and (G)	95
Figure 6.27: Comparison of vane wake measurements – Helmholtz vane design.....	96
Figure 6.28: Helmholtz vane with markers for channel height.....	96
Figure 6.29: Helmholtz vane and zoom in for roughness visualisation	97
Figure 6.30: PWL^+ change of cut-on modes – Helmholtz vanes.....	97
Figure 6.31: PWL^- change of cut-on modes – Helmholtz vanes.....	98
Figure 6.32: Rotor wake impinging TEGV	98
Figure 6.33: Frequency spectra - Configurations (A) and (B).....	99
Figure 6.34: Overall PWL comparison - Configurations (A) and (B)	100
Figure 6.35: Frequency spectra - Configurations (A) and (C).....	101
Figure 6.36: Overall PWL comparison - Configurations (A) and (C)	101
Figure 6.37: Frequency spectra - Configurations (A) and (D).....	102
Figure 6.38: Overall PWL comparison - Configurations (A) and (D)	103
Figure 6.39: PWL^+ change of cut-on modes – Configurations (B), (C), and (D).....	104
Figure 6.40: PWL^- change of cut-on modes – Configurations (B), (C), and (D)	104
Figure 6.41: Aerodynamical comparison - Configurations (A), (B), (C), and (D).....	105
Figure 6.42: Aerodynamical flow fields – Configurations (A), (B), (C), and (D).....	105
Figure 6.43: Frequency spectra - Configurations (I) and (J)	106
Figure 6.44: Overall PWL comparison - Configurations (I) and (J).....	107
Figure 6.45: PWL^\pm change of cut-on modes – Configuration (I).....	107
Figure 6.46: Aerodynamical comparison - Configuration (I) and (J)	108
Figure 6.47: Aerodynamical flow fields – Leaned vane design	109
Figure 6.48: Frequency spectra - Configurations (A) and (H).....	110
Figure 6.49: Overall PWL comparison - Configurations (A) and (H).....	110
Figure 6.50: PWL^\pm change of cut-on modes – Configuration (H).....	111
Figure 6.51: Aerodynamical comparison - Configurations (A) and (H).....	111
Figure 6.52: Aerodynamical flow fields – Configurations (A) and (H).....	112
Figure 6.53: Frequency spectra - Configurations (A) and (K).....	113
Figure 6.54: Overall PWL comparison - Configurations (A) and (K)	114
Figure 6.55: PWL^\pm change of cut-on modes – Configuration (K).....	114
Figure 6.56: Aerodynamical comparison - Configurations (A) and (K).....	115
Figure 6.57: Aerodynamical flow fields – Configurations (A) and (K).....	116
Figure 6.58: Comparison of vane wake measurements - Configurations (A), (G), and (K) ..	116
Figure 6.59: PWL^+ change of interaction modes and their scatted modes – Standard, Helmholtz, and Resonator vane designs	118
Figure 6.60: PWL^- change of interaction modes and their scatted modes – Standard, Helmholtz, and Resonator vane designs	118
Figure 6.61: PWL^+ change of interaction modes and their scatted modes – Leaned vane design	119
Figure 6.62: PWL^- change of interaction modes and their scatted modes – Leaned vane design	120

Figure 6.63: Change of rotor - TEC interaction modes - Configuration (A) and (I)	120
Figure 6.64: PWL^+ change regarding the mode spinning direction – Standard, Helmholtz, and Resonator vane designs.....	121
Figure 6.65: PWL^- change regarding the mode spinning direction – Standard, Helmholtz, and Resonator vane designs.....	122
Figure 6.66: PWL^+ change regarding the mode spinning direction – Leaned vane design....	122
Figure 6.67: PWL^- change regarding the mode spinning direction – Leaned vane design	123
Figure 6.68: Frequency spectra – Configurations (L), (M), and (N).....	125
Figure 6.69: Frequency spectra of Configurations (L) and (M)	126
Figure 6.70: Frequency spectra of configurations (L) and (N).....	126
Figure 6.71: Overall PWL^\pm – Configurations (L), (M), and (N).....	127
Figure 6.72: Aerodynamical comparisons – Rotor-exit – Configurations (L), (M), and (N).128	
Figure 6.73: Aerodynamical flow fields – Rotor exit – Configurations (L) (M) and (N).....	129
Figure 6.74: Aerodynamical comparisons – TEC-exit – Configurations (L), (M), and (N) ..	130
Figure 6.75: Oilflow visualizations – Vane suction side – Configurations (L) and (M).....	130
Figure 6.76: Aerodynamic flow fields of the reference setup (L) and configurations (M) and (N) – TEC exit.....	131
Figure 6.77: Oilflow visualisations - Configurations (M) (1, 2, and 3) and (L) (4).....	132
Figure 6.78: Vane wake measurements results - Configurations (L), (M), and (N)	132
Figure 6.79: Oilflow visualizations – Pressure side – Configurations (L) and (M).....	133
Figure 7.1: Sound power level at 1 st BPF for all investigated configurations	135
Figure 7.2: Overall PWL comparison in and against flow direction – All configurations....	136
Figure 12.1: Reflection and transmission of incident radial modes at an treated/untreated duct interface (adapted from [15]).....	153
Figure 12.2: Frequency spectra – Configurations (L), (M), and (N) – Off-design point	157
Figure 12.3: Overall PWL^\pm - Configurations (L), (M), and (N) - Off-design point	158
Figure 12.4: Aerodynamical comparison - Configurations (L), (M) and (N) - Off-design point	159
Figure 12.5: Aerodynamical flow fields – Configurations (L), (M) and (N) – Off-design point	159
Figure 12.6: Inverse cut-off vane design (left and middle) and section of the equipped TEC	160
Figure 12.7: Frequency spectra – Configurations (O) and (P).....	161
Figure 12.8: Frequency spectra – Configurations (O) and (P) – Zoom in.....	161
Figure 12.9: Overall PWL^\pm - Configurations (O) and (P)	162
Figure 12.10: PWL^\pm change of cut-on modes – Configurations (O) and (P)	162
Figure 12.11: PWL^\pm change regarding the mode spinning direction – Inverse cut-off TEC .163	
Figure 12.12: Asymmetric Helmholtz absorber (taken from [102])	163
Figure 12.13: Reflection coefficient result - Inverse cut-off TEC (adapted from [94]).....	163
Figure 12.14: Frequency spectra	164
Figure 12.15: Frequency spectra with filtered result (left) and filtered distribution alone (right)	164
Figure 12.16: Filtered signal with lower envelope.....	165
Figure 12.17: Comparison of lower envelopes	165

10 List of Tables

Table 4.1: Operating Point.....	49
Table 4.2: Stage geometry details	49
Table 4.3: Overview of investigated configurations	50
Table 4.4: Absorber positions – Helmholtz vane.....	51
Table 4.5: Geometrical details of the Helmholtz vane absorber.....	52
Table 4.6: Calculated resonance frequencies with and without Ma number - Helmholtz vane.....	52
Table 4.7: Geometrical details of the Resonator vane absorber	53
Table 4.8: Axial positions of absorbers – Soft end walls	56
Table 4.9: Geometrical details of the soft end walls	56
Table 4.10: Calculated resonance frequencies with and without Ma number – Soft end walls	57
Table 4.11: Cut-on frequencies of the impedance tube in [Hz]	59
Table 5.1: Location of the microphones.....	64
Table 5.2: Calibration range of the five-hole-probe.....	66
Table 5.3: Radial measurement points for the FHP in percent of the channel height.....	70
Table 5.4: Measurement uncertainties of the five-hole-probe	71
Table 6.1: Comparison of measured and calculated resonance frequencies – Helmholtz vane	80
Table 6.2: Comparison of measured and calculated resonance frequencies – Soft end wall	83
Table 6.3: Airfoil interaction modes and their scattered modes on the TEC.....	88
Table 6.4: Aerodynamic parameters – Helmholtz vane	96
Table 6.5: Aerodynamic parameters - Configurations (A), (G), and (K).....	117
Table 6.6: Change of PWL^{\pm} - Spinning modes.....	124
Table 6.7: Results of wake measurements - Configurations (L), (M), and (N).....	133
Table 6.8: Shape factor – Configurations (L), (M), and (N).....	133
Table 7.1: Calculated and measured resonance frequencies of soft end walls	135

11 References

- [1] E. Comission, "Flightpath 2050 - Europe's Vision for Aviation," 2011.
- [2] R. Astley, A. Agarwal, K. Holland, P. Joseph, R. Self, M. Smith, R. Sugimoto and B. Tester, "Predicting and Reducing Aircraft Noise," *14th International Congress on Sound and Vibration*, 2007.
- [3] [Online]. Available: <https://www.rolls-royce.com/products-and-services/civil-aerospace/airlines/trent-7000.aspx#section-related-stories>. [Accessed 04 March 2020].
- [4] [Online]. Available: <http://theflyingengineer.com/flightdeck/pw1100g-gtf/>. [Accessed 04 March 2020].
- [5] [Online]. Available: <https://academieairespace.com/wp-content/uploads/2018/05/prattw.pdf>. [Accessed 04 March 2020].
- [6] A. Kempton, "Acoustic liners for modern aero-engines," [Online]. Available: https://www.win.tue.nl/ceas-asc/Workshop15/CEAS-ASC_XNoise-EV_K1_Kempton.pdf. [Accessed 04 March 2020].
- [7] W. J. Bräunling, *Flugzeugtriebwerke*, Springer, 2015.
- [8] W. Herkes, R. Olsen and S. Uellenberg, "The Quiet Technology Demonstrator Program: Flight Validation of Airplane Noise-Reduction Concepts," *12th AIAA/CEAS Aeroacoustics Conference (27th AIAA Aeroacoustics Conference)*, 8-10 May 2006.
- [9] H. Batard, "Aircraft noise reduction: Airbus industrial needs in terms of new materials for nacelle liners," *Journées scientifiques de l'ONERA*, 2003.
- [10] J. Tyler and T. Sofrin, "Axial Flow Compressor Noise Studies," *SAE Transactions*, vol. 70, pp. 309-332, 1962.
- [11] M. Möser, *Messtechnik der Akustik*, Springer, 2010.
- [12] L. Enghardt, L. Neuhaus and C. Lowis, "Broadband Sound Power Determination in Flow Ducts," *Proceeding of the 10th AIAA/CEAS Aeroacoustics Conference*, 2004.
- [13] H. H. Hubbard, "Aeroacoustics of Flight Vehicles: Theory and Practice - Vol. 2: Noise Control," *NASA Reference Publication 1258, Vol.2; WRDC Technical Report 90-3052*, 1991.

- [14] S. Rienstra and A. Hirschberg, *An Introduction to Acoustics*, Eindhoven University of Technology, 2018.
- [15] F. Montétagaud and H. Batard, "About the complexity of propagation and radiation of duct modes," *6th AIAA/CEAS Aeroacoustics Conference and Exhibition*, 2000.
- [16] F. Montétagaud, H. Batard and P. Lempereur, "Modal Conversion from Untreated to Treated Cylindrical Ducts," *4th AIAA/CEAS Aeroacoustics Conference*, 1998.
- [17] C. Tam, H. Ju and E. Chien, "Scattering of acoustic duct modes by axial liner splices," *Journal of Sound and Vibration Vol. 310*, pp. 1014-1035, 2008.
- [18] D. Broszat, "Aircraft engine noise footprint reduction via a non-uniform inlet liner concept," *PhD Thesis at Technical University of Munich*, 2008.
- [19] T. J. Cox and P. D'Antonio, *Acoustic Absorbers and Diffusers - Theory, Design and Application - Third Edition*, CRC Press, 2017.
- [20] H. von Helmholtz, "Theorie der Luftschwingungen in Röhren mit offenen Enden," 1859.
- [21] J. Roche, L. Leylekian, G. Delattre and F. Vuillot, "Aircraft Fan Noise Absorption: DNS of the Acoustic Dissipation of Resonant Liners," *15th AIAA/CEAS Aeroacoustics Conference*, 2009.
- [22] U. Ingard, "On the Theory and Design of Acoustic Resonators Vol. 25," *The Journal of the Acoustical Society of America*, pp. 1037-1061, 1953.
- [23] R. Chanaud, "Effects of Geometry on the Resonance Frequency of Helmholtz Resonators, Part II," *Journal of Sound and Vibration Vol. 204(5)*, pp. 829-834, 1997.
- [24] E. Rice, "A Model for the Acoustic Impedance of a Perforated Plate Liner with Multiple Frequency Excitation". *NASA Technical Memorandum NASA TM X-67950*.
- [25] D.-Y. Maa, "Potential of microperforated panel absorber," *Journal of the Acoustic Society of America, Vol. 104 (5)*, pp. 2861-2866, November 1998.
- [26] Y. Qian, D. Kong, S. Liu, S. Sun and Z. Zhao, "Investigation on micro-perforated panel absorber with ultra-micro perforations," *Applied Acoustics Vol. 74(7)*, pp. 931-935, July 2013.
- [27] L. Langston, "Secondary Flows in Axial Turbines - A Review," *Annals of the New York Academy of Sciences Vol. 934*, pp. 11-26, 2001.
- [28] C. Sieverding, "Recent Progress in the Understanding of Basic Aspects of Secondary Flows in Turbine Blade Passages," *Journal of Engineering for Gas Turbines and Power Vol. 107*, pp. 248-257, 1985.
- [29] H. Wang, S. Olson, R. Goldstein and E. Eckert, "Flow Visualization in a Linear Turbine Cascade of High Performance Turbine Blades," *Journal of Turbomachinery, Vol. 119*, January 1997.
- [30] B. Lakshminarayana and J. Horlock, "Review: Secondary Flows and Losses in Cascades and Axial-Flow Turbomachines," *Int. J. Mech. Sci., Vol. 5*, pp. 287-307, 1963.
- [31] B. Lakshminarayana, *Fluid Dynamics and Heat Transfer of Turbomachinery*, Wiley & Sons, Inc, 1996.
- [32] M. Yaras and S. Sjolander, "Effects of Simulated Rotation on Tip Leakage in a Planar Cascade of Turbine Blades: Part I - Tip Gap Flow," *Journal of Turbomachinery, Vol. 114*, pp. 652-659, July 1992.

- [33] J. Denton, "Loss Mechanisms in Turbomachines," *Journal of Turbomachinery Vol. 115*, pp. 621-656, October 1993.
- [34] M. T. Schobeiri and J. John, "A Study of the Development of Steady and Periodic Unsteady Turbulent Wake Through Curved Channels at Positive, Zero, and Negative Streamwise Pressure Gradients, Part I," *NASA Contractor Report 198448*, 1996.
- [35] H. Schlichting and K. Gersten, "Grenzschicht Theorie, 10. Auflage," 2005.
- [36] T. Selic, "Experimental Investigation of the Aerodynamics and Acoustics of Exit Guide Vanes for Future Aircraft Engines," *PhD Thesis at Graz University of Technology*, 2015.
- [37] D. Bechert, G. Hoppe and W.-E. Reif, "On the drag reduction of the shark skin," *23rd Aerospace Sciences Meeting*, 1985.
- [38] Bionic Surface Technologies GmbH, [Online]. Available: <https://www.bionicsurface.com/en/drag-reduction-with-shark-skin-technology-riblets-and-coating/>. [Accessed January 2020].
- [39] A. Hafizovic, "Einfluss innovativer Oberflächenstrukturen auf die Schallabstrahlung moderner Zweikreistriebwerke," *Master thesis at Graz University of Technology*, 2019.
- [40] H. Choi, P. Moin and J. Kim, "Direct numerical simulation of turbulent flow over riblets," *Journal of Fluid Mechanics Vol. 225*, pp. 503-539, 1993.
- [41] E. Skudrzyk and G. Haddle, "Noise Production in a Turbulent Boundary Layer by Smooth and Rough Surfaces," *The Journal of the Acoustic Society of America, Vol.32*, pp. 19-34, 1960.
- [42] M. Lighthill, "On sound generation aerodynamically I. General theory," *Proceedings of the Royal Society of London A Vol 211*, pp. 564-587, 1951.
- [43] M. Lighthill, "On sound generated aerodynamically II. Turbulence as a source of sound," *Proceedings of the Royal Society of London A Vol. 222*, pp. 1-32, 1953.
- [44] ICAO, "Environmental technical manual on the use of procedures in the noise certification of aircraft, Technical Report," 2004.
- [45] L. Rayleigh, *Theory of Sound*, Second edition, New York: Dover Publications.
- [46] R. Panton and J. Miller, "Resonant frequencies of cylindrical Helmholtz resonators," *Journal of Acoustical Society of America Vol. 57*, pp. 1533-1535, 1975.
- [47] A. Selamet, N. Dickey and J. Novak, "Theoretical, computational and experimental investigation of Helmholtz resonators with fixed volume: Lumped versus distributed analysis," *Journal of Sound and Vibration, Vol. 187(2)*, pp. 358-367, 1995.
- [48] R. Chanaud, "Effects of Geometry von the Resonance Frequency of Helmholtz Resonators," *Journal of Sound and Vibration, Vol. 178(3)*, pp. 337-348, 1994.
- [49] S. Seo and Y. Kim, "Silencer design by using array resonators for low-frequency band noise reduction," *Journal of the Acoustical Society of America, Vol. 118(4)*, pp. 2332-2338, October 2005.
- [50] J. Anderson, "The Effect of an Air Flow on a Single Side Branch Helmholtz Resonator in a Circular Duct," *Journal of Sound and Vibration, Vol. 52*, pp. 423-431, 1977.
- [51] B. Phillips, "Effects of High-Wave Amplitude and Mean Flow on a Helmholtz Resonator," *NASA Technical Memorandum, NASA TM X-1582*, 1968.

- [52] E. Selamet, A. Selamet, A. Iqbal and H. Kim, "Effect of Flow on Helmholtz Resonator Acoustics: A Three-Dimensional Computational Study vs. Experiments," *SAE International*, 2011.
- [53] W. Bell, B. Daniel and B. Zinn, "Acoustic Liner Performance in the Presence of a Mean Flow and Three-Dimensional Wave Motion," *AIAA 12th Aerospace Sciences Meeting*, 1974.
- [54] A. Serrano and G. Torres, "Estimation of Turbine Noise Benefits due to Acoustically Treated Outlet Guide Vanes," *Proceedings of 11th European Conference on Turbomachinery Fluid dynamics & Thermodynamics*, 23-27 March 2015.
- [55] D. Elliot, R. Woodward and G. Podboy, "Acoustic Performance of Novel Fan Noise Reduction Technologies of a High Bypass Model Turbofan at Simulated Flight Conditions," *15th AIAA/CEAS Aeroacoustic Conference*, 2009.
- [56] D. Broszat, U. Tapken, L. Enghardt, D. Lengani and A. Marn, "Validation of an Integrated Acoustic Absorber in a Turbine Exit Guide Vane," *17th AIAA/CEAS Aeroacoustics Conference*, 2011.
- [57] D. Bechert, M. Bruse, W. Hage, J. Van der Hoeven and G. Hoppe, "Experiments on drag-reducing surfaces and their optimization with an adjustable geometry," *J. Fluid Mech. Vol. 338*, pp. 59-87, 1997.
- [58] P. Luchini, F. Manzo and A. Pozzi, "Resistance of a grooved surface to parallel flow and cross-flow," *Journal of Fluid Mechanics Vol. 228*, pp. 87-109, 1991.
- [59] C. Fang, T. Yan-Ping and C. Mao-Zhang, "An Experimental Investigation of Loss Reduction with Riblets on Cascade Blade Surfaces and Isolated Airfoils," *Gas Turbine and Aeroengine Congress and Exposition, Brussels, Belgium*, 1990.
- [60] M. Boese and L. Fottner, "Effects of Riblets on the Loss Behavior of a Highly Loaded Compressor Cascade," *Proceedings of ASME Turbo Expo 2002*, June 3-6 2002.
- [61] C. Lietmeyer, K. Ohlert and J. R. Seume, "Optimal Application of Riblets on Compressor Blades and Their Contamination Behavior," *Journal of Turbomachinery Vol. 135(1)*, January 2013.
- [62] J. Debisschop and F. Nieuwstadt, "Turbulent Boundary Layer in an Adverse Pressure Gradient: Effectiveness of Riblets," *AIAA Journal Vol. 34(5)*, pp. 932-937, 1996.
- [63] F. Nieuwstadt, W. Wolthers, H. Leijdens, K. Krishna Prasad and A. Schwarz-van Manen, "The reduction of skin friction by riblets under the influence of an adverse pressure gradient," *Experiments in Fluids Vol. 15*, pp. 17-26, 1993.
- [64] X. Miao, Q. Zhang, L. Wang, H. Jiang and H. Qi, "Application of Riblets on Turbine Blade Endwall Secondary Flow Control," *Journal of Propulsion and Power, Vol. 31, No. 6*, 2015.
- [65] H. Koch and D. Kozulovic, "Outlet Guide Vane Airfoil for Low Pressure Turbine Configurations," *42nd AIAA Fluid Dynamics Conference and Exhibition, Paper Nr. 2012-2979*, 2012.
- [66] S. Kang and C. Hirsch, "Three Dimensional Flow in a Compressor Cascade at Design Conditions," *Proceeding of ASME Turbo Expo 1991, Orlando, Florida*, 3-6 June 1991.

- [67] D. Halstead, D. Wisler, T. Okiishi, G. Walker, H. Hodson and H. Shin, "Boundary layer development in axial compressors and turbines - Part 1 of 4: Composite Picture," *Journal of Turbomachinery Vol. 119(1)*, pp. 114-127, January 1997.
- [68] D. Halstead, D. Wisler, T. Okiishi, G. Walker, H. Hodson and W. Shin, "Boundary layer development in axial compressors and turbines - Part 2 of 4: Compressors," *Journal of Turbomachinery Vol. 119(3)*, pp. 426-444, July 1997.
- [69] D. Halstead, D. Wisler, T. Okiishi, G. Walker, H. Hodson and W. Shin, "Boundary layer development in axial compressors and turbines - Part 3 of 4: LP Turbines," *Journal of Turbomachinery Vol. 119(2)*, pp. 225-237, April 1997.
- [70] D. Halstead, D. Wisler, T. Okiishi, G. Walker, H. Hodson and W. Shin, "Boundary layer development in axial compressors and turbines - Part 4 of 4: Computations and analysis," *Journal of Turbomachinery Vol. 119(1)*, pp. 128-139, January 1997.
- [71] A. McCarter, X. Xiao and B. Lakshminarayana, "Tip Clearance Effects in a Turbine Rotor: Part II - Velocity Field and Flow Physics," *Journal of Turbomachinery, Vol. 123*, pp. 305-313, April 2001.
- [72] X. Xiao, A. McCarter and B. Lakshminarayana, "Tip Clearance Effects in a Turbine Rotor: Part I - Pressure Field and Loss," *Journal of Turbomachinery, Vol. 123*, pp. 296-304, April 2001.
- [73] S. Yoon, E. Curtis, J. Denton and J. Longley, "The Effect of Clearance on Shrouded and Unshrouded Turbines at Two Levels of Reaction," *Journal of Turbomachinery, Vol. 136*, February 2014.
- [74] T. Selic, D. Lengani, A. Marn and F. Heitmeir, "Aerodynamic Effects of an Unshrouded Low Pressure Turbine on a Low Aspect Ratio Exit Guide Vane," *Proceedings of ASME Turbo Expo*, June 2012.
- [75] S. Bauinger, B. Lindenthaler, R. Willinger, A. Marn and F. Heitmeir, "Impact of Different Shroud Configurations on Leakage Flow of a LP Rotor," *Proceedings of 12th European Conference on Turbomachinery, Fluid dynamics & Thermodynamics*, 3-7 April 2017.
- [76] M. Moser, G. Kahl, G. Kulhanek and F. Heitmeir, "Construction of a Subsonic Test Turbine Facility for Experimental Investigations of Sound Generation and Propagation for Low Pressure Turbines," Beijing, China, 2007.
- [77] M. Moser, "Untersuchung der Niederdruckturbinenlärmmmission von Flugtriebwerken in einem neuen Turbinenakustikprüfstand," *PhD Thesis, Graz University of Technology*, 2008.
- [78] A. Marn, T. Selic, F. Schönleitner, S. Zerobin, D. Broszat, M. Hoeger and F. Heitmeir, "Acoustic Comparison of Different Turbine Exit Guide Vane Designs Part 2: Experimental Analysis," *21st AIAA/CEAS Aeroacoustics Conference*, 22-26 June 2015.
- [79] A. Marn, D. Broszat, T. Selic, F. Schönleitner and F. Heitmeir, "Comparison of the Aerodynamics of Acoustically Designed Exit Guide Vanes and a State-of-the-Art Exit Guide Vane," *ASME Journal of Turbomachinery, Vol.137*, April 2015.
- [80] D. Broszat, F. Kennepohl, U. Tapken, M. Moser and F. Heitmeir, "Validation of an Acoustically 3-D Designed Turbine Exit Guide Vane," *16th AIAA/CEAS Aeroacoustics Conference*, 2010.
- [81] R. Brunnader, "Aufbau und Programmierung der 2p Messmethode im Impedanzrohr für die Messung akustischer Materialparameter," *Master Thesis at Graz University of Technology*, 2002.

- [82] A. Lugmair, "Helmholtzresonatoren mit veränderlichem Volumen, in den Seitenwänden von Turbinenausstrittsgehäusen," *Bachelor Thesis at Graz University of Technology*, 2019.
- [83] A. Sanada, "Extension of the frequency range of normal-incidence sound-absorption-coefficient measurement using four or eight microphones," *Acoust. Sci. & Tech. Vol 38, 5 (2017)*, pp. 261-263, 2017.
- [84] V. Dehe, "Kalibrierbericht der pneumatischen Fünflochsonde mit Temperaturmessstelle 1/06," 2019.
- [85] T. Arnold and M. Eifel, "Kalibrierbericht der pneumatischen Fünflochsonde 01/06 mit Temperaturmessstelle," 2006.
- [86] Acoustical Society of America, "ANSI S1.4: 1983 - Specifications for Sound Level Meters," *American National Standard*, 1983.
- [87] L. Enghardt, U. Tapken, O. Kornow and F. Kennepohl, "Acoustic Mode Decomposition of Compressor Noise Under Consideration of Radial Flow Profiles," *11th AIAA/CEAS Aeroacoustic Conference*, pp. 1-13, 2005.
- [88] L. Enghardt, U. Tapken, W. Neise, F. Kennepohl and K. Heinig, "Turbine Blade/Vane Interaction Noise: Acoustic Mode Analysis Using In-Duct Sensor Arrays," *7th AIAA/CEAS Aeroacoustic Conference*, pp. 1-8, 28-30 May 2001.
- [89] L. Munjal, "Acoustics of ducts and mufflers," *Wiley*, 2014.
- [90] P. Sijtsma and J. Zillmann, "In-Duct and Far-Field Mode Detection Techniques for Engine Exhaust Noise Measurements," *13th AIAA/CEAS Aeroacoustics Conference, Rome*, 21-23 May 2007.
- [91] U. Tapken and L. Enghardt, "Optimization of Sensor Arrays for Radial Mode Analysis in Flow Ducts," *12th AIAA/CEAS Aeroacoustics Conference*, pp. 1-20, 2006.
- [92] C. Morfey, "Sound Transmission and Generation in Ducts with Flow," *Journal of Sound and Vibration*, vol. 14, no. 1, pp. 37-55, 1971.
- [93] R. Kabral, H. Bodén and T. Elnady, "Determination of Liner Impedance under High Temperature and Grazing Flow Conditions," *20th AIAA/CEAS Aeroacoustics Conference*, 13-20 June 2014.
- [94] J. Liu, X. Hua and D. Herrin, "Estimation of effective parameters for microperforated panel absorbers and applications," *Applied Acoustics Vol. 75*, pp. 86-93, 2014.
- [95] L. Barro Savonuzzi, "Experimental Assessment on the Noise Absorbing Capability of Turbine Exit Guide Vanes Equipped with Helmholtz Resonators," *Master Thesis at Politecnico di Milano and Graz University of Technology*, 2017.
- [96] F. Schönleitner, "Schwingungsanregung verschiedener Turbinenausstrittsgehäuse zukünftiger Flugtriebwerkskonzepte," *PhD Thesis, Graz University of Technology*, 2016.
- [97] W. Devenport, D. Grissom, W. Alexander, B. Smith and S. Glegg, "Measurements of roughness noise," *Journal of Sound and Vibration Vol. 330 (17)*, pp. 4250-4273, 15 August 2011.
- [98] J. Golliard and J. Bruggeman, "Broadband Noise of Flow-Excited Cavities: Comparison of Prediction Models with Experimental Data," *4th AIAA/CEAS Aeroacoustics Conference*, 1998.

- [99] Q. Zhang, M. Goodro, P. Ligrani, R. Trindade and S. Sreekanth, "Influence of Surface Roughness on the Aerodynamic Losses of a Turbine Vane," *Journal of Fluids Engineering*, Vol. 128(3), pp. 568-578, 2006.
- [100] R. Motsinger and R. Kraft, "Aeroacoustics of flight vehicles, Theory and Practice, Chapter 14: Design and performance of duct acoustic treatments," *Acoustical Society of America*, 1995.
- [101] B. Elhadidi and H. Atassi, "Passive Noise Control by Blade Lean and Sweep," *10th AIAA/CEAS Aeroacoustics Conference*, 10-12 May 2004.
- [102] L. Simonassi, M. Zenz, S. Zerobin, T. Selic, F. Heitmeir and A. Marn, "On the Influence of an Acoustically Optimized Turbine Exit Casing Onto the Unsteady Flow Field Downstream of a Low Pressure Turbine Rotor," *Journal of Turbomachinery* Vol. 141, April 2019.
- [103] N. Etaix, K. Crawford, R. Voisey and H. Hopper, "Redesigning Helmholtz resonators to achieve attenuation at multiple frequencies," *Proceedings of the 22nd International Congress on Acoustics*, 5-9 September 2016.
- [104] C. Cai and C. Mag, "Acoustic performance of different Helmholtz resonator array configurations," *Applied Acoustics* Vol. 130, pp. 204-209, January 2018.
- [105] A. Sanada and N. Tanaka, "Extension of the frequency range of resonant sound absorbers using two-degree-of-freedom Helmholtz-based resonators with a flexible panel," *Applied Acoustics* Vol. 74(4), pp. 509-516, April 2013.
- [106] D. Broszat, T. Selic and A. Marn, "Verification of the Inverse Cut-off Effect in a Turbomachinery Stage Part 1 - Numerical results," *18th AIAA/CEAS Aeroacoustics Conference (33rd AIAA Aeroacoustics Conference)*, 04-06 June 2012.
- [107] D. Broszat, T. Selic and A. Marn, "Verification of the Inverse Cut-off Effect in a Turbomachinery Stage Part 2 - Comparison to experimental results," *19th AIAA/CEAS Aeroacoustics Conference*, 27-29 May 2013.
- [108] H. Joslyn and R. Dring, "Axial Compressor Stator Aerodynamics," *Journal of Engineering of Gas Turbine and Powers* Vol. 107, pp. 485-492, April 1985.

12 Annex

12.1 Change of Modal Content due to Impedance Discontinuity

As mentioned in section 2.1.5, impedance discontinuities lead to an exchange of energy between acoustic duct modes.

In [15] it is stated, that each impedance discontinuity results in a significant redistribution of the modal energy. If the duct geometry is axisymmetric the redistribution takes place at each circumferential mode. In this work two effects are stated which affect an acoustic wave inside a duct between the source and the duct end:

- A reflection and transmission at every impedance discontinuity
- A modal conversion between an untreated and a treated part of the duct

Figure 12.1 shows the behaviour of incident radial modes concerning their reflection and transmission at an interface between a treated and an untreated duct. A transmission concentrates the energy of a wave in the duct centre and a reflection dissipates it to the walls.

For a simple axisymmetric duct as they investigated an energy redistribution on each radial mode is possible, within the same azimuthal mode order. But they also mentioned that, if the geometry gets more complex, a redistribution also between the azimuthal modes takes place.

The second phenomenon is the so-called mode conversion (see also [16]). There a certain mode becomes a different mode due to the treated duct section. So this can change the modal content of a sound field completely.

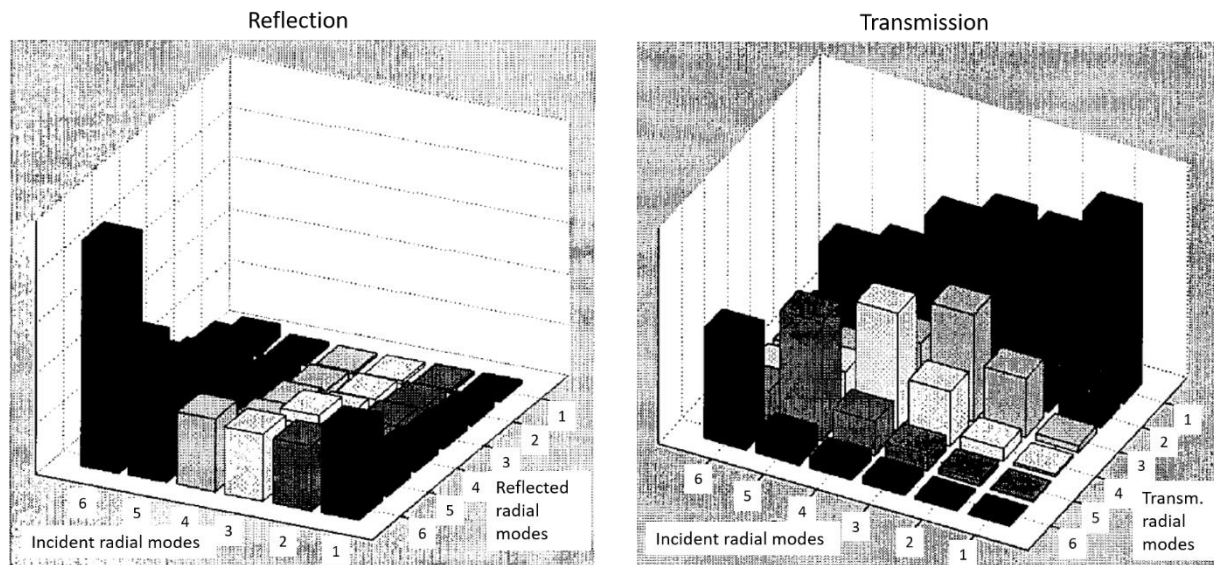
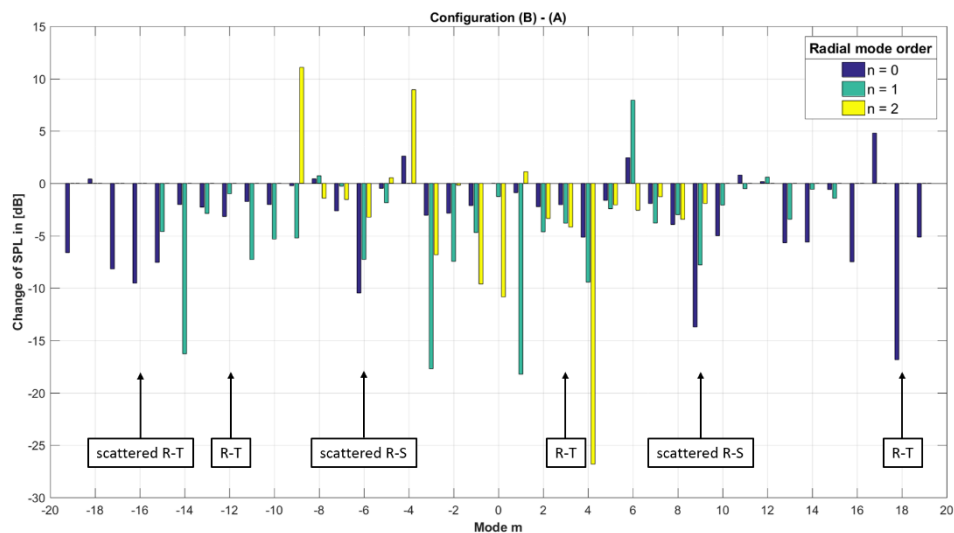
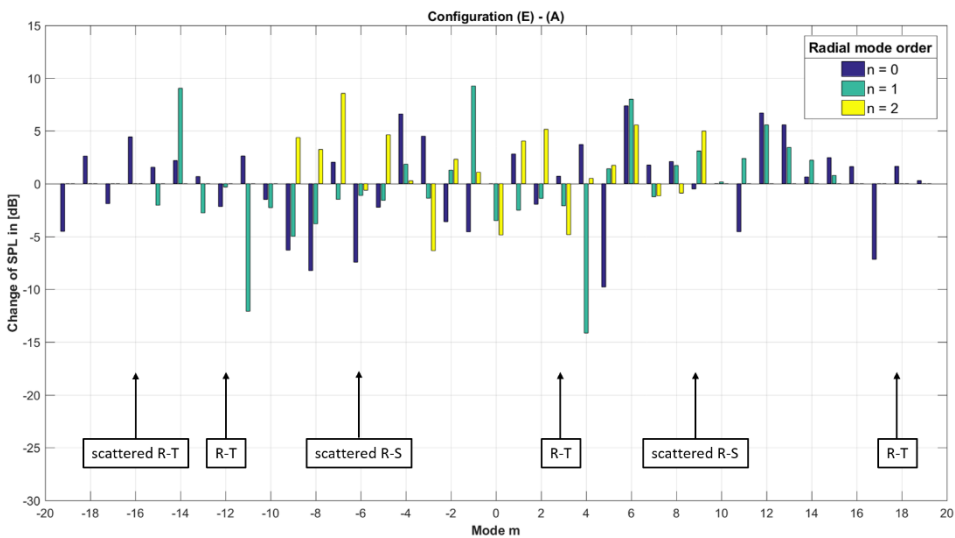
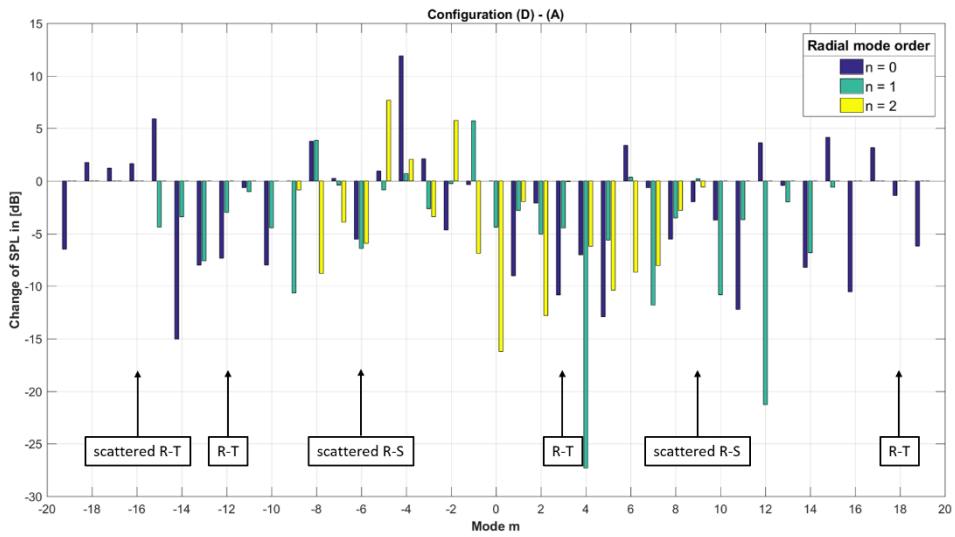
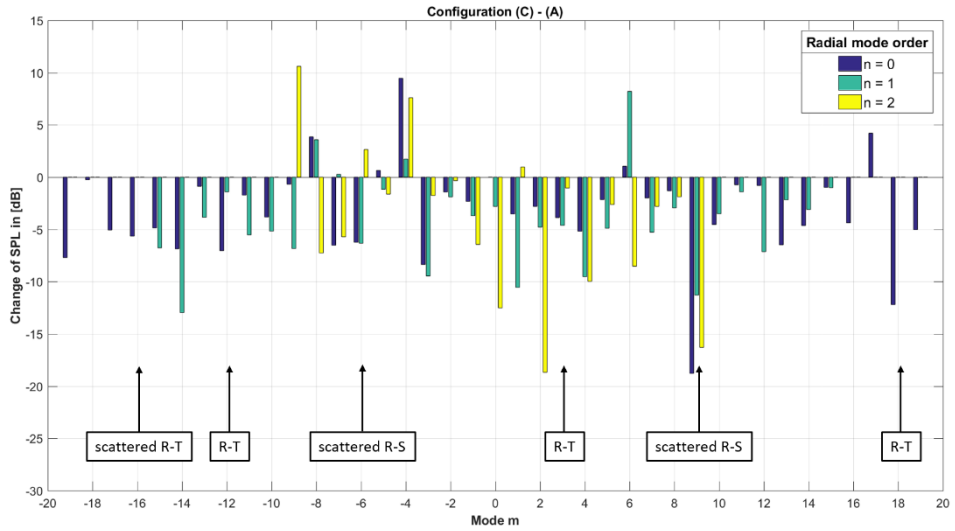


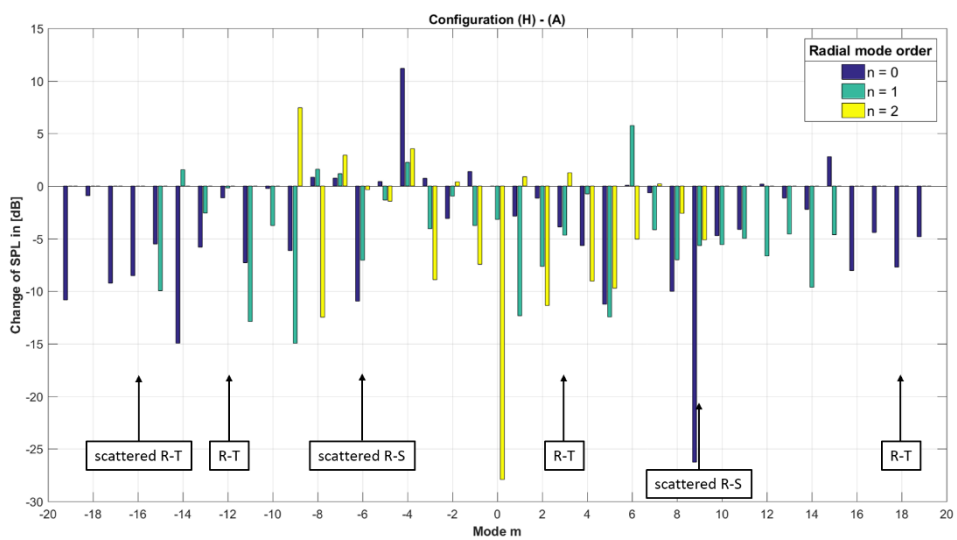
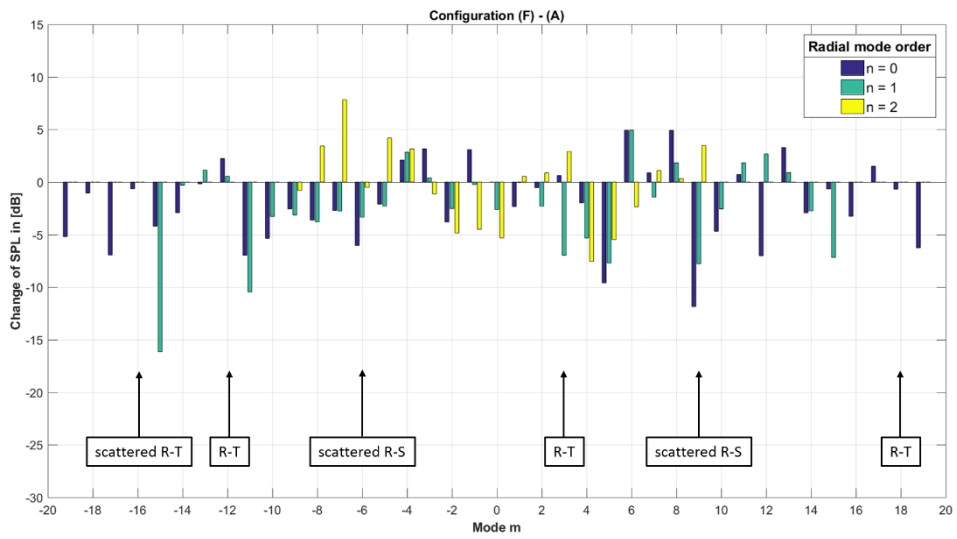
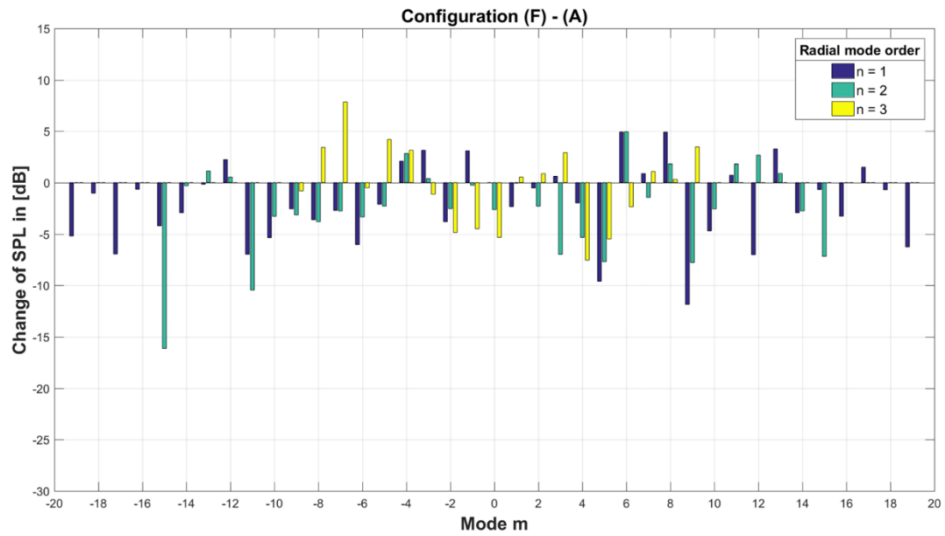
Figure 12.1: Reflection and transmission of incident radial modes at a treated/untreated duct interface (adapted from [15])

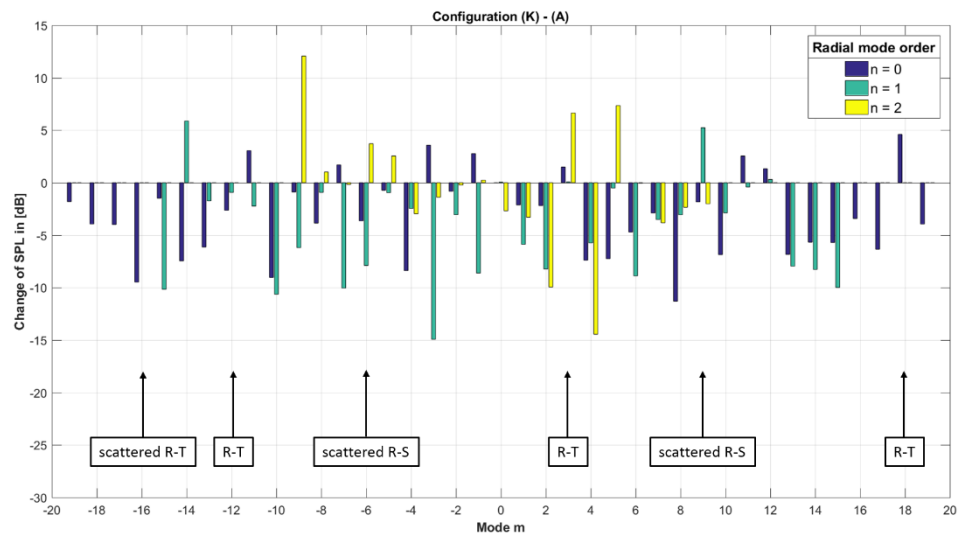
As seen in the section 4 concerning the investigated setups, multiple junctions between treated and untreated segments are located in the TECs. Additionally, vanes with and without included absorbers are used. These extremely complicated situations cannot be solved that easy concerning the energy redistribution between the modes. One possibility would be an intensive numerical investigation, which is not possible due to the needed computational power. Another possibility would be to perform more complex measurements of the incident sound field upstream of the liners as well as the one directly downstream. Unfortunately, there is not enough space in the test rig to implement another set of microphones in the needed number.

Therefore, no accurate investigations onto this topic could be realized within this thesis. Nevertheless, the following figures show that there is a significant energy change between the cut-on modes. For each setup, a comparison of the sound pressure level for all cut-on azimuthal modes, split up into the radial mode orders is given. All observations are done for a wave propagation direction equal to the flow direction. To see the change in SPL for each mode, the result of the baseline setup (A) is subtracted from the respective setup which is under investigation. It is noticeable, that all comparisons look different and no obvious pattern can be identified. This shows, that there is no predictable mode scattering due to the liners.









12.2 Riblets Investigations in an Off-design Point

The riblet designs explained in section 6.2.6 have not only be investigated in the design point of the riblets geometry but also in an off-design point because it is important to examine the influence of this surface structure also at off-design conditions. Using them in a real aero engine would lead exactly to such a situation. Therefore, the selected off-design point is a scaled version of the one during cruise.

The geometries of the riblets are equal to the ones examined in section 6.2.6. Because of the different operating point, the flow conditions are of course different and hence the streamlines on the TEGV suction side are changed.

Acoustics

In the following Figure 12.2, a direct comparison of the sound pressure level, given over the frequency, of the three configurations (L), (M), and (N) is shown. The reference setup is indicated with black and the two riblets setups are shown in orange and blue. It can already be seen, that there is no reduction of the background noise as observed in case of the design point investigations in section 6.2.6. But a reduction of the peaks over the whole frequency range can be observed, as it is also visible in the design point investigations. Especially in case of configuration (N) compared with the baseline setup (L). At the first and the second BPF, a decrease of 1 dB is achieved. The third BPF is reduced by a value of 1.3 dB. These three characteristic frequencies have the highest SPL and therefore also a reduction of the overall sound power level is achieved, which can be seen later on.

The setup (M) on the other side does not show a significant change in the SPL distribution compared to the reference case.

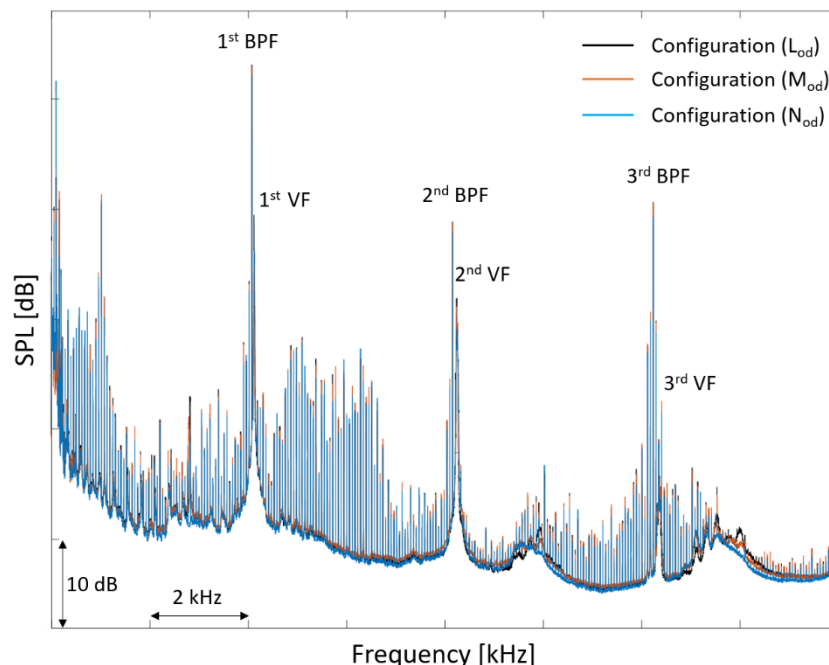


Figure 12.2: Frequency spectra – Configurations (L), (M), and (N) – Off-design point

Figure 12.3 shows the result concerning the overall sound power level in and against flow direction for the three setups (L), (M), and (N) for the off-design point. The PWL with a wave propagation direction in flow direction is indicated by the black bars and the one against the flow direction with yellow bars. As already seen at the results of the design point, also here a

reduction of the overall PWL could be achieved by using riblets. Between the reference case (L) and the setup (M) a difference of 0.3 dB is detected, which can be neglected due to the measurement uncertainty. Comparing the second riblets configuration (N) with the reference case (L), a PWL reduction of 1 dB can be seen when taking a look at the propagation direction equal to the flow direction. Against the flow direction, a reduction of 2.2 dB can be observed. In case of setup (M), no difference with respect to case (L) can be detected.

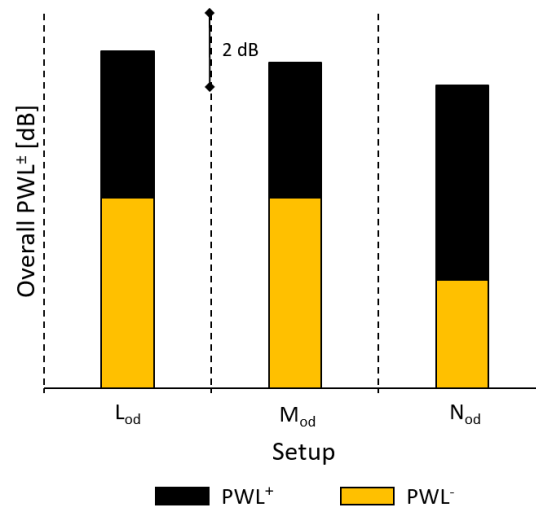


Figure 12.3: Overall PWL[±] - Configurations (L), (M), and (N) - Off-design point

Aerodynamics

Because it was recognized before that there is no upstream effect of the riblets, only the results concerning the aerodynamical parameters downstream of the turbine exit casing are shown.

Figure 12.4 gives the radial distribution of the circumferentially mass averaged values concerning the aerodynamical parameters total pressure normalized by the total pressure at stage inlet, the Mach number and the yaw angle. All parameters are shown over the relative channel height.

First it should be mentioned that the last measurement point at 95% relative channel height of setup (N) has an unconventional value due to a small area in which a measurement error occurred. These values have been excluded from the averaging procedure which results in these shapes of the radial distributions.

The normalized total pressure distributions show that the level is higher over the whole radial height for the two riblets configurations (M) and (N) with respect to the reference case (L). When comparing the shape of the radial distribution, it is visible that the one from setup (L) is slightly different over the whole relative channel height.

Concerning the Mach number, the shape of the radial distribution of (N) is slightly diverse to both other cases (L) and (M). The lower Mach number of the two riblet setups (M) and (N) indicate a better performance of the TEC having the microstructure applied on the vanes.

When looking at the yaw angle distribution it can be observed, that the result for setup (M) is again shifted to more positive values as already seen for the design point in section 6.2.6 but there is no additional shift in the centre of the channel height. Therefore, it is assumed that the riblets do not work in this off-design point but they also don't worsen the aerodynamical performance of the vane row.

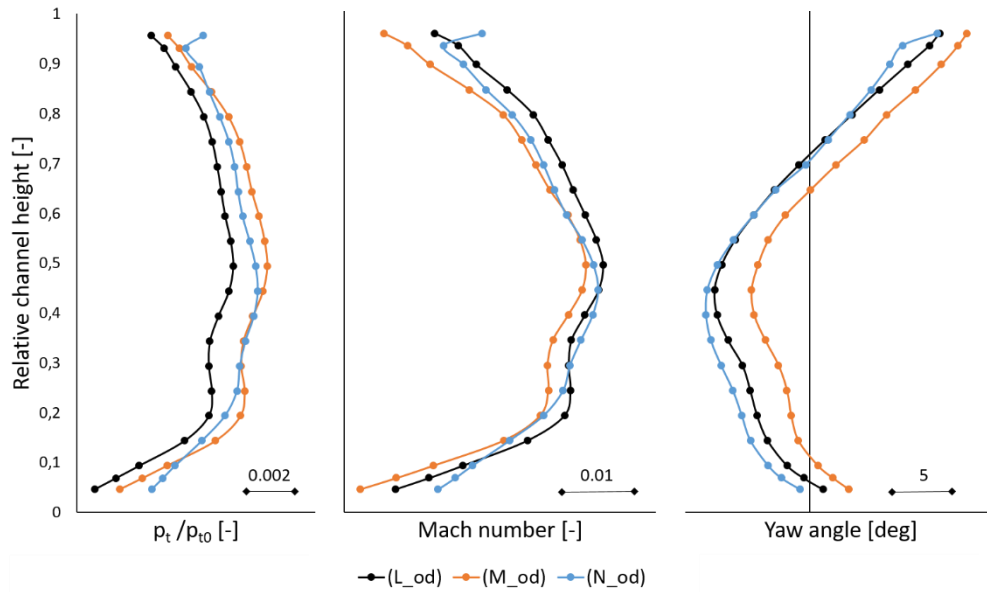


Figure 12.4: Aerodynamical comparison - Configurations (L), (M) and (N) - Off-design point

Figure 12.5 shows the corresponding flow fields to the discussed radial distributions. Herein, the vane wake is indicated by the black dashed line having the vane suction side on the left and the pressure side on the right side. Four regions are marked with numbers (I, II, III, and IV) which are related to secondary flow effects in the vane passage. The top three plots show the normalized total pressure of the configurations (L), (M), and (N) and the lower ones the yaw angle.

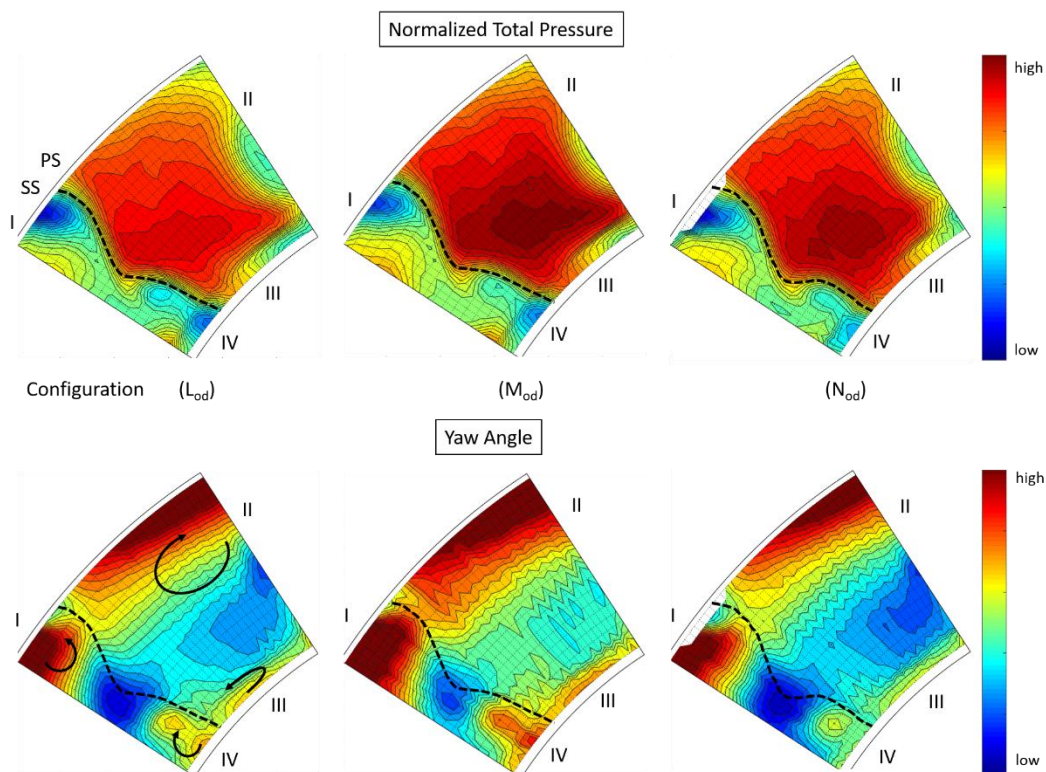


Figure 12.5: Aerodynamical flow fields – Configurations (L), (M) and (N) – Off-design point

12.3 Inverse Cut-off Vane Design Including Microperforated Absorbers

This section is about further acoustical investigation results, started with the work of Barro Savonuzzi [95], onto a vane design including the same acoustic absorbers as integrated in the Resonator vane design, described in section 4.3.2. Both designs are identical with respect to the number of openings per cavity and their diameter as well as the volume size of the cavity.

Figure 12.6 shows the TEGV with the three included resonators indicated by the sixty small openings for each cavity. It is obvious, that the number of vanes is much higher compared with the Standard turbine exit casing. This TEC is named Inverse Cut-off TEC and is intended to remove the acoustic interaction modes of the rotor and the turbine exit guide vanes. Also the scattered modes of any other airfoil interaction are cut-off. Further information concerning the vane design can be found in Broszat et al. [106], from a numerical point of view, and in Broszat et al. [107] in which an experimental comparison of the Standard TEC and the Inverse Cut-off TEC is presented.

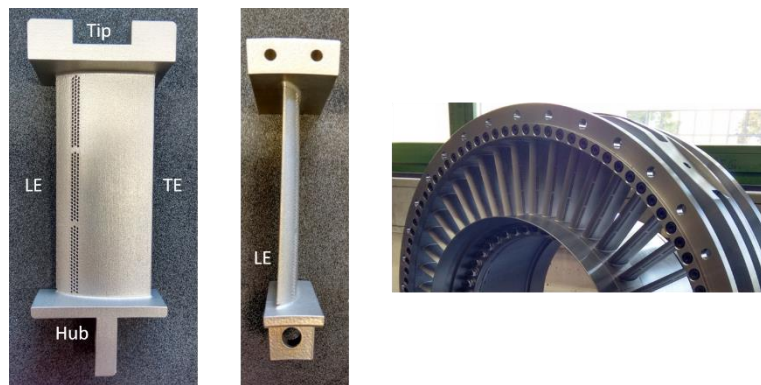


Figure 12.6: Inverse cut-off vane design (left and middle) and section of the equipped TEC

In the work [95] also this vane design showed different resonance frequency in the test concerning the reflection coefficient and the side branch tests, as was already mentioned for the Resonator vanes. It is assumed, that this variance (between 5 and 8%) is due to the different incident angle of the incoming sound wave. Test rig investigations did not show much of a change in the sound power level. Some conclusions were drawn, that maybe the neck diameter is too small for such an application and the area is too small respectively, or that the dimensions of the resonator cavity exceed the length of a quarter wavelength. At the frequency of interest, almost half of the wavelength fits into the cavity, which could be another reason of why the calculated resonance frequency does not fit to the tested one.

Nevertheless, later investigations showed with a wide reduction of the broadband noise a different result, which are shown in this section of the appendix. This result also fits to the theory behind this type of absorber.

It is again a comparison of a baseline setup consisting of acoustically hard vanes as well as acoustically hard end walls and a setup including absorbing vanes. The baseline design is named from now on configuration (O) and the setup including the absorbing vanes configuration (P).

Following Figure 12.7 presents the comparison of the sound pressure level over whole measured frequency range for both setups. It can be clearly seen, that using setup (P) results in a reduction of the broadband noise in a wide region of almost 6 kHz. The difference is nearly constant with a value of around 1.2 dB. A peak reduction of 1.9 dB at the 1st BPF and 2.2 dB at the 2nd BPF is achieved. At the 1st vibration frequency (VF) a decrease in SPL of almost 3 dB is visible.

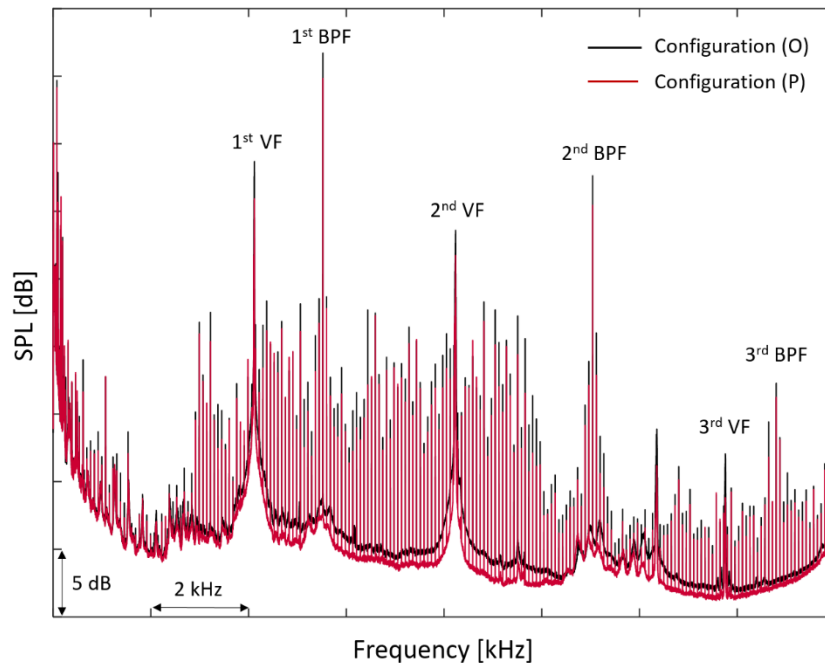


Figure 12.7: Frequency spectra – Configurations (O) and (P)

A zoom into the frequency range of reduced SPL is given in Figure 12.8. It can be seen, that there is not an obvious area of peak reduction as seen in the cases of the configurations using soft end walls. Also when comparing with the setup containing the Resonator vanes (see section 6.2.4), which include the same absorbers from a geometrical point of view, no such wide broadband noise reduction could be identified there.

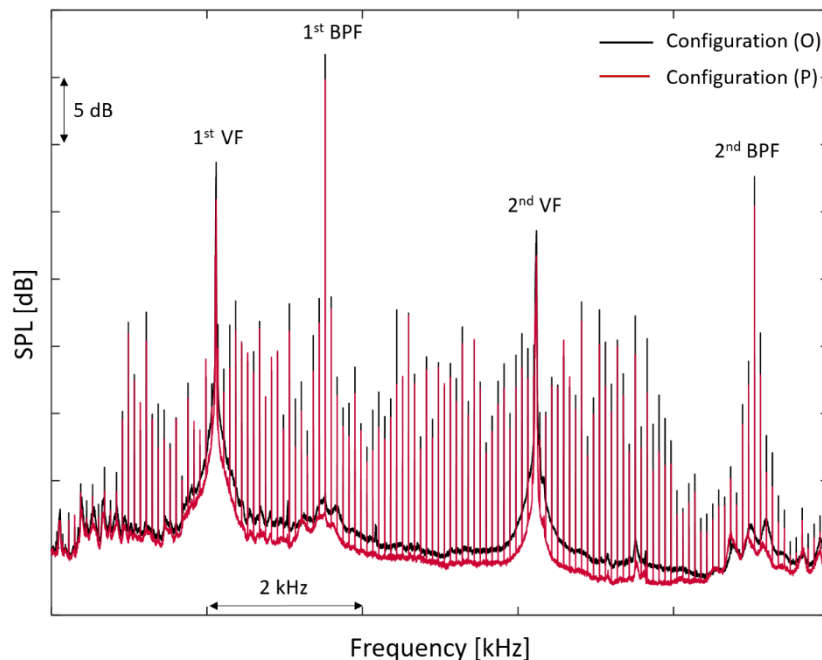


Figure 12.8: Frequency spectra – Configurations (O) and (P) – Zoom in

The overall sound power level for all cut on modes is presented in Figure 12.9, showing in black a propagation direction in flow direction and in yellow against the flow direction. A reduction of 2.9 dB in flow direction is obtained by using the vanes including absorbers (setup

(P)). Against the flow direction, the reduction is of 1.5 dB. It is assumed, that the wide decrease of broadband noise can be addressed to this significant reduction.

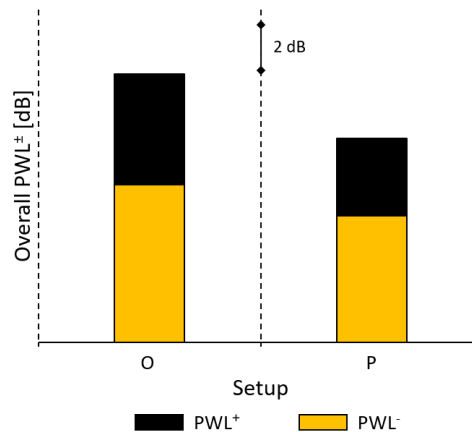


Figure 12.9: Overall PWL[±] - Configurations (O) and (P)

Figure 12.10 presents a comparison of both setups concerning the PWL change of each mode order m in and against flow direction. Although all interaction modes with the TEGVs are cut-off, a remarkable reduction concerning other modes is visible. Especially the modes against flow direction indicated by the orange bars seem to have a more significant decrease.

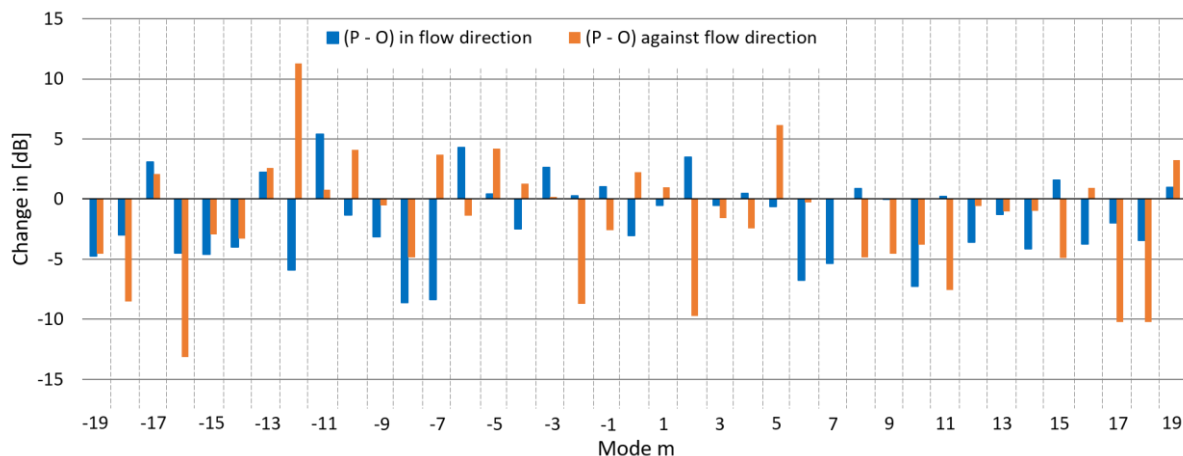


Figure 12.10: PWL[±] change of cut-on modes – Configurations (O) and (P)

Figure 12.11 presents a comparison of both designs focused on the difference in PWL with respect to the spinning direction of the modes. The shown values result from a subtraction of the baseline setup (O) from the acoustically treated one (P). It can be observed, that the positive spinning modes are reduced by 4.1 dB, followed by the 0 mode with 3.1 dB and the sum of the negative spinning modes with 1.2 dB, all in flow direction, when using setup (P). This result with having the highest attenuation in flow direction for positive spinning modes is different to the ones observed in section 6.2.5. There, all vane designs including absorbers had the highest reduction in flow direction at a negative spinning direction.

For the propagation direction against the flow direction, this setup shows an increase of 2.3 dB concerning the 0 mode and a reduction of 1.1 dB and 1.9 dB for the positive and negative spinning modes respectively. This result is equal, besides the increase of the 0 mode, to the ones found in section 6.2.5.

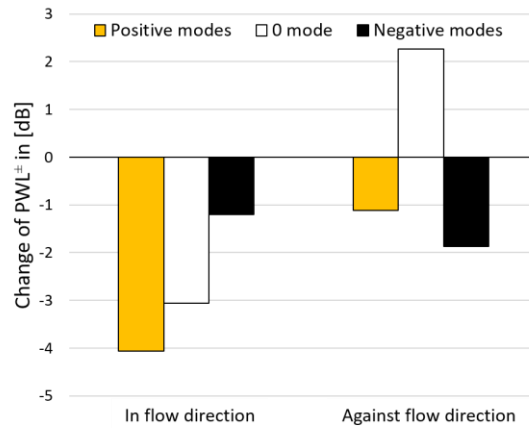


Figure 12.11: PWL^\pm change regarding the mode spinning direction – Inverse cut-off TEC

In the work of [95] a result concerning impedance tube measurements was found, which showed a double peak of low absolute reflection coefficient, but could not be explained at that time. A similar result was stated in the work of Etaix et al. [103] and is shown in Figure 12.12. They tested an asymmetric absorber cavity with respect to the neck opening. This resulted in a second peak of high transmission loss (indicated by the red line in Figure 12.12)

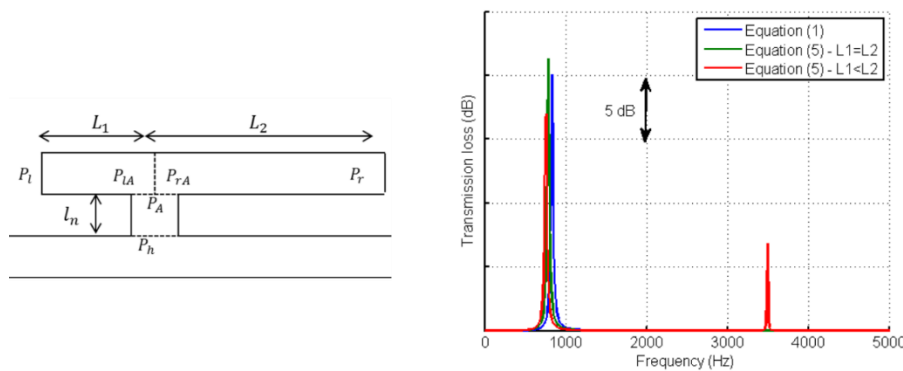


Figure 12.12: Asymmetric Helmholtz absorber (taken from [103])

Comparing this geometry with the one investigated in [95], similarities can be found. Also there, the cavity volume is not symmetric with respect to the neck openings, which can be seen on the left side of Figure 12.13. On the right side of this figure, the reflection coefficient distribution concerning a different number of open absorber necks is shown. Herein, the double peak can be clearly seen. This leads to the assumption, that this is the same behaviour as presented by [103].

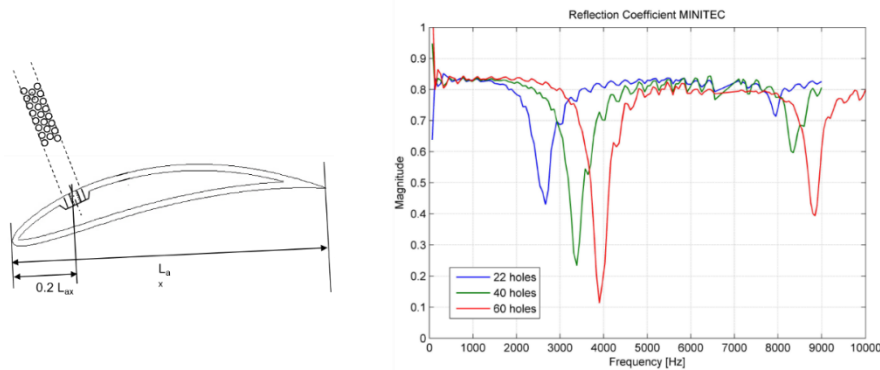


Figure 12.13: Reflection coefficient result - Inverse cut-off TEC (adapted from [95])

12.4 Peak Reduction Procedure

One of the results after post processing the data obtained by performing acoustical measurements is a distribution of the sound pressure level over the frequency, shown in following figure.

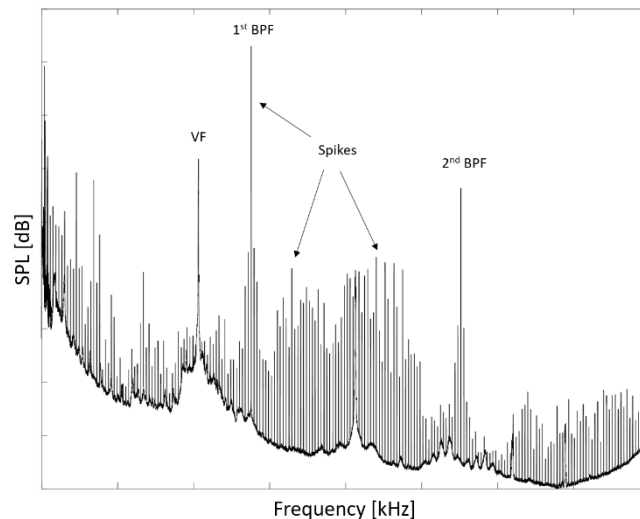


Figure 12.14: Frequency spectra

As can be seen, there are many spikes included which are not of use when investigating the background noise. Therefore, firstly a filtering of those spikes is done using the matlab command *medfilt1*. After doing so, the result looks like follows. On the left side of Figure 12.15, the frequency spectrum and the distribution without spikes are shown in black and red respectively. The right side presents only the curve excluding the unneeded spikes. It can be seen, that there are still peaks included (VF, 2nd VF) which have to be reduced in order to obtain only the background noise.

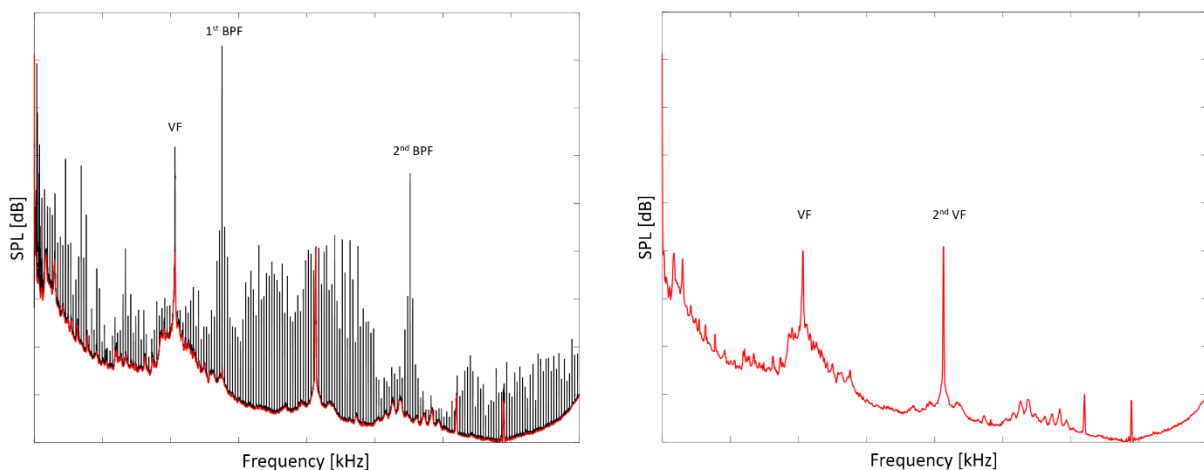


Figure 12.15: Frequency spectra with filtered result (left) and filtered distribution alone (right)

Therefore, another filtering of the result is done using the matlab function *envelope*. With this function, the lower as well as the upper envelope of a curve can be calculated. This leads to the following result shown in Figure 12.16, where the signal without spikes is indicated in red and the lower envelope of this distribution is given in green. It is visible, that now the unwanted peaks are gone and only the background noise is left.

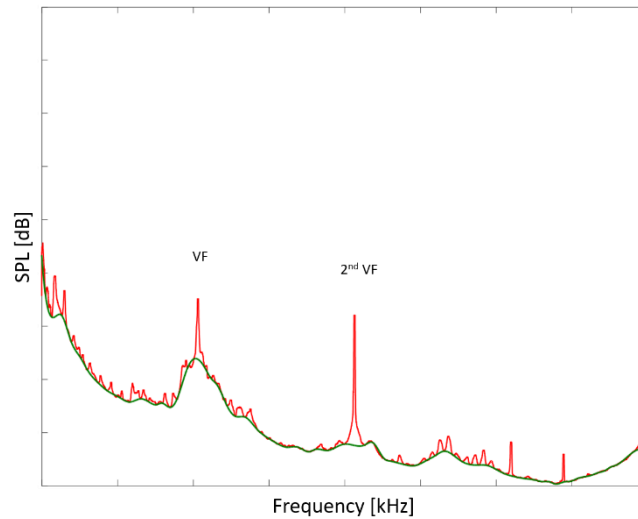


Figure 12.16: Filtered signal with lower envelope

After running this procedure for the wanted setups, the resulting envelopes are simply subtracted. This results than in the SPL difference shown for the riblets configurations in section 6.2.6 (see Figure 6.69 and Figure 6.70).

During the investigation made onto this procedure, it could be seen that making first a filtering of the signal followed by the envelope function gives a better result than simply calculating the envelope at first place. The following figure shows the difference. In red, again the SPL distribution without the spikes is shown, in green the envelope of this distribution and additionally in blue, the envelope of the frequency spectra shown in Figure 12.14 is presented. It can be clearly seen, that the green line is following the red one, which is basically the result of Figure 12.14 but without peaks, much better than the blue curve.

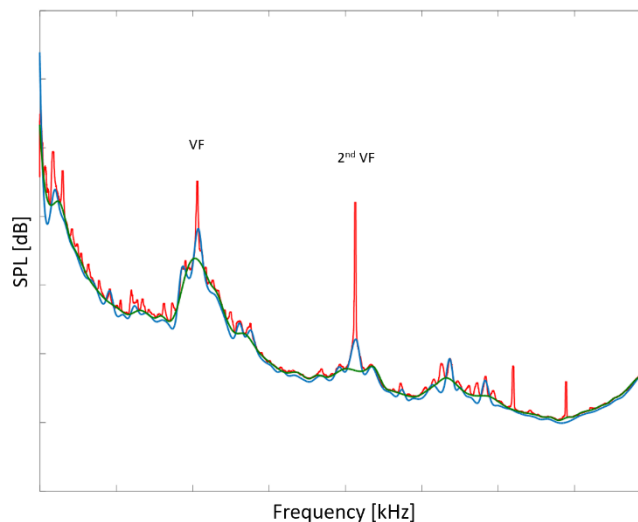


Figure 12.17: Comparison of lower envelopes